Initiation and Growth of Reaction in LLM-105

Sara French

Newnham College

May 2018

This dissertation is submitted for the degree of Doctor of Philosophy

Declaration

This dissertation is the result of my own work and includes nothing which is the outcome of work done in collaboration except as declared in the Preface and specified in the text. It is not substantially the same as any that I have submitted, or, is being concurrently submitted for a degree or diploma or other qualification at the University of Cambridge or any other University or similar institution.

Abstract

The aim of the research conducted in this thesis was to understand the behaviour of LLM-105, a new explosive material, when subjected to impact. Explosive reactivity under impact can be thought of in terms of safety (sensitiveness) and response to shock loading (sensitivity). The experimental work presented addresses both regimes, using hot-spot theory to support the observations made.

The literature review discusses material properties that contribute to changes in sensitivity. This motivated modification of LLM-105 to provide different particle sizes and morphologies for assessment and comparison with other explosives. Impact sensitiveness is of particular interest for LLM-105 as there are some discrepancies in the literature data, owing to different methods being used to assess it in different countries and laboratories.

Improved methods for characterising impact sensitiveness had to be developed in order to fully evaluate the LLM-105, enhancing a glass anvil drop-weight technique with multiple diagnostics, including high speed camera, mass spectrometer, photodiode and microphone. This equipment provided an ideal research tool for simultaneously assessing the reaction outputs of an explosive, and highlighted limitations of standard techniques used by industry.

The characteristics of pristine and modified LLM-105 were evaluated using the drop-weight. It was found that particle size influenced reactive response, though presence of defects had a greater effect on initiation sensitiveness. Also, reaction growth was more strongly related to the particle shape and overall bulk density of the material, likely to be linked to packing efficiency of the particles. It was also found that LLM-105 was more sensitive to impact in general than previously thought, when compared to explosives such as HMX and TATB.

The final chapter of this thesis examines LLM-105 behaviour under shock loading. LLM-105 was formulated with a fluoropolymer binder and detonated under a one dimensional shock regime with in-material gauge analysis. Data was acquired for two new LLM-105 formulations with respect to detonation velocity and growth of reaction within the explosive. The results showed that fine particle size LLM-105 has a shorter run distance to detonation than coarse, which is likely caused by the number of potential hot-spot sites available in voids within the pressed formulation.

Acknowledgements

The research described in this thesis was sponsored by AWE, and I am grateful for both the funding and the support received from the staff in the Explosive Materials group (too many to name). The people that gave me time for useful technical discussions, and those that tolerated me being away from my day job to allow me to complete this work part-time over a number of years.

I have to thank the Surfaces, Microstructure and Fracture Group for making my time at Cambridge enjoyable, and for clearing lab space for me when I was desperately working to a deadline – which was often. Particular thanks go to Andy Jardine and David Williamson for their everlasting patience with my chaotic schedule. The people at the Cavendish made it a great place to work and I am incredibly fortunate to have been able to conduct my studies there.

A portion of the experimental work was completed at Cranfield University, Shrivenham, and thanks go to the Formulations team for their assistance; and to Andy and Mike in the gun sheds - for both their expertise and enthusiasm.

"There is no education like adversity" – *Benjamin Disraeli*

Contents

Acronyms

CHE	Conventional High Explosive
CJ	Chapman-Jouget
CL-20	Hexanitrohexaazaisowurtzitane
DDT	Deflagration to Detonation Transition
DMF	Dimethyl Formamide
DMSO	Dimethyl Sulfoxide
DSC	Differential Scanning Calorimetry
EMTAP	Energetic Materials Test and Assessment Panel
ESEM	Environmental Scanning Electron Microscopy
FT	Fourier Transform
HE	High Explosive
HMX	Octahydro-1,3,5,7-tetranitro-1,3,5,7-tetrazocine
HNS	Hexanitrostilbene
HTPB	Hydroxyl-terminated Polybutadiene
IHE	Insensitive High Explosive
LANL	Los Alamos National Laboratory
LED	Light Emitting Diode
LLM-105	2,6-diamino-3,5-dinitropyrazine-1-oxide
NMP	N-methyl-pyrrolidinone
NO	Nitric Oxide
NQR	Nuclear Quadrupole Resonance
NTO	3-nitro-1,2,4-triazol-5-one
PBX	Polymer Bonded Explosive
PETN	Pentaerythritol tetranitrate
PV	Particle Velocity
RDX	1,3,5-trinitro-1,3,5-triazinane
RS-RDX	Reduced Sensitivity RDX
SEM	Scanning Electron Microscopy
SDT	Shock to Detonation Transition
TATB	1,3,5-triamino-2,4,6-trinitrobenzene
TMD	Theoretical Maximum Density
TNT	2-methyl-1,3,5-trinitrobenzene

Chapter 1: Introduction

A chemical explosion is an exothermic reaction driven by the release of heat and a positive entropy change (the evolution of gases), which is both rapid and irreversible. An energetic material is a substance containing stored chemical energy which has the ability to be released quickly; it is able to undergo such a reaction owing to its chemical nature.

Organic energetic molecules typically contain $–NO_2$, $-ONO_2$ or $–NHNO_2$ groups, which decompose rapidly upon a sufficiently strong stimulus to give highly stable (and hence thermodynamically favourable) combustion products such as carbon dioxide, carbon monoxide and dinitrogen. The energetic molecules have a relatively high nitrogen content, and are often comprised of a strained ring molecular structure.

It is possible for an energetic reaction to be created with a compound where the energetic reactive constituents are not molecularly bound together; these are mixtures of oxidisers and fuel which can be held together with a binder component, or simply a mixture of air and fuel, which is given the appropriate stimulus to release energy. The energy is released in the form of heat, pressure, light and sound; which can be applied to a variety of purposes such as mining, demolition or military applications, depending on the rate of the decomposition reaction in the material.

Energetic materials are employed in a variety ways; for explosives, propellants and pyrotechnics. Propellants and pyrotechnics are designed to deflagrate or burn (subsonic combustion) and produce heat - these are known as low explosives. A high explosive (HE) is an energetic material capable of detonation, where the reaction moves through the material faster than the speed of sound.

Explosives do not spontaneously detonate; they require an initial stimulus which can be provided by shock, impact, heat, friction or static for example. An explosive that requires very little energy input in order to react (i.e. it is very sensitive) is known as a primary explosive. These are typically only used in small quantities in order to prevent any unintentional damage to surroundings. Suitable applications may include a detonator, to trigger larger explosive components in an initiation train. The larger explosive part is chosen to be safer to handle (more difficult to initiate), and be what is known as a secondary explosive.

A secondary explosive requires more energy to be initiated, and because they are less sensitive, they are used in a wider variety of applications. An example of a secondary conventional high explosive is HMX (octahydro-1,3,5,7-tetranitro-1,3,5,7-tetrazocine, **Figure 1.1**), which possesses comparatively high thermal stability, high density and high detonation velocity [1]. These properties make it suitable for use as a pressed powder, in castable mixes and as a polymer bonded explosive (PBX). Other common examples of conventional high explosives include 1,3,5-trinitro-1,3,5-triazinane (RDX) and 2-methyl-1,3,5-trinitrobenzene (TNT).

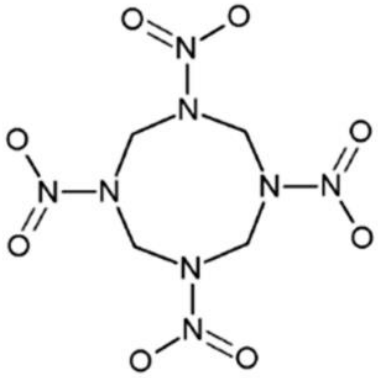

Figure 1.1: Molecular structure of HMX

1.1 The Requirement to Formulate a Polymer Bonded Explosive

PBXs are formulated to improve mechanical and safety properties of an explosive. This typically involves blending crystalline energetic powder with inert polymers, plasticisers and antioxidants. The result is a molding powder consisting of explosive particles that are evenly coated with a layer of polymeric binder, where the binder proportion for solid PBXs is often between five and fifteen weight percent of the formulation. However, the addition of inert ingredients dilutes the power output of the explosive, and a compromise must be met between optimising mechanical and safety characteristics, and achieving the performance required. It is possible to formulate compositions with energetic plasticisers; these contribute somewhat to the energetic output and this reduces the deficit.

Once formulated with the relevant ingredients, PBX powder is pressed into a consolidated body, or charge, which is heterogeneous in nature. The polymer component

holds the composite together, and prevents cracking of the pellet. Physical properties of the pre-formulated binder may translate to the physical and mechanical properties of the pressed PBX; for example a low viscosity binder may result in a product that slumps or creeps. A stiff binder can lead to a hard or brittle PBX that may be more susceptible to impact or friction sensitiveness.

It is of interest to note that the long-term life ageing of a material is a key issue, as all components of a PBX will degrade over time. Cured polymers such as HTPB can cross-link further resulting in hardening and embrittlement of the formulation, which potentially leads to changes in the mechanical and therefore safety properties of the material. A harder or more brittle explosive would be expected to be more sensitive to impact or friction. However antioxidants can be included in formulations with binders that may be vulnerable to this mechanism, to inhibit this ageing effect.

Typically explosive formulations have the following material requirements; mechanical integrity so that a pressed pellet will maintain its shape and physical status over a period of time; and the performance of the explosive must be such that it will initiate reliably from a shockwave and propagate a detonation wave. These factors cannot compromise the safety of the material. For an explosive to be safe, it must remain in an inert state when not required, and react predictably when initiated [2]. As such, it is a necessity to thoroughly characterise new explosive materials, and sensitiveness can be measured by likelihood of reacting to certain levels of impact, friction, heat and electrostatic discharge. If an explosive or its formulation fails to qualify as ‘safe’ for its intended purpose and environment, it is immediately rendered unusable.

1.2 The Detonation of an Explosive

Detonation is a decomposition reaction where the propagation velocity of that reaction is greater than the speed of sound in the explosive material [1]. It is a supersonic reaction wave; gas and heat are produced as a result of the reaction, and this hot, high pressure gas can be applied to do useful work.

A detonation wave exists as an explosive material reacts to a shockwave or initiation source, and just behind the shock front is the reaction zone. The reaction zone can be within a range of sizes depending on the material, from 1 mm up to 12 mm thick in the case of ammonium nitrate/fuel oil (ANFO) [3]. The exothermic reaction is constantly contributing to the energy of the ongoing detonation wave. Steady state detonation is

achieved when the energy lost to heat and expanding gas is in equilibrium with the energy generated at the shock front, and the wave is stable and self-sustaining; hence the wave travels at constant velocity.

The mass, momentum and energy are conserved across a one-dimensional shock front; this process may described using the Rankine-Hugoniot jump relations. The original pre-shocked material at rest has a pressure of P_0, with a density of ρ_0 and an internal energy of E_0. A shock travelling at the speed U_s is introduced and once the shock front has passed through, the material is under a new pressure P_1, at density ρ_1 and has internal energy per unit volume of E_1. The shocked material propagates in the direction the shock is travelling in at a particle velocity, u_p (see **Figure 1.2**). The relationship between these properties is governed by the Rankine-Hugoniot equations;

$$\rho_0 U = \rho_1 (U - u_p), \qquad \text{(eq 1)}$$

$$P_1 - P_0 = \rho_0 U u_p, \qquad \text{(eq 2)}$$

$$E_1 - E_0 = \frac{1}{2} u_1^2 \left(\frac{P_1 + P_0}{P_1 - P_0}\right) \qquad \text{(eq 3)}$$

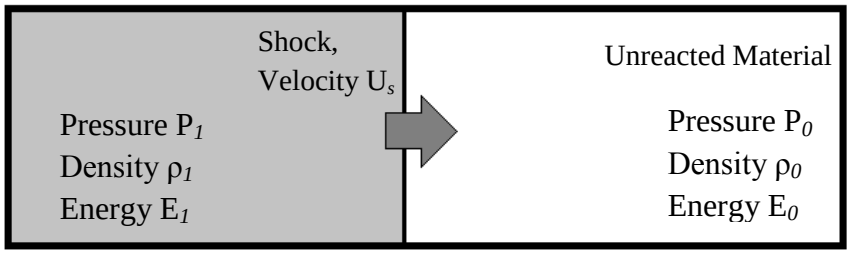

Figure 1.2: A diagrammatic representation of the shock transition moving through unreacted material. The pre-shocked material has a pressure of P_0, with a density of ρ_0 and an internal energy of E_0. A shock travelling at the speed U_s is introduced and the material takes on a new pressure P_1, at density ρ_1 and has internal energy per unit volume of E_1. The shocked material is travelling at a particle velocity, u_p

A Hugoniot (the graphical representation of all of the possible thermodynamic states of the singly shocked material (**Figure 1.3**) can be plotted by experimentally

deriving the equation of state and plotting the variables in U_s - u_p or P-v space, where v is the specific volume. Many materials have a linear Hugoniot in the U_s - u_p plane. For a particular shock velocity or shock pressure, the mass and momentum equations can be used to draw a line in the same space as the Hugoniot, termed the Rayleigh line.

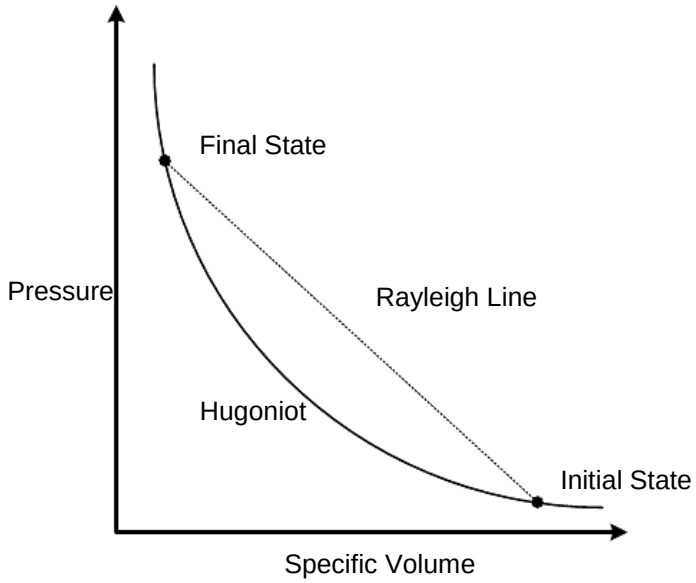

Figure 1.3: An example of a shock Hugoniot, intersected by the Rayleigh line

The Rayleigh line defines the possible shock states of the material for a given shock parameter, as it transitions from the ground state onto the Hugoniot. The intersection of the Rayleigh line with the Hugoniot defines the shock state of the material at that shock velocity or pressure.

Once shocked, a material will transition down to an end state through a number of releases, known as rarefaction or relief waves. The relief waves are not steady state, and they will eventually reach the shock front and destroy the steady state shock wave. These release waves exist as a large number of small steps with differing velocities and bring the pressure in the material back down to zero. The release is along an isentrope (line of constant entropy) rather than the Hugoniot, but the condensed material in the release wave exists as states on the P- u_p curve, meaning that the difference between the Hugoniot and the relief wave is very small for practical assessment and therefore they can be treated as the same. This assumption applies to inert materials only.

Shock and detonation waves have similar properties, and therefore a Hugoniot can also be used to represent a detonated explosive, however the material before and after

detonation will have two different Hugoniots due to the chemical reaction undertaken. In a pressure-volume plot where the unreacted Hugoniot is plotted next to a reacted Hugoniot (**Figure 1.4**), the point at which the Rayleigh line connects the two is known as the Chapman-Jouget (CJ) point.

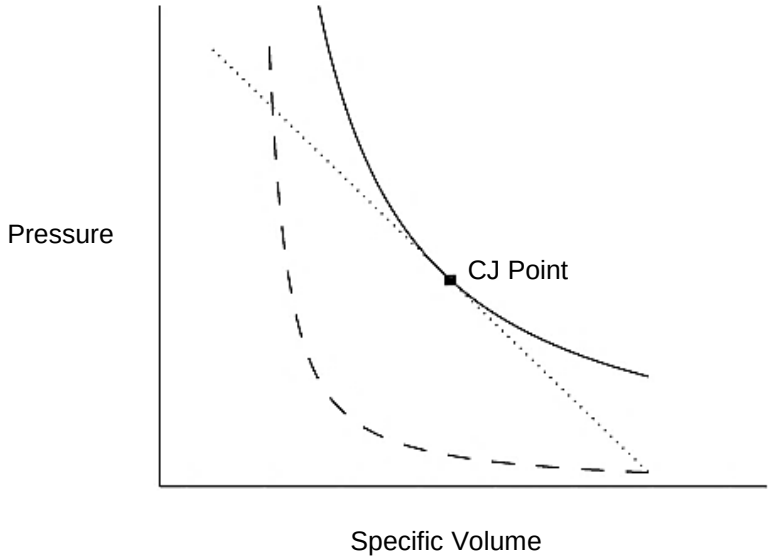

Figure 1.4: An unreacted Hugoniot (dashed line) is mapped next to a reacted Hugoniot (solid line). The point at which the Rayleigh line (dotted line) tangents the reacted Hugoniot is known as the CJ Point, representing the instantaneous transition from unreacted to fully reacted material states

The CJ point represents the instantaneous transition from unreacted to fully reacted material states, though the analogy is a simplification, and since the 1940s ZND theory (owing to Zeldovich, Von Neumann and Doering) has suggested that the reaction zone has a finite thickness, which varies according to material as it transitions through several Hugoniot states before reaching a fully reacted state.

The detonation wave is structured with a leading spike – referred to as the von Neumann spike. In reference to **Figure 1.4**, the Rayleigh line intersects the unreacted Hugoniot at the Von Neumann spike pressure. Hence it is possible to experimentally determine the Von Neumann spike if the unreacted Hugoniot of a material is known. Behind this spike lies the reaction zone, and the Chapman-Jouget (CJ) plane, which is characteristic of individual formulations and their densities. The CJ state describes the chemical equilibrium of the products in the reaction zone of the detonation wave. As the

reacting material produces expanding gases, there is a drop in pressure, which is known as the Taylor wave.

Detonation of an explosive is usually initiated by a detonator to instantly cause the transition from unreacted to reacted state from a single point-like source. However, experimentally, the input shockwave to achieve detonation should be considered one dimensional; planar rather than a point source; as a three dimensional assessment is too complex for both the design of an experiment, and the data analysis.

An experiment can be considered one dimensional by ensuring the material is subjected to uniaxial strain only; i.e. along the axis of the shock and with a sample geometry designed to be unaffected by lateral release waves. A high velocity flyer can be used to input a sustained one dimensional single pulse into the explosive for assessment, see **Figure 1.5**. The following reaction is then monitored using appropriate gauge diagnostics, which are placed in the 1D region of the sample. There is greater discussion on this topic in Chapter 6.

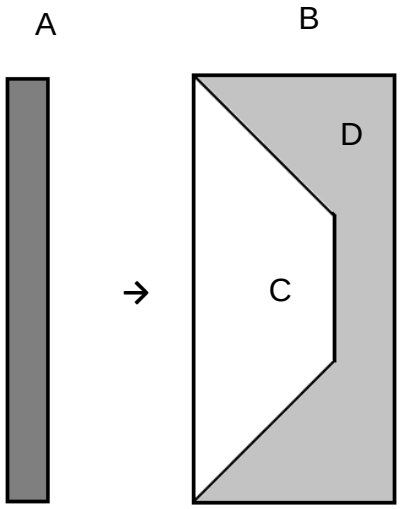

Figure 1.5: The flyer plate (A) impacts the target sample (B) and generates a shock through the material. Diagnostics are placed in the 1D zone (C) which is unaffected by the release waves moving inwards from the regions around the edges of the sample material (D)

The input shock velocity that the target receives can be varied by altering the velocity the flyer is travelling at, and the acoustic impedance of the flyer itself. A

material's characteristic acoustic impedance is a constant relating to the propagation of sound waves through it, and is defined as the product of its density and velocity according to Equation 4:

$$Z = \rho\, U_s \qquad \text{(eq 4)}$$

The impedance of a material can be experimentally determined by plotting the material's Hugoniot in the $U_s - u_p$ plane (which is linear in many cases) and determining the bulk sound speed, C_0. The bulk sound speed is the y-axis intersection of the graph, as per the following relationship:

$$U_s = C_0 + S\, u_p \qquad \text{(eq 5)}$$

Additionally, C_0 can be calculated by measuring the materials adiabatic bulk modulus (K_s), and S varies with K_s as shown below in Equations 6 and 7:

$$C_0 = \sqrt{\frac{K_s}{P}} \qquad \text{(eq 6)}$$

$$S = \frac{dK_s}{dP} + 0.25 \qquad \text{(eq 7)}$$

If the response of a material in $U_s - u_p$ space is linear, then material states can be represented in the Pressure Volume plane (as shown in **Figure 1.4**), transitioning from an initial state (P_0, V_0) to a reacted state (P_1, V_1) and linked by Equation 8:

$$P = \frac{C_0^2(V_0 - V_1)}{\left(V_0 - S(V_0 - V_1)\right)^2} \qquad \text{(eq 8)}$$

This equation represents defines the locus of final states accessible from single shock loading. The transition between the two states (i.e. graphically, the Rayleigh line) is defined by Equation 9.

$$P = \frac{U_s^2}{V_0}\left(1 - \frac{V_1}{V_0}\right) \quad \text{(eq 9)}$$

For a detonation to occur, the explosive material must be initiated. Initiation can be caused by impact, friction, heat, spark or shock being imparted upon the explosive. In the majority of designed applications for explosives, initiation is supplied by a purpose-built detonator which provides the shock wave to initiate the HE and thus detonation of the charge is achieved.

1.3 Initiating an Explosive: Hot-spot Theory

It is generally understood that initiation in heterogeneous explosives begins in localised heated regions known as hot-spots [4]. These are caused by the application of a stimulus to the explosive that heats a small volume of material around a heterogeneity, which will then begin to decompose and propagate reaction. Growth of reaction occurs through competing mechanisms of energy release (heating the explosive) and energy dissipation (cooling the explosive). If there is enough heat generated, the result is an accelerating and self-sustaining reaction which will propagate through the HE.

Hot-spots capable of causing ignition are in the order of 0.1-10 μm, require a temperature of at least 700 K and must last for 10^{-5} seconds [4]. These are known as critical hot-spots. It has been stated that there is no single dominant mechanism for the development of hot-spots [5], and the process of their formation will depend on the chemical, thermal, physical and mechanical properties of the explosive.

There are several mechanisms that contribute to the evolution of hot-spots. The most widely recognised mechanism is adiabatic compression of gases inside voids [5] (i.e. tiny bubbles) within the composition. The voids are compressed due to the shockwave passing through the material around them, they collapse asymmetrically, and the gas within the void is subjected to adiabatic heating. Multiple hot-spots occur across a small volume and heat the surrounding material. It is suggested that if these pockets were not present in the composition, sufficient propagation of the reaction would not occur; this is

true for both liquid and pressed solid explosives [4], and higher sensitivity is observed for more porous explosives [6].

There will be a material density (dependant on the individual formulation) that detonation via the hot-spot mechanism cannot take place [7]. Hence to allow for detonation, PBXs are not pressed to one hundred percent of their theoretical maximum density, although in practice this would be difficult to achieve.

Other hot-spot mechanisms include the cavity collapse of binder material that has undergone viscous heating. Friction between sliding or impacting surfaces, or any particulate contamination which may be in the composition can lead to hot-spots developing, as can the viscous heating of material that is rapidly squeezed between impacting surfaces [5]. Heating can also be caused by localised adiabatic shear bands formed by plastic deformation; if the bands are greater than a 1 μm sized area, then critical hot-spots are formed [8]. Heating at crack tips or at dislocation pile ups can occur [5]; all of the scenarios discussed here are likely causes of the formation of hot-spots in PBXs.

There are two additional mechanisms for hot-spot initiation to be aware of; these consist of ignition caused by spark discharge or triboluminescent discharge [5]. These mechanisms are less influential in this study due to the nature of the testing undertaken.

The relatively slow propagation of reaction in an explosive from hot-spots to detonation is known as the deflagration to detonation transition (DDT) [9], and a shock front is eventually created. The rate of acceleration of the reaction to steady state detonation will depend on the physical properties of the pressed formulation, such as density and void structure. Voids can be trapped within the explosive crystal, or within a region of binder, and they also form at crystal-binder interfaces, particularly for particles with rough surfaces.

The energy released from the reacting sites (hot-spots) creates small regions of high pressure and temperature that coalesce and continue to grow. If the reacting sites are too few in number or on too short a timescale then the reaction will decay and die out. However, if the reaction growth reaches a critical temperature and pressure, and acceleration to detonation is supported, then DDT is achieved.

Under the correct conditions high explosives can undergo an almost instant transition to detonation, when subjected to a sufficiently strong shock. Detonators are often used for this purpose. This is referred to as a shock to detonation transition (SDT), and requires a high level of compression to cause sufficient adiabatic heating for the detonation

to take place. The duration of the hot-spots is shorter compared with DDT; therefore the pressure within the material must be higher to result in the required temperature increase.

Primary explosives can be initiated to detonation with a small amplitude shock, with less than microsecond timescale pulse widths. A more sensitive secondary explosive requires a few kbar pressure and a microsecond timescale pulse width to initiate, but a secondary high explosive that may be used in a large charge application requires several kbars of pressure to initiate [10].

The pulse width of the shock must sustain the exothermic reaction until the SDT has occurred; otherwise relief waves sweeping over the area reduce and decay the shock. Steady state detonation (i.e. detonation at constant velocity, where the loss of energy is in equilibrium with the reacting material and propagating shock) is not achieved at the boundary where a shock is introduced to an explosive. The energy released from the chemical reaction has to support the shock in order to accelerate toward a steady state detonation.

At very high shock input pressures, a competing initiation mechanism takes place. This is known as thermal homogeneous initiation [10] and is caused by bulk temperature increase raising the mass of explosive above its critical thermal initiation temperature. As the material thermally explodes, additional high pressure waves build towards a steady state detonation. This mechanism is typically seen in homogeneous explosives (liquids), but it becomes active in heterogeneous explosives at very high shock pressures [10].

It has previously been shown that particle size and structure in heterogeneous charges can affect the time to detonation transition [11], and experiments using RDX (cyclotrimethylene-trinitramine) have shown there is also a significant effect on the critical diameter of detonation [12] caused by varying particle size; thus it is probable that particle size of the HE will affect the build-up to detonation and other reactive properties in this study. This theory is discussed in greater detail in the next Chapter.

1.4 LLM-105 as a Candidate Low Sensitiveness Explosive

There is a drive to replace conventional high explosives (CHEs) with low sensitiveness, low explosiveness materials, formerly referred to as insensitive high explosives (IHEs) which have improved safety properties and are less likely to detonate in an accident scenario. TATB (1,3,5-triamino-2,4,6-trinitrobenzene; **Figure 1.5**) is an example of such an explosive, and it has reduced sensitivity to impact and shock. The

reduction is due to the graphitic nature of TATB molecules; they are arranged in planes linked by π-stacking interactions, which allow layers to slide over one another and disperse impact pressure [13]. An issue with improving the safety of a material by using TATB as the explosive filler is that it is less powerful and more difficult to initiate, therefore care is required to prevent unreliability in an initiation train.

Recently, LLM-105 (2,6-diamino-3,5-dinitropyrazine-1-oxide; **Figure 1.6**) was developed as a potential low sensitiveness, low explosiveness (IHE-type) candidate at Lawrence Livermore National Laboratory. Like TATB, it consists of a planar conjugated molecular structure, with spacing between layers [14], however these layers form zig-zag packing sheets similar to solid state benzene [13], [15]. This structure contributes to LLM-105 possessing thermal and shock sensitivities lower than HMX, but greater than those of TATB [16]. Its energy content has previously been calculated to be 85 % of HMX and 20 % more than that of TATB, whilst demonstrating a high thermal stability [17][18].

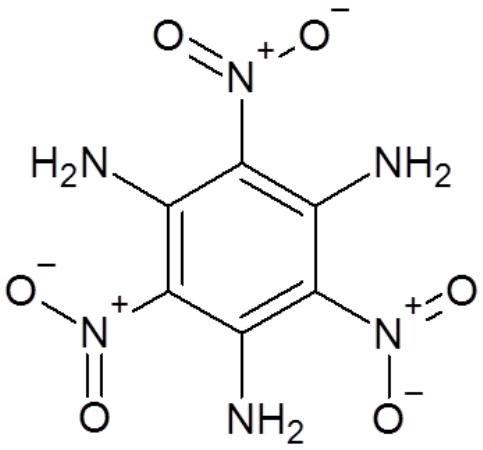

Figure 1.6: Molecular structure of TATB

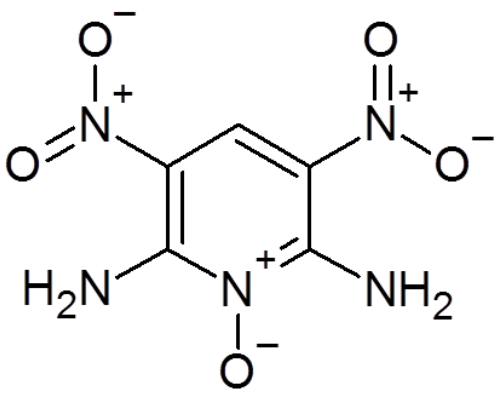

Figure 1.7: Molecular structure of LLM-105

The properties of LLM-105 that position its safety and performance characteristics between a CHE and an IHE-type material make it an interesting explosive to study, with the potential to produce formulations with improved safety characteristics and a comparable power output to HMX.

1.5 Research Objectives

LLM-105 is currently a new material of interest for developing explosive formulations with improved sensitiveness while maintaining a high level of performance. The aims of this research are to understand how LLM-105 responds to mechanical stimuli and compare it with existing explosives. It's sensitiveness with respect to impact is of particular interest as a range of different methods for assessment exist, and can lead to conflicting results. As such, LLM-105 has been modified in its particle size and shape (Chapter 3), investigated for impact sensitiveness using an improved experimental technique (Chapter 4 and Chapter 5), and two different particle sizes of material have been formulated and characterised for performance using a high fidelity in-material gauge technique (Chapter 6). The conclusions from this work will provide comparison of LLM-105 with existing explosive materials, and yield insights into its underlying behaviours.

Chapter 2: The Sensitivity of Explosives

The sensitivity of an explosive is important to understand for both safety and material performance reasons. Sensitivity refers to an explosive response to shock, where sensitiveness is a safety-related term (to be discussed in greater detail in Chapter 4). In an accident scenario, understanding the sensitiveness of a composition to a relevant stimulus allows for mitigation of risk of detonation.

From a performance perspective, it is beneficial to know how a material behaves in response to various stimuli to aid the design of new materials. For certain applications a formulation may need to have particular reaction characteristics, which initiation and growth of hot-spots will affect depending on the materials sensitivity.

Shock sensitivity is a measure of the stimulus required to initiate detonation in an explosive, when subjected to a shock through a high velocity impact mechanism or design-built detonation. There are both safety and design implications related to the assessment of an explosive's shock sensitivity. For example, it is possible that high velocity impact on a system containing explosives may lead to sympathetic detonation in an accident scenario. It is useful when designing explosives and their initiation trains to understand where the transition to detonation occurs with either increasing or decreasing shock, or the thickness of the containment.

There are a number of ways to measure the shock sensitivity of an explosive. The most widely used characterisation technique is the gap test [10]; where a shock is supplied by a detonating donor charge and attenuated through a barrier which can have variable thickness. A witness plate is used to determine a "Go"/ "No go" reaction in the explosive being tested. A typical experimental configuration is shown in **Figure 2.1**. A "Go" or "No go" simply denotes if a reaction has occurred within the material of interest.

The method is low cost and relatively simple to implement, however the input is poorly characterised and typically divergent (rather than a planar one dimensional shock), with no assessment of reverberation within the barrier plate. The results are presented as a gap thickness in accordance with the barrier threshold for reaction; the density and size of the explosive heavily influence the results and must be noted. No indication of the run distance to detonation is obtained.

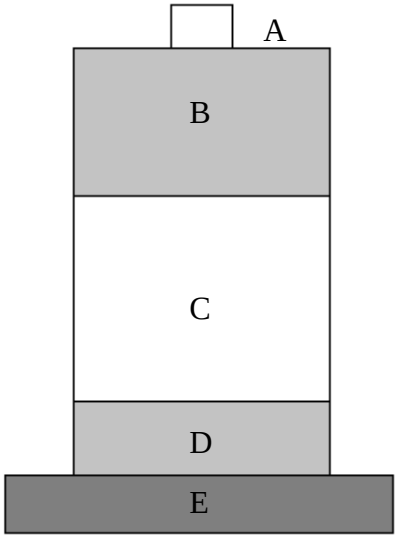

Figure 2.1: An example test configuration of a Gap test; a shock is supplied by a detonator (A), initiating a donor charge (B), which is attenuated through a barrier (C), which can have variable thickness. A witness plate (E) is used to determine a "Go"/ "No go" reaction in the sample (D)

An alternative and more useful method is a wedge test [10]. This imparts a one dimensional shock into a wedge shaped sample of explosive via a similar initiator/attenuator system, or by plate impact (to be discussed in more detail in Chapter 6). The wedge is illuminated with a light source and a streak camera monitors time resolved light changes along the wedge surface as it interacts with the shock; shock contact reduces the reflectivity and light intensity. The results can be used to interpret the distance or time to detonation for a particular pressure input, which is judged by adjacent gauges. Carrying out several experiments at different pressures allows the compilation of pressure against distance or time to detonation data, which can be presented on a Pop plot; named after Ramsay and Popolato. These can be used to compare reactivity characteristics between explosives.

Shock sensitivity data presented in the literature has often been obtained through one of these methods. Current experimental practice tends to favour gas-gun driven plate impact to input the shock into explosives, with the advantage that the resulting shock is a well characterised flat wave. Additionally, magnetic and manganin pressure gauges can be used to take in-situ measurements of the growth to detonation; this will be discussed in detail later in Chapter 6.

When an explosive is processed for an application, it is typically coated with a binder to reduce sensitiveness, and then pressed into a solid and machined to the required shape. It is therefore considered heterogeneous with regions of binder and filler, and also small voids. As discussed in Chapter 1, these irregularities interact with a shock or detonation wave to form hot-spot regions. Hot-spots occur as a shock passes through voids via adiabatic compression; as it propagates through irregularly shaped particles causing complex interactions; any crystal breakage results in shearing; and interactions between particles and voids can cause jetting. As such, it is expected that the physical attributes of the explosive such as the particle size have an effect on its shock properties.

In this Chapter, we review the available literature concerning the effects of physical particle parameter variations with shock sensitivity in explosives. It includes work carried out from the 1960s to the present day, and covers a number of experimental techniques. The materials in question are generally conventional explosives or their formulations; this reflects the historic interest in the materials for military research purposes.

2.1 Particle Size Effect on Shock Sensitivity of Explosives

There are often contradictions in the literature concerning the shock sensitivity of explosive material in relation to its particle size. From very early work carried out by Campbell *et al*. [19], finely graded pressed TNT was reported to be more shock sensitive than the coarse; 20-50 μm powder was compared with 200-250μm. These conclusions were based on data obtained from wedge tests, where a shock was applied to a pressed wedge of explosive and the time to detonation was measured.

Soon afterwards, alternate conclusions were drawn from gap test data on PETN [20], in which the shock sensitivity increased with larger particle sizes of PETN. These experiments were carried out at varied densities in a range of 0.95-1.4 g/cm^3, all of which showed the same trend. Scott published further work carrying out gap testing on differing particle sizes of PETN [21], and this study again indicated larger particles of PETN were more sensitive than the smaller particles. It was also noted that although the larger particles were more readily initiated, the smaller particles were able to reach detonation faster once they had been initiated. Scott's investigation also involved RDX and tetryl, and these materials conformed to the same observations.

Roth [22] agreed that fine grain RDX was less sensitive than the coarse grain – again using gap tests; and aside from that also found that raising the initial temperature of

the explosives in the experiment increases the sensitivity for all particle sizes. This is expected to be due to higher temperatures promoting the growth of hot-spot regions.

In the late eighties, Price suggested that the spread of results observed could be associated with the pressure at which material is shocked; coarse powder ignites at lower pressures, but the fine powder demonstrates a more rapid rate of reaction when ignited (i.e. at higher pressures) [23]. When the input shock pressure is less than the pressure required for detonation reaction (noted as P_r), then the response of the material is determined by its ease of ignition; which will mean that the coarser particle sizes appear more shock sensitive than the fine particle sizes, until P_r has been matched or exceeded by the input shock pressure. After which, the rate of reaction governs which is more sensitive; as such the fine powder will appear more sensitive as it will possess a greater surface area and hence demonstrate a faster reaction rate.

If this theory is correct, then it implies that the reaction leading to detonation is too complex to study using gap testing, as the gap test always identifies the lowest pressure resulting in detonation. The purpose of decreasing the gap is to gradually increase the shock delivered to the explosive until the minimum initiation threshold is reached, which will always favour the large particle sizes appearing more sensitive than their smaller counterparts. This observation is in agreement with an earlier study by Chick [24]; who noted that in gap tests, compacts of coarse powders were always more sensitive that the compacts of fine powders. As noted, gap testing is not the most suitable experimental method for a study on particle size.

Price's concept is derived from an explanation involving hot-spot theory [25]. It may be expected that owing to the packing of larger particles, the voids in larger particle size materials would be fewer but larger in size compared with smaller particle sizes. Hot-spots generated in these larger voids could survive longer than those in the smaller voids as the smaller hot-spots in fine grades of material allow the thermal energy to dissipate faster. As such, at low pressures the coarse particles appear to ignite more readily. At higher pressures, when there are an increased number of smaller hot-spots, the total number of hot-spots throughout the material will determine the time to reaction rather than the size of the hot-spot, and the finer particle sizes become more sensitive.

The above interpretation is a reasonable solution; one would therefore expect that the threshold pressure required for initiation would be higher for smaller particles than for larger particles of the same material. However, this concept is not necessarily based on experimental evidence and the hypothesis is also strongly affected by the manufacturing

route and subsequent density of the material produced. A more porous or lower density material is expected to ignite more readily regardless of particle size.

In other work, a short duration planar shock wave was applied using explosively propelled thin flyer plates to cast RDX samples formulated with 30 % polyurethane binder [26][27]. These results showed the fine RDX to be less sensitive than the coarse, and the authors also agreed with the analogy that a crossover in sensitivity would be achieved when the formulations were subjected to higher pressures.

However, in the same year as Price proposed her hypothesis, experimental observations contradicted the theory in a paper published on HNS [28]. An impacting flyer plate test graded three particle sizes of HNS on the pressure required to reach the initiation threshold, and the finer grades required a lower pressure for initiation than the coarse particles. The measurements were made at constant shock pulse duration, generating pressures in the region of 5-7 GPa. A follow-up study still using HNS, but with an experimental method utilising a longer duration pulse, established that the shock sensitivity can decrease or increase with decreasing grain size, dependant on the duration of the shock pulse, i.e. results will vary with experimental parameters [29].

Moulard continued working on cast RDX formulations, studying three monomodal particle sizes; 6 µm, 134 µm and 428 µm in a 70 % filler weight ratio of polyurethane [30]. He found that at an impact shock pressure of 4.4 GPa in a wedge test rated the 428 µm RDX formulation the most sensitive; at 5.4 GPa the 6 µm formulation was the least sensitive, but the results from the 134 µm and 428 µm compositions were comparable. At 6.6 GPa the three readily demonstrated an equal fine to coarse sensitivity range (with the fine being the least sensitive), and at 12.0 GPa the 6 µm formulation was the most sensitive, and the 428 µm least sensitive. A study on HMX PBX compositions with coarse and fine grades of explosive fillers has also found the coarse HMX to be more sensitive [30].

These results are in agreement with Price's earlier suggestion; the time to thermal explosion can be controlled by the void sizes and distribution in the formulation, which relate directly to particle size. Applying the ignition and growth analogy [31][32], the shock to detonation transition occurs in two stages – primarily with ignition of hot-spots and secondly with those hot-spots growing into a reaction if there is enough energy input from the shock. At low shock pressures SDT is controlled by the ignition of hot-spots, favouring large particle sizes with large voids. At high pressures SDT is dominated by the

growth step, which is driven to faster completion by a greater number of smaller hot-spots generated by higher surface area from smaller particles.

This two stage ignition and growth theory is backed up by some experimental results, where RDX PBXs pressed to 80-90% TMD showed increasing sensitivity with increasing particle size, but for PBXs pressed above 95% TMD the sensitivity increased with decreasing particle size [33]. In the lower density materials there is a greater opportunity for the ignition of hot-spots, and the free space will increase as the particle size increases – the initiation of this material is dominated by the ignition stage. For the higher density PBXs, the reaction is dominated by the growth stage as the particle size decreases.

There are some anomalies to this relationship, and it is not as simple as is implied. Wedge tests analysed with radiometry for HMX have shown that a decrease in sensitivity is notable when the particle size is reduced below 20 μm. However the study did not look at particle sizes below 5 μm [34]. It also found that the sensitivity of 60 μm HMX was greater than that of 110 μm HMX or 1700 μm HMX. The author concludes that this observation can again be explained by changes in growth rate of hot-spots.

In the most recent trend for explosive particle engineering research, energetic materials containing submicron and nano-sized particles are being developed, with the aim of creating formulations with enhanced energy density and energy release rate [35]. Such properties are achieved via the larger surface area provided by the smaller particles. 60 nm particles of TATB have been produced [36], but the most interesting results come from conventional (non-IHE-like) explosives because of the effects observed on their sensitiveness.

Nano-HMX has been produced [37][38] and synthesized as a formulated composition [39]. It has been claimed that nano-HMX has a 44 % improvement on shock sensitivity when gap tested and compared to a commercially available micron-sized HMX [40]. Similarly nano-RDX has been manufactured [41], and has been shown to exhibit lower shock sensitivity and mechanical impact sensitiveness [42][43], though a 500 nm crystal size was less sensitive than the equivalent 200 nm particles. Nano-sized explosive particles are expected to be mechanically stronger than larger particles and therefore would be less reactive to mechanical insults such as impact and friction. They would also be expected to contain far fewer defects per crystal; to be discussed in a later Section.

The most beneficial use of this technology so far has been seen with 2,4,6,8,10,12-hexanitro-2,4,6,8,10,12-hexaazaisowurtzitane (CL-20), which has superior energy output

to HMX, but is more sensitive [44]. Just recently published, nanometric CL-20 has been prepared [45][46] and produced as a formulation [47]. Early characterisation of the neat material shows improved sensitiveness to impact and friction [48], with further work needed to understand the effects on shock sensitivity.

Another consideration for testing explosives with respect to their particle size is how the shock actually interacts with the explosive crystal itself. Short duration shocks can more readily span the distance of a smaller grain before weakening [49]. As such, internal hot-spots are more likely to develop in smaller particle sizes, and hot-spot formation in larger crystals will be less efficient. The finer particles also have a larger surface area, allowing for more rapid shock energy transfer [49].

2.2 Crystal Surface Effect on Shock Sensitivity of Explosives

It is common understanding that increasing the surface area of a reacting material will increase the rate of reaction as there is a greater region available for reactive sites to develop. This analogy relates to another mechanism of explosive reaction; the grain burn concept [50]. The grain burn concept suggests the reaction rate for a particular explosive at a certain density is related to the characteristic burning rate and specific surface area of the grains. The specific surface area of a material is defined as its total surface area divided by its volume, and for energetic materials it is more conventionally referred to than surface area alone. Of course, the surface area of a material is very directly linked with its particle size; smaller particles will always have a larger surface area in a unit of volume or mass.

Khasainov published a comprehensive literature review in the 1990s [51], using many of the previously reported references to support the theory that the shock sensitivity of an explosive strongly depends on the particle grain size, because it directly changes the properties of the specific surface area, and therefore the region available for grain burning. He suggests that in wedge tests at constant impact pressure, the run distance to detonation will increase linearly with reciprocal specific surface area (assuming that the pressure is above P_r).

It is important to remember in such cases that sensitivity tests are pressure dependent. The ignition phase of SDT is dependent on the rate and size of hot-spot formation, and the grain burning process contributes to the hot-spot growth rate leading to build-up to detonation [52][53]. This was highlighted in Price's earlier literature review [23], and means that understanding shock sensitivity relies on defining the correct experimental conditions.

Khasainov states that at high pressures with finer particle sizes, hot-spot formation is fast and all voids are able to form growing reaction centres. The burning surface is comparable to the available specific surface area and the sensitivity is dependent on the growth rate of the hot-spots; which in turn will increase with larger specific surface areas. At lower pressures smaller voids do not contribute to the growth of hot-spots (i.e. there are fewer critical hot-spots), and the resulting burning surface is smaller than the available specific surface area. In this case larger voids are more likely to generate a successful reaction, associated with coarser grain sizes.

These theories agree with earlier conclusions made in the community [23], but focus on the surface burn growth phase of the mechanism in more depth than the hot-spot ignition stage. The surface burn feature of the mechanism helps explain how detonation can be achieved with extremely short duration shocks (for example 20 ns using an electric gun [54]); if the specific surface area is large enough then the grain burning phase will carry forward to detonation.

Experimentally, a gap-test study using different classes of RDX in tapped powder columns, found that the sensitivity of RDX could be related to the powders specific surface area [55][56]. The sensitivity of the RDX increased as the specific surface area was enlarged, which is likely to be because the chance of achieving a transition to detonation is dependent on the burning surface area; as discussed the burning surface area is greater with a larger specific surface area. More data and further samples in this particular study are required to understand the correlation from the investigation with greater clarity, but the nature of the research links with current interests.

2.3 Internal Crystal Defects Effect on Shock Sensitivity of Explosives

Changes in particle size also directly affect other features of a composition apart from the surface area and porosity; specifically the imperfections (or defects) within the crystals, and the quantity of surface defects. An investigation was carried out using a coarse sample and a fine sample of RDX from a standard batch, and comparing it with a coarse lot and a fine lot of a reduced sensitivity grade of RDX (RS-RDX) [57]. The reduced sensitivity RDX is manufactured via a recrystallization method to give a smoother surface roughness and contain fewer pores or cracks (defects) than the standard RDX. This reduction in surface and internal defects in the RDX particles in theory provides fewer sites for hot-spots to develop, and therefore an overall reduction in the sensitivity of the material is obtained.

Four formulations were made, each with 73 % solid RDX and 27 % HTPB binder, and compacted discs were produced and sandwiched with four gauge packages for each material. These samples were shocked in a gun launched flyer experiment, and results from the gauge packs were collected.

In both cases for the standard and the RS-RDX, the build-up of reaction was greater in the larger particles compared with the smaller particles. The author suggests that this is because the larger particles have a greater number of internal crystal defects, rather than simply a larger porosity between crystals. When comparing the standard RDX results with RS-RDX results, the RS-RDX exhibited lower sensitivity for both the large and small particles. The required input pressure for the large particle RS-RDX was nearly 2 GPa higher than that of the large particle standard RDX. The RS-RDX with fewer internal defects behaves differently to standard RDX of a similar particle size, showing that increased internal defects do lead to higher sensitivity.

The results are reasonable, as heterogeneities in the explosive crystal should provide areas for hot-spots to develop when a stimulus is applied. It also contributes to the explanation of why nano-sized RDX exhibits lower sensitivity to shock and mechanical insult [42][43] as it is expected that nano-sized crystals would contain far fewer defects owing to their small size. This demonstrates the need to be aware of how the altering particle size may change any other physical characteristics of the crystals, when carrying out such experiments.

An interesting study to probe the crystal quality effects on shock sensitivity used nuclear quadrupole resonance (NQR) to assess the defect density in batches of RDX before formulating and gap testing the material. NQR measures the environment of the quadrupolar nitrogen nuclei; the produced line width varies with differences in the environment of the nuclei, relating to the defects in the particles [58]. It found that the finer particles were less sensitive, but attributed the rise in sensitivity of larger particles to greater defect density, in the form of pores and cracks [59]. The greater number of inner-crystal defects in the larger particles meant that the formulation had a shock initiation pressure of 0.3 GPa less when compared with smaller particle formulations containing fewer defects.

The data discussed above contributes towards the theory that defects in the explosive crystals allow for the formation of hot-spots. Porosity within charges increases sensitivity to shock, whether the pores are in the binder or at the binder-crystal interface; the same effect occurs within the crystals themselves. The difficulty in taking forward

investigations of this nature is a lack of accurate measuring methods for such characterisation, and also the processing control during manufacture of explosives to purposely create or eliminate porosity in the crystal.

Borne has used a technique known as the ISL sink-float method, where weighing particles in different liquid mixture densities estimates the particle density distribution [60]. The intragranular (internally within the explosive crystal) void volume can then be calculated as a percentage per unit crystal volume from the apparent density distribution of the material.

Three formulations with 200-300 μm HMX particles were produced, each containing 30 % wax binder. The intragranular void volumes of the formulations were calculated to be 0.15, 0.30 and 0.45. Samples of the formulations were subjected to projectile impact at low shock pressures, and the velocity threshold for each was 1100 m/s, 830 m/s and 730 m/s respectively [61]. This correlation between internal crystal void volume and velocity threshold demonstrates an increase in shock sensitivity for a larger quantity of defects within the crystal.

Borne later calculated the extragranular void volume (within binder and binder-crystal interface, excluding the internal crystal voids) using a measured density and theoretical maximum density. The extragranular void volumes show no direct correlation with the other results, being 0.30, 0.60 and 0.001 respectively [62]. This result implies the extragranular voids have a minor effect on the formulation sensitivity.

The study was extended to RDX [62][63], using a number of samples of commercially supplied RDX and a batch of RDX produced in the ISL laboratory. The ISL slow-cool-crystallisation RDX had a low percentage of intragranular (internal crystal) voids and a reduced surface porosity which would also lead to a reduced number of extragranular (binder-interface) voids owing to the smoother surface. The batches supplied from the commercial source had different internal void populations.

The different batches of RDX were again cast into a formulation with 30 % wax binder and subjected to projectile impact. The formulations with the highest volume percentage of intragranular porosity showed greater shock sensitivity, and the ISL batches with the lowest level of intragranular voids had the lowest shock sensitivity; a threshold velocity of 920 m/s compared with 1180 m/s respectively. Formulations with a similar number of intragranular voids, but varying levels of extragranular voids were found to demonstrate an intermediate impact velocity threshold around 1100 m/s; reinforcing the

suggestion that the effects from the intragranular defects dominate those of the extragranular defects.

An interesting side note from Borne's study [62] showed that the percentage of extragranular voids increases when the particle size is reduced. This means the number of voids within the binder and at the interface increases with increasing specific surface area, for the batches of materials studied. It is therefore reasonable to assume that many of the extragranular voids occur at the crystal-binder interface. If this is the case, the surface smoothness of the crystals and their interaction with the binder also play a factor in their sensitivity. A separate investigation deduced that it was not just the roughness of the surface, but the distribution and consistency of any defects across that particle surface could affect its sensitivity [64].

It was at least a decade until another investigation similar to Borne's took place, again using RDX, utilising small and ultrasmall angle neutron scattering (SANS/USANS) [65]. The research showed that variances in the internal void structure can cause a fluctuation in large scale gap test results from 2.39 to 5.17 GPa; this variation is considered a significant change in the shock sensitivity. Further work is still ongoing to characterise the microstructure of the void surfaces.

2.4 Particle Morphology Effect on Shock Sensitivity of Explosives

There is some disagreement that the internal defects cause changes in the sensitivity of an explosive [55]. Czerski claimed that no obvious correlation could be observed between the number of internal voids in the crystals and their sensitivity, and that crystals with internal defects could be found to be insensitive. However the single crystal morphology and its overall effect on the bulk powder morphology has a direct influence, with more angular crystals and those with surface imperfections being more sensitive.

A comparison between spherical HMX and HMX needles showed that the spheres possessed lower impact sensitiveness and higher thermal stability [66]. It is suggested that this is because the needles have highly asymmetric crystalline regions, where spheres would be more uniform internally. The sensitivity of NTO (3-nitro-1,2,4-triazol-5-one) was seen to be in lower spheres and cubes [67], and the shock sensitivity of RDX is also reduced with spherical particles [68].

Crystal twinning is another phenomenon that has been shown to affect sensitivity. The existence of dislocations at twinning sites results in a difficult slide region for shear bands to move through, and the release from overcoming this obstruction may lead to more

significant localized heating (i.e. hot-spots). Two different research groups have observed that twinned crystals are more sensitive, with the greatest influence being noted for HMX [69][70]. The work also directly opposes the views of earlier investigations, observing that other particle morphology variations have no effect [69], but a great difference in sensitivity can be seen with the internal porosity (also referred to as the crystal density in this investigation) and twinning.

2.5 Summary

Despite some contradicting and unexplained results, the research community generally agrees that finer particle sizes are less shock sensitive at low pressures than coarse particle sizes. At higher pressures the smaller particle sizes react more quickly, whether considering the mechanism from a hot spot distribution or a grain burning surface area perspective.

What may have not been taken into account in many early studies is that altering the particle size of an explosive leads to a series of complex issues with other parameters when considering its shock sensitivity. As noted, the particle size directly influences the specific surface area and the number of defects in a crystal. It is therefore important to fully characterise the particles using techniques such as scanning electron microscopy, as well as surface and particle size analysis. It may be that some results are influenced by these competing effects. For example many of the afore-mentioned investigations have been carried out using RDX. The results from a "Round Robin" (inter-lab comparison study) of RDX yield some interesting data to note [71]. Seven types of RDX from five different manufacturers were formulated in one particle size to make seven batches of PBXN-109. Gap testing the samples showed differences in sensitivity between RDX manufactured by the Bachmann process, and the RDX manufactured using the Woolwich process. The main difference between the two materials is the quantity of HMX impurity, as the particle classes were kept constant. It does demonstrate that it is important to consider any chemical as well as physical differences in the samples used for sensitivity studies.

It is also of interest to note that the historic studies have been carried out on conventional HEs, such as RDX and PETN. It will be a valuable investigation to establish how LLM-105 (a candidate low sensitiveness HE) behaves, and if it is comparable to the other explosives. The subsequent Chapters in this thesis describe how different particle

size and shape LLM-105 materials were produced, and investigation into their comparative sensitivity and sensitiveness to impact is discussed.

Chapter 3: Modifying LLM-105 to Produce Materials for Impact Studies

In Chapter 1 LLM-105 was introduced as a relatively new explosive material that could be considered to be low sensitiveness with high performance characteristics. Chapter 2 reviewed how different physical aspects of explosive particles affect their sensitivity, including particle size, shape and quality. This Chapter describes how LLM-105 has been modified to produce a number of samples suitable for further investigation into its behaviour as an explosive.

Particle size and shape modification of LLM-105 can be used to create different grades of material to investigate and characterise. The standard LLM-105 available has a grain size of approximately 50 µm in diameter and the simplest way to modify this is by milling or recrystallization. Several batches of different particle shape and size are desirable for a reasonable spread of data to study each effect. In this section we review the possible techniques for particle modification, including preliminary trials using an inert simulant. Ultimately, we summarize the production of experimental LLM-105 batches for use in the research described later in the thesis.

3.1 Particle Size Modification

Milling is widely used to reduce the particle size of granular materials. A number of traditional milling options exist; these are summarised below in **Table 3A** [72].

Required Product Size	**3 mm - 50 µm**	**< 50 µm**
Types of Mill	Ball Mill	Ball Mill
	Pin Mill	Colloid Mill
	Tube Mill	Fluid Energy Mill

Table 3A: Methods for milling and reducing particle size

Ball milling utilises ceramic or metal balls available in a range of sizes. These are put in a container with the material, which is sealed and mounted into an agitator or rotator

for an amount of time. The movement of the balls fractures the material and there is attrition caused by particle-particle interactions. Tube mills also work on a similar principle, but are long in shape, and are often partitioned so smaller balls sit towards one end, resulting in finer grinding.

Pin mills and colloid mills grind by relative rotation of two metal plates; one remains stationary throughout the process. The pin mill is based on two parallel discs fitted with interlocking pins. The moving plate spins at high speed and the movement between the pins on the opposite plate results in grinding of the material. A colloid mill involves a stationary cone in which a smaller cone containing holes sits, and this smaller cone spins at high speed. A slurry of material is passed through the gap between the cones as the smaller cone rotates.

Fluid energy mills are fed with high pressure jets of air, which form regions of high speed rotating slurry. The most common variety is a spiral jet mill; a high velocity spiral of air rotates about the centre and when the slurry is introduced, the particles collide with one-another and the inner wall of the ring, resulting in comminution.

All of these processes put energy into the particles in order to reduce their size. The energy results in friction, shear forces, thermal stresses, and eventually fracture, all of which are not advisable to apply to energetic materials. Therefore explosives are milled in the form of a slurry, usually in low concentration with water, to desensitise the material and significantly reduce the risk of ignition. There is a report of a case of fluid energy milling being used to successfully reduce the size of CL-20 particles, by milling dry powder [73], though this is a rare example.

Sonication in deionised water has previously been used to reduce the particle size of an energetic material [74]. Sonication of a sample in a liquid medium applies acoustic cavitation to the material through the formation, growth and implosion of tiny bubbles. The technique is typically used for dissolution or dispersal of a sample, but some molecules are unstable to sonication. For example sonication can damage a protein's quaternary, tertiary, and secondary structure.

A high shear milling technique which achieves direct impact to particles is desirable in order to induce physical breakage without any risk of changing the molecular, or chemical, nature of the LLM-105. Of interest for this particular study is milling using a stator rotor homogeniser, in a suspension of material in deionised water. The technique is appropriate because it is carried out in low concentration of the HE, making the process comparably safe, and the equipment is relatively inexpensive when compared with larger

industrial milling machines. Teipel has previously shown that this equipment is suitable for use with materials such as HMX, RDX and CL-20 (known to be highly sensitive) [75][76]. In that work, the CL-20 was reduced in particle size from over 100 µm, to less than 10 µm, while keeping a concentration below 15 wt. % in water in a batch size of 1 kg. The end attachment of the stator rotor (**Figure 3.1 –** showing the toothed appliance with a rotating inner device) is lowered into the suspension of HE, and the opposite end, fitted to a driving motor, does not come into contact with the experimental medium.

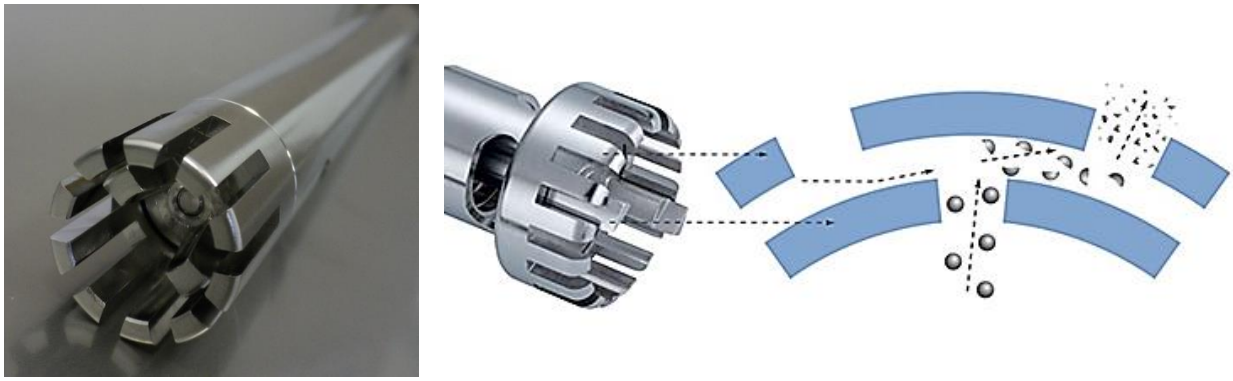

Figure 3.1: The end attachment of a stator rotor (left); the stator outer ring remains stationary and the central rotor acts as the moving part driven by a motor. The slurry is driven between the two toothed rings and the particles are milled by a shearing motion. The diagram on the right is taken from the IKA website for the Ultraturrax stator rotor model, and demonstrates the milling mechanism for a stator rotor

Stator rotors are readily available and reasonably inexpensive, as bench top equipment. A number of brands and models of stator rotor were considered for this work, and due to the availability of additional attachments, the IKA Ultraturrax T25 was chosen. A number of studies have taken place using a stator rotor to reduce powder sizes in aqueous suspension. These materials range from glass [77], pharmaceutical products [78], silver [79] and silica and alumina [80]. All experiments were successful in reducing the particle size of the product, which implies that this is a suitable technique and relatively straightforward method for milling LLM-105.

3.1.1 Inert Milling Trials

Particle size modification of LLM-105 would ideally be performed in batches and scaled up with larger milling attachments after preliminary trials. Initial studies were carried out using an inert simulant, melamine, in order to understand the milling process prior to the application to explosive material and the subsequent safety implications. The aim of milling the melamine was to obtain a qualitative understanding of the stator rotor capabilities, before its use with LLM-105. Melamine has a nitrogen containing cyclic structure similar to that of some energetic materials (see **Figure 3.2**). It is a readily available hard powder with particle sizes on the micron scale, comparable with many explosive powders.

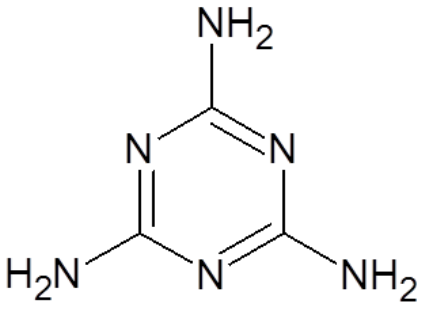

Figure 3.2: Melamine; a nitrogen containing cyclic molecule which is used as an inert simulant for explosive materials

The first trials were conducted on small quantities of powder (less than 10 g); this is because when the process is converted to HE, good practice requires low masses of material be produced initially to prove any new material is safe to handle. The material's safety properties are tested after processing and a staged scale-up procedure allows for larger batches to be manufactured as desired. The variables of interest for the milling experiments included adjustment of the water suspension concentration, the speed of the stator rotor, and the amount of time required to effectively reduce the particle size of the melamine.

The required quantity of melamine powder was weighed into a beaker, and deionised water added to achieve a predetermined concentration by weight. The stator rotor was used with variations in operating parameters between several experiments as

discussed above. The speed at which the stator rotor was set, the concentration of the powder in solution, and the time the rotor was allowed to run for were all adjusted with the aim of obtaining a reduced size product. A matrix of these factors is shown in **Table 3B**. The table captures all of the variables for each of the experiments; all generally used small quantities of melamine in suspensions concentrated between 5 and 15 weight %. Two different disperser speeds were chosen for the initial study, with a set grinding time which was doubled, then quadrupled to assess the efficiency of the stator rotor.

	Sample	Mela-mine Mass (g)	Water Volume (ml)	Conc. (wt. %)	Disperser Speed (RPM)	Grind Time (mins)
Effect of Change in Concentration	1melA	2.5	47.5	5	12000	5
	1melB	5.0	45.0	10	12000	5
	1melC	7.5	42.5	15	12000	5
Increased Rotor Speed, Different Concentrations	2melD	2.5	47.5	5	24000	5
	2melE	5.0	45.0	10	24000	5
	2melF	7.5	42.5	15	24000	5
Increased Grinding Time, Different Concentrations	3melG	2.5	47.5	5	24000	10
	3melH	5.0	45.0	10	24000	10
	3melI	7.5	42.5	15	24000	10
Extending Grinding Time	4melJ	2.5	47.5	5	24000	20

Table 3B: Test matrix for initial melamine grinding experiments

None of the experiments resulted in any measurable heating of the liquid medium; this was checked periodically by inserting a thermometer into the slurry. After grinding, the samples were filtered using a buchner funnel and specialist filter paper (graded at a pore size of 0.45 μm) to prevent the loss of fine particles. They were dried in air for 16 hours before particle size analysis using a Malvern Mastersizer 2000.

The Mastersizer measures by laser diffraction; a particle sizing method that passes light through a suspension of the sample. The angle at which that light is diffracted is inversely proportional to the particle size. The result is a volume distribution curve with average data provided for the sample. The parameters of interest are the volume median diameter (noted as d[0.5]), which represents the diameter where 50 % of the distribution is above and 50 % lies below; and also the volume mean diameter (abbreviated to mean [4,3]), which is sensitive to larger particles and hence aids in their detection.

The technique of laser diffraction uses the Mie theory of light scattering, which assumes that all particles measured are spherical, and that introduces an inherent error to each measurement. As the particles are three dimensional objects, it is not possible to describe them using one number, unless a sphere (or cube) is assumed. There are many particle sizing techniques that rely on the spherical assumption; image recognition, electrozone sensing, and sedimentation. All of these particle sizing techniques measure one dimension of a particle and provide the diameter of the equivalent sphere as its size. No single technique provides a more real representation of particle size other than the laborious method of manually counting particles that have been subjected to microscopy, which then factors in different diameters for irregularly shaped particles, and would give more than one numerical result.

The magnitude of error depends on the technique used and the actual shape of the particle measured. The mathematical complexities introduced by non-spherical geometry usually prevent models from being derived for other shapes, and these same complexities prevent predicting exactly how the error affects the reported results. Depending on the sizing technique and the shape of the particles, the effect may be negligible or may be severe, and it cannot be predicted reliably, with little definitive guidance in the open literature. Hence particle size is generally not reported with an associated error.

A condition of using Mie theory is that the refractive index of the sample material is known. If the refractive index has an uncertainty of +/-5%, the relationship of this error to the error in result is considerably more complex. It is unlikely that effects from this error can accurately be predicted, and may only be realized by reducing the experimental data multiple times using a number of values of refractive index covering the range of the uncertainty.

However, despite the error from the spherical assumption, laser diffraction has a number of advantages as a particle sizing method including its capability for assessment of a wide range of sizes, repeatability, ease of verification, and speed of measurement. It is the preferred technique for particle sizing in a wide range of industries, such as pharmaceuticals and food development, and hence it has been determined to be suitable for use in this study. Many of the experimental errors for this technique can be controlled by ensuring adequate sampling, effective dispersion of the particles and solubility of the material is considered.

Melamine is sparingly soluble in water (approximately 3 g per litre of water) so all samples were run in a pre-prepared saturated solution which had been filtered to remove

any remaining original material. The Mastersizer sampling method is relatively fast (complete within minutes) which limits the opportunity for the melamine crystals to exchange with the solution. An agitator was used in the Mastersizer sampling chamber to ensure adequate dispersion of the particles, and limit effects of agglomeration.

A sample of the pristine melamine was run for comparison with the milled powders; the complete set of results is presented in **Table 3C**. Each of the samples examined here relates to the experimental variables outlined in **Table 3B**. All of the experiments were successful in reducing the melamine particle size comparable to the pristine material.

There are some general comments applicable to all of the samples; increasing the speed of the stator rotor resulted in smaller particles. Effectively adding more energy to the process means that this is an expected outcome. The same also applies to extending the time period over which the stator rotor is run for, a longer processing time leads to smaller particles. The suspension concentration did not have an obvious effect on the particle size; at lower rotor speeds the 5 wt. % experiment (1melA) was the most effective for particle size reduction. When the speed of the stator rotor was increased both the 5 wt. % and 15 wt. % experiments (2melD and 2melF) gave a roughly equivalent product, with the 10 wt. % batch (2melE) being less successful. However when both the stator rotor speed and grinding time were increased, the 10 wt. % suspension was most efficient for producing reduced particle size material (3melH). The raw particle size distributions are recorded in **Appendix A**.

The appearance of a second peak, to give a bimodal distribution in experiments 3melG, 3melH, 3melI and 4melJ, is caused by agglomeration of smaller particles. The agglomeration effect is obvious as the measurement of the second peak is at a larger particle size than the particle size of the pristine melamine, and a large proportion of the particles in the distribution are still biased towards the smaller scale. It is highly likely that the small particles of melamine formed agglomerates and stuck together on drying. To prevent this occurring when grinding LLM-105, the suspension was not filtered and dried before characterisation, to enable a true measurement of particle size to be made.

One of the ground melamine samples was examined under an optical microscope at 10x magnification; **Figure 3.3(a)**; and compared with the pristine melamine at the same magnification; **Figure 3.3(b)**. It can be seen that the pristine melamine has a rough surface and larger particles, and melamine from sample 1melA (i.e. even at a low motor speed and a relatively short grinding time) has smooth surfaces where the stator rotor has sheared the

faces of the crystals, and a reduced particle size. These images are generally representative of the sample average.

	New Particle Size		
Sample	**d[0.5] (µm)**	**Mean [4,3] (µm)**	**Comments**
Pristine Melamine	134.8	146.6	Original particle size before grinding
1melA	88.8	103.0	Single peak. Reduction in particle size as expected. Relatively small change, likely to be due to slow speed
1melB	104.6	116.6	Single peak. Larger particle size product with higher powder concentration
1melC	116.3	127.9	Single peak. Larger particle size product with higher powder concentration
2melD	58.3	94.1	Small shoulder peak at higher particle size, caused by agglomeration of product. Higher motor speed results in smaller particles
2melE	105.3	119.1	Single peak. Apparently unsuccessful experiment for particle size reduction. Comparable to 1melB at which motor runs at half the speed
2melF	57.1	78.0	Small shoulder peak at higher particle size, caused by agglomeration of product. Higher motor speed results in smaller particles
3melG	72.3	255.8	Bimodal, 44 % of material is below 63 µm. Second peak caused by agglomeration
3melH	54.5	120.5	Bimodal, 56% of material is below 63 µm. Second peak caused by agglomeration
3melI	78.8	112.4	Large shoulder peak - agglomeration
4melJ	41.1	77.7	Slightly trimodal - small peak at 0.7 um. Grinding for longer times gives smaller particle size

Table 3C: Particle size analysis results for milled melamine. In general a higher stator rotor speed and longer grinding time resulted in a smaller particle size product when compared with the baseline pristine melamine

(a) 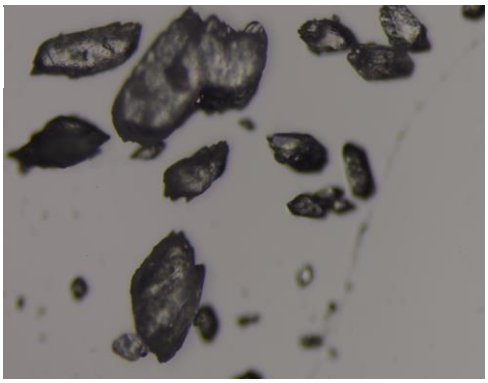 (b) 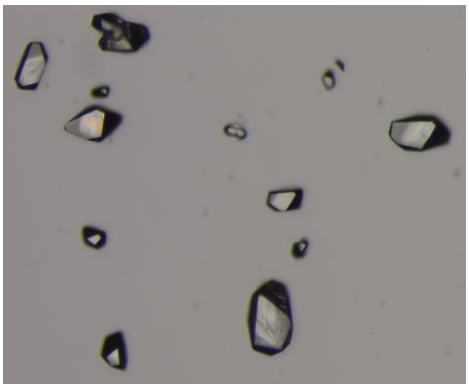

Figure 3.3: Optical images of (a) pristine melamine of a coarse nature (left) and (b) sample 1melA (right), which has smaller particles and sheared smooth faces

The aim of these small scale experiments was to test and refine the stator rotor method in order to produce different particle size batches of LLM-105. It has been shown that use of a stator rotor is a suitable method to achieve particle size reduction of a granular powder in a reasonable time. Experiments 3melH and 4melJ with a higher stator rotor speed and longer grinding times were particularly effective, and will form the basis of the conditions used with LLM-105 in the next section.

3.1.2 Milling LLM-105

Based on the results of the melamine trial, the first experiment with LLM-105 was run at 24000 rpm for 15 minutes (a compromise on the time between 3melH and 4melJ). A concentration of 10 wt. % was planned, however, with 0.5 g of explosive (a relatively small amount; accounting for safety assessment for first use with energetic material) a concentration of 5 wt. % was used initially, with the aim of raising this to 10 wt. % when the method had been safely proven. After homogenising, the suspension underwent particle size analysis; the particle size distributions of the milled LLM-105 and pristine LLM-105 are shown in **Figure 3.4**.

It can be seen from **Figure 3.4** that milling the LLM-105 with the stator rotor is effective. The pristine LLM-105 was measured to be 47 μm (d[0.5]), and the milled particles measured 13 μm, which is a very large reduction in size (around 70 %) and shows that the process is suitable for generating smaller particles of LLM-105. In the particle size distribution for the milled material there is a secondary smaller peak at 0.5 μm, likely to be from the attrition of the particles during size reduction. The sample was also characterised by Differential Scanning Calorimetry (DSC) which assesses the thermal stability of the

material. The milled LLM-105 peaked for decomposition at 352.5 ºC which is very similar to the pristine LLM-105 (352.6 ºC), indicating that the milling process has not resulted in any chemical degradation of the explosive.

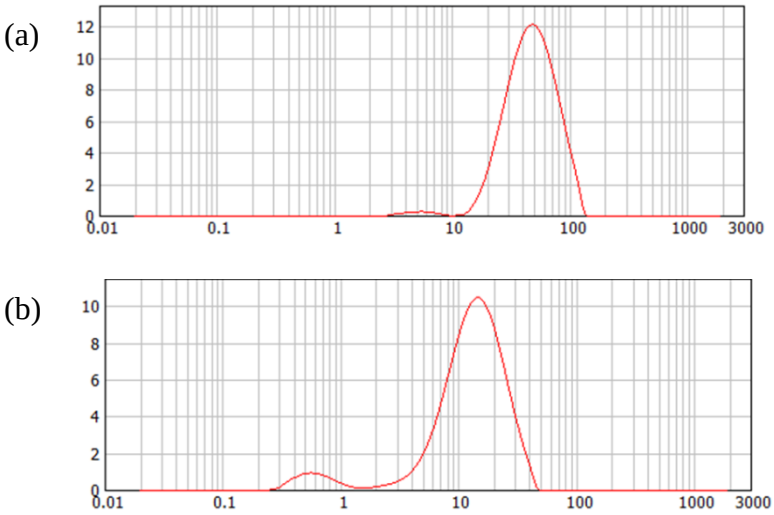

Figure 3.4: Particle size distributions for (a) pristine LLM-105 and (b) milled LLM-105. The LLM-105 was milled at 24000 rpm for 15 minutes, shifting the D[0.5] from 47 µm to 13 µm

3.1.3 Method Optimisation

Having proven that the stator rotor is suitable for milling LLM-105, additional trials were carried out on melamine for method development prior to production of explosive batches. Further work was needed to understand how the grinding time affected the milled product and whether the time variable was the appropriate parameter to alter in order to produce a number of particle size options. Evidence of reproducibility was examined, as was an understanding of the implications for scaling up the process.

The results of these experiments are presented in **Table 3D**; all were carried out at a concentration of 10 wt. % which is representative of the planned LLM-105 method. Some of the experiments required a long run time, which caused concern for the generation of heat from the energy put in by the stator rotor, when an explosive would be present. The temperature was monitored, and even on a larger milling scale with a

processing time of hours, the temperature of the suspension did not rise above 50 ºC. A processing temperature in this region is considered safe for LLM-105 as the decomposition temperature is above 300 ºC as characterised by DSC. Additionally, from a quality perspective, a temperature of 50 ºC will not cause the water to boil and change the process parameters.

	Sample	Mela-mine Mass (g)	Water Volume (ml)	Conc. (wt. %)	Disperser Speed (RPM)	Grind Time (mins)	New Particle Size (µm)
Effect of Grinding Time	5melK	10	90	10	24000	30	40.9
	5melL	10	90	10	24000	60	37.2
	5melM	10	90	10	24000	120	28.9
	9melT	10	90	10	24000	240	19.0
	9mel U	10	90	10	24000	480	15.3
	10melV	10	90	10	12000	15	71.2
	10melW	10	90	10	12000	30	57.8
	10melX	10	90	10	12000	60	48.3
	10melY	10	90	10	12000	120	45.3
	10melZ	10	90	10	12000	240	34.9
	10melAA	10	90	10	12000	480	28.1
Reproducibility of Result	6melN	10	90	10	24000	15	52.3
	6melO	10	90	10	24000	15	54.1
	6melP	10	90	10	24000	15	54.2
Scale-Up of Process	7melQ	50	450	10	24000	15	66.0
	7melR	100	900	10	24000	15	89.9
	11melBB	5	45	10	24000	10	55.8
	11melCC	10	90	10	24000	20	53.5
	11melDD	20	180	10	24000	40	51.8
	12melEE	60	540	10	20000*	15	79.0
	12melFF	60	540	10	20000*	30	69.5
	12melGG	60	540	10	20000*	60	65.0
	12melHH	60	540	10	20000*	120	29.3

Table 3D: Method development for milling LLM-105 using the inert simulant melamine. The aim is to understand the milling time effect on the product, and the implications on reproducibility and scale-up of batches. The new particle size was measured for the product after milling. *a reduced speed of 20000 rpm was used in place of 24000 rpm as the scaled-up process caused greater agitation of the suspension and spillage

The effect of the grinding time on the milled particles at different speeds is plotted in **Figure 3.5**. As expected, smaller particles are produced at faster stator rotor speeds, though the rate of reduction of the particle size as time progresses is approximately the same for the experiments run at 12000 rpm compared to those at 24000 rpm. It appears as though little change occurs to the particles after 240 minutes in both cases indicating a maximum useful grinding time.

The batch reproducibility was tested in experiments 6melN, 6melO and 6melP (**Table 3D**), keeping all the variables constant, and provided a good result. The range of particle sizes produced in each batch was between 52.3 - 54.2 µm, with an average of 53.5 µm. The error in this range is 3.5 % which is considered acceptable given that individual milled batches of a given material are typically blended before any further processing. However it became apparent in experiments 7melQ and 7melR (carried out using a larger rotor attachment) that scaling effects for larger batches interfere with the product, independent of the concentration of the suspension and grinding time; the resulting particle size is not consistent.

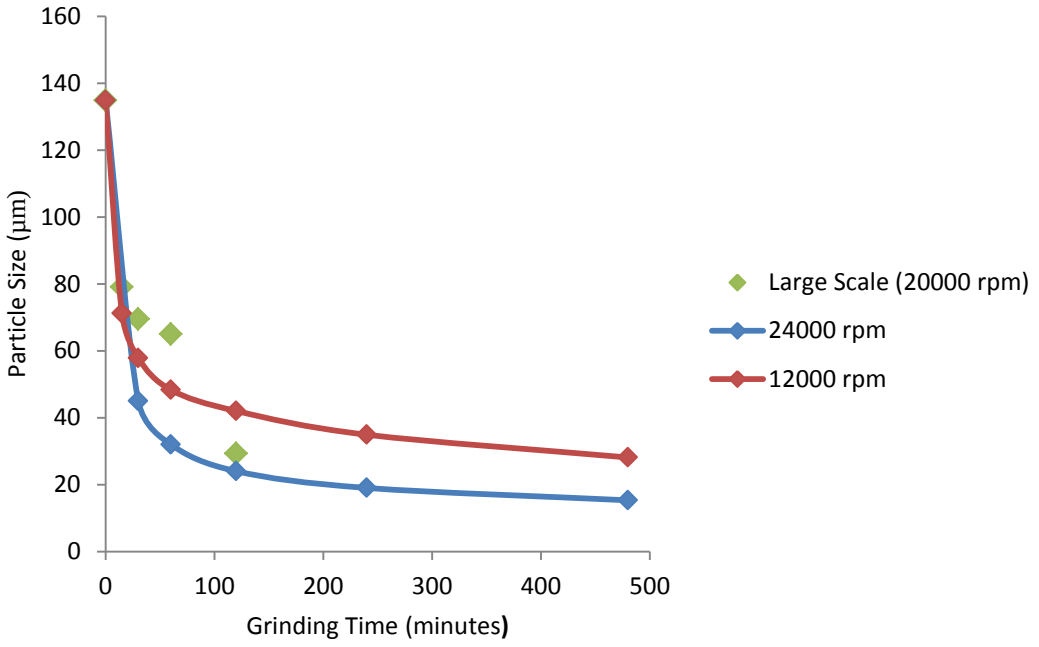

Figure 3.5: The variation of milled particle size with grinding at different stator rotor speeds. The experimental results for small scale batches produce a smooth curve when plotted, and a higher stator rotor speed produces smaller particles. In comparison, when the process is scaled-up, the resulting particle size is not predictable from the smaller batches.

Experiments 11melBB, 11melCC, 11melDD showed that the grinding time could be increased as the quantity scale increased to give a more predictable product (55.8 – 51.8 µm with a larger error of 7 %). The higher error in scaling is a foreseeable issue for all chemical process operations, not just milling. For the materials used in this investigation it confirmed that all batches used for characterisation should be made on the same scale prior to blending, and that predicting the eventual particle size of LLM-105 from a smaller batch would be difficult. This is verified by the plot of the large scale milled batches in **Figure 3.5**; the particle size in the scaled-up process decreases over a shorter time period than the materials carried out on the small scale.

3.1.4 Application to LLM-105

The inert study using melamine helped to define the processing conditions for milling the LLM-105. An important factor for processing explosives, which is not a concern when dealing with inert materials, is how safe the handling properties of the product are. Hazard assessment of explosives will be discussed further in Chapters 4 and 5, but for the purpose of characterising the milled material, its sensitiveness to impact, spark and thermal insult will be examined here. These hazard properties are most likely to vary with particle size, and any significant difference in sensitiveness from the pristine material could indicate that the smaller particle size is unsafe to handle, and therefore would be inadvisable to manufacture.

It is good practice to begin with small quantities of modified explosive and scale up, preventing the creation of large quantities of material that could be unusable, or hazardous, and must be disposed of. Batches of LLM-105 were milled 10 g at a time as summarised in **Table 3E**, and were assessed for hazard sensitiveness using the standard Rotter impact test (to be discussed further in Chapter 4) and the Temperature of Ignition (ToI). The result from the Rotter test is quoted as a Figure of Insensitiveness (FoI), which is compared with the standard, RDX, which has a FoI of 80 by definition. TATB is considered to be very low sensitiveness and its FoI is usually above 100.

The results from hazard testing LLM-105 batches are presented in **Table 3E**. The pristine LLM-105 achieved a FoI of 66, however batch LLMB, the first of the scaled-up 10 g milled batches, gave a FoI of 38. 38 is a very low value and typically secondary explosives with a FoI below 50 are rejected. LLMB was the first larger batch produced and it can be seen in **Table 3E** that the particle size reduction aspect was successful (14 µm on

the 10 g scale compared with 13 µm on the 0.5 g scale). Three further attempts were made with the aim of improving the FoI using a less aggressive milling speed and reducing the grinding time. These three batches held FoIs in the range of 36 – 40, which is still too low to produce useful milled material for further work.

Sample	**LLM-105 Mass (g)**	**Water Volume (ml)**	**Conc. (wt. %)**	**Disper-ser Speed (RPM)**	**Grind Time (mins)**	**Particle Size (µm)**	**FoI**	**ToI (ºC)**
Pristine LLM-105	N/A	N/A	N/A	N/A	N/A	45.0	66	323.2
LLMA	0.5	9.5	5	24000	15	13.0	N/A	N/A
LLMB*	10	90	10	20000	10	14.4	38	323.6
LLMC	10	90	10	12000	20	N/A	39	320.1
LLMD*	10	90	10	12000	10	N/A	40	319.5
LLME*	10	90	10	12000	5	N/A	36	319.3

Table 3E: Milling parameters of LLM-105 batches and the impact and thermal sensitiveness assessment for each batch. *indicates that two batches of this size were milled and blended into one 20 g batch for hazard assessment

The milled batches were also subjected to the temperature of ignition, or ToI test, which assesses bulk thermal stability and highlights any chemical changes to the explosive. The pristine LLM-105 had a ToI of 323.2 ºC and the milled batches ranged from 319.3 – 323.6 ºC. The difference between the ToI for the neat and milled LLM-105 is not considered to be a significant change, therefore the observed shift in sensitiveness of the milled LLM-105 is attributed to a physical change rather than any chemical degradation.

It is also of note to mention that all of the batches were characterised for sensitiveness to electrical spark for the safe handling of dry powder, and all of the batches including the pristine LLM-105 consistently produced no ignitions at 0.45 J. A value of 0.45 J indicates that there is little risk of an initiation hazard presented by spark generation through electrostatic discharge.

Given the shift in impact sensitiveness caused by the milling, it was hypothesized that the mechanism for milling may cause different physical features in the material. The theory is supported by the ToI data that verifies that the pristine and milled materials have the same thermal and therefore chemical stability. The stator rotor mills particles by employing a shearing motion as particles are caught between the rotor's teeth, possibly aided by the flow of the suspension. Other milling methods such as ball milling actively crush the particles. It is possible that the stator rotor shearing action chips edges but introduces stress and fracturing within the remaining material without breaking the whole particle. These stresses are potentially weak points in the particle that in theory qualify as defects. Cracks and other similar defects can act as initiation sites for reactions under impact due to the adiabatic compression of the air contained within, leading to a greater likelihood of the generation of hot-spots.

It is expected that a larger number of defects would lead to an increase in sensitiveness as they are points where hot-spots can develop with an appropriate stimulus (in this case, insult by impact). The milled particles were examined using Scanning Electron Microscopy (SEM with a Carl Zeiss EVO MA 10) in **Figure 3.6**, which confirms the presence of such defects on the particles. The defects are highlighted with red circles; sheared faces and cracks can be seen on the surface of the particles, and it is also possible to identify some deeper internal cracks in larger particles.

The images of milled LLM-105 in **Figure 3.6** can be compared with **Figure 3.7** showing the pristine LLM-105 with the higher FoI (meaning that it is less sensitive to impact). The pristine LLM-105 has no surface cracks or defects, supporting the theory that these sites increase a material's sensitiveness to impact through the adiabatic compression mechanism. This result shows the importance in fully characterising a material that has undergone particle size reduction in order to assess whether more than one aspect of its physical nature has been altered, and disambiguate any changes in its sensitiveness between particle size and introduction of defects or damage.

a)

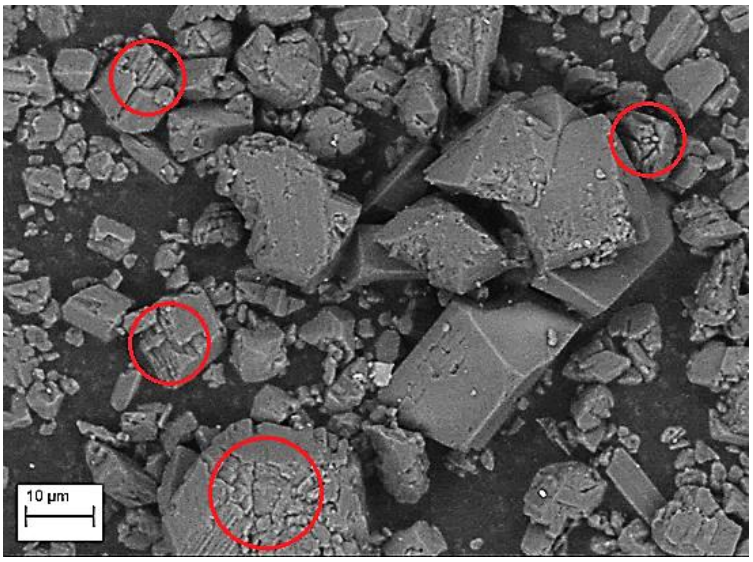

b)

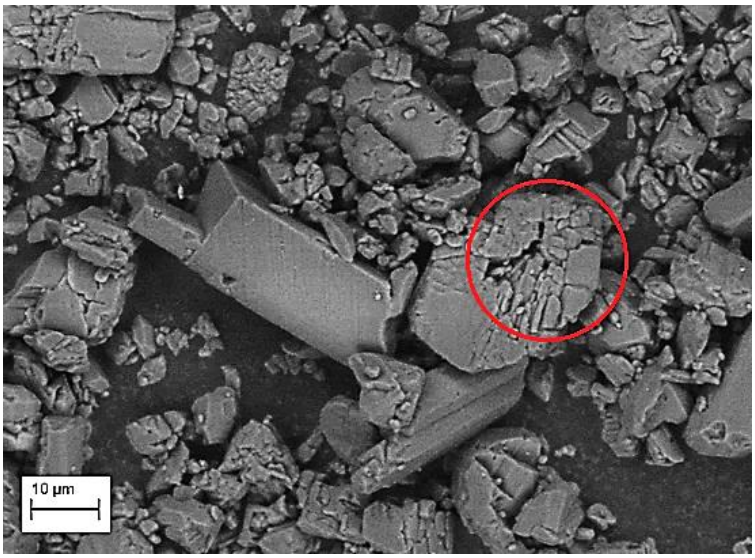

Figure 3.6: SEM images of the stator rotor milled LLM-105 showing the presence of damage and defects. Multiple particles containing sheared areas on the surface are present (a) and it is also possible to observe an internal fracture through a crystal on larger particles (b). In general these images show a range of particle sizes and some unmilled material as the process was not optimised at this stage

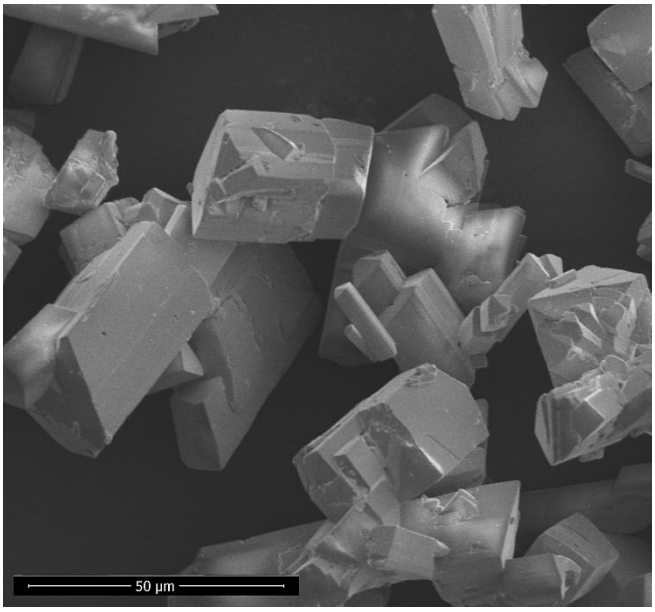

Figure 3.7: SEM image of the pristine LLM-105 with generally smooth faces and a block-like morphology

The LLM-105 that was milled using the stator rotor was deemed unsuitable for further development as it had a FoI below 40, with the typical acceptance criteria for secondary explosives being 50 (considering safety of scale up, formulation and transport on public roads). Following further investigation, it became possible to source smaller particles of LLM-105 from a single supplier that had recently developed a scaled-up ball milling method of particle size reduction for LLM-105. The ball milled LLM-105 that was procured had a particle size of 8.3 µm, ToI of 320.5 ºC and a FoI of 57. Its ToI is similar to the other batches of LLM-105, but with a significantly improved FoI which makes it suitable for further assessment and formulation.

Teipel previously used a stator rotor to mill the explosives HMX, RDX and CL-20, but focused on the particle size reduction aspect of the process and did not characterise the new materials with respect to their hazard properties [75][76]. From the evidence presented, we conclude that the stator rotor milling method is not suitable for use with explosive materials. The subsequent experiments in this thesis requiring milled LLM-105 utilise ball milled LLM-105. As a more extensive assortment of particle size and shape was required for examination, other methods of producing explosive particles were explored.

3.2 Particle Morphology Modification

Non-mechanical methods for particle modification are available as an alternative to milling; reprecipitation of powder allows crystals to be re-grown without applying any stresses. The process requires an understanding of the solubility of the material and the conditions under which nucleation will occur. It has successfully produced TATB particles between 2 and 5 μm in batches up to 150 g [81], and more complicated experiments employing antisolvents and controlling nucleation with sonication (sonocrystallization) to give CL-20 crystals with an average size of 5 μm have been carried out [82].

Chemical methods are also currently a basis for investigating nano particle production of energetic materials, though nano materials are beyond the current scope of work. A brief summary of techniques is given in **Table 3F**, showing that it is possible to modify a number of explosives with different molecular structures using reprecipitation.

Energetic Material	**Method**	**Particle Size**	**Reference**
HMX	reprecipitation	50 nm	[83]
RDX	spray drying super critical fluids	110-220 nm	[84]
HMX/PETN	spin coating	100-200 nm	[85]
CL-20	reprecipitation in a non-solvent	95 nm	[86]

Table 3F: Chemical methods used to generate nano particles of energetic materials

Reprecipitation, or recrystallization, means dissolving the material in a solvent and allowing it to recrystallize either slowly or using an anti-solvent to crash precipitate particles out of solution. Further steps such as spray drying or spin coating are procedures that mechanically process the solution to create specific particle shapes.

3.2.1 Recrystallization of LLM-105

The aim of recrystallizing pristine LLM-105 was to produce new material to characterise and further develop understanding of the effect particle size and shape has on sensitiveness. As practiced with the milling experiments, small batches of new materials were produced to account for safe working procedures, and 1 g of pristine LLM-105 was

recrystallized at a time. Before the experimental parameters could be defined, a solubility study on LLM-105 took place.

LLM-105 possesses strong intra and intermolecular hydrogen bonding which affords a layered structure with an insensitive nature [14]. This type of bonding system is also seen in molecules such as TATB which possesses a graphitic molecular arrangement, in theory contributing to its low sensitiveness as the layers are able to slide over one-another when mechanically insulted. TATB is also characteristically insoluble, which can also be attributed to these interactions. Dissolving such molecules is difficult and usually requires strong hydrogen-bond disruptors, such as strong acids or bases.

A number of solvents were used to assess LLM-105 solubility, including acetone, methyl ethyl ketone, methanol, tetrahydrofuran, xylene, dimethyl sulfoxide (DMSO), dimethyl formamide (DMF) and N-methyl-pyrrolidinone (NMP). Of all the solvents, DMSO was the most efficient at dissolving the LLM-105, followed by DMF and NMP, indicating the increased effectiveness of more polar solvents. The COSHH hazards associated with using DMSO are lower than that of DMF and NMP, therefore DMSO was chosen as the recrystallization solvent.

Initially the LLM-105 was dissolved in 90 ml DMSO at 110 ℃, with stirring, for fifteen minutes; the solution was then left to cool slowly in the oil bath to ambient temperature without stirring. The process was repeated, but then the solution was cooled quickly using an ice bath rather than the oil bath, cooling with residual heat from the dissolution stage (experiments 105A and 105B respectively, as outlined in **Table 3G**). Neither of these solutions produced crystals of LLM-105. The next approach to particle production was to employ anti-solvent crystallization.

Anti-solvent crystallization achieves crystals of a material in solution by exposing it to another solvent in which the material is sparingly soluble, inducing supersaturation leading to rapid crystallization. The term supersaturation refers to the saturation of a solution where it is at the critical point of crystal nucleation. The anti-solvent technique is capable of controlling the crystalline properties such as particle size and morphology [87] by changing the supersaturation level using process parameters. Typically large crystals grow from slow supersaturation and small crystals grow from rapid supersaturation. The physical and chemical properties of the anti-solvent used can also alter the rate of mixing (or miscibility) with the solution containing the product, affecting the rate of nucleation and crystal growth. Parameters of the crystallization experiments can strongly influence the crystal formation mechanism, and therefore control its size and shape [87].

Exp	Anti-solvent	DMSO (ml)	Anti-solvent (ml)	Temp (ºC)	Anti-solvent Addition Temp	Cooling Rate	Yield Mass (g)	Yield (%)
105A	None	90	N/A	110 with stirring	N/A	ambient	N/A	N/A
105B	None	90	N/A	110 with stirring	N/A	with ice bath	N/A	N/A
105C	Cold water	90	90	110 with stirring	cold water added to ambient solution	with ice bath	0.782	78.4
105D	Water	25	6 added drop-wise	110 with stirring	ambient with stirring	at ambient	0.853	88.9
105E	Cold water	25	250	80 with stirring for a further 5 mins	cold water added to hot stirred solution	at ambient with stirring	0.919	92.5
105F	Xylene	25	10 in two 5 ml portions	80 with stirring for a further 5 mins	xylene added to hot solution with stirring	placed in ice bath for 15 min, and ambient for 15 min	0.149	15.0
105G	Xylene, water	25	10 ml xylene in two 5 ml portions followed by excess water	80 with stirring for a further 5 mins	xylene added to hot solution with stirring. Water added at ambient	placed in ice bath for 15 min after xylene, left at ambient after water	0.465	47.0

Table 3G: Recrystallization experiment parameters to produce different LLM-105 particle size and morphologies. The highest yields were recovered using water as the anti-solvent in a reduced quantity of DMSO. The addition of the anti-solvent was trialled with and without stirring, whilst the solution was either still hot or cooled to ambient temperature

The anti-solvents chosen from the previous solubility study were water and xylene; this is because the LLM-105 was least soluble in these. The temperature, quantity and rates of addition of the anti-solvents were varied through trial and error as noted in **Table 3G** for experiments 105C through to 105G. Each of these experiments produced yellow crystals of LLM-105, with varying rates of yield success.

Experiment 105F in particular yielded very little product at only 15 % conversion; this experiment used xylene alone as the anti-solvent. Using a combination of xylene with water in experiment 105G proved to be more efficient with a yield of 47 %. This study has shown that water is a very effective anti-solvent for LLM-105 crystallization in DMSO as the highest yields were obtained using water when compared with xylene. The result could be explained by the solubility parameters of the solvents used.

The Hildebrand solubility parameter [88] is a numerical estimate of the degree of interaction between a specific solvent and other materials. It is related to the internal energy of the molecules in the solvent. In turn, the internal energy of the solvent molecules is determined by the van der Waals forces holding those molecules of the liquid together. The solubility parameter of DMSO, which LLM-105 is soluble in, is 26.4 MPa. It would be expected that LLM-105 would be soluble in other solvents with comparable numerical solubility parameters to DMSO, reflecting similar internal energies of the solvent and hence interactions with the LLM-105 molecules. The solubility parameters of xylene and water are 18.2 MPa and 48.0 MPa respectively. Remembering that an anti-solvent is a solvent in which the product is less soluble; the solubility parameter of water has a greater numerical difference to DMSO than xylene, therefore LLM-105 is less soluble in water and it is therefore more effective at precipitating crystals and yielding product.

However efficient each reaction was in yielding product, a range of materials were successfully recovered, requiring analysis for further study.

3.3 Characterisation of Materials

The pristine LLM-105 and the modified batches that were obtained required characterisation to distinguish features that energetic properties may later be attributed to. It is important to fully characterise new materials in order to understand and draw conclusions from any phenomena observed during later experiments. The appropriate techniques for characterisation and results are discussed in this section.

3.3.1 Physical Characterisation

The purpose of the LLM-105 milling and recrystallization was to generate materials of varying particle size and shape for further study. The particle size and shape characterisation methods carried out were laser diffraction (using a Malvern Mastersizer 2000) and scanning electron microscope (FEI Magellan 400L SEM) on each of the batches. The characterised materials include pristine LLM-105, ball milled LLM-105 and the recrystallized products from experiments in the previous section.

The pristine LLM-105 has a particle size of 47 µm in an elongated equant shape; referred to as block morphology (**Figure 3.8**). The ball milled LLM-105 (**Figure 3.9**) is rounded on the edges due to the milling action, and the particles are categorised as rounded blocks. The milled particles were 8 µm in size. The appearance of the particles in **Figure 3.9** is in contrast to the sheared particles seen in the stator rotor milling technique, shown in **Figure 3.6**.

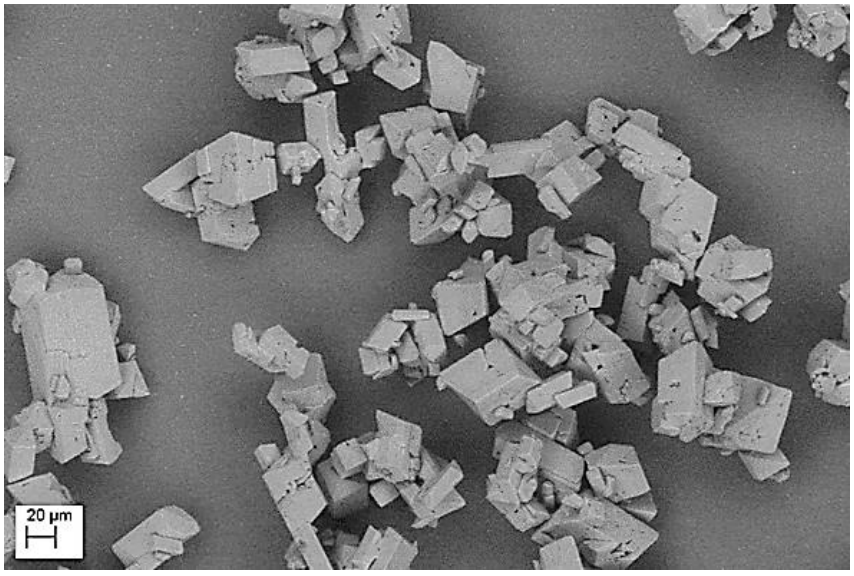

Figure 3.8: Particles of pristine LLM-105 have block morphology which is a three-dimensional rectangular shape; 47 µm in size

The first recrystallized LLM-105 sample, 105C (found to be 38 µm in size), was observed to exhibit twinning behaviour in a star-like configuration; **Figure 3.10** and **Figure 3.11**. These structures are three dimensional and sit about an axis of symmetry.

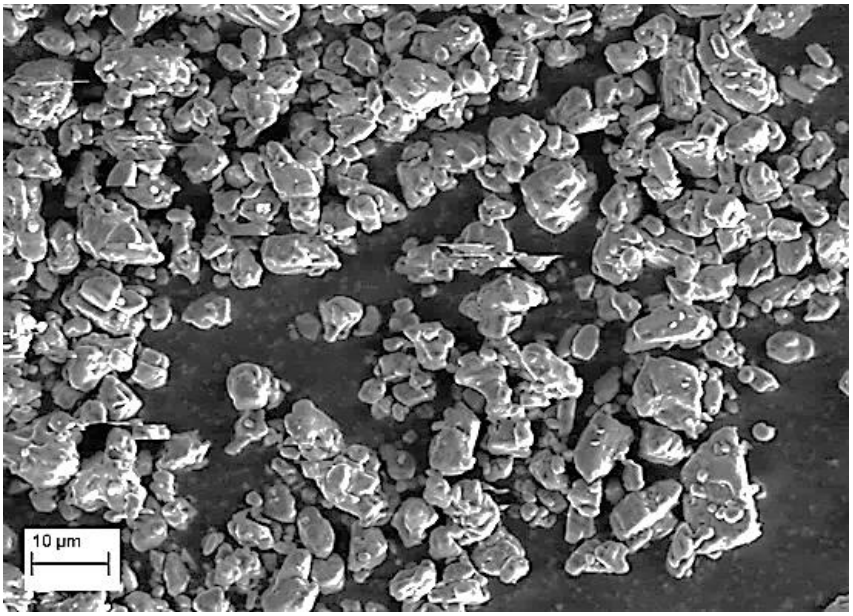

Figure 3.9: Particles of ball milled LLM-105 have rounded block morphology where edges have been smoothed by the milling process; 8 µm in size

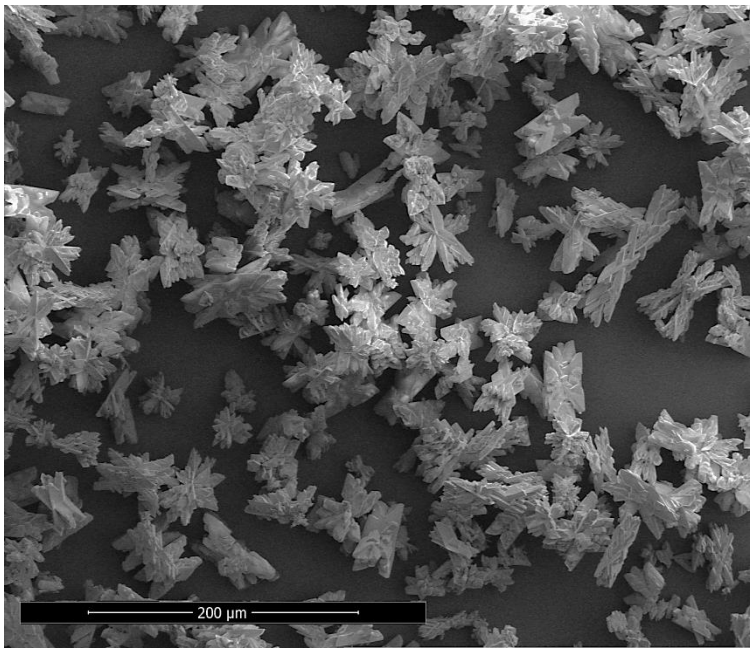

Figure 3.10: Particles of 105C which are twinned crystals grown about a single point of nucleation; 38 µm in size

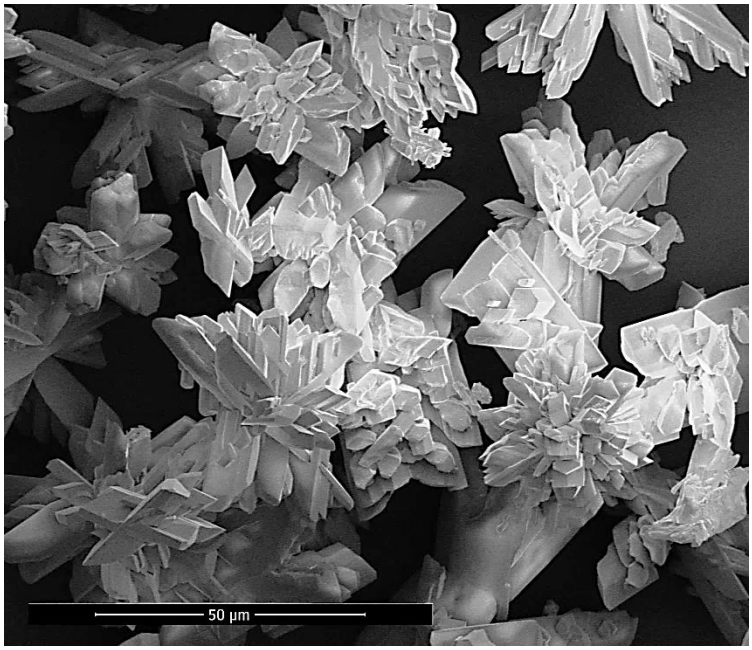

Figure 3.11: A closer view of 105C particles; the crystals are twinned in three dimensional star shapes about an axis of symmetry

It was found that the particles produced in the other batches of recrystallized LLM-105 were significantly smaller in size than for batch 105C. These materials were too small to effectively view using the Magellan SEM; insulating specimens charge up in the electron beam making imaging small features problematic. Therefore an environmental scanning electron microscope (ESEM) was used to characterise the remaining samples. The particles in batch 105D are small and needle-like in shape, also referred to as acicular morphology (**Figure 3.12**).

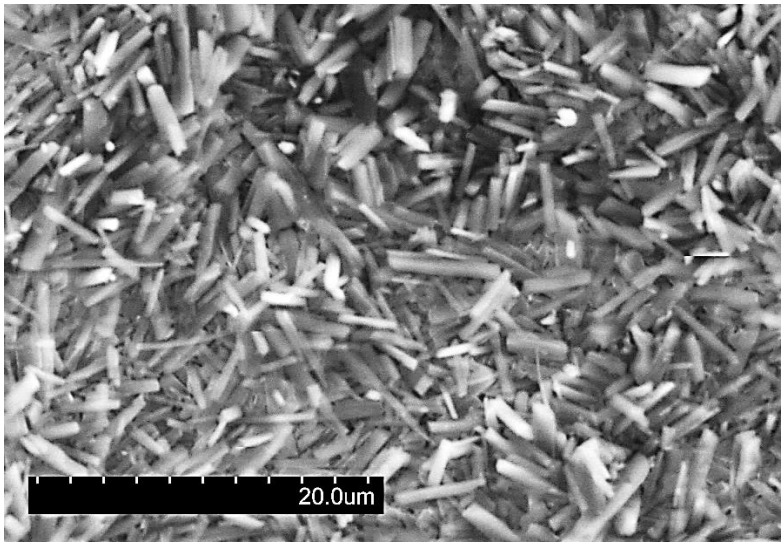

Figure 3.12: 105D is a small needle morphology, known as acicular; 4 µm long

The Mastersizer identified the particle size of 105D as 2 µm, however examination with ESEM shows this value underestimates the length of the needles. Inspection of a number of sample areas shows the needles to be approximately 4 µm long. The error in the instrument measurement is because the laser diffraction technique assumes that particles are spherical when it calculates the particle size from the scattered light, as discussed earlier in Section 3.1.1. Therefore particles with a high aspect ratio will be underestimated in length when allowed to move around different orientations lengthways in suspension. This effect makes the Mastersizer less useful for long particle shapes, and needs to be accounted for. Here it is possible to manually measure a sample of particles and estimate a needle length of 4 µm.

The result of 105E is a 2 µm mixture of blocks and needles (**Figure 3.13**); the combination is probably a result of the excess anti-solvent added to produce the batch. The batch of 105F particles are long, high aspect ratio needles (**Figure 3.14**) which the Mastersizer also underestimated in length owing to the same rationale as for batch 105D. The particle size was measured with laser diffraction to be 8 µm, but inspection of various sample areas using ESEM shows the needles to be approximately 20 µm long.

Finally, batch 105G resulted in the smallest particle produced, at just under 1 µm in particle size. From what can be distinguished on the ESEM (**Figure 3.15**), they are also small block-shaped grains, only just discernible due to their barely-micron size.

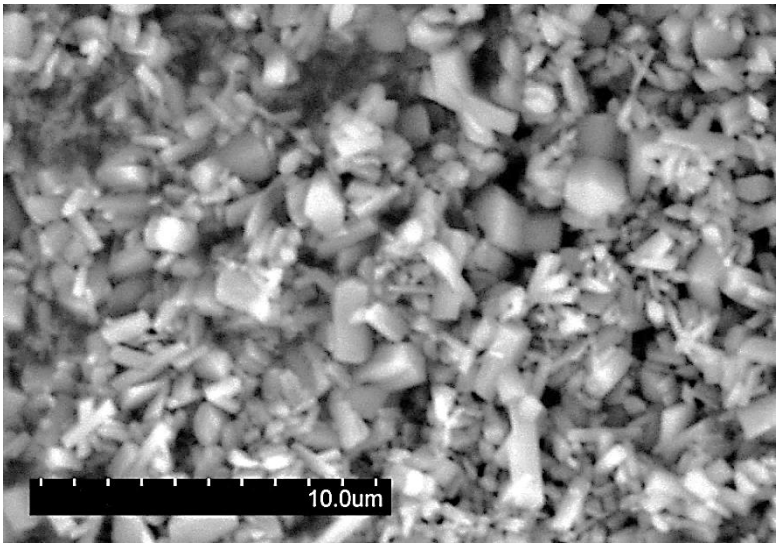

Figure 3.13: Batch 105E is a mixture of small particle shapes in needle and block morphology produced by excess antisolvent; 2 µm in size

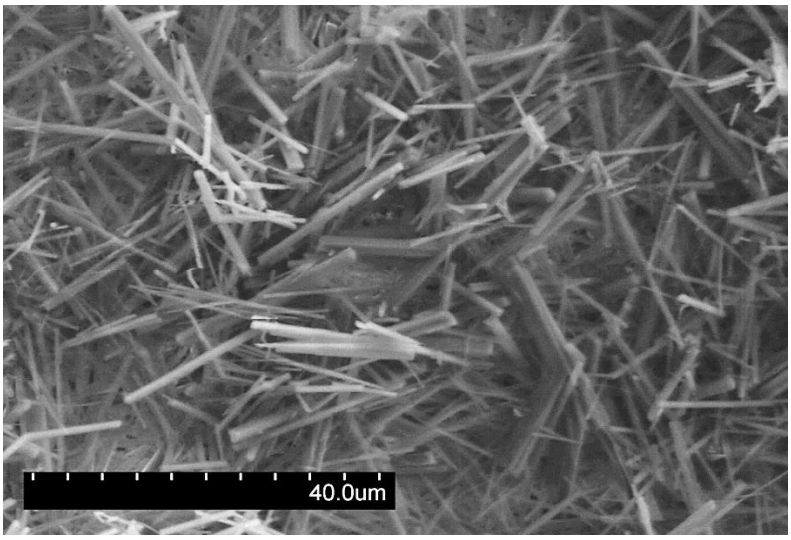

Figure 3.14: 105F is made of long, high aspect ratio needles 20 µm in length

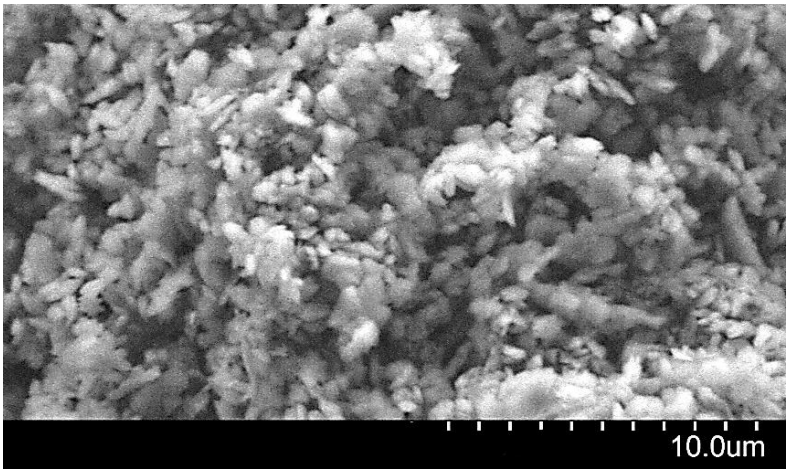

Figure 3.15: 105G is the smallest particle size sample below micron scale, and appears to be block-shaped grains

From examination of these SEM images it can be seen that LLM-105 has a preference for forming block or needle morphologies from DMSO. The highest yield batches were 105D and 105E, with 88.9 % and 92.5 % recrystallized product recovered. Batches 105D and 105E were both characterised to be comparable in particle size, with 105D being small needles and 105E being a mixture of needles and blocks. A slow, drop-wise addition of water in batch 105D produced the needles, while the mixture of morphologies was obtained from crash precipitation using excess water as the anti-solvent in batch 105E.

The lowest yield batch was 105F which used xylene to produce long, narrow needles with only 15.0 % product recovered. The low yield suggests that blocks form preferentially over the needles. Using a combination of water and xylene as the anti-solvent produced batch 105G which had the smallest particle size and a relatively average yield of 47.0 %.

When there is no stirring during addition of anti-solvent, as for batch 105C, the lack of dispersal of anti-solvent appears to result in twinning as multiple facets can be observed protruding from a single point in a particle. Crystal twins are also referred to as enantiomorphic particles. Twinning occurs when two crystals share some of the same crystal lattice points and symmetrical features form. These particles clearly formed readily as 78.4 % of recrystallized product was yielded from the original material. Twinned LLM-105 crystals have been produced before [89], though it required the use of a specialist solvent (1-butyl-3-methylimidazolium trifluoromethanesulfonate) and resulting crystals demonstrated a lesser extent of twinning; thin rods formed around a single central point, comparable to a zinc oxide crystal. The author describes these particles as flower-like three dimensional microstructures; batch 105C has wider rods and a higher level of twinning, designated as star-like.

To ensure that there were no alternative crystal structures or polymorphs of LLM-105 present in any of the batches, X-ray diffraction was carried out. Different polymorphs can be distinguished as an X-ray diffraction pattern is unique to a particular crystal phase in a substance. The samples were tested using a powder X-ray diffractometer; which operates on Cu Kα radiation (λ = 0.15406 nm) in a fixed sample mode. The diffraction patterns of pristine and milled LLM-105 are shown in **Figure 3.16**; recrystallized batches follow in **Figure 3.17**.

It can be seen in the X-ray diffraction patterns in **Figure 3.16** and **Figure 3.17** that the peaks fall at the same 2θ values for each of the batches, indicating that there are no different crystal polymorphs present in any of the samples.

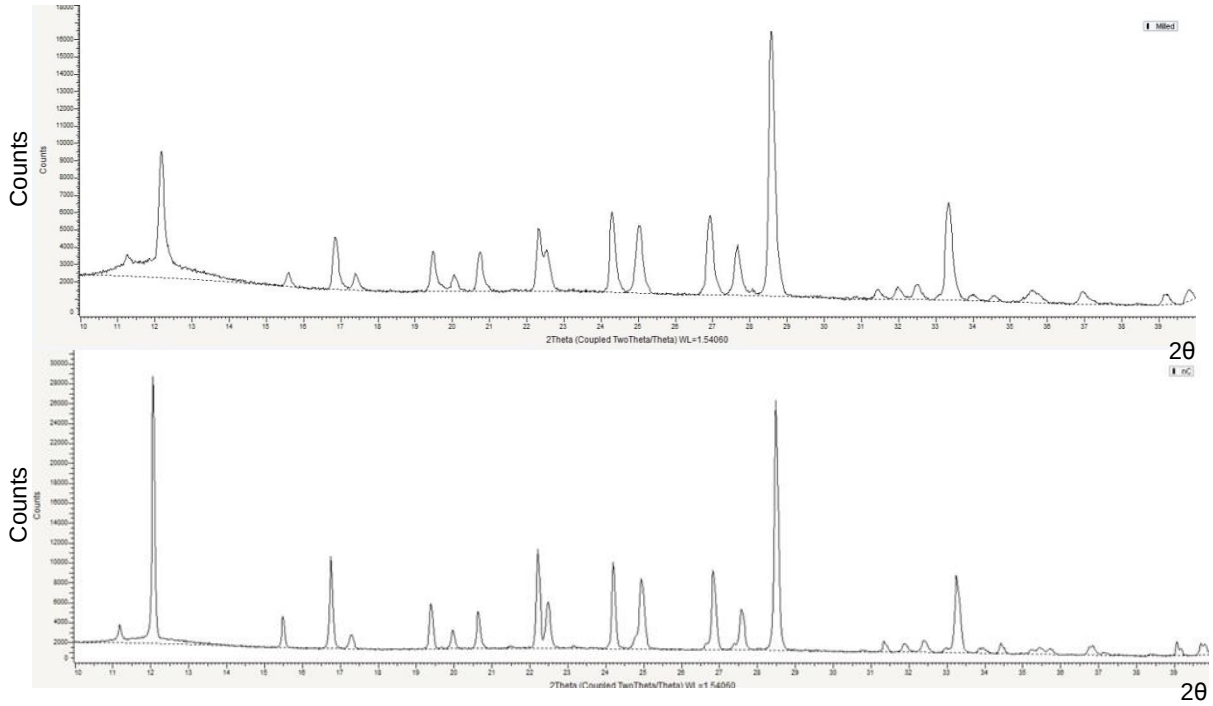

Figure 3.16: X-ray diffraction patterns of pristine LLM-105 (top) and milled LLM-105 (bottom) showing peaks aligning at the same 2θ values

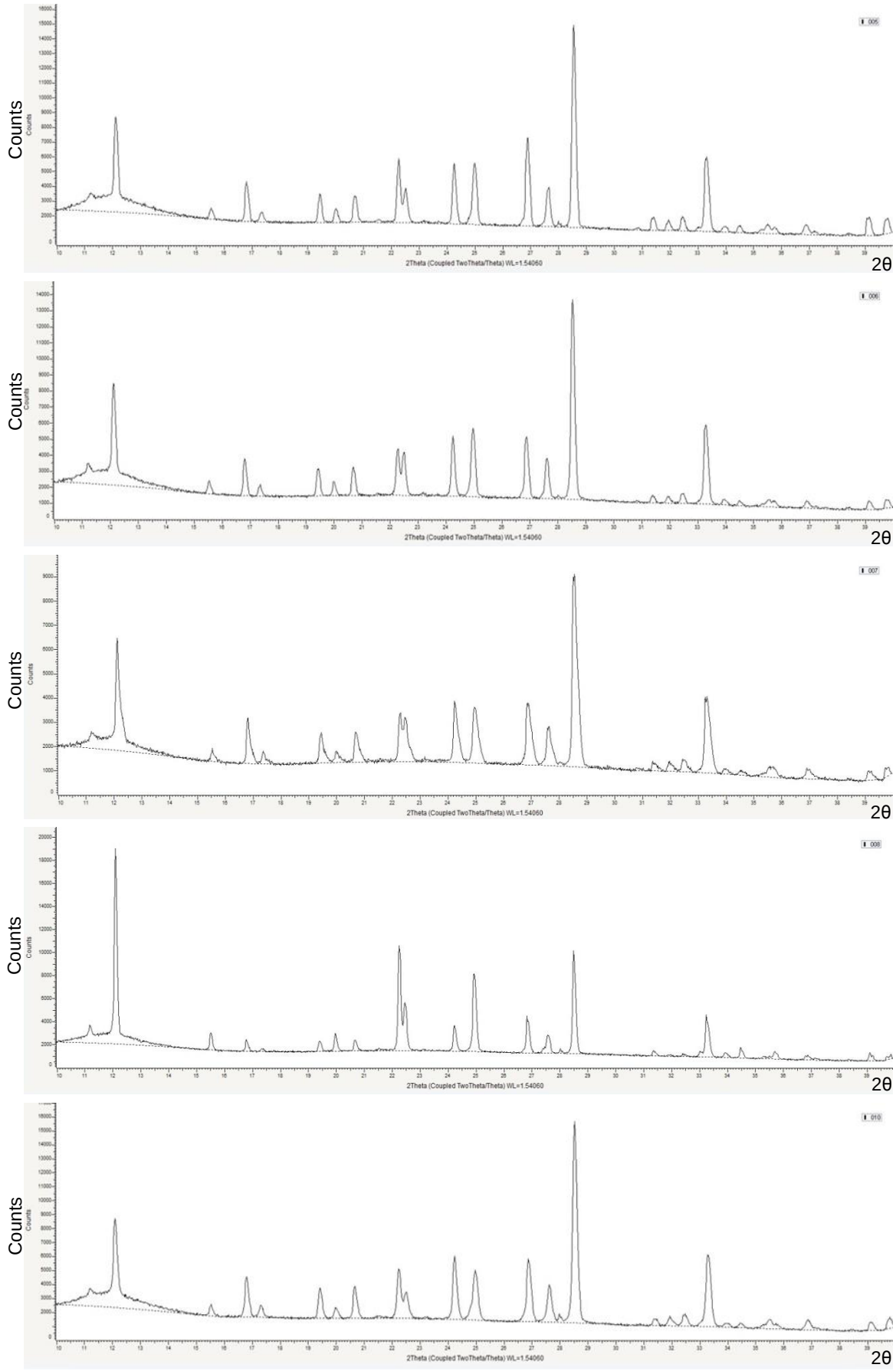

Figure 3.17: X-ray diffraction patterns for (top-bottom) 105C, 105D, 105E, 105F, 105G

3.3.2 Chemical Characterisation

Chemical characterisation of the new materials is necessary to ensure that any differences observed between batch characteristics can be solely attributed to the particle size or shape. DSC traces examining the temperature of decomposition were taken using an instrument up to 400 °C at a rate of 10 °C per minute with 0.8 – 1.2 mg of sample. The decomposition temperatures were measured using sealed pans initially, which were then adjusted with a pin-hole in the lid as the build-up of reaction gases in the sealed pans were causing inaccuracies in measuring the thermal traces due to juddering of the pan. The effect is exacerbated by LLM-105 beginning to sublime around 260 ºC in a pressurised atmosphere (sublimation can be observed around 300 ºC in an unconfined powder). The decomposition results of each batch are presented in **Table 3H**.

	Decomposition Peak (ºC)		
Pristine LLM-105 (sealed)	342	356	363
Milled LLM-105 (sealed)	319	352	365
Pristine LLM-105	343	353	
105C	325	349	
105D	322	349	
105E	340	359	
105F	321	348	
105G	320	345	

Table 3H: Decomposition temperatures of the LLM-105 batches measured using a DSC. The sample pans were adjusted with a pin-hole in the lid to release reaction gases

LLM-105 appears to undergo a two stage decomposition process and the batches hold a range of decomposition temperatures. References for the decomposition peak of LLM-105 also vary widely from 339 °C [89], 343 °C [89], 342 °C [90], 348 °C [91], and 354 °C [17]. It is suggested that the decomposition of LLM-105 is complex and strongly affected by the particle shape and size in relation to its surface area. It is known that a larger surface area of a chemical experiences a faster rate of reaction, and in the case of milled and recrystallized particles (which are smaller than the pristine material) there is more surface area exposed to heat and therefore a lower temperature is required to heat through the bulk of the powder. As such, the smaller, high surface area particles exhibit a lower thermal decomposition.

3.4 Material for Comparison with LLM-105

Other explosive particles were analysed for comparison with the LLM-105 batches. Different sizes of HMX and TATB were chosen, as LLM-105 is often compared with these explosives in literature. HMX type A has a particle size (d[0.5]) of 405 µm, with some larger particles present (**Figure 3.18**) in a block morphology. HMX type C is colloid milled from HMX type A and has a particle size of 4 µm with a rounded block shape. TATB type B (**Figure 3.19**) and TATB type C are both milled materials, therefore appear rougher on the surface and broken in areas. TATB type B in particular has a wider particle size distribution, though its d[0.5] is 20 µm in size, and TATB type C is 5 µm.

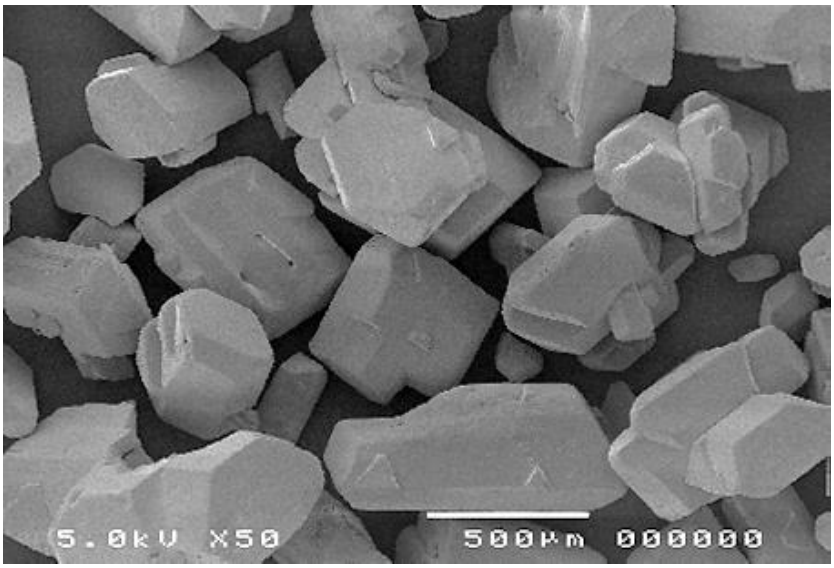

Figure 3.18: SEM image of HMX A comprised of large particles with a block morphology

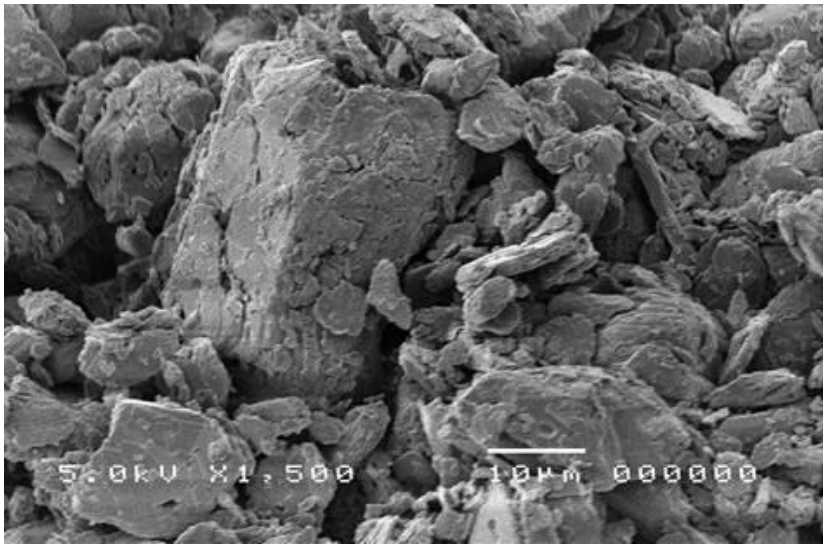

Figure 3.19: SEM image of TATB type B with block-shaped particles which are roughened and broken by milling

3.5 Summary

The aim of this Chapter was to produce and characterise LLM-105 with different particle sizes and shapes for further study, which has been achieved. The materials were characterised with respect to their particle size and shape. The new products were also confirmed as the same crystal polymorph. Some variation in thermal stability was observed, which is attributed to differences in the particle surface area. The samples available for further work are summarised in **Table 3I**.

Sample	Particle Size (µm)	Morphology
Pristine LLM-105	47	Block
Milled LLM-105	8	Rounded block
105C	38	Twinned stars
105D	4 (length)	Small needles
105E	2	Small block and needle mixture
105F	20 (length)	Long needles
105G	1	Small block

Table 3I: LLM-105 with different particle size and shapes available for further work

In the next Chapter we will examine techniques used to assess sensitiveness of explosive materials, and detail the experimental development of new methods to analyse the materials produced here.

Chapter 4: Development of Improved Methods to Assess Impact Sensitiveness of Explosives

As discussed previously in Chapter 1, the initiation of an explosive is caused by the ignition and growth of hot-spots, where the sensitivity of the explosive is related to the generation of critical hot-spots which spread and ultimately lead to a reaction. When the stimulus for that reaction is provided unintentionally (i.e. in an accident scenario) then the ensuing response is a safety issue; this measure is referred to as sensitiveness. Sensitiveness is different to sensitivity, which relates to shock or physics performance.

Sensitiveness is a term used to express how likely an explosive is to respond to an insult. An explosive can be sensitive to any number and combination of hazards depending on its chemical and physical nature; these include impact, friction, electric spark, heat and open flame [92][93]. In this Chapter, the requirement to understand an explosive's hazard properties is discussed, and in particular the characterisation of impact sensitiveness. The routine techniques and methodology available for measuring the impact sensitiveness of an explosive are evaluated before discussing improvements made to the Cavendish glass anvil drop-weight, to further examine the reactivity of explosive materials.

For the purpose of developing new explosives or monitoring changes to an existing composition, sensitiveness and explosiveness data acquired through various test methods is assessed to evaluate the potential hazard presented by an explosive. Sensitiveness and explosiveness are different parameters; the sensitiveness is defined as the probability of reaction to a specific insult, and explosiveness is the violence of the consequent reaction. Both can be measured and numerically quantified, but sensitiveness is generally more frequently used to rank materials against each other.

Explosives that possess a high thermal conductivity and high specific heat usually produce less violent reactions [94], and would be termed lower explosiveness. The reduction in violence is due to energy being more readily dissipated away from locally heated regions owing to thermal conduction. Impact testing on explosive powders is used to assess a material's sensitiveness, which ranks against other explosives that have been characterised.

Assessment data is obtained through small scale hazard testing from representative samples of powder or pressed and machined test pieces. The hazard properties of the powder are indicative of how sensitive the material is overall, however explosiveness would be expected to increase in a pressed charge versus a free flowing powder (owing to the increased dissipation of heat in a powder). The purpose of collating the resulting data is to provide confidence for the safe handling, manufacturing, transporting and storing of explosives. The hazard properties of a material should be regularly assessed throughout its lifecycle to monitor any changes through ageing effects. Some of the material properties that can influence the impact sensitiveness of explosives are discussed in the following section.

4.1 Parameters Affecting Impact Sensitiveness

The sensitiveness of explosives to mechanical impact can vary with a number of physical parameters. Particle size is known to have an effect [95][96], and coarser or larger particles are generally found to be more readily initiated (i.e. more sensitive) [97]. Nano-sized explosive particles are being fabricated with the aim of producing reduced-sensitiveness compositions; this has been successfully demonstrated using RDX [42] though an unexpected resensitization to both shock and impact was seen below 500 nm.

Increasing the number of defects and/or porosity in the particles also increases the impact sensitiveness [98-100] owing to the higher likelihood of hot-spot ignition in the heterogeneities (as discussed in Chapter 1). For this same reason angular particles are considered to be more sensitive [101][102], with spherical or cubic shapes being preferred particle shapes for reduced sensitiveness [67][103].

The effects on impact sensitiveness due to the physical parameters of the particles are comparable to the effects seen on a material's shock sensitivity, as discussed in Chapter 2. The analogous behaviour is because the physical characteristics of a particle can influence its mechanical response to impact or shock. Plastic deformation of explosives under impact can lead to hot-spot formation, and voids or defects promote this mechanism under mechanical loading.

4.2 Techniques for Assessing Impact Sensitiveness

Guidance for assessment of the sensitiveness of energetic materials is provided in the United Nations Manual of Tests and Criteria Recommended for the Transport of

Dangerous Goods [104]; and more specifically for the UK in the Energetic Materials Testing and Assessment Policy (EMTAP) Manual [105]. These are compilations of accredited sensitiveness and explosiveness tests which are used to evaluate the hazard properties of explosives. This data is needed for the development of new materials, transport of explosives and qualification purposes. All industrial manufacturers and developers of explosive materials recognise one or both of these manuals and the procedures contained as a requirement for the fundamental assessment of an explosive's hazard properties.

Experimentally, measuring impact sensitiveness appears relatively uncomplicated; a sample is subjected to the impact of a standard mass falling from different heights and a "Go" or "No go" is awarded in accordance with observations of the resulting reaction. In some cases a height of 50 % probability of reaction is determined, denoted as H_{50}. The results from testing various materials are used to rank the materials in order of impact sensitiveness.

The UK EMTAP manual currently recognises two powder sample impact sensitiveness tests, which are the Rotter test (EMTAP test Number 1) [106-108] and the BAM Impact test (EMTAP test Number 43) [109][110]. These also feature in the UN Manual of Tests. Most of the powder impact sensitiveness data acquired in the UK is carried out via one of these methods. The UN Manual of Tests lists six impact tests in total, adding further options for the assessment procedure. International agreement for the use and evaluation of different methods has not been reached.

The Rotter test (**Figure 4.1**) employs a 5 kg weight (C) which is held in place by an electromagnet (A) and guide rails (B). When released, the weight falls on a drift (D) which then strikes the chamber (E) housing an anvil and the powder sample (shown in more detail in **Figure 4.2**). The "Go" criterion for a reaction is that at least 1 cm^3 of gaseous products are observed using the attached manometer (F, **Figure 4.1**). It is seen to be an advantage of the Rotter test over others that the availability of gas volume data from ignitions can be used to quantify small scale explosiveness [105].

The fifty shot Bruceton staircase procedure [111] is used to establish median drop heights for the test material and a Figure of Insensitiveness (F of I) is calculated in proportion to the median height of reaction. An explosive's F of I can be compared to other materials' and hence rank its sensitiveness; the standard used in this test is RDX which by definition has an F of I of 80.

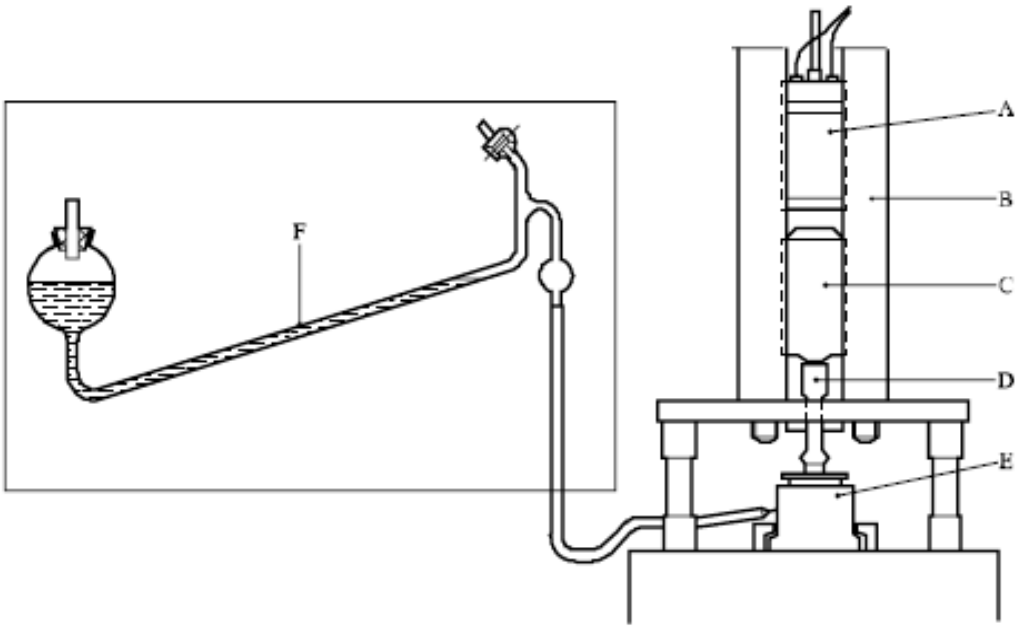

Figure 4.1: Schematic of the Rotter test from reference [104]. The weight (C) drops onto the striker (D) hitting sample chamber (E) and the resulting reaction from the sample is assessed by the connected gas output on the manometer (F)

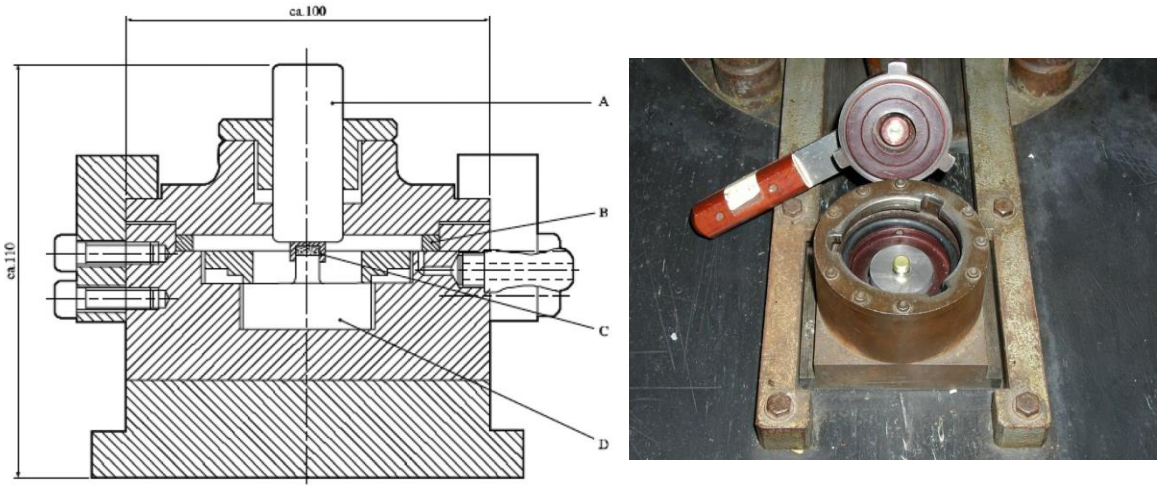

Figure 4.2: Sample housing for the Rotter test from references [104] (left) and [105] (right). Powder is placed in a cap (C) which is mounted on an anvil (D); the sample is confined. The anvil is then placed in housing which is hit by the striker (A)

It should be noted that the source of RDX used of an F of I standard is not specified; therefore some variation between different test-houses would be expected in the calibration of the Rotter machine owing to different sources of the RDX, which could have been produced using different manufacturing methods.

The BAM Impact test (**Figure 4.3**) uses a similar weight and guide rail arrangement. The sample is, however, confined between two coaxial steel cylinders (A, **Figure 4.4**) held together with a hollow cylindrical ring (B). This is mounted on an anvil and inserted into the BAM apparatus (**Figure 4.3**).

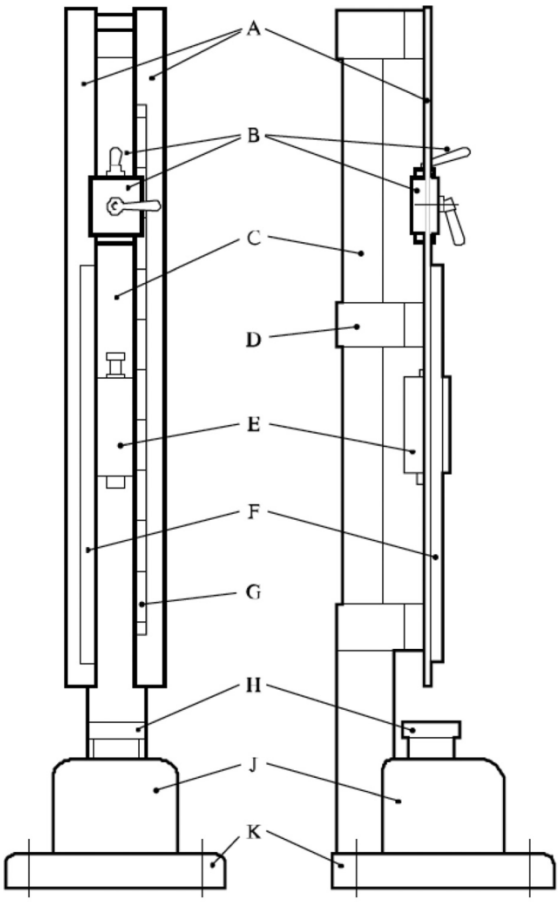

Figure 4.3: Schematic of the BAM Impact test from reference [104]. The weight (E) is released by (B) and guided (A) to the anvil (H) which contains the sample. The base (J)(K), column (C) and cross piece (D) provide structural support to the equipment and a toothed rack (F) catches the rebounding weight. A graduated scale (G) measures the drop height

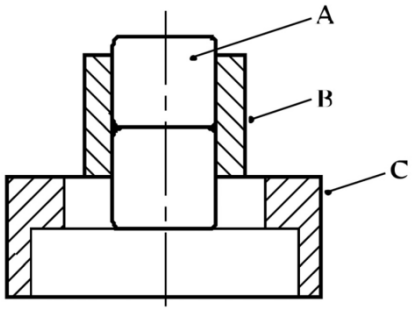

Figure 4.4: Sample housing for the BAM Impact test from reference [104]. The sample is held between two steel cylinders (A) held in place by a steel ring (B) which is mounted on an anvil (C)

For the BAM Impact test, the sensitiveness of the explosive is characterised by the limiting impact energy, which is defined as the lowest impact energy at which the "Go" is obtained by at least one out of six trials. A "Go" is characterised by an audible output, a change of colour in the material or an odour of decomposition. The impact energy used is calculated by the mass of the drop weight multiplied by the fall height (i.e. $U = mgh$); for a 1 kg weight at drop heights of 10 cm, 20 cm, and 30 cm, the impact energies are 1 J, 2 J and 3 J respectively. The limiting energies can be compared between explosives and hence materials can by ranked by sensitiveness. Dry RDX has a limiting impact energy of 5 J, PETN is 3 J [104].

The EMTAP guidance is relevant to UK legislation, however as previously mentioned, outside of the UK there are different tests to Rotter and BAM Impact used to measure the sensitiveness to drop-weight impact. The following are also listed in UN Manual of Tests; the Bureau of Explosives Impact Machine; the 30 Kg Fallhammer; the Modified Type 12 Impact Tool (a version of which is employed in the US referred to as the ERL drophammer [112]); and the Impact Sensitivity test.

In the case of the 30 Kg Fallhammer, deformation of the sample tray indicates reaction or a "Go". The Bureau of Explosives Impact Machine, Modified Type 12 Impact Tool, and Impact Sensitivity Test all distinguish a "Go" reaction by an audible output, smoke, odour or any visual evidence of ignition (discolouration or soot) observed after a drop. There are variations to the equipment in these tests in the case of sampling a liquid explosive rather than a crystalline powder, however the determination of reaction is interpreted in the same manner.

There have been historic attempts to compare how effective these tests are at characterising explosive sensitiveness. In 1980 a total of nine institutions characterised PETN, HMX, RDX, Tetryl and TNT using either the Rotter or BAM method [113]. Both of the tests ranked the materials in the same order of sensitiveness; however the study highlighted that there was closer agreement in the results between the Rotter machines than between the BAM equipment. A later study presented a different outcome; sensitiveness ranking for the same materials between the BAM and Rotter did not correlate [114]. The difference was attributed to the type of confinement the sample is subjected to in the different methods. All five of the impact test methods [104] have been compared using pyrotechnic formulations, and they failed to rank materials in the same order [115]. Overall, different machines have shown evidence that they can produce different values for material sensitiveness [116][117].

The variability in results for sensitiveness can partially be blamed on the difference of statistical method used to interpret the overall run of experiments [118]. The Rotter test's calculated F of I is based on the drop-height where 50 % of the samples produce a "Go". On the other hand, the BAM uses different criteria and calculates a Limiting Impact Energy, which is based on the lowest drop-height that produces a "Go" in one in six drops. These two test methods therefore define different levels of reaction in generating an overall numerical outcome.

The other factor that contributes to the uncertainty of results is the method by which the actual "Go" or "No go" reaction is defined. The Rotter uses the volume of gas to determine the outcome of reaction, and the other tests use a variety of subjective descriptions; an audible output, a change of colour in the material, smoke or an odour of decomposition. All of these criteria are dependent on the operator at the time leading to variation in results [119] and (with the exception of the use of a calibrated microphone) the data is not quantitative. Even gas collected in the manometer in the Rotter test is not analysed, therefore is not definite proof of a decomposition reaction.

All of the impact sensitiveness techniques discussed do not allow the operator a method to visually observe what is occurring in the sample during the impact, or monitor potential hot-spots prior to initiation. Additionally, the inaccuracy in determining impact sensitiveness appears to be exacerbated for sub-micron sized particles [120], which given the recent interest in nano-sized explosive particles introduces new difficulties.

In summary, the existing impact tests that are widely used by industry [104][105] are designed to impart a reproducible mechanical insult onto an explosive sample in order

to rank materials by their sensitiveness. In some cases there can be a lack of agreement in material ranking between test methods, and the results can be dependent on both the statistical method used and the interpretation of the operator. It is reasonable to conclude that the standard tests as they currently exist do not provide effective means for accurately determining an explosive's sensitiveness, as demonstrated between different test-houses examining the same material.

The accredited tests do not observe reactions directly and do not follow the progression of a reaction during the test. Often the results are qualitative unless a calibrated microphone has been introduced. All of these reasons provide a strong motivation for the development of additional diagnostics that accurately follow exactly what happens during the impact of explosives, and the ability to relate the observations to standard tests. There are improvements that could be made to these tests in order to further understand impact sensitiveness of explosives; this is discussed in the next section.

4.3 The Glass Anvil Drop-weight

The previous section noted that implementing an impact sensitiveness test is relatively uncomplicated; however the reproducibility of results between different tests is variable. This is partly because these methods do not allow visibility of the reaction during impact and interpretation of the reaction between operators can be inconsistent. In addition, the complexity of the problem is increased as these techniques do not provide any information that helps to determine what the mechanisms that cause initiation by impact might be.

The primary mechanism by which an explosive is initiated by impact is the conversion of kinetic energy into heat energy [121]. If that heat energy is sufficient to raise the temperature of the material and the voids within it, it is possible to create hot-spots. The generation of hot-spots by this method was proposed in the 1930s [122][123], and was confirmed as a mechanism in both liquid and solid explosives [124-126]. Another study found that the speed at which hot-spots can form can vary in different materials, and that there could be more than one mechanism under which the hot-spots initiate [127]. In addition to adiabatic void collapse, friction, viscous heating and adiabatic shear caused by impact have also been shown to generate hot-spots [8][128].

The advantage of using the glass anvil drop-weight when compared to the other machines is the ability to visualise what is happening to the explosive sample while it is

being impacted. The technique was developed at Cambridge in the 1950s, employing a rotating drum camera to record the initiation on impact of a drop-weight onto a gun powder sample sandwiched between two glass anvils [129]. Later, the equipment was modified so that the top glass anvil was attached to the weight, and a periscopic arrangement of a mirror and prism allowed a beam of light to be passed through the anvils so visualisation of the sample was possible beneath the weight [130][131]. A diagram of this arrangement is presented in **Figure 4.5**, taken from reference [132].

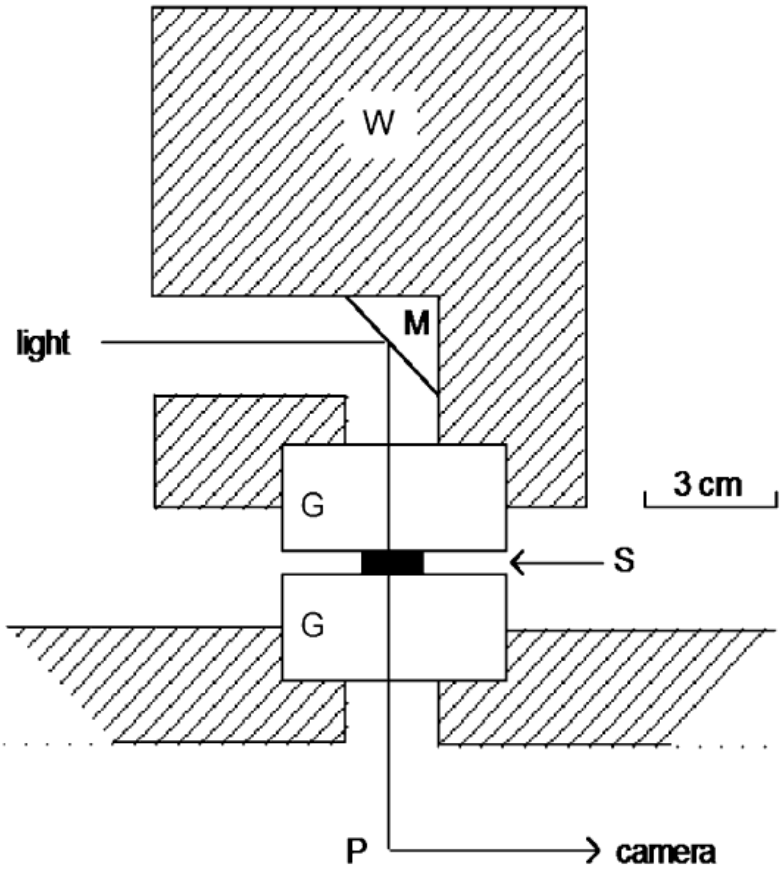

Figure 4.5: Schematic of the glass anvil drop-weight taken from reference [132]. The weight (W) is dropped from a height, taking the top glass anvil (G) with it. The sample (S) is positioned on the lower anvil (G), and when the weight hits it, the periscopic arrangement of the mirror (M) and prism (P) allow a light beam to pass through to a recording camera

Historically an AWRE C4 rotating mirror camera was used to record the reactions of the explosives during impact; an example of a film is shown in **Figure 4.6** taken from reference [130]. It can be seen in **Figure 4.6** that the glass anvil method is effective for

monitoring reaction. In this experiment PETN was impacted, and was observed to melt (turning translucent) prior to initiation, with one hot-spot igniting in Frame 7.

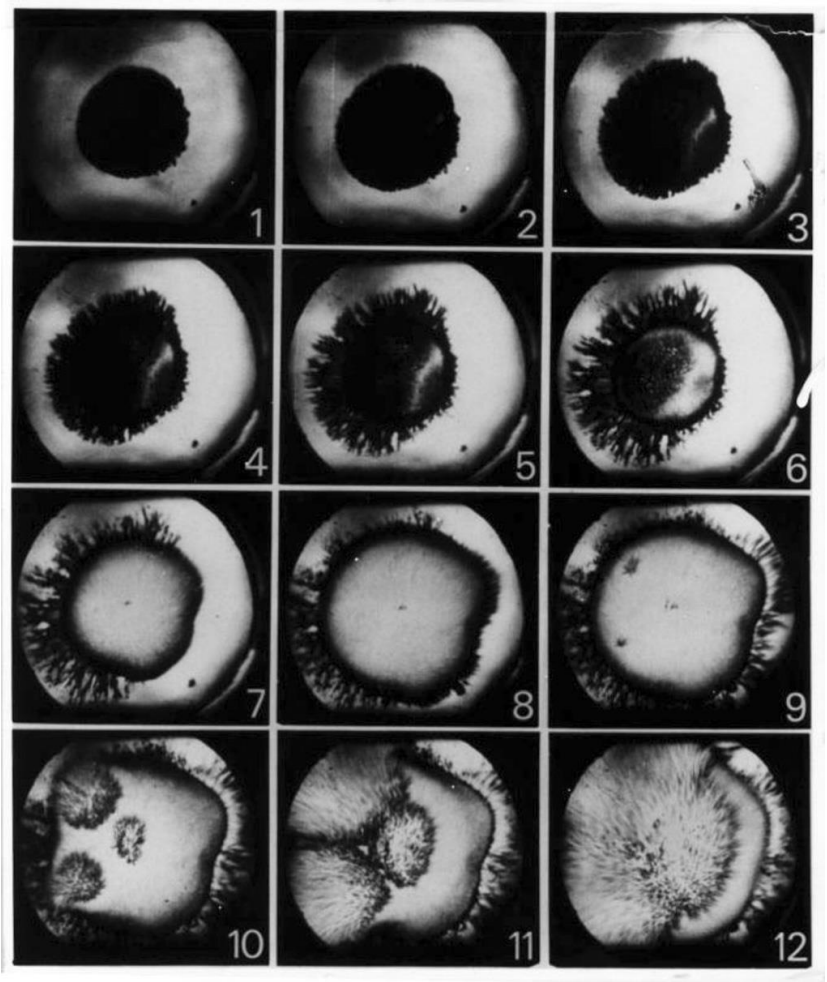

Figure 4.6: The reaction of PETN in the glass anvil drop-weight as recorded by the C4 rotating mirror camera (taken from reference [130]). The PETN changes phase after impact (possibly melting) and the first hot-spot appears in Frame 7, followed by two more in Frame 9. Growth of the reaction can be seen through to Frame 12

Two further hot-spots develop in Frame 9 and continue to grow all the way through to Frame 12 before the growing reaction consumes the sample. Photographic sequences of this type, obtained through use of glass anvils, provided the first visual proof of the existence of hot-spots.

A comparison of **Figures 4.1-4.5** shows how the glass anvil drop-weight differs from the accredited impact sensitiveness tests. Its purpose is to monitor how reaction develops during impact, not just rank materials numerically and compare them to others.

The obvious advantage of this technique is that it allows the clear visualisation of the ignition and growth of hot-spots which can improve understanding of the hot-spot mechanisms in energetic materials [5][130][133-138]. The Cambridge design has recently been replicated in China to carry out similar studies [139][140].

Based on the reasoning discussed above, the Cavendish glass anvil drop-weight provides an excellent basis upon which additional quantitative diagnostics can be added. The rest of this Chapter focuses on how that was achieved in order to assess the materials described in Chapter 3.

It became apparent on revisiting the Cambridge drop-weight machine that some substantial improvements could be made to the equipment in order to carry out an investigation on new materials. **Figure 4.7** shows the old drop-weight, which had first been used in the 1970s.

Whilst using the old drop-weight machine, integral parts such as bearings fixed to the weight would come loose when it was dropped. This indicated that the guide rails that guide the weight were no longer parallel, and therefore each drop could fall at a slightly mis-aligned angle resulting in an unreproducible experiment. The old base unit on the anvil was also difficult to modify in order to add new diagnostics to (aside from the camera, which had already been present). A new drop-weight machine was designed (credited to David Williamson) and manufactured by the Cavendish Laboratory Workshop, with the advantage of being better mechanically aligned, easier to fix diagnostics to, and also incorporated a catcher mechanism for the rebound of the weight.

On the new machine both the falling weight and lower anvil are mounted on the same coaxial rail system and sit on phosphor-bronze sliding bearings, maintaining alignment. The optical pathway through the glass anvils remains the same in the new drop-weight, again employing a periscopic arrangement of mirrors through the weight to allow an image to be recorded by a camera (**Figure 4.8**).

Figure 4.7: The old drop-weight machine based at Cambridge (picture credited to D Williamson). The weight (a) slides on rails which form the main structure (b), and is held it place by (c) while a sample is loaded. The weight is released via an electromagnet (d) and hits the anvil assembly (e) containing the sample. The old drop-weight has a protective screen (f), however the new drop-weight is operated remotely. An extract trunk (h) removes any reaction gases and the lower assembly sits on a steel unit (i)

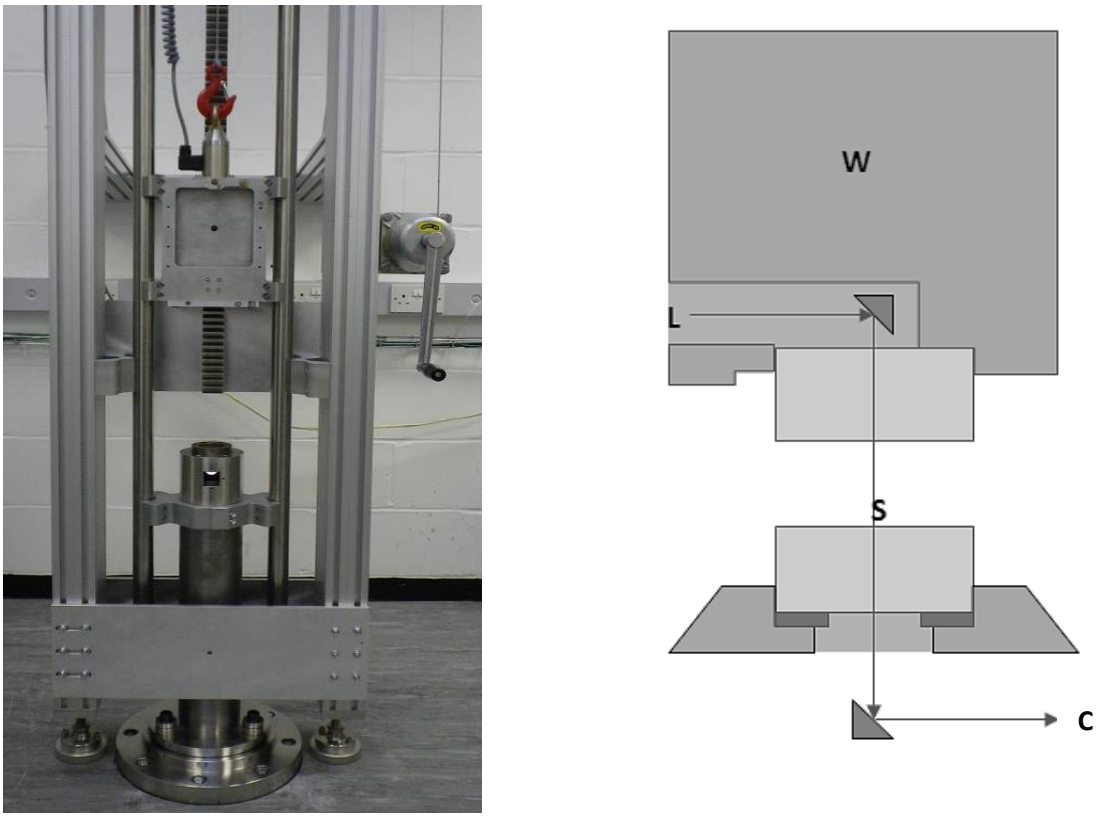

Figure 4.8: The new Cavendish drop-weight (left) and schematic glass anvil arrangement (right). The light beam (L) is directed through the weight (W) and sample (S) held between the anvils toward the camera (C)

Commissioning of the drop-weight was successfully carried out with both inert and then explosive materials contained within toughened soda-lime glass anvils. The drops were reproducible, giving the same results (as seen in **Figure 4.6**) using a sample of PETN. It is known that if sampling of a material is conducted in a non-reproducible manner, variation can be observed in the results of a drop [141], for example if different quantities of powder could mistakenly be measured. As such, a repeatable technique was required. A sampling cup typically used for both the BAM and Rotter method was utilised, in which one scoop equates to 40 mm^3 of sample – this measures approximately 25 mg of material each time. Once commissioned, the new drop-weight was ready for the addition of diagnostic techniques.

To summarise, the glass anvil drop-weight is a useful technique to help develop understanding in how energetic materials behave under impact. A new glass anvil drop-

weight has been designed and fabricated by the Cavendish Laboratory Workshop, with improved alignment to allow reproducible experiments. The next section discusses how diagnostics are implemented on the new drop-weight.

4.4 Adding Diagnostic Techniques to the Drop-weight

The glass anvil drop-weight is an instrument that allows interpretation of reactions in energetic materials. As the machine is a research tool, diagnostic instrumentation is required to assess the response of the explosive sample as it is impacted by the weight. In addition to probing the mechanism of reaction, the diagnostics are also useful to determine an overall "Go" or "No go" response from the explosive, which often relies on the judgement of the operator in the standard tests. In order to compare a number of different diagnostics with respect to their effectiveness, it was decided that a number of different techniques should be applied to the drop-weight simultaneously. This would determine which diagnostics were the most useful for discerning a reaction, and if there was variation between how effective the method is for different materials.

The obvious initial choice for the glass anvil technique was to continue to utilize photography to visualise the entire process; as discussed in the previous section this was historically the purpose of its design. A modern, digital, high speed camera could be incorporated easily. Secondly, audible output is typically monitored for the standard impact test methods, therefore a microphone was also of interest to investigate its effectiveness as a baseline diagnostic.

The output of an explosive reaction is often sound, but there are other effects that can be observed. An explosion or burning reaction also results in the creation of heat and light. Heat reactive film is not compatible with the glass anvil technique as it would block the optical path and impair the vision of the camera. Light is possible to measure as it is visible through the transparent anvils, therefore suitable instrumentation could be used to quantify the light produced during a reaction.

Whilst the research captured in this thesis was being conducted, a separate study which independently took place in the US also tried to quantify light emitted from impact experiments on explosives [142]. The investigators used a digital camera in a darkened room to image the reaction, which was then colour mapped using computer software. This technique proved to be of limited success as there was poor clarity of images and no obvious method by which to quantify the light output; the authors concluded that its ability

to define an explosive “Go” or “No go” reaction was of low confidence. The technique employed in this research instead uses a photodiode, which can accurately measure the intensity of light, providing more quantifiable results.

Finally, reaction product gases are generated during explosion or burning, and the Rotter impact test exploits this, measuring the quantity of unspecified gas to discern a “Go”. A mass spectrometer would allow for analysis of the reaction gas products and could assist in determining the extent or nature of reaction. Therefore the last addition to the diagnostic evaluation of the drop-weight was a mass spectrometer.

A method that was considered for the study was assessment of the stress that the sample is subjected to during impact. The measurement of stress requires a strain gauge which can be challenging to implement as it is necessary for the gauge to impedance match the sample in order to accurately measure the stress pulse. Furthermore, the relative sizes of the constituents within the gauge inhibit the development of the stress waves, resulting in difficulty achieving a clear measurement [132]. For these reasons, the stress assessment was rejected.

The final consideration given to the diagnostics was monitoring the input to the sample provided by the weight on impact. Studies on an impact machine that had been fitted with an accelerometer found that the velocity of the weight affected the result of the experiment more so than the kinetic energy of the impact [133-135]. As such, the weight was fitted with a marker flag-bar, designed to cut through a light gate with two incorporated laser beams, which was fitted to the structure of the drop-weight. The light gate was mounted just above the sample, so that the time between breaking the beams could be measured in order to calculate the velocity of the weight just before impact. The measured value for velocity should be equivalent to that calculated using the drop height of the weight (i.e. $mgh = ½mv^2$).

This section has discussed the motivation for choosing certain diagnostics for the assessment of impact sensitiveness of an explosive. The following sections describe how these diagnostics were applied to the glass anvil drop-weight and commissioned with an explosive to assess their performance.

4.4.1 High Speed Optical Diagnostic

Positioning a high speed camera in front of the periscopic mirror arrangement on the drop-weight is relatively uncomplicated, and had been achieved previously at the

Cavendish. However there is some careful adjustment required to ensure the assembly is illuminated correctly to allow the image of the sample to be visible and in focus. The advantages of using an electronic high speed camera over the old rotating C4 camera are that there is no need to process film, the animation is instantly available, and, with advancing technology, the images obtained are of better quality. An additional benefit of using a modern camera is that there is no need to trigger a timed flash in synchronisation with the drop-weight, and the illumination and focussing can be manually optimised prior to any experiment. The result is that digital photography allows significantly more experiments to be carried out in a given time period.

A Phantom v1610 high speed camera fitted with a Nikon 50 mm 1:1.2 lens and PK-12 extension ring was used for the investigation. The lighting arrangement was positioned behind the drop-weight as demonstrated in **Figure 4.9**. An LED panel was used as a light source, which was dispersed with a diffusion lens and refocused into a beam which was passed through the weight and glass anvils (containing the sample) to the camera. The brightness of the beam could be adjusted by altering the input voltage to the LED panel, which was optimised for the camera lens setting to obtain a high quality image.

In order to focus the camera, a clear acetate film marked with a grid was placed where the sample would usually sit between the two glass anvils (S in **Figure 4.9**) with the weight lowered and the back lighting illuminated. A typical framing rate of 130030 per second and nominal exposure time of 0.452 μs was used to film the samples in the drop-weight (each frame to frame time lasting 7.69 ± 0.2 μs). The camera was triggered using an output signal from the light gate mounted on the drop-weight frame.

PETN was used to calibrate the set-up of the camera as it is known to readily initiate and provide a visual reaction, based on historic studies [130]. Recording the growth of reaction was successfully replicated at a drop height of 220 cm and the framing sequence is shown in **Figure 4.10**. It is comparable to the historical observation in **Figure 4.6**; the sample turns transparent on impact – possibly indicating a melt – followed by initiation of a hot-spot. The hot-spot grows to a full burning reaction, consuming the sample.

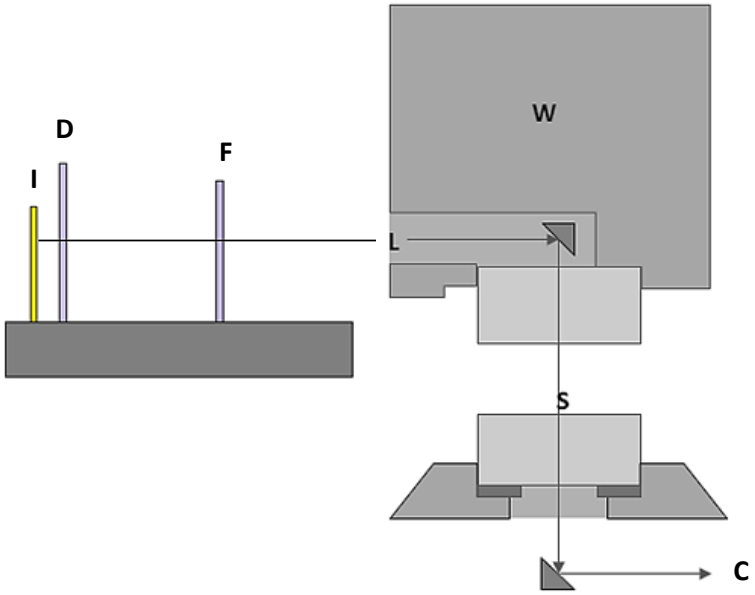

Figure 4.9: The glass anvil arrangement requires backlighting (L) to achieve a photographic image. This is done using a LED lighting panel (I), where the bright light is first softened with a diffusing lens (D) and focused into the drop-weight with a focussing lens (F). The light passes through the periscopic mirror arrangement in the weight (W), through the sample (S) held between the glass anvils, and into the camera lens (C)

The results presented in this section have shown that a high speed camera can be implemented effectively. The images are of a high quality and allow the user to discern hot-spots and reaction growth. The advantage of the modern technology is that the resulting images require no post-processing and are immediately available as an animation. As a result, the overall process is faster and allows more time efficient experimentation.

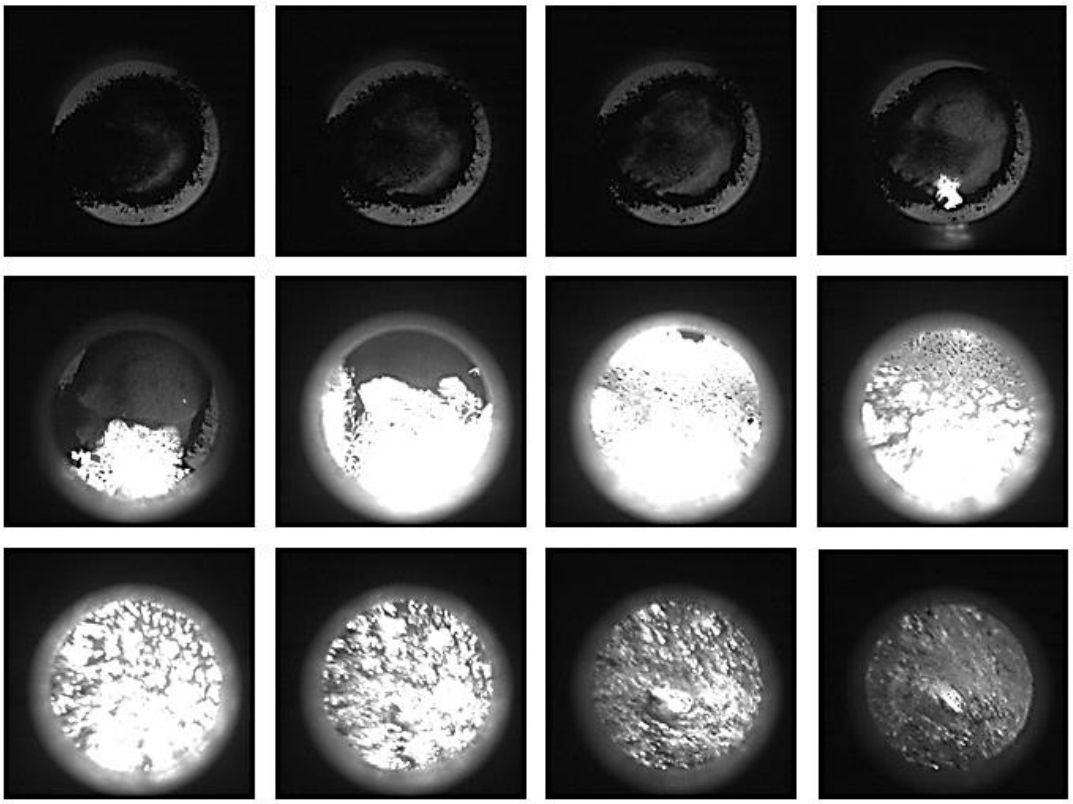

Figure 4.10: high speed photographic sequence of PETN reacting in the drop-weight (frame sequence left to right). The powder is flattened under impact and turns transparent. A hot-spot appears in the fourth frame which continues to grow to full reaction. Frames are 7.69 µs apart

4.4.2 Auditory Diagnostic

As previously noted, many impact test methods assess ignition criteria of an explosive sample based on an audible assessment of the drop experiment. It is not a requirement to use a calibrated microphone with these techniques; the ERL drophammer [112] is the exception. As a result, assessment is often reliant on the judgement of the operator and is not quantitative. The study described here uses a microphone in order to examine the waveform produced and quantify the difference between a “Go” and a “No go” reaction and assess how effective analysing the audible output is.

A Shure SM57 dynamic microphone, chosen for its high frequency response (up to 15 kHz), was used for measuring the sound of the glass anvil drop-weight. It is a dynamic microphone, meaning the internal parts consist of a wire coiled around a magnet with a

diaphragm on the top. When the diaphragm vibrates (as it does when picking up sound waves), it vibrates the coil in turn which generates a current in the magnetic field that is passed along a cable into an audio interface. Dynamic microphones allow for high volumes (sound pressure levels) to be passed through them without damaging the internal equipment, compared with condenser microphones which are more sensitive to higher frequencies, but are made up of more fragile inner components. Given the audible output from the impacting weight is both loud and sharp; a condenser microphone would not be suitable for repeat experiments on the drop-weight.

The microphone was positioned on a floor mounting near the drop-weight frame, 10 cm away from and pointing at the sample. This position was maintained for all of the testing undertaken. The Shure SM57 is a unidirectional cardioid microphone which means the polar pattern (or sensitivity to sound relative to the direction or angle of the source) is rotationally symmetrical about the microphone axis. A cardioid microphone is most sensitive at the front/top and least at the back of the microphone, making it more successful at removing unwanted ambient sound. The removal of ambient sound is beneficial to an experimental set-up in a laboratory where a number of processes or diagnostics might be running at once.

The microphone was connected to a Focusrite Scarlett 2i2 audio interface, which was then connected to a computer to record the subsequent waveform. The experimental layout is shown in **Figure 4.11**.

A series of inert drops were carried out using melamine as a sample, the non-explosive powder used previously for the milling experiments in Chapter 3. This allowed a baseline reading to be made for the sound of the glass anvils containing a powder sample under the drop-weight, minus the noise of any reaction caused by an explosive. The process was repeated twenty times with highly reproducible results; a selection of the data is presented in **Figure 4.12**.

The amplitude of the signal (**Figure 4.12a)**) is representative of a voltage output from the microphone (i.e. a larger amplitude indicates a louder noise). There is a sharp initial peak from the impact lasting approximately 1.5 ms, followed by a longer decaying tail which is likely to be caused by vibrations in the equipment following the impact. A Fourier Transform (FT) analysis was carried out on the signals (**Figure 4.12b)**), which demonstrated there was little difference between the data collected for each drop.

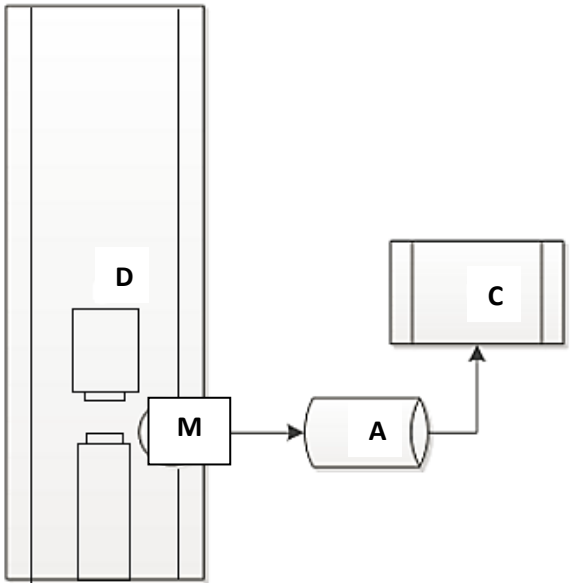

Figure 4.11: Representation of the microphone set-up for the drop-weight. The microphone (M) is attached to the drop-weight (D) frame near to the position of the sample between the anvils. The microphone is connected to an audio interface (A) which links to a computer (C) running a programme able to map the output signal (voltage) from the microphone

The FT shows a broad spread of frequencies, generally dropping off with increasing frequency, and, as the microphone is not recording data above 15 kHz, anything above this region on the FT is not useful for analysis. The frequency spectrum of the background noise (or vibrations from the machine) is spread out evenly over the entire spectrum, with no individual spectral elements identified. Any peak present in a FT represents the most dominant frequency in the signal under analysis, therefore it can be interpreted that there are no strong specific frequencies, making the FT less useful than the unprocessed data to draw any conclusions from. It was anticipated that the results obtained for the melamine would be replicated in a "No go" reaction for an explosive sample.

Following the inert samples, PETN was used to study an explosive response for the microphone. As previously noted, it was chosen as it will reliably initiate and can therefore be used to calibrate all of the new diagnostics. The signal from an explosive sample "Go" event is clearly different to the inert sample; it is shown in **Figure 4.13** and correlates with a "Go" as determined by the high speed camera. The amplitude from the initial impacting peak is significantly larger than for the inert material, and the experiment was repeated a number of times to confirm the signal was reproducible. The decaying signal in the raw data after the initial peak is very similar to that produced by the inert samples.

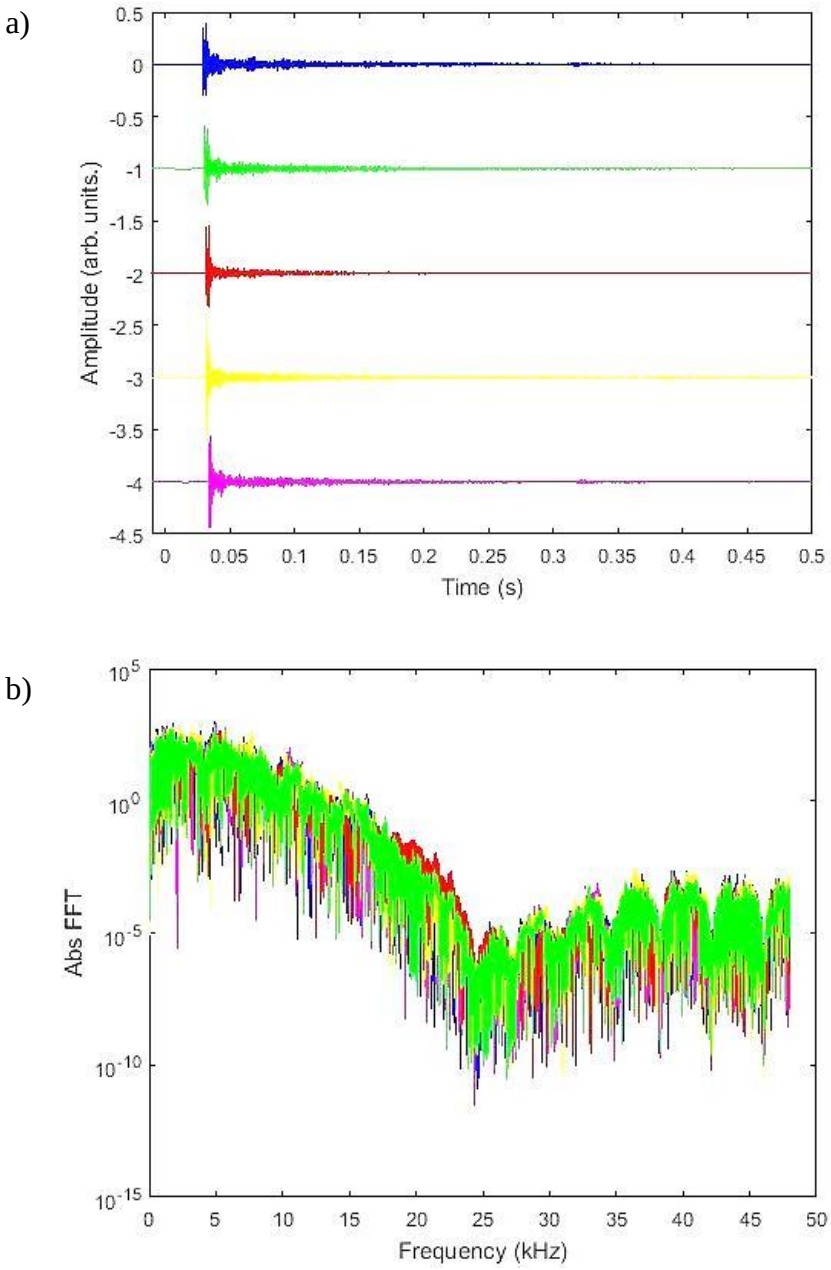

Figure 4.12: Microphone data collected from an inert sample in the drop-weight. The raw signals (a) are highly reproducible; artificial spacing demonstrates the similarities between five different example drops. A sharp peak is indicative of the weight impacting the anvils, then the declining signal represents vibrations within the drop-weight itself rather than any sound from a sample. A FT analysis (b) indicates little difference between the raw signals

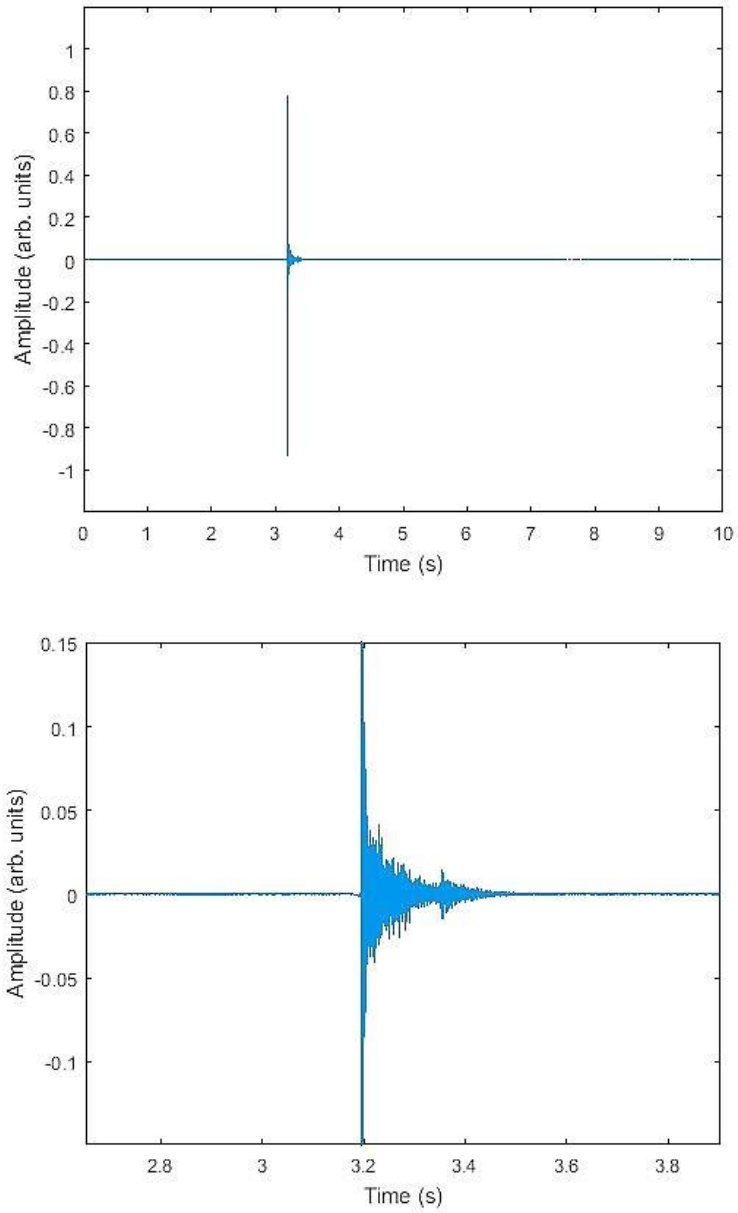

Figure 4.13: Raw data from the microphone for a PETN "Go" reaction. The initial peak amplitude is larger than an inert response (top), and a close-up of the signal (bottom) shows a decaying tail which is caused by vibrations in the equipment

Further experiments were carried out to adjust the gain on the audio interface, ensuring that the signal could not be clipped and misinterpreted. This calibration of the audio interface was noted and set to a consistent level, so that no variation could be introduced to the sound measurement during the investigation of further materials.

The "Go" and "No go" data is compared in **Figure 4.14**. When comparing a close-up of the two raw data signals, the immediately distinguishable feature is the larger amplitude initial peak in the "Go" explosive reaction. The decay in both signals is not

directly representative of any kind of chemical reaction happening in the samples, but of vibrations in the equipment. Fourier Transform analysis was carried out on the data and is also presented in **Figure 4.14**.

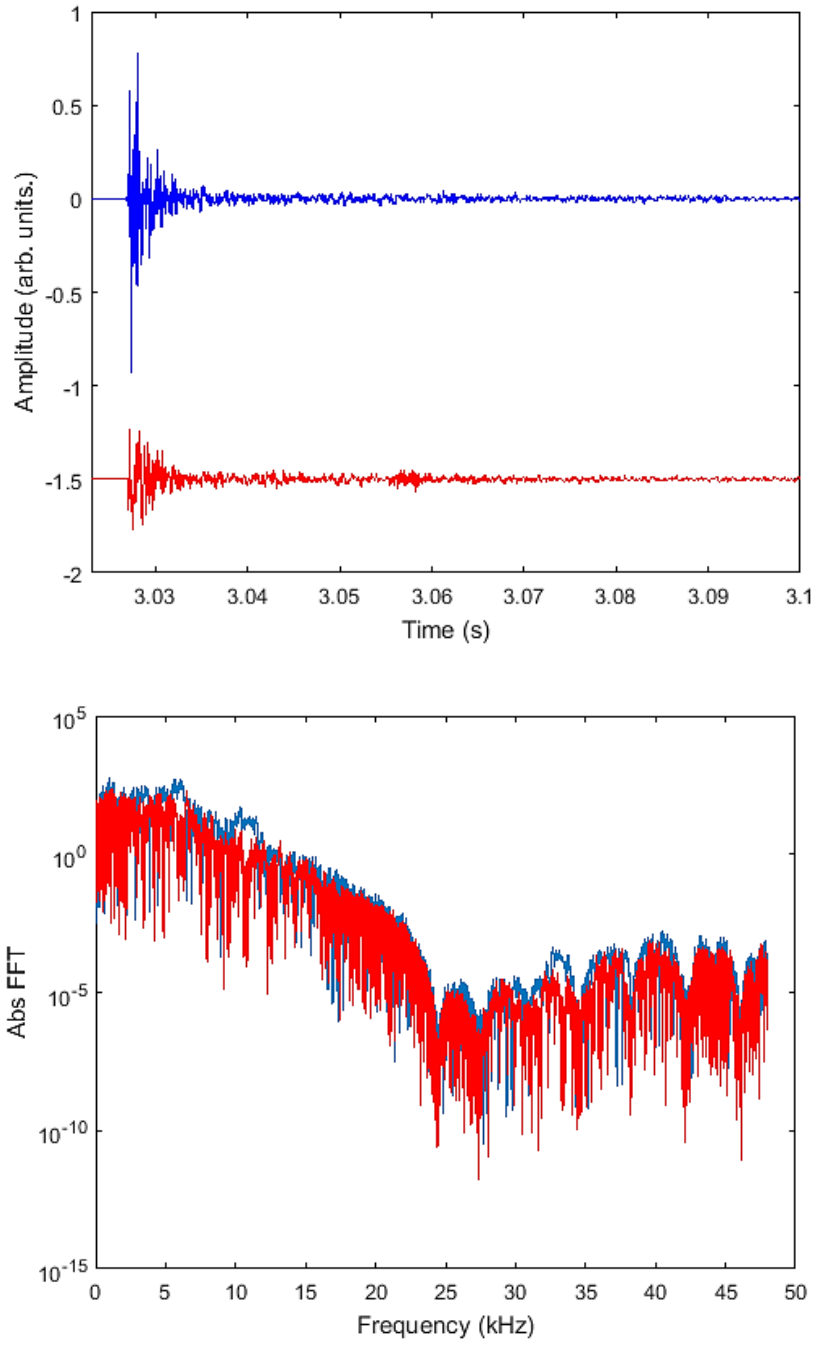

Figure 4.14: (top) A comparison of the raw data signals obtained for a "Go" (blue) and "No go" (red) reaction in the drop-weight. The "Go" has a larger amplitude initial peak. A Fourier Transform of the data does not show an obvious difference between the signals (bottom)

In the **Figure 4.14** Fourier Transform analysis a broad range of frequencies can be observed; this spectrum is more representative of the drop-weight equipment and microphone response than the explosive sample, therefore interpreting the Fourier Transform of the full waveform is not a useful tool to distinguish a “Go” or “No go”. A higher time resolution on the initial spike from the raw data would be beneficial, however it is of limited use to measure the frequency in sound over a period of microseconds as the sound waves are slower than microseconds.

Further interpretation of the data using a histogram of the amplitude responses is presented in **Figure 4.15**. A plot of “Go” events produced from PETN (and also HMX, which is presented later in the chapter) was aligned with “No go” baseline data. The resulting histogram is a simplistic interpretation of the data, with the decaying tail cancelled between the “Go” and “No go” events. The apparent cut-off between a “Go” and “No go” is an amplitude value of 0.4 V; though this output voltage from the microphone is not an absolute value as it is multiplied by a gain from the audio interface (this gain is set to a continuous value for all of the experiments). As such, when the raw data from the microphone is obtained, an initial peak value of 0.4 V or more can be considered a “Go”.

Overall examination of the data shows that the most useful part of the signal is the initial peak. It is the most obvious way to differentiate between a “Go” or “No go”, and in its simplicity does not require further analysis. The lack of analysis required is beneficial in some ways as it allows for a faster experimental turn-around time for an extensive programme of work. It is also very reproducible as ten further drops were carried out on PETN with similar results for the initial peak. Assessment of that data using a histogram has shown that a “Go” can be identified with an initial peak amplitude above 0.4 V.

The method described here for assessing the extent of reaction is not too dissimilar to the technique that the ERL drophammer uses [112]. It also exploits the initial peak, transmitting it to a voltmeter, and a “Go” response is obtained if a value equal to or greater than a previously defined reading on the voltmeter is registered. A "No go" is a response which causes the voltmeter to read less than this value. The "Go" at ERL was defined as 480 mV until the microphone and electronics were upgraded, then it was re-calibrated to a very different number; 1.3 V.

The voltage level which defines a “Go” is clearly very specific to the test and how the equipment is set up. Based on the early results from our drop-weight apparatus, any initial peak signal below 0.4 V can be classified as a “No go”, and anything above

qualifies as a “Go”. This is based on the results from two materials and further understanding will be gained from the examination of more explosive samples later.

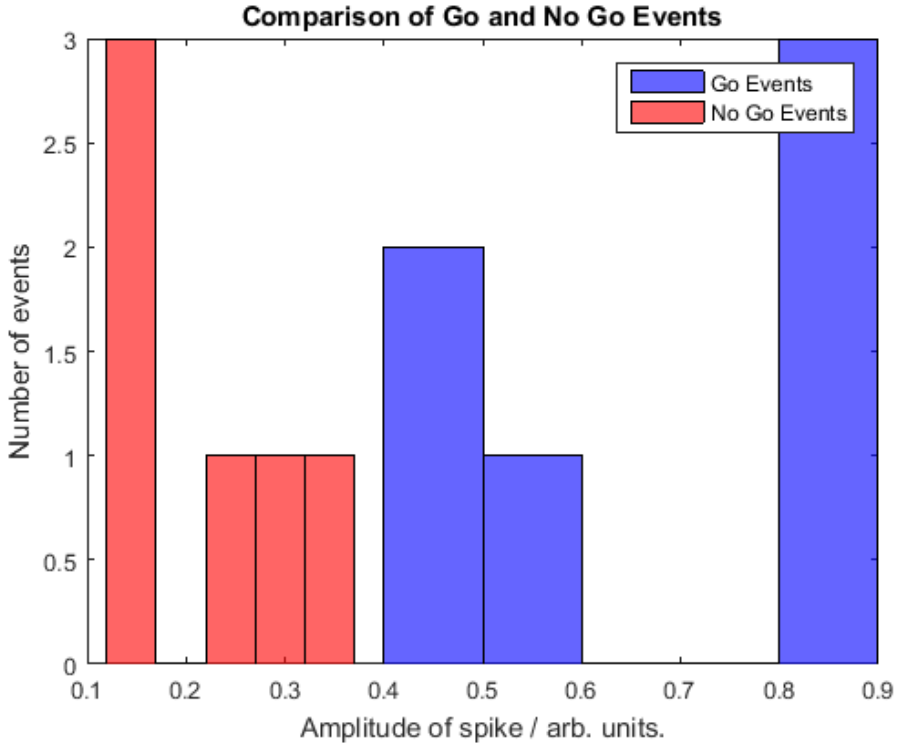

Figure 4.15: Histogram of the raw data points from the microphone on the drop-weight under a selection of “Go” and “No go” reaction circumstances. The “Go” events are denoted by data-points above 0.4, and the initial peak from “No go” events fall in the 0.2 – 0.4 region. It is anticipated that there are also “Go” data-points in the 0.1 - 0.2 range (representing the decaying tail), overlaid by the second dataset

4.4.3 Photodiode Diagnostic

The purpose of using a photodiode alongside the high speed camera is to quantify the integrated intensity of the light produced by hot-spots in reacting material. Whilst the camera provides a qualitative visual aid, a photodiode operates by producing a current when photons are absorbed, and the measured output current from the photodiode is directly proportional to the power of the light source. The data is useful for comparing different materials as it provides some information about the intensity of the reaction light

from the hot-spots. The camera compliments the technique as the photodiode cannot provide an insight into the area covered by the hot-spot; both diagnostics are time resolved.

In order to add this diagnostic to the drop-weight, a beam splitter was attached to the bottom of the periscopic mirror arrangement, allowing transmission of the image to the high speed camera while simultaneously directing the light to a photodiode (as shown in **Figure 4.16**). A Thorlabs DET10A photodiode was used to trial the technique; this is a photoconductive (reverse bias) silicon photodiode, with a bandwidth of 150 MHz and spectral range covering both the visible and infra-red regions. The photodiode was connected to the beam splitter using an optical fibre. An oscilloscope (Tektronix DPO5054B) was used to measure the output signal via a transimpedance amplifier, applied to magnify the signal and convert the low current output from the photodiode to a measureable voltage.

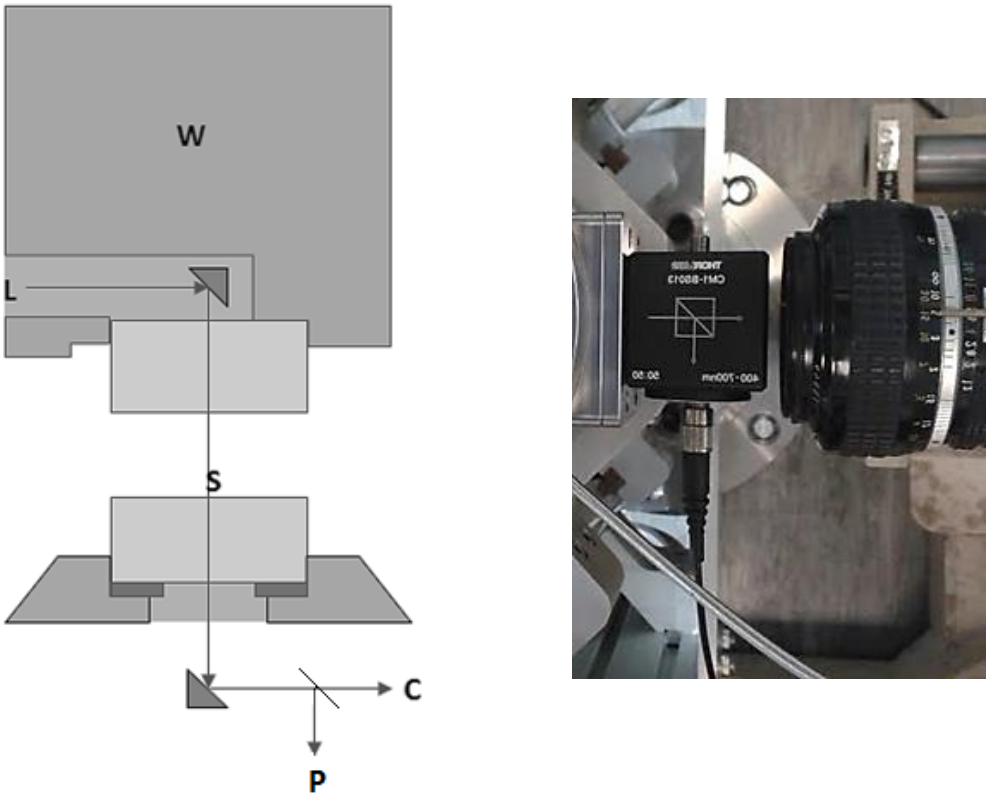

Figure 4.16: (left) The addition of a beam splitter to the base of the drop-weight allows the high speed camera (C) to continue viewing the experiment while directing light to a photodiode (P). A birds-eye view of the arrangement is shown on the right

It was considered whether it would be necessary to build in a series of lenses between the beam splitter and the optical fibre in order to focus the light into a beam onto the end of the fibre. This would enhance the detected signal from the photodiode if it appeared too weak to analyse. The backlighting that allows the camera to capture an image was not strong enough to interfere with the photodiode signal, no response was measured when the drop-weight was lowered and illuminated.

The spatial resolution of the photodiode response is also a key factor in the experimental set-up and output. The angular response of the photodiode, *R*, varies via the relationship

$$R = R_0 \cos \theta$$

and θ is determined using the total length of the light pathway (i.e. from the sample on the glass anvil to the surface of the fibre optic), and the maximum radius of the material sample on the surface of the glass anvil. In this case the maximum value of θ is equal to 1.140° as the light pathway from the reacting material is far greater than the radius of the sample. As per the product specification, R equals 0.44 A/W for the DET10A, meaning an error of 0.02 % can be expected at the furthest edge of the sample from its centre (or maximum θ).

Another consideration for the experimental set-up is whether the optical path is actually capturing all of the light that could potentially appear across the sample, and if any ignition at the edge of the sample is visible to the photodiode. To ensure this, an assessment of θ with the numerical aperture (NA) of the fibre optic is necessary, using the definition

$$\text{NA} = n \sin \theta$$

The NA is a dimensionless number that describes the range of angles of light that can be accepted and transmitted along the fibre optic. The NA of the fibre optic used is 0.5, as defined in its product specification. Substituting for θ, the NA calculated for the experimental set-up is 0.020 (n = 1 in air), which is within the acceptable range for the fibre optic. This means that the photodiode and fibre optic should identify any ignition across the full area of the sample.

PETN was used as a calibration material again for this diagnostic, as it is known to initiate and produce light. During the experiments (also monitored by the high speed camera) it was found that the light produced by the reaction was sufficient to produce a well-defined signal on the oscilloscope and a focussing lens arrangement was not required. Typical signals produced by PETN reacting under impact are shown in **Figure 4.17**, where a maximum peak denotes the brightest stage of the reaction.

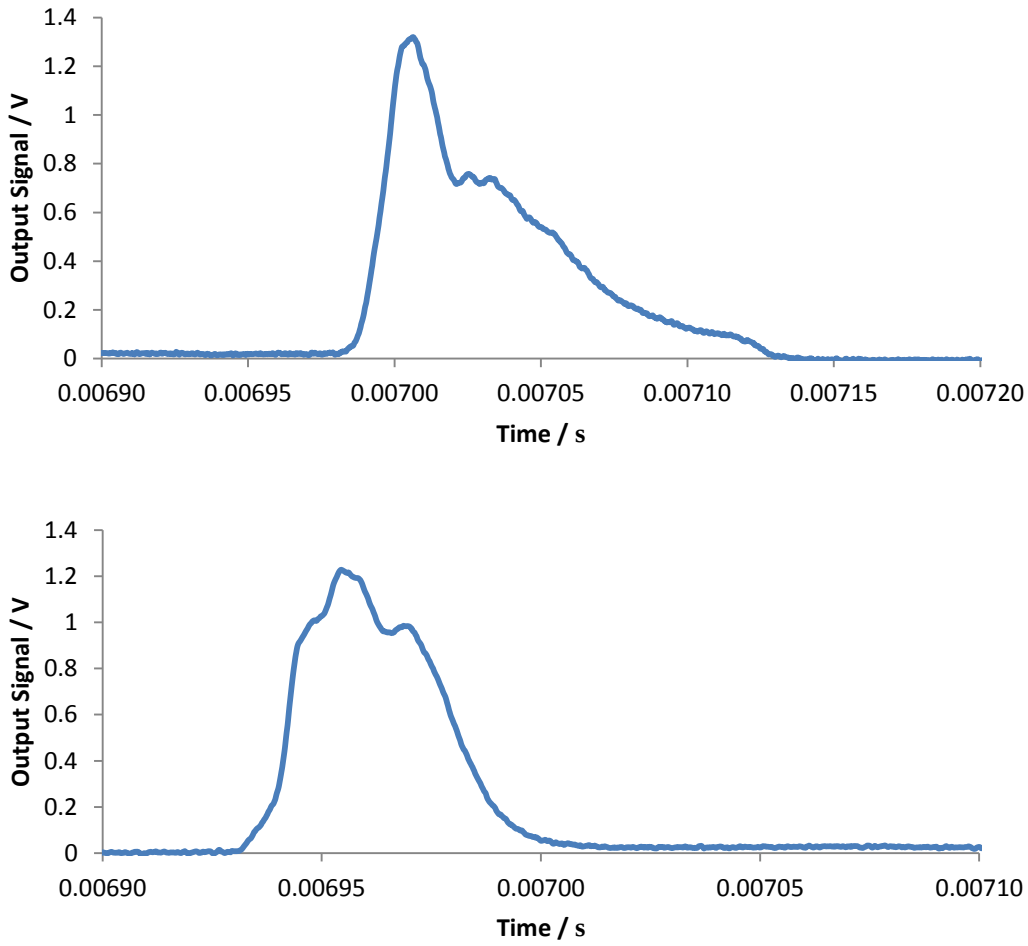

Figure 4.17: Two different examples of output signal measured from the photodiode when PETN is impacted in the drop-weight. Though the highest peak intensity is very similar for both, the shape of the traces varies. In the case of the first experiment (top), more initial hot spots were identified by high speed camera than in the second experiment (bottom). In general the signal increases as hot-spots grow or appear, and it decreases as burning declines

The start time of the measured output current correlates with that of the hot-spot images recorded using the high speed camera, therefore the signal measured is directly attributed to reaction light. **Figure 4.17** shows two examples of how the intensity of the hot-spots grows over time, and the output signal varies as they expand or shrink in area on the surface of the sample. The signal decays as the reaction dies out and the sample is consumed. No signal was observed for inert materials, and later TATB (which does not produce a "Go" under drop-weight conditions) also failed to produce a peak in the photodiode data.

The traces measured by the photodiode compliment observations from the high speed photography. Using **Figure 4.17** as an example, the camera captured six hot-spots initially, corresponding to the top trace, while only two initial hot-spots were present in the bottom trace, which grew and combined to give the same overall maximum intensity value as the first experiment. This result provides more information than originally anticipated, monitoring light intensity throughout the whole reaction with clear time resolution. This gives more detailed insight into the behaviour of reaction growth between samples, on top of the maximum light intensity which may vary between different materials. It was found that the maximum peak value was consistent for PETN, ranging between 1.04 V and 1.28 V.

The photodiode is however less effective than the high speed camera at distinguishing the end of the light producing reaction. The end of reaction is determined by the film going dark for the high speed camera (subjective to human interpretation), and the point at which the photodiode trace becomes flat after the reaction. Referring back to **Figure 4.17,** the total reaction time from first experiment (top) is measured to last 130 µs by the photodiode, and the duration of the second experiment (bottom) is 90 µs. This is compared to the high speed video recording which evaluates reaction length to be 131 µs and 108 µs respectively.

Although the difference between two diagnostics in the first experiment is small (1 µs between the two techniques), the second experiment shows a difference of 18 µs. This is because decaying burning reaction for the second experiment produced a very dim light as it was finishing, which was clearly too low for the photodiode to pick up, but visible to the more sensitive human eye.

The gain of the photodiode could be increased, however this caused clipping of the maximum peak in some instances. It would also be feasible to replace the photodiode with a more sensitive model or use two in parallel; though coupled with the high speed camera,

it was possible to obtain the data required for both reaction time and development of hot-spots for these experiments. The high speed camera is a costly piece of equipment, and if the experiment was set up without it, the use of two photodiodes with a three-way beam splitter could be investigated further.

Overall, the photodiode has demonstrated that it is a very useful diagnostic as it is able to quantify the intensity of light produced by hot-spots in a time resolved manner, following the reaction through ignition and growth via the light produced. It is complimentary to the high speed photography which identifies the number of hot-spots and the area that they occupy (but not how bright they are). The high speed camera is a better tool for monitoring dim light, such as that occurring at the end of the reactions. The quantifiable information provided by the photodiode will be valuable when comparing different explosive materials.

4.4.4 Mass Spectrometry Diagnostic

A mass spectrometer is an exceptionally useful diagnostic tool as it allows for the assessment of gas samples and identification of products. In the drop-weight impact experiments, the products of interest would be those generated by a burning reaction. Using a method to capture and transfer the gas sitting around the explosive sample, the mass spectrometer can be used determine if the gas collected during an experiment contains any reaction products in order to discern the response of a sample under impact. Such an approach is not currently used, but could give better insight into the processes occurring during impact. To make this adaptation to the drop-weight possible a number of amendments to the experimental set-up were required.

First, the sample chamber for the single base glass anvil was modified for two sealed glass anvils designed to contain reaction gas to sit below the impacting anvil (totalling three glass anvils – see **Figure 4.18** and **Figure 4.19**). The new sample chamber holding the anvils was also fitted with two pipes which could be opened or closed via manual needle valves. The mass spectrometer was connected to the outlet, and the other was left open to atmosphere to maintain a constant pressure within the sample chamber whilst a pumping system drew gas through to the mass spectrometer. The modifications ensure that the other diagnostics; the photodiode, high speed camera and microphone; are still suitable for use on the drop-weight. As such, the mass spectrometer is fully integrated and a number of methods measuring the explosive sample response can be deployed at the same time during the experiment.

The mass spectrometer used for the drop-weight experiments was a high resolution quadrupole mass analyser (Hiden Analytical HAL PIC 301) designed for analysing gas and vapour species in vacuum chambers. It was operated via a two stage differential pumping arrangement (with thanks to Sue Guymer for the assembly), which sucked air through a narrow stainless steel pipe connected to the port on the sample chamber of the drop-weight. The valve on the inlet port on the opposite side of the sample chamber was manually adjusted to allow a minimum airflow across the sample to prevent the anvils being pulled together, and also to maintain a suitable pressure in the vacuum system.

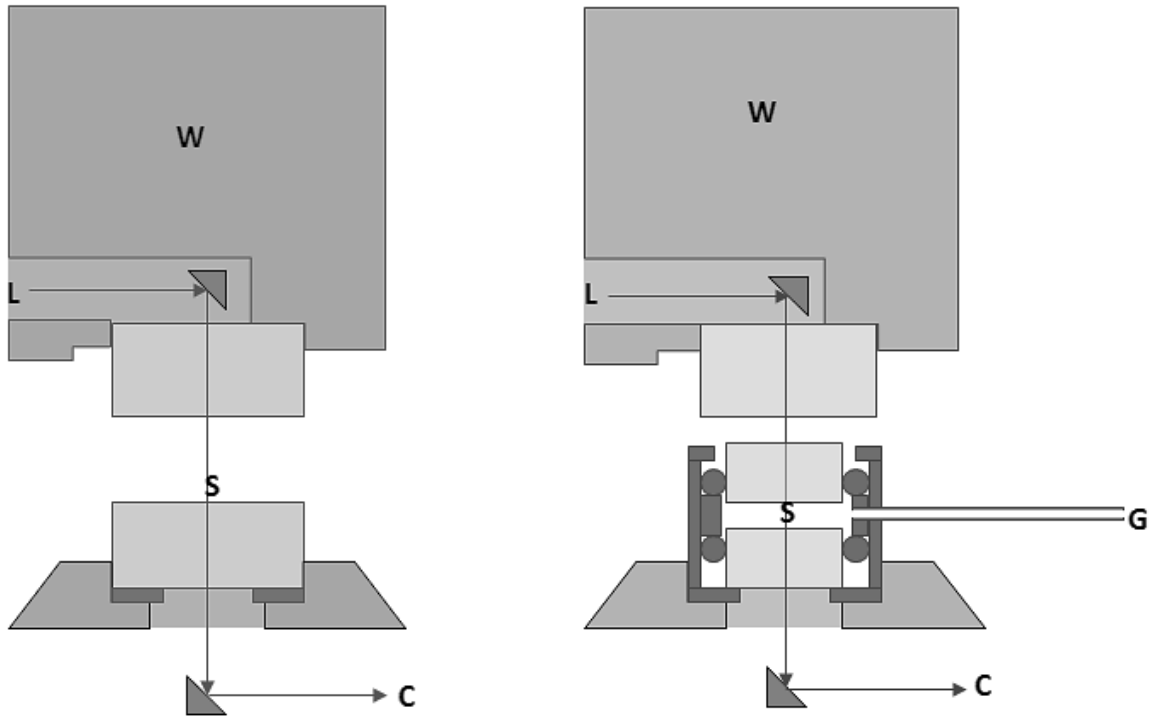

Figure 4.18: Schematic of the original glass anvil arrangement (left) and modified unit to incorporate the mass spectrometer diagnostic (right). The new format holds the sample (S) between two smaller sealed glass anvils with an outlet for a gas-capturing pipe (G) connected to the mass spectrometer. The periscopic mirror arrangement directing light (L) through the weight (W) to the camera (C) remains unchanged

Figure 4.19: The new sample chamber for the drop-weight which sandwiches the powder sample between a sealed unit containing two glass anvils. The outlet pipe which connects to the mass spectrometer is positioned on the right

A standard background measurement was taken with an empty sample chamber to calibrate the electron emission current required to produce an adequate signal with respect to the needle valve inlet on the sampling ports (**Figure 4.20**). The background spectrum shows peaks around expected amu (atomic mass unit) values for atmospheric gases and their fragments. Hydrogen (2 amu and 1 amu), water (18 amu and 17 amu) and di-nitrogen (28 amu) feature strongly. Additionally, there are a number of peaks between 40 amu and 45 amu that are attributed to hydrocarbon oil traces from the vacuum system. Carbon dioxide (44 amu) is a relatively minor peak when compared with the other atmospheric gases, which is beneficial as it is a major product from a burning reaction and would be useful to track as a reaction product during impact testing.

Having optimised the airflow and signal counts (electron emission at 30 μA) for the mass spectrometer, a time resolved mode (MID mode) was chosen to track the species existing throughout the whole time period of the drop-weight experiment. The MID mode tracks the presence of particular mass values which are specified by the user. In this instance the particles of interest are reaction products from the explosive sample burning, which include nitrogen, carbon monoxide, hydrogen, water, carbon dioxide, ammonia, NO, NO_2, N_2O and hydrocarbon fragments such as CH_3OH.

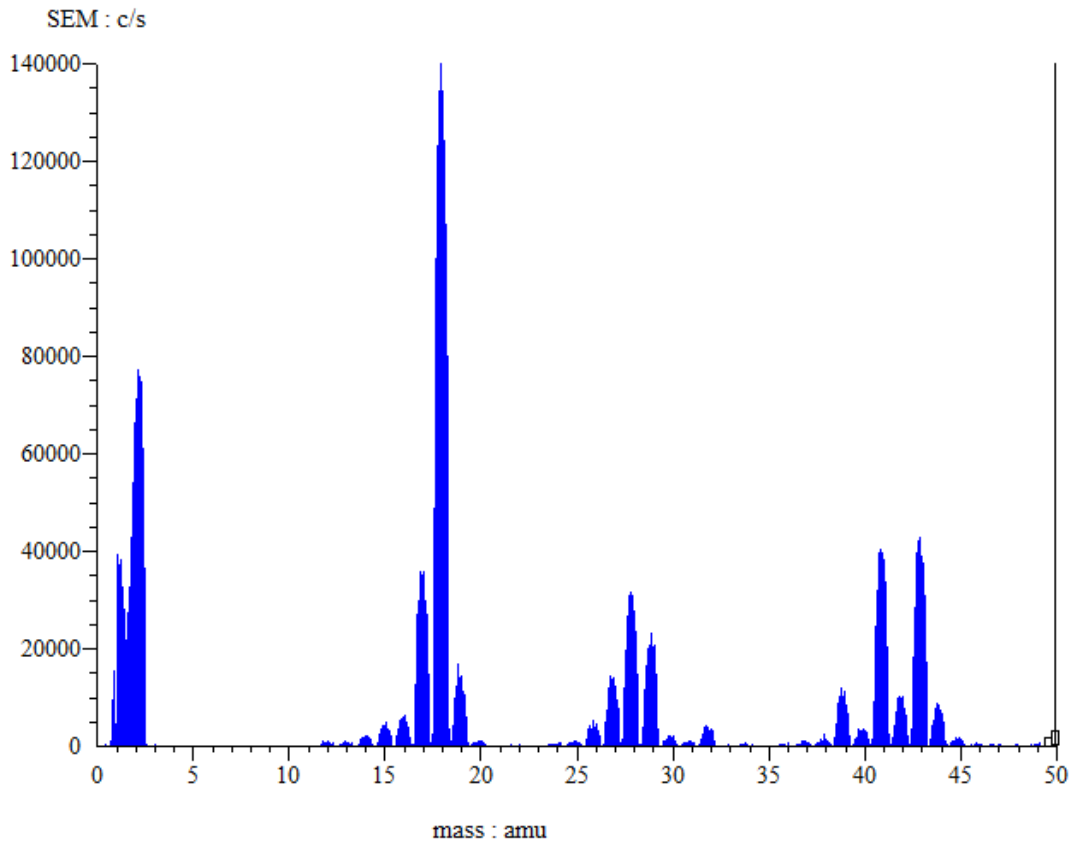

Figure 4.20: Mass spectrum of the background airflow through the empty sample chamber. Atmospheric gases such as hydrogen (2 amu and 1 amu), water (18 amu and 17 amu) and di-nitrogen (28 amu) feature strongly. A group of peaks between 40 amu and 45 amu represent hydrocarbon traces from pump oil in the vacuum system. Carbon dioxide features at 44 amu

The merits and complications of monitoring each of these products is summarised in **Table 4A**, but the majority of these species are not suitable to trace owing to their (or one of their mass analogues) presence in abundance in the atmosphere. From all of the products, carbon dioxide, NO and NO_2 were down-selected for investigation.

PETN was used to calibrate the technique, consistent with the previous diagnostics. Some of the particles monitored have more than one possible species associated with their mass, for example CO_2 and N_2O are both identified by 44 amu. To remedy this, a model of expected reaction products for the burning of PETN was generated using a thermochemical code (Cheetah, as developed by LLNL in the US). It suggested that the quantity of CO_2 produced is 155 times greater than the relative N_2O produced during burning. As such the amount of N_2O potentially present in the 44 amu peak can be

considered negligible in comparison. However NO_2 (46 amu) is only 4 times more abundant than CH_2O_2 as a reaction product; this means that a fifth of a 46 amu signal peak should be attributed to CH_2O_2.

Product	**Mass / amu**	**Mass Spectrometer Application**
H_2	2	Present in abundance as easily lost by molecules (reaction product or not), therefore unsuitable
NH_3	17	Signal swamped by secondary water peak, therefore unsuitable
H_2O	18	Present in abundance in atmosphere, therefore unsuitable
CO/N_2	28	N_2 is present in abundance in the atmosphere, therefore unsuitable
NO	30	Can be used to detect reaction
CH_3OH	32	O_2 (32 amu) is present in abundance in the atmosphere, therefore unsuitable
CHNO	43	Inaccurate due to hydrocarbon contamination from vacuum system
CO_2/N_2O	44	Can be used to detect reaction
NO_2/CH_2O_2	46	Can be used to detect reaction

Table 4A: Reaction products expected from a "Go" under impact in the glass anvil drop-weight. NO, CO_2 and NO_2 are the most suitable species to monitor for reaction within a sample as they will not be swamped by signals from atmospheric gases

The final consideration for the mass spectrometer diagnostic was how to measure that the airflow through the system was consistent and that there were no blockages present in any of the sample tubes during the experiment. This was achieved by monitoring the presence of argon (40 amu) which is present in the atmosphere in low quantities therefore would not interfere with other signals, but should remain constant while the gas sampling takes place. The argon signal also calibrates the overall measurement.

The PETN was subjected to impact in the new sample configuration (see **Figure 4.18** and **Figure 4.19**) and monitored using the mass spectrometer. The results from the configured trial are presented in **Figure 4.21**. It can be seen from the argon trace that this method is a suitable way to monitor overall airflow through the system. The argon trace increases when the needle valve is opened to sample gas from the glass anvil chamber, and its value is consistent until the valve is shut and the trace decreases again. The peaks in the traces in **Figure 4.21** correlate with the PETN reacting as it is impacted; it can be seen that strong readings for CO_2 and NO were observed, however the quantities of NO_2 were still

too low to detect, and the emission could not be increased further otherwise the other peaks become too high.

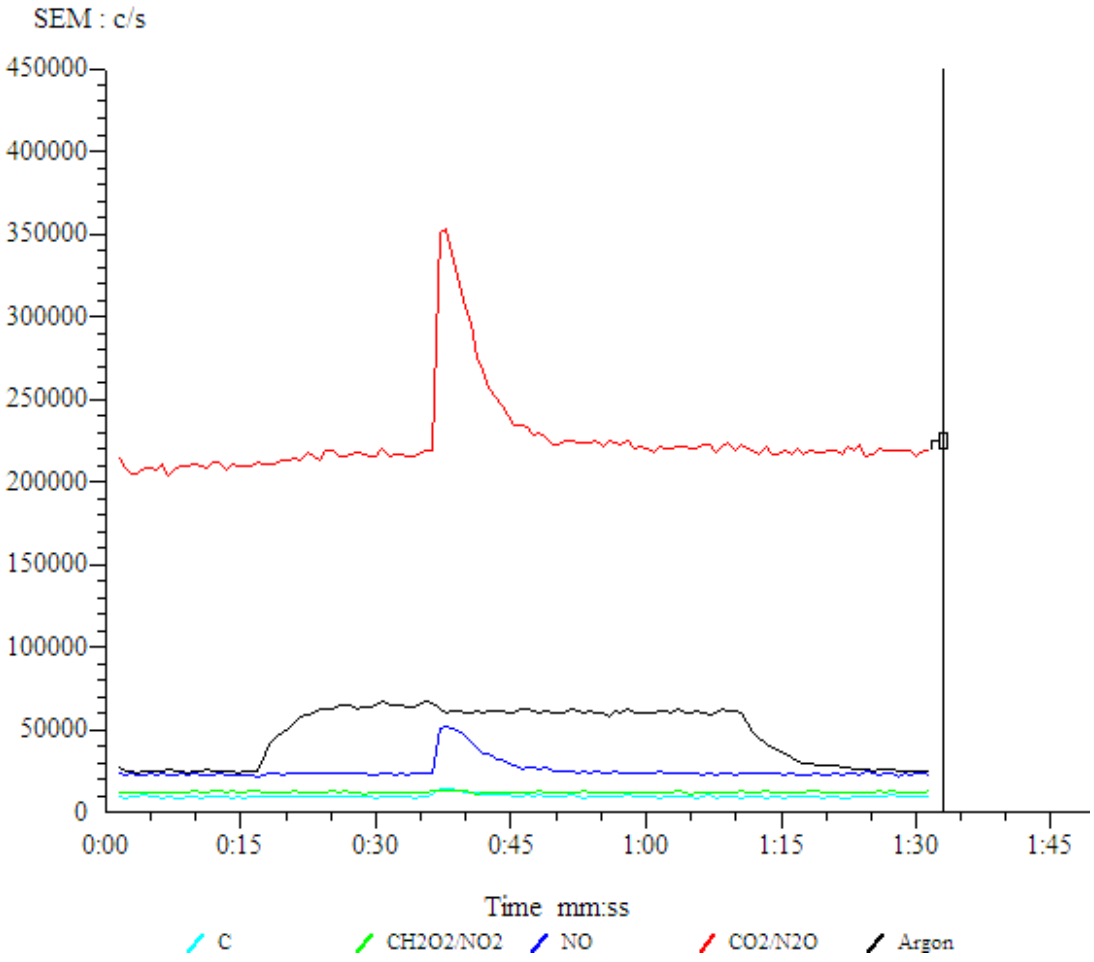

Figure 4.21: The trace produced by the mass spectrometer for PETN reacting in the drop-weight, taken using time resolved MID mode. The point of reaction is noted by the peaks in CO_2 and NO. Monitoring the argon trace is an effective method to assess airflow throughout the system as it can be seen to rise and fall in conjunction with the needle valves opening and closing. No other product gases can be observed to be present from the traces.

The quadrupole mass spectrometer could successfully detect CO_2 and NO reaction gases, however was not sensitive enough to detect NO_2. Burning produces CO_2, water and nitrogen; as previously noted water and nitrogen are not appropriate to monitor owing to their presence in abundance in the atmosphere. PETN contains four nitrate ester groups ($RO\text{-}NO_2$) which thermally decompose to produce NO and NO_2, both of which are

reactive radicals which will undergo secondary reactions. When exposed to oxygen, the NO will convert to NO_2, however NO_2 readily dimerises and exists in equilibrium with dinitrogen tetroxide (N_2O_4). At low temperatures and pressures (i.e. in a vacuum) the equilibrium is favoured towards the N_2O_4. However it is not possible to detect this species in the experiment as the mass of N_2O_4 is 92 amu, which is beyond the capability of the current mass spectrometer to measure.

Referring back to the thermochemical code, the expected ratio of NO_2 produced is significantly lower than that of NO. This combined with its tendency to dimerise makes it very difficult to detect. It is also possible that the mass of the NO_2 species (46 amu) is not subject to great sensitivity in changes on the actual mass spectrometer owing to the presence of hydrocarbon fragments from vacuum oil in this mass region, potentially masking any changes in concentration. As such, the species taken forward for monitoring were CO_2 and NO, which were successfully reproducible for assessment in a number of PETN experiments. It was found that although actual count values from the mass spectrometer could vary between experiments (though the values can be calibrated using the argon signal), the height ratio of the NO to CO_2 peak was reasonably consistent, where NO : CO_2 was equal to 1 : X and X varied between 5.71 and 6.00.

In an attempt to reduce the variability of X, it was decided that the experiment should be trialled in an inert gas environment, and the absence of oxygen could reduce the conversion of NO to NO_2, potentially giving more accurate measurements. The outlet port on the sample chamber which had previously been open to atmosphere was connected to an argon supply and the system was flushed before the drop-weight experiment. The drop-weight failed to initiate PETN in this configuration. No peaks were observable in any of the reaction product traces and the lack of initiation was confirmed with high speed photography.

Exothermic chemical reactions in explosives involve a limited set of reaction steps, all of which involve oxidation. As most of the energy release comes from the oxidation reactions, the amount of oxygen available around the material is a critical factor in how an explosive responds. If there is insufficient oxygen to react with the available carbon and hydrogen in an explosive molecule, the explosive is considered to be oxygen deficient; or is termed to have a negative oxygen balance. Clearly, in the case of PETN in the drop-weight, the presence of oxygen is required to promote the reaction, and the inert gas attachment was removed, resuming the process open to atmosphere.

The results presented in this section have demonstrated how a mass spectrometer can be used to analyse gas contained after a drop-weight experiment and prove the presence of species attributed to reaction from an explosive sample. Two gases, CO_2 and NO, have been identified for monitoring the reaction, and their visibility is reproducible with a reasonably consistent product ratio for PETN. This diagnostic unequivocally determines between a chemical reaction "Go", and co-ordinating it with the other diagnostic techniques is discussed in the next section.

4.4.5 The Triggering System and Experimental Set-up

A number of diagnostics have been applied and calibrated to experiments on the glass anvil drop-weight. Using a number of techniques together provides greater insight into the reactions taking place during the process, and may be able to differentiate between discrete material properties; the physical aspects as well as chemical nature. Additionally, the comparison of the concurrent techniques evaluates how useful each method is under the same experimental conditions.

It was noted earlier in the Chapter that some modifications were required to the original equipment in order to install the new diagnostics. These are mainly focused on the sample holder region of the drop weight; refer back to **Figure 4.16** and **Figure 4.18**. These combined adjustments resulted in a beam splitter being mounted at the end of the periscopic mirror arrangement, allowing for the camera view and photodiode fixture via an optical fibre. The double glass anvil sample holder is fitted with a stainless steel pipe to feed reaction gases to the mass spectrometer.

The high speed camera and photodiode benefit from being time resolved, and therefore need to be triggered simultaneously. This is less important for the microphone and mass spectrometer, for which the data has obvious large peaks at the moment of impact and reaction. The schematic of the triggering arrangement is represented in **Figure 4.21**. A light gate mounted on the frame of the drop-weight is activated when a marker fitted to the weight cuts the laser beams on the way to impacting the sample. This light gate is connected to a signal box which simultaneously activates the recording function on the high speed camera and the oscilloscope measurement of output voltage from the photodiode.

The PETN experiments that were used to calibrate the individual diagnostic techniques were successfully replicated on the combined system. Each diagnostic reproduced the same result when operated separately as for the simultaneous triggering,

demonstrating the robustness of the process. The method for triggering was repeatable and captured all the data required for each piece of equipment.

To summarise, new diagnostics were added to the glass anvil drop-weight to run simultaneously in order to assess the reaction taking place in an explosive sample under impact. The visual aspect of analysis has been improved by the addition of a photodiode which quantifies the light output from reaction, as well as capturing the event on high speed camera. The microphone is a technique used by accredited impact sensitiveness tests and is therefore a useful comparison method, and the mass spectrometer has shown that it can successfully identify reaction product gases. The next section will address how suitable this system is when applied to other explosive materials.

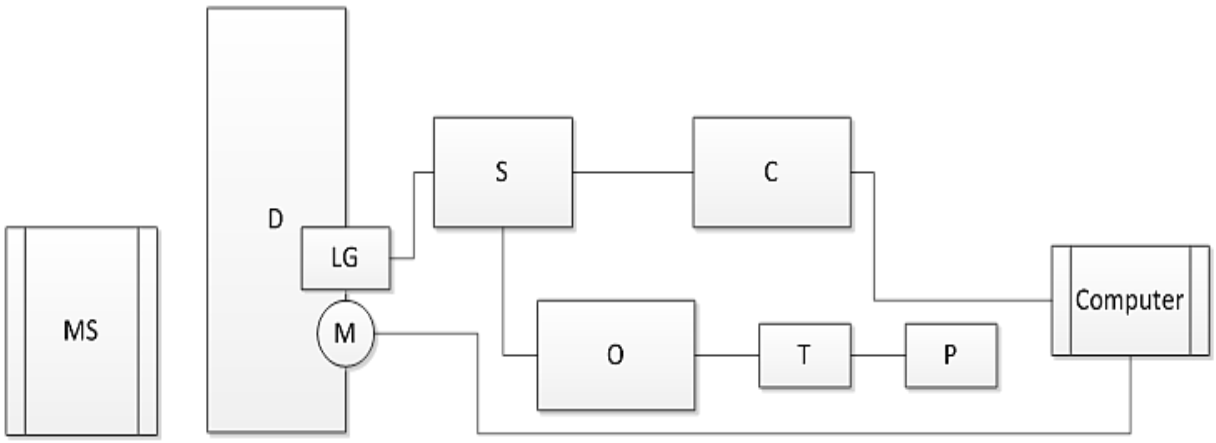

Figure 4.21: Schematic of the triggering system for the multiple diagnostics on the drop-weight (D). The falling weight cuts a through a light gate (LG) which activates a signal box (S) to initiate recording on the camera (C) and measurement for the oscilloscope (O) which is connected to the photodiode (P) via a transimpedance amplifier (T). The photodiode is connected to the beamsplitter on the anvil with an optical fibre (not displayed here). The microphone (M) and mass spectrometer (MS) are triggered prior to the experiment and collect data for a longer time period

4.5 The Impact Sensitiveness of Explosives on the Drop-Weight

The glass anvil drop-weight has been improved with diagnostics which have been calibrated to detect a "Go" in an explosive material under impact. These diagnostics are able to follow the development of a reaction in more detail, giving more information about how a material behaves. In particular, calibration has been made against PETN, which is known to initiate repeatably giving clear indication of a "Go" through light, sound and gas production. Before using this set-up to study new and novel materials it is pertinent to investigate the robustness of the method using other established explosive materials.

In this case HMX and TATB were chosen, owing to their availability in different particle sizes and an understanding of their hazard properties. HMX is expected to be less sensitive to impact than PETN, but will still produce a "Go" when impacted in the drop-weight. TATB is a very low sensitiveness explosive so would not be expected to produce any reaction in the drop-weight, and the diagnostics should reflect this. These two explosives will also be useful as a baseline comparison to LLM-105 materials later, as the LLM-105 is often compared to HMX and TATB with regard to its performance and safety properties.

The classes of HMX used were HMX type A (405 μm) and HMX type C (4 μm) as discussed in Chapter 3. The TATB varieties used were TATB type B (20 μm) and TATB type C (5 μm). All of the explosives selected were tested under the same conditions as the PETN, using a drop-height of 220 cm. Any error that could be introduced by sampling was avoided by the use of a 40 mm^3 cupped scoop, where a sample was taken from the bulk of the material and the volume of sample obtained was kept constant. This is consistent with the method for sampling explosives in the accredited impact tests. The explosives were also dried in an oven for 24 hours prior to testing.

Typical results from the HMX type A (larger particle size) are presented in **Figure 4.22** – **Figure 4.25**. The HMX type A visibly produces a "Go" in the experiment, demonstrating clear reaction initiation and growth in the high speed photography, a peak above the 0.4 V threshold for the microphone, an intensity of light captured by the photodiode, and gaseous reaction products measured by the mass spectrometer. This result not only shows the behaviour of HMX type A under impact, but proves the effectiveness of the drop-weight's new diagnostics applied to another material.

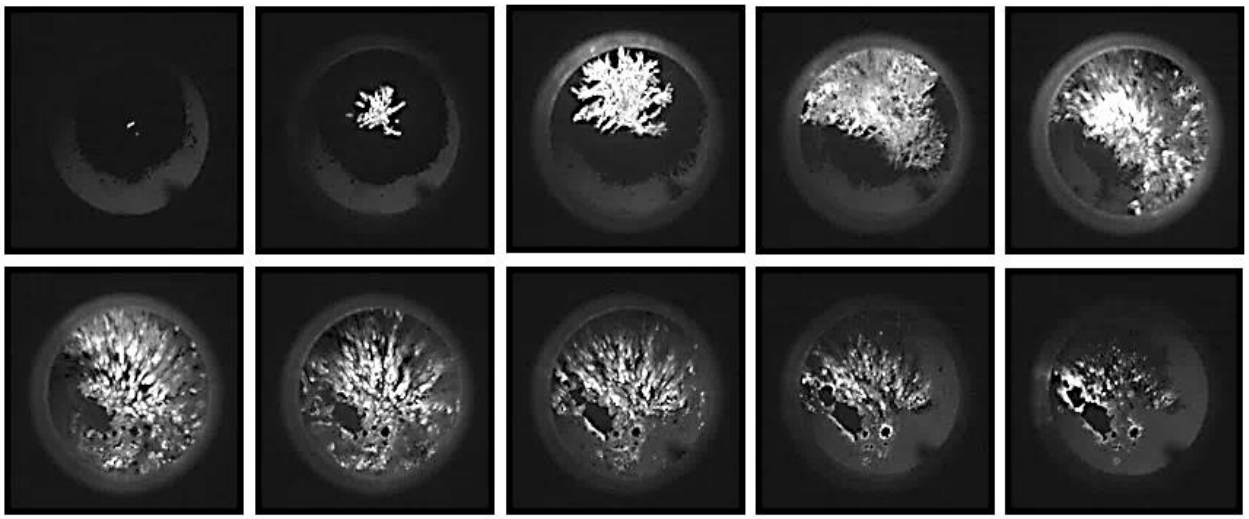

Figure 4.22: High speed photography of the reaction of HMX type A in the glass anvil drop-weight (sequence runs left to right from the top left, frames 7.69 µs apart, diameter of lit circle 15 mm). There are several initial hot-spots and the reaction grows over a series of frames before dying out and leaving some residue, identified by the dark patches in the frames along the bottom row

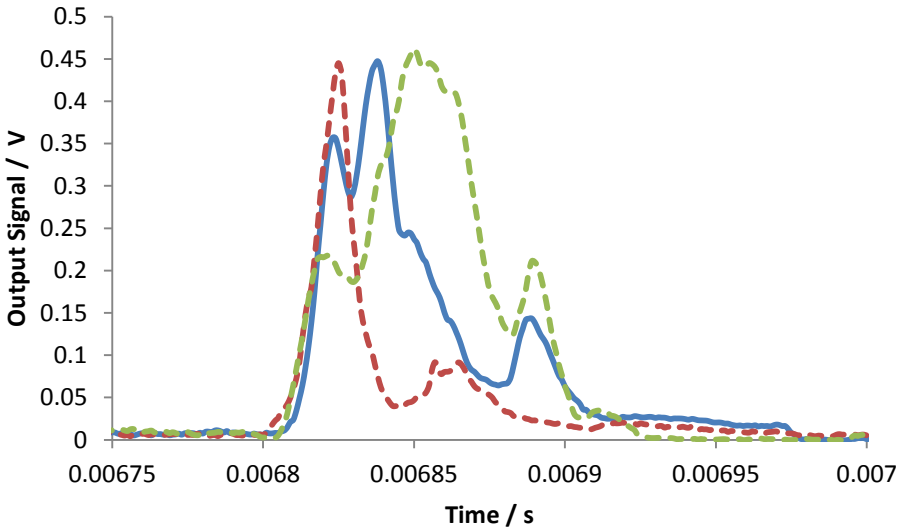

Figure 4.23: The output signal from the photodiode for a number of HMX type A experiments, indicating light intensity of the burning reaction. The blue solid line is representative of the corresponding camera footage shown in **Figure 4.22**. The brightest peak is at 0.45 V, corresponding with frame 5 from the high speed photography sequence in **Figure 4.22**. The third peak alludes to a slight increase in burn as the reaction is dying. A similar growth/shrinkage mechanism can be seen in all of the experiments

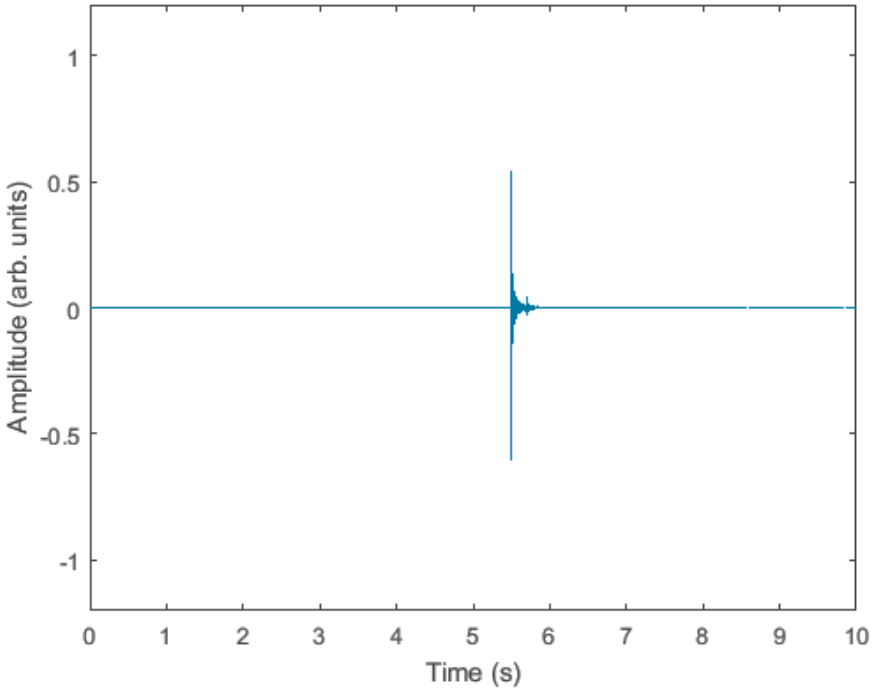

Figure 4.24: The output peak from the microphone when HMX type A is impacted. This is above the threshold value of 0.4 V where the "Go"/ "No go" boundary is, indicating "Go"

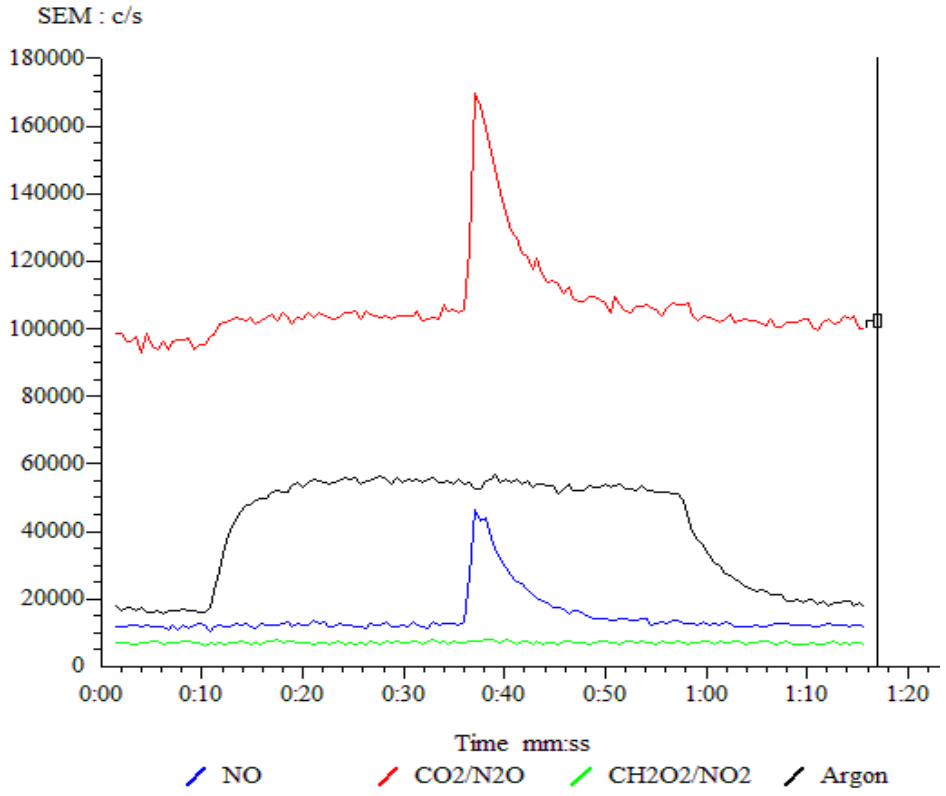

Figure 4.25: The gases measured by the mass spectrometer for HMX type A when impacted. There is a peak in measurement of CO_2 and NO upon impact, indicating a "Go"

Reactions from HMX type C are shown in **Figure 4.26** – **Figure 4.29**. Its particle size is one hundred times smaller than HMX type C, therefore it is of interest to assess whether the new diagnostics are sensitive enough to distinguish between the grades of material beyond their chemical differences. The results from the diagnostics also exhibit the features of a "Go" reaction. The results from the high speed photography show that the initial hot-spots form in clusters of smaller size individual hot-spots (**Figure 4.26**) when compared with the HMX type A (**Figure 4.22**) and PETN (**Figure 4.10**). This makes the initial hot-spots difficult to quantify numerically for the HMX type C. Both the high speed photography (**Figure 4.26**) and photodiode data (**Figure 4.27**) indicate that the intensity of light from the burning reaction is brighter in HMX type C than HMX type A, with typical photodiode peak output voltages of 1.9 V and 0.4 V respectively.

Differences in how HMX type A and HMX type C react under impact can be seen in the high speed photography and photodiode output. For HMX type C the length of reaction is longer (**Figure 4.22** and **Figure 4.26**) and brighter (**Figure 4.23** and **Figure 4.27**) than type A, though the initial hot-spots are dimmer and form in clusters. The readings taken from the microphone and mass spectrometer are however broadly similar for both the HMX types when compared with PETN.

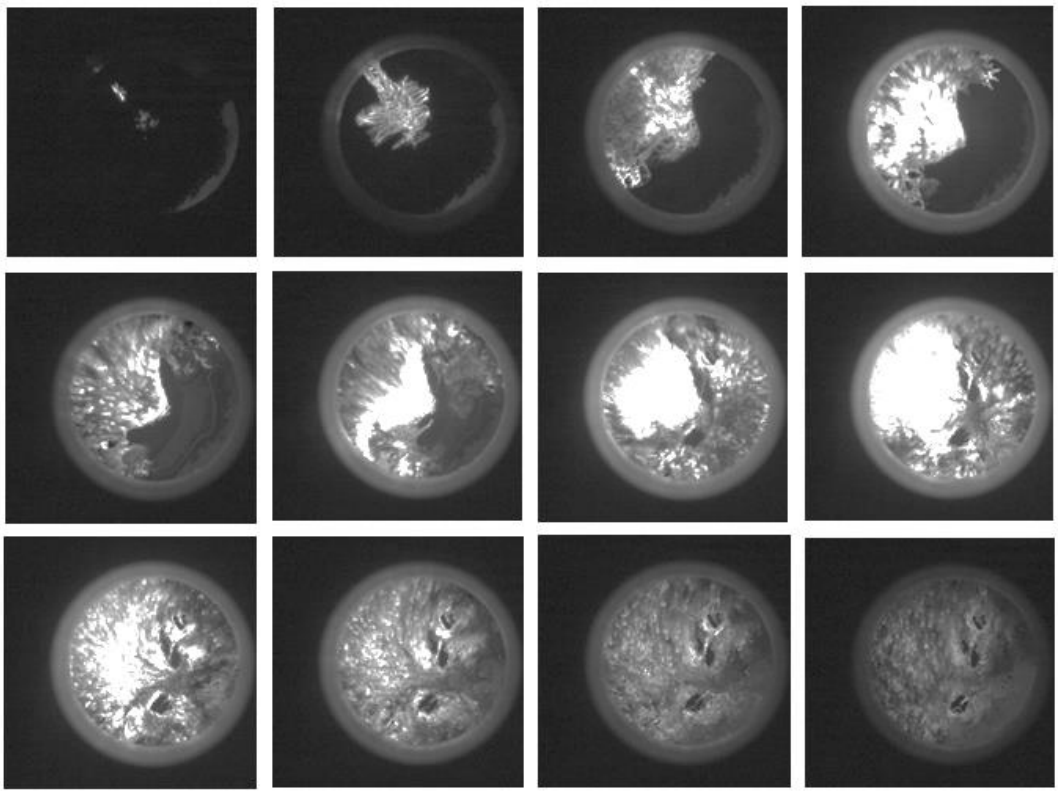

Figure 4.26: Reaction of HMX type C in the glass anvil drop-weight (sequence runs left to right from the top left, frames 7.69 μs apart, diameter of lit circle 15 mm). The initial hot-spots are not distinguishable as individuals, but instead form small clusters, which join together and spread. The burning reaction is longer than that observed in HMX type A and also brighter, though there is also residue left at the end of the reaction (denoted by the dark patches seen in the bottom row of frames)

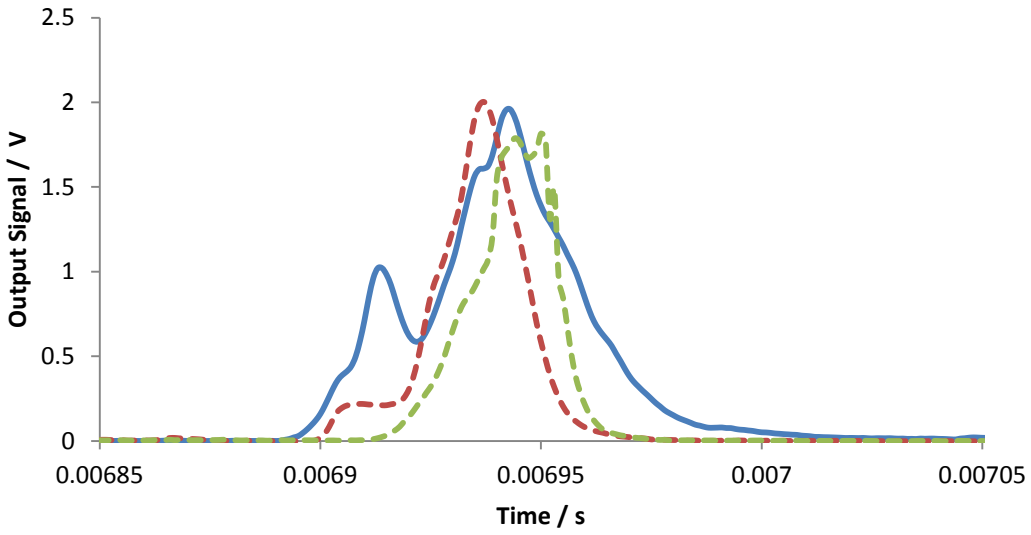

Figure 4.27: A number of output signals from the photodiode for HMX type C under impact. The blue solid line corresponds with the film presented in **Figure 4.26**. The burning reaction typically appears to shrink after several microseconds and then grow again. The maximum peaks range from 1.87 V to 1.98 V; brighter than HMX type A in **Figure 4.23**

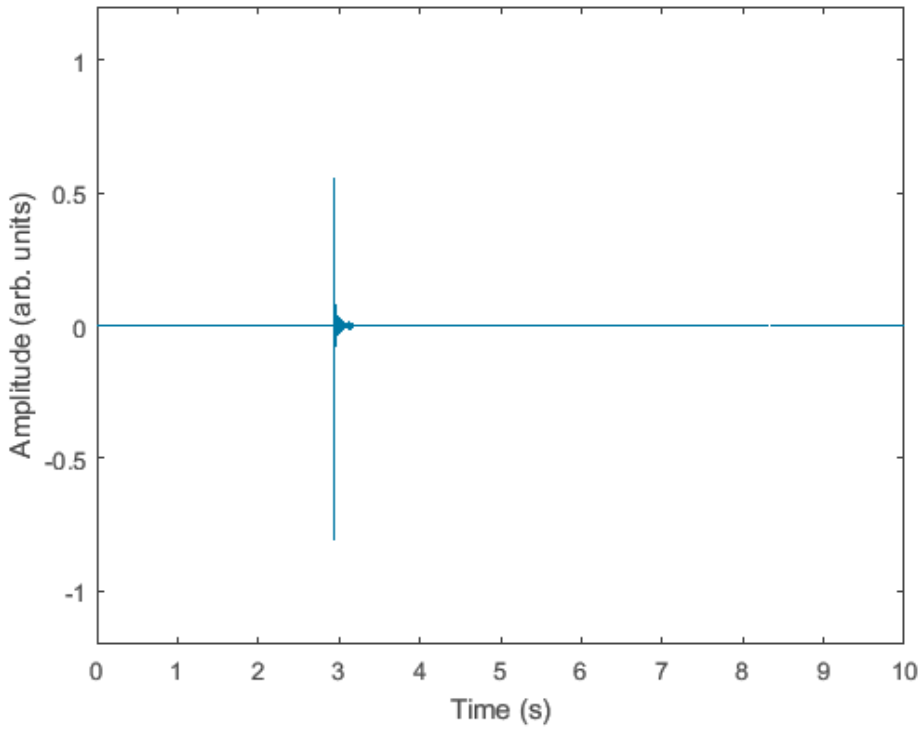

Figure 4.28: The output peak from the microphone when HMX type C is impacted. This is above the threshold value of 0.4 V where the "Go"/ "No go" boundary sits, indicating a "Go"

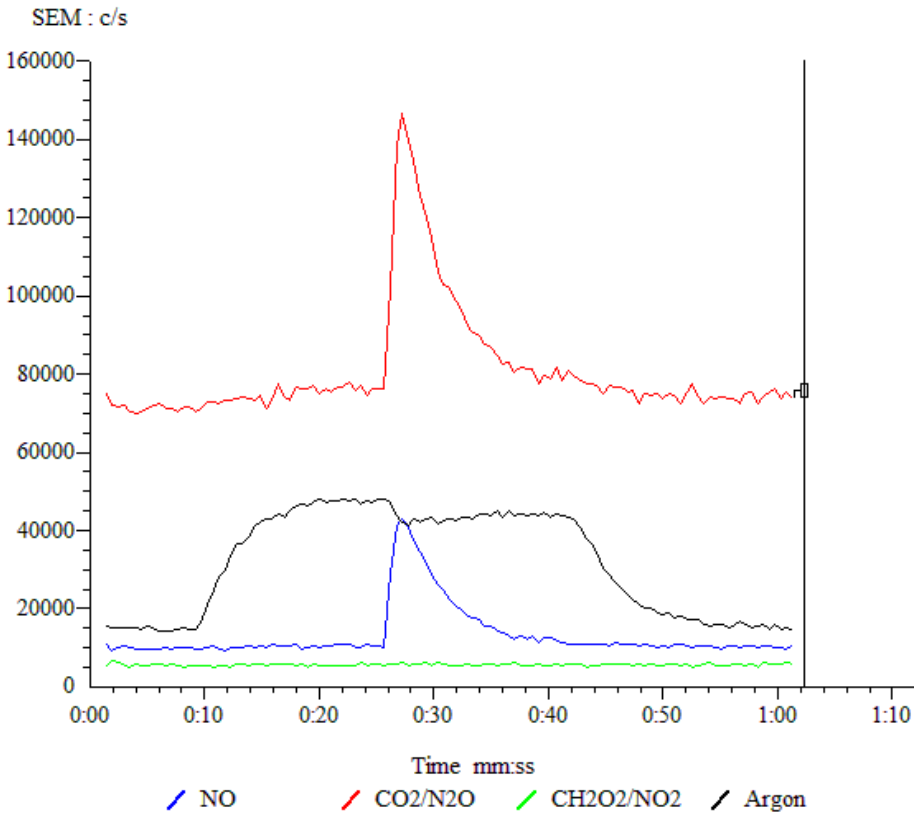

Figure 4.29: The gases measured by the mass spectrometer for HMX type C when impacted. There is a peak in measurement of CO_2 and NO upon impact, indicating a "Go"

Results for TATB type C are shown in **Figure 4.30** – **Figure 4.33**. TATB is an explosive of low sensitiveness and low explosiveness, with a very high FoI from the Rotter test – typically above 100. The results from the diagnostics when the TATB was impacted are all consistent with "No go" criteria; there are no visible hot-spots identified by the high speed camera (**Figure 4.30**), and this correlates with a non-signal measured by the photodiode (**Figure 4.31**).

There is a very slight increase in light measured by the photodiode (**Figure 4.31**) likely to be caused by the background lighting from the experimental arrangement, or noise in the output signal. The backlighting from the experiment would only be visible to the photodiode when the two glass anvils come into contact owing to the periscopic arrangement of the mirrors through the drop-weight and the base of the equipment (refer back to **Figure 4.9**). It is also possible that TATB exhibits triboluminescence when impacted; where a material generates light when it is crushed or subjected to friction

owing to chemical bonds breaking. However there is no direct evidence to support this in the literature, and no light is visible in the high speed video.

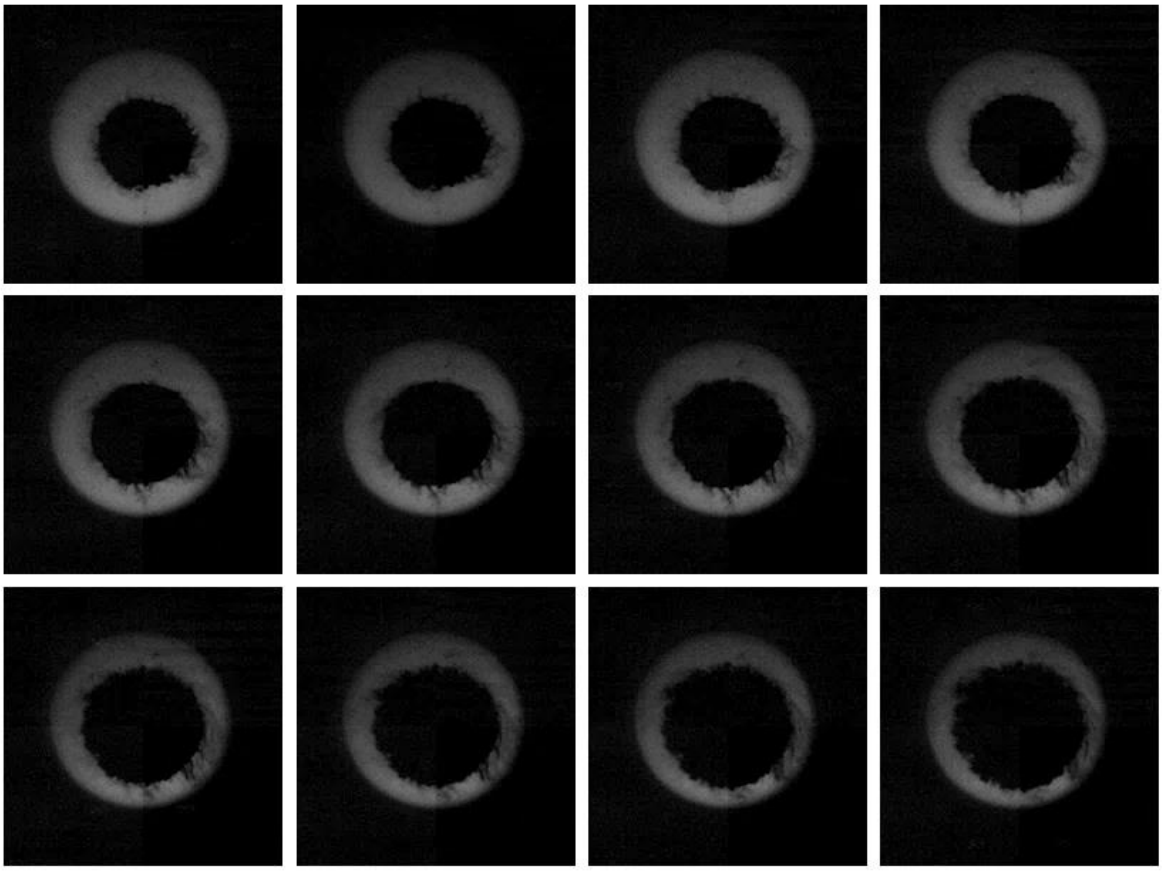

Figure 4.30: TATB type C in the glass anvil drop-weight (sequence runs left to right from the top left, frames 7.69 μs apart). The TATB spreads out as it is compacted, but there is no indication of ignition of any hot-spots. The very fine particles are jetted outwards by the force of compaction and pulled towards the direction of the vacuum on the mass spectrometer; observable on the periphery of the sample. This does not appear to block any of the gas sampling system for the mass spectrometer as evidence of air is being drawn through is shown by the argon trace in **Figure 4.33**

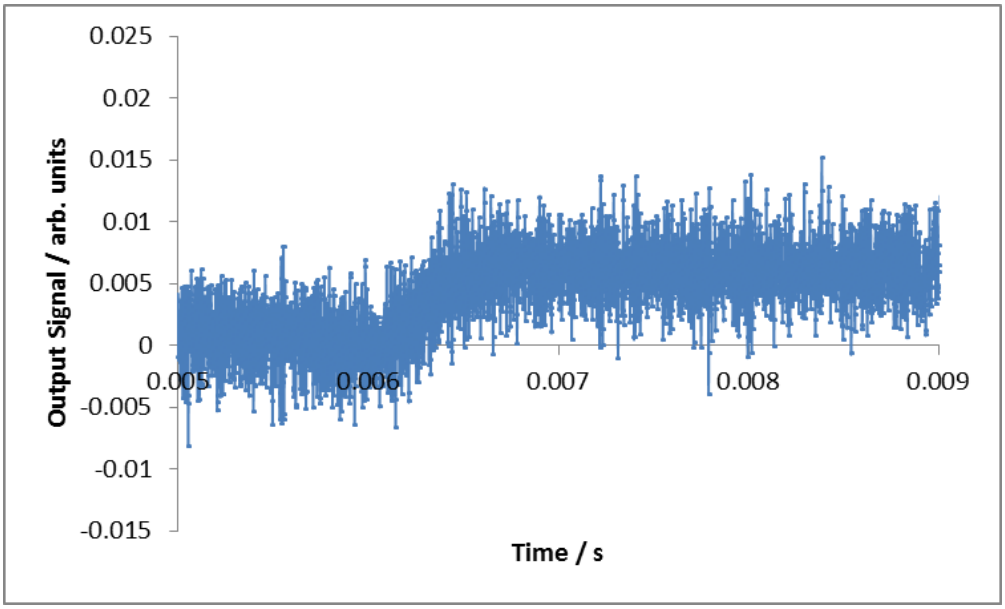

Figure 4.31: The photodiode data for TATB type C in the drop-weight. The measurement has been zoomed to correlate with the moment of impact (the upwards step in datapoints); a lot of noise in the signal is visible. There is no visible light peak owing to the lack of hot-spots, though it is possible to see a small increase of around 0.005 units which is caused by the background lighting from the periscopic mirror arrangement. The lack of peak ties in with the footage from the high speed photography in **Figure 4.30**

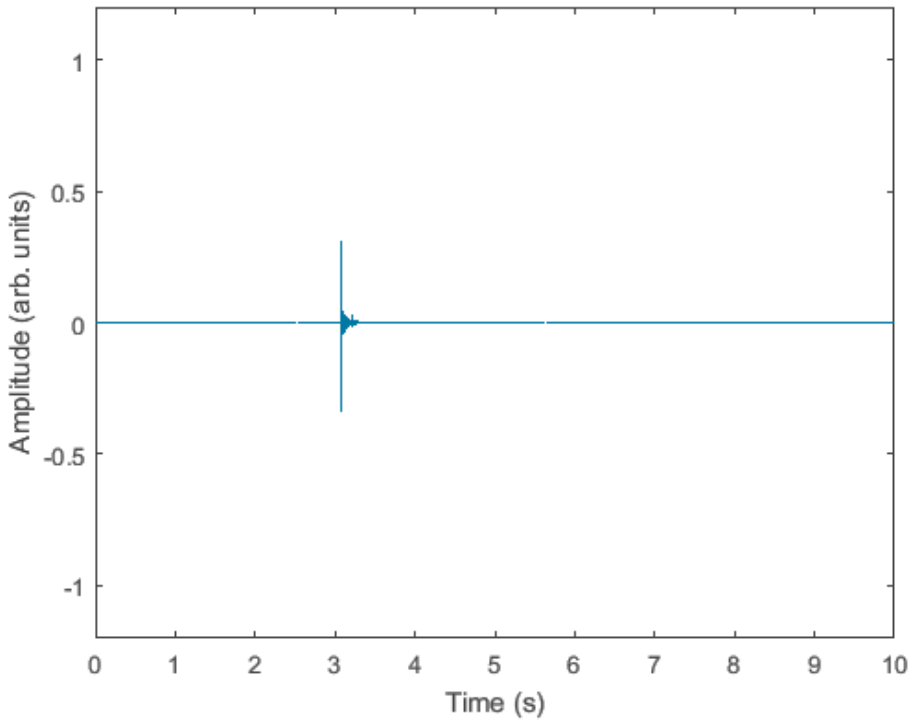

Figure 4.32: The output peak from the microphone when TATB type C is impacted. This is below the threshold value of 0.4 V, indicating a "No go"

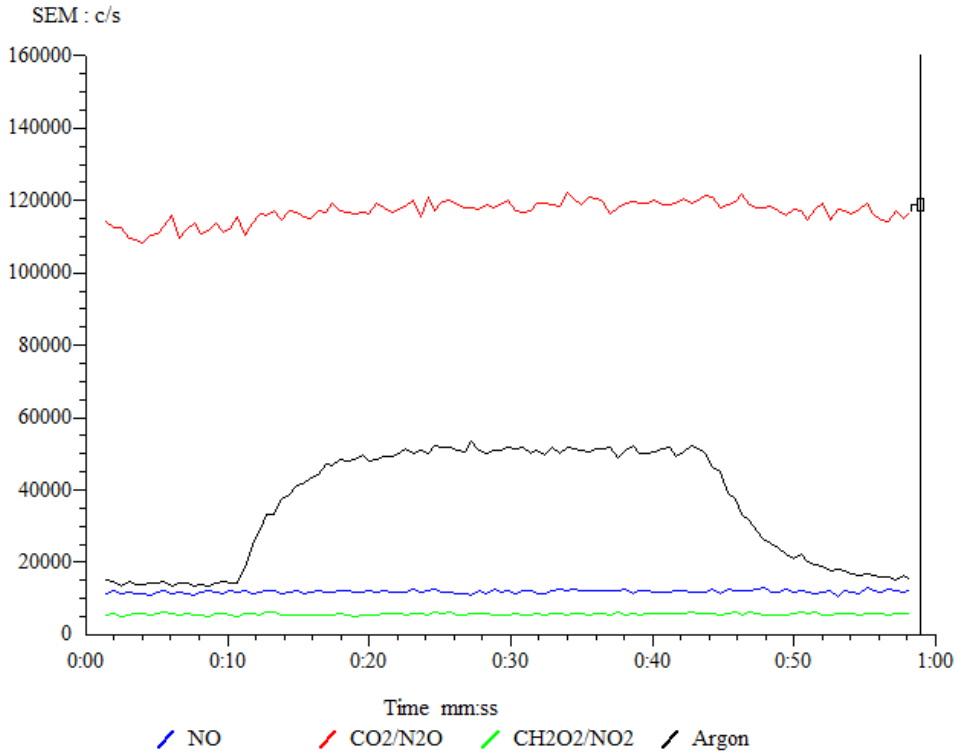

Figure 4.33: The trace given by the mass spectrometer for TATB when impacted. There is no peak in the measurement of CO_2 or NO upon impact, indicating a "No go". The trace of argon confirms that air is being drawn through the sampling system to the mass spectrometer

The threshold of 0.4 V has not been reached on the microphone (**Figure 4.32**) and the peak is therefore only attributed to the impact of the equipment, not any reaction of explosive. The mass spectrometer has also failed to identify any gaseous reaction products (**Figure 4.33**), whilst the equipment is unquestionably analysing the gas from the sample chamber (i.e. none of the steel tubes are being blocked by particles of the sample); confirmed by the presence of air being pulled through the system using the argon trace. Each individual diagnostic has successfully identified a "No go" when implemented simultaneously.

The drop-weight experiments on HMX and TATB were found to be reproducible and the range of data acquired is presented in **Table 4B**. Between three and ten experiments were performed on each material, subject to variation of results obtained. TATB consistently showed no reaction, and the results from HMX reactions are compared with those of PETN.

Diagnostic		Material			
		PETN	**HMX type A**	**HMX type C**	**TATB**
Camera	Go/ No go	Go	Go	Go	No go
	Number of Hot-spots	3 - 6	5 - 10	Indisting-uishable cluster	N/A
	Type of Hot-spots	Large and bright	Bright	Small bright clusters	N/A
	Time to Reaction / µs	220 - 300	320 - 380	310 - 390	N/A
	Reaction Length / µs	100 - 130	45 - 60	190 - 220	N/A
Micro-phone	Go/ No go	Go	Go	Go	No go
	Voltage Peak	0.78 - 0.96	0.41 - 0.60	0.45 - 0.56	N/A
Photo-diode	Go / No go	Go	Go	Go	No go
	Voltage Peak	1.04 - 1.11	0.44 - 0.45	1.87 - 1.98	N/A
Mass Spec	NO increase	Yes	Yes	Yes	N/A
	CO_2 increase	Yes	Yes	Yes	N/A
	Avg NO:CO_2	1 : 5.7	1 : 2.3	1 : 2.6	N/A
Additional Comments		Sample melts first	None	More residue left than HMX type A	Sample compacts
Sample Consumed		Yes	Mostly, some white residue	Mostly, some white residue	N/A

Table 4B: Comparison of the results taken from all of the drop-weight diagnostics when TATB, HMX and PETN are impacted. The difference between HMX type A and HMX type C is particle size (400 µm and 4 µm respectively). Key differences between the PETN and both grades of HMX include number of hot-spots, length of reaction and brightness of reaction. The microphone data and mass spectrometer measurements are broadly similar for the two grades of HMX, but different to PETN

It was found that the number of hot-spots produced by impacting HMX were generally greater in number than in PETN, especially for the HMX type C which appeared to produce very small hot-spots in indistinguishable clusters, which then joined together and spread rapidly to give a bright reaction overall. Video with higher resolution, both in picture and time, would provide more evidence towards this conclusion; the current camera has a resolution of 256 x 256 and a sample rate of 130000 frames per second. Interestingly, the PETN sits between HMX type A and HMX type C in terms of how long the reaction lasts for (as measured using the high speed video), and how bright the peak of the burning reaction is (measured using the photodiode). This shows that particle size does have an effect on the reaction characteristics of a material, and the diagnostics that have been applied are able to discern that.

The values obtained from the microphone data and mass spectrometer gas product ratio are broadly similar between the two HMX grades, but different to PETN, highlighting that these techniques are capable of identifying a differences in the nature of the material being analysed. The next section compares and discusses how useful each diagnostic is.

4.6 Comparison of the Diagnostics

Four different materials have been used to calibrate and assess diagnostic techniques applied to the glass anvil drop-weight in order to investigate a material's response to impact. To first address the "No go" reactions, the low sensitiveness explosive TATB, which does not produce light or gas reaction products, gave similar microphone and gas analysis results to melamine, an inert simulant material. This was expected for a powder sample that does not produce a burning reaction when impacted. In order to effectively compare the diagnostics for their application to reacting explosives, they are discussed with respect to their capability (what the diagnostic achieves); reliability (the level of confidence in the results); and sensitivity (the ability to detect differences in material grades).

The high speed camera is extremely useful as it provides a visual representation of the whole reaction event from beginning to end, including defining the number of hot-spots. The video output makes it clear to the operator what process is occurring at a high level of confidence. However, while the high speed camera can detect the area of light produced in a hot-spot, it cannot easily quantify the intensity of that light; the photodiode

is needed to achieve this. The camera is moderately sensitive to differences in materials as it is possible to count the number of hot-spots (i.e. reaction sites) on impact.

The photodiode adds a complimentary method of analysis to the camera that has been shown to correlate well with the growth of reaction. The photodiode has highlighted that the intensity of burn varies between HMX type A and HMX type C, with the smaller particle size being brighter. The difference was not possible to observe or quantify using the high speed camera alone. The PETN was also shown to differ to both HMX grades in the intensity of light produced during burning. The sensitivity to material grades is interesting and had not been previously observed with film. The confidence in the results is considered to be less than the high speed camera as the testing carried out so far has been on material that is known to produce either a significant burn, or a complete lack of response. This means that data needs to be obtained and assessed for materials that may react to a lesser extent, producing dimmer and fewer hot-spots.

The mass spectrometer has exhibited a highly effective ability to detect the difference between a "Go" and "No go" reaction. The identification of reaction product gases unambiguously confirms that the light emitted by a sample is from burning. Both grades of HMX produced a comparable ratio of NO : CO_2, and the mass spectrometer could differentiate that PETN had a different product ratio. This seems rational as PETN is chemically different to HMX, however it demonstrates that the mass spectrometer does not differentiate physical differences in explosive grades.

The microphone produces a signal peak in the event of a reaction, and it was not expected that the microphone would be able to discriminate between a "Go" in PETN and a "Go" in HMX. This could be caused by differences in the hardness of the crystalline materials. The peak in HMX is significantly smaller, though consistently passes the threshold. However, the threshold could readily move if a different level of response was produced by a new explosive. This feature makes the microphone the weakest diagnostic as it calls into question whereabouts the "Go"/ "No go" threshold should sit and the most effective method of calibrating it. This result is of interest as the method used in these experiments is a variation of a typical technique used with some of the accredited impact sensitiveness tests.

The comparison of the diagnostics directs the ranking of each technique against one-another, presented in **Table 4C**. When scoring each individual technique's performance against capability, reliability and sensitivity in relation to the discussion above, the high speed camera is individually the best diagnostic. The photodiode and mass

spectrometer are joint second, whilst the microphone received the lowest score. However, the calculated score only reflects the individual application of the diagnostic, and it has been shown that using all of the techniques together is achievable, and the best way to unambiguously obtain a full understanding of the reaction characteristics.

	Rank				Overall
Diagnostic	**Capability**	**Reliability**	**Sensitivity**	**Score**	**Rank**
Camera	4	= 4	3	11	1
Photodiode	2	2	4	8	= 2
Microphone	1	1	2	4	4
Mass Spec	3	= 4	1	8	= 2

Table 4C: Ranking of the individual diagnostic's performance against eachother. The highest capability and reliability scores were allocated to the camera and mass spectrometer based on the quality and certainty of data obtained. The camera and photodiode were most sensitive to physical differences between material grades. Overall, the microphone provided the least amount of useful information as an individual diagnostic technique

The diagnostic kit's ability to detect and differentiate "Go" reactions in PETN, HMX type A and HMX type C have all proven to work individually and simultaneously. The most useful overall diagnostic individually is the high speed camera. It is the most accurate way of measuring the complete length of reaction (frames containing areas of the sample emitting light), identifying the number of hot-spots, and gives an overall picture of the processes occurring.

The benefit of using all of the diagnostics simultaneously removes any doubt from the resulting reaction and therefore this is a much more credible way of assessing the level of response from an explosive under impact. In the event of one system being incapable of recognizing reaction, or being calibrated incorrectly, there are three other techniques present that give alternative data for evaluation. Though the glass anvil drop-weight is a research tool, the method of analysing a material using these techniques is an improvement to how current testing is conducted, and could be applied to future standard tests.

4.7 Summary

This Chapter has compared and evaluated the current techniques available for analysing the impact sensitiveness of explosives. These methods, described in Section 4.2, are accredited practices which are important because an awareness of the hazard presented by an explosive is needed to safely store and handle explosive materials. The glass anvil drop-weight differs from these accredited tests as it is designed to be a research tool and develop understanding in material behaviours, rather than only rank them in order of sensitiveness.

The addition of the new diagnostics, and running them simultaneously on the same experiment taking place on the drop-weight, means quantifiable, complimentary and meaningful data can be obtained efficiently. The techniques have shown that they are sensitive to different explosive materials and can detect physical variations such as particle size too. This gives the opportunity to gain a great deal of understanding about the impact hazard behaviour of a material, and how it varies with small physical changes.

The next Chapter will use the methods developed here to evaluate the LLM-105 samples that were synthesized and described in Chapter 3 on the glass anvil drop-weight.

Chapter 5: Impact Sensitiveness of LLM-105

The previous Chapter presented diagnostic techniques developed in order to distinguish and quantify how different materials behave under impact with the glass anvil drop-weight; here they are utilised further to investigate how various particle sizes and shapes of LLM-105 (produced in Chapter 3) react. The batches of LLM-105 for study are different in particle size and shape, whilst being chemically equivalent. It is anticipated from the results seen in Chapter 4 that use of the new diagnostics will provide the best chance to observe variability in reaction characteristics owing to the physical nature of the particles – hence the purpose of the diagnostic development. Simultaneous application of all of the techniques removes any ambiguity from distinguishing a reaction and could provide insight into hot-spot mechanisms.

5.1 Pristine LLM-105

Pristine LLM-105 was characterised as a baseline for the new materials, using the experimental arrangement described in Chapter 4, Section 4.4.5. Fifteen drops were carried out in total, and the outputs from the four diagnostics during a "Go" in the glass anvil drop-weight are presented below in **Figure 5.1** – **Figure 5.6**.

The development of the reaction, as recorded by high speed photography, is shown in **Figure 5.1**, with the ignition and growth of hot-spots. The initiation of hot-spots and the subsequent growth of reaction is comparable to that observed in HMX and PETN, however the background lighting for this experiment was significantly reduced (such that virtually no background light is visible to the high speed camera) in order to distinguish the reaction. For all of the experiments, the light produced by LLM-105 was dimmer than that of the other explosives; its quantification by photodiode is discussed in a subsequent passage. It was also possible to observe a visible burst of gas in the high speed photography before the development of the hot-spots, and this is illustrated in **Figure 5.2**, where a bubble can be seen ejecting powder in the bottom right corner of the sample. It is possible that the gas could be created by randomly trapped gas or solvent, or it could be the product of a reaction. It is a very reproducible feature when studying the impact of

LLM-105 in the drop-weight; it occurred during every reaction. This makes it more likely to be reaction product gas.

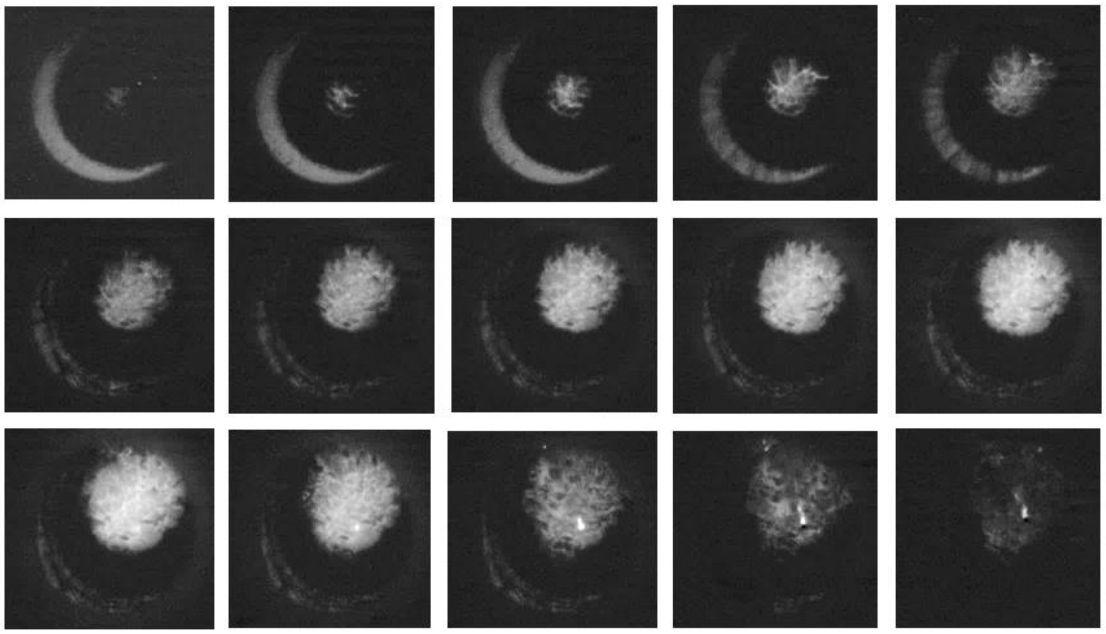

Figure 5.1: High speed camera images of pristine LLM-105 reacting in the drop-weight (sequence runs left to right, frames are 7.69 μs apart). The powder is compacted and ignition of hot-spots can be seen. The hot-spots are small and dim compared to the other explosives, and form in a dense cluster of multiple ignitions rather than individual points

As noted, a reduction in the experimental back-lighting was required to allow visualisation of the reaction by the high speed camera; similarly the photodiode also needed an adjustment to allow a signal peak to be distinguished for LLM-105. The gain on the transimpedance amplifier was increased by a factor of 10 and showed that the intensity of the light produced by LLM-105 reacting upon impact is in the order of one hundred times smaller than that observed for HMX and PETN (**Figure 5.3**). The reduced backlighting in the experimental arrangement does not produce a reading in the photodiode output.

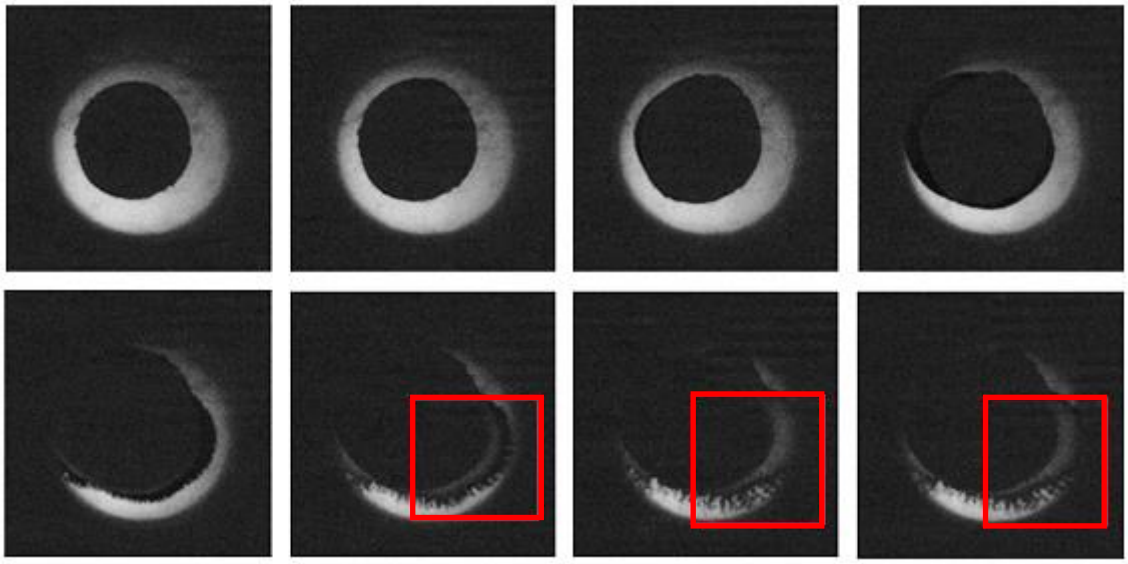

Figure 5.2: High speed photography images of the gas burst in LLM-105 prior to hot-spot development (sequence runs left to right, frames are 7.69 µs apart). The burst of gas is seen in the bottom right corner of the sample. The frames are dark due to the reduced backlighting required to observe the reaction. The gas burst is seen in every LLM-105 experiment prior to visual hot-spots, it is most probably reaction product gas as it is a reproducible feature

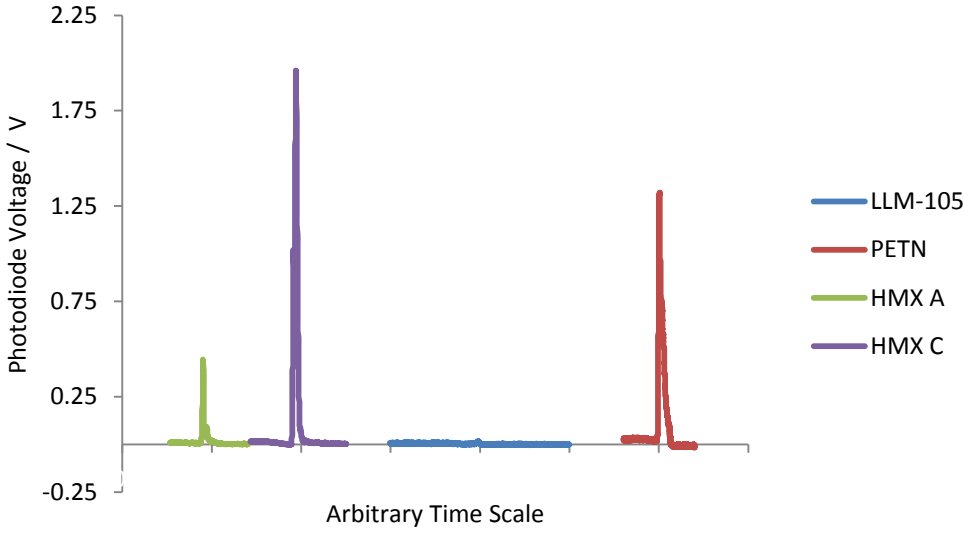

Figure 5.3: Photodiode signal given by the reaction of LLM-105 in the drop-weight compared with other explosives. The LLM-105 signal is significantly smaller, by a factor of around one hundred, indicating that the burning reaction is dimmer. Each peak lasts between 80 µs and 130 µs

The most challenging diagnostic to apply to the LLM-105 impact reaction was the microphone. Using the previously established criteria, the majority of the reactions that were identified as a "Go" by the camera and the mass spectrometer (shown to be the most reliable diagnostics in Chapter 4) were misdiagnosed as a "No go" by the microphone. An example of the microphone correctly representing a "Go" is given in **Figure 5.4**, where the initial peak is above the 0.4 V threshold, and the more commonly observed incorrect "No go" is presented in **Figure 5.5**. Both reactions were a "Go" as interpreted by other diagnostics, so it would be expected that both peaks should sit above 0.4 V at the maximum point. Lowering the threshold in support of improving LLM-105 assessment is not feasible as the signals generated by the vibrations in the machinery mask the region that would correlate with the LLM-105. Also, the values obtained for LLM-105 were not consistent, and varied more widely than for HMX or PETN. These circumstances mean a 'standard' diagnostic (the microphone) is not useful when applied to LLM-105 assessment, and is not likely to be useful for the rest of this investigation.

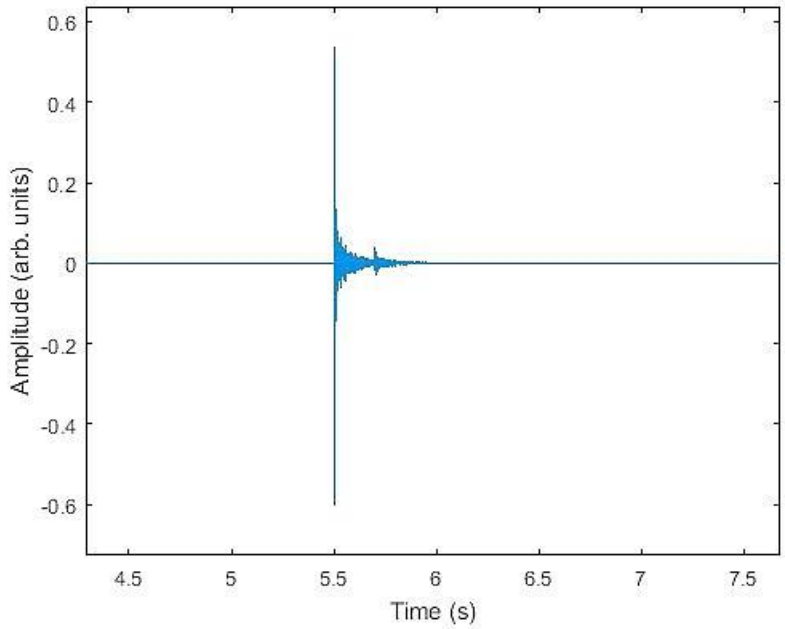

Figure 5.4: Microphone signal for correct identification of a 'Go' reaction in LLM-105 on the drop-weight. The amplitude of the initial peak is above 0.4 V

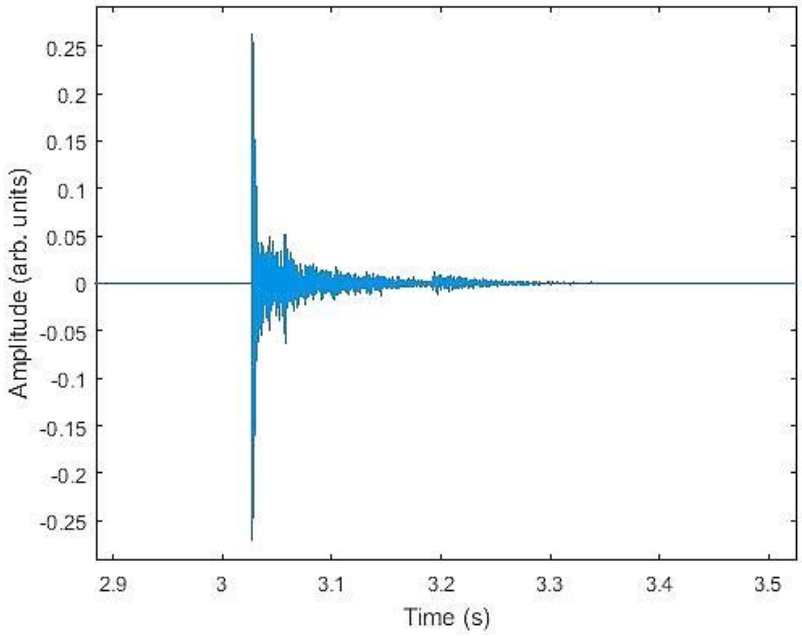

Figure 5.5: Misdiagnosis of a 'Go' reaction represented as a 'No go' in LLM-105 by the microphone. The amplitude of the initial peak is below 0.4 V

Of all the diagnostics applied to the drop-weight, the mass spectroscopy results proved to be the most reliable for conclusively determining reaction in LLM-105, particularly taking into consideration that the background lighting for the high speed camera had to be reduced to observe the burn, and the photodiode signal is very small. Evaluation of the combination of results in order to identify a reaction consistently highlighted the effectiveness of the mass spectrometer. A typical mass spectrum from LLM-105 producing a "Go" on the drop-weight is presented in **Figure 5.6**.

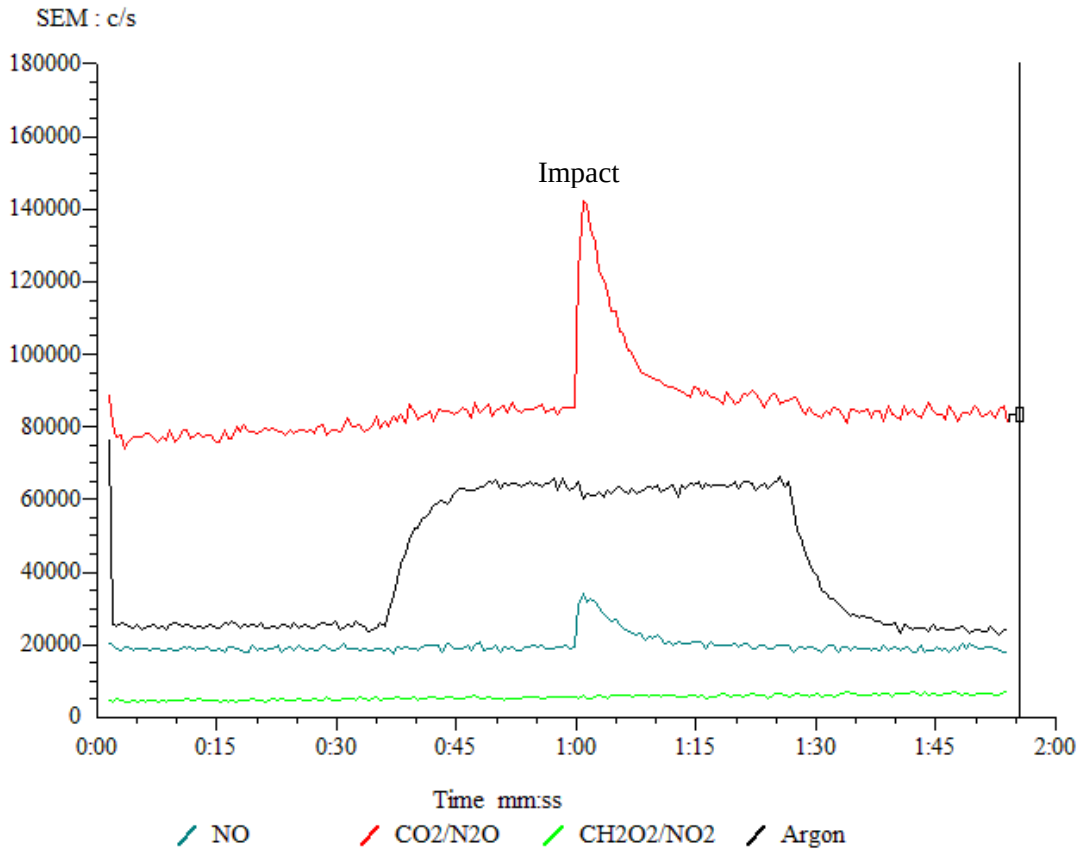

Figure 5.6: Time resolved mass spectrum of reaction gases produced by the burning reaction of LLM-105 in the drop-weight. The peaks in the CO_2 and NO traces show the presence of the gaseous products corresponding with impact of the explosive. The argon trace demonstrates the presence of air; the sample is exposed to the atmosphere and isn't confined in vacuum

Of the fifteen drops carried out on LLM-105, seven were a 'Go', indicating approximately 50 % chance of reaction in the experimental set-up with its standard configuration. The most reliable of the above diagnostics for determining the "Go"/ "No go" state of the sample under impact were the camera and the mass spectrometer, as expected from Chapter 4. The photodiode required further calibration for the dimmer reaction light produced by the LLM-105 compared to the other explosives; this meant reducing the enhanced background lighting to virtually nothing – relying on the ambient lighting of the surroundings (a windowless room) rather than the beam of light sent through the periscopic mirrors. The dimmer backlighting reduced the clarity of images taken with the high speed camera when no reaction light was present, but it was possible to capture the ignition and development of hot-spots during a reaction.

Individual hot-spots during ignition of reaction were difficult to discern as the response in LLM-105 appears dimmer; and the smaller, dimmer hot-spots are formed in clusters, or groups without single discreet points of light visible to the human eye (**Figure 5.1**). This differs from PETN and HMX type A where individual hot-spots are often distinguishable, though the cluster observation is replicated in HMX type C.

The ability to observe hot-spots as single points using this method may relate to the particle size of the material tested; HMX type A has a particle size of 405 μm, and the PETN tested was of a comparable size. HMX type C has a small particle size of 4 μm, and the pristine LLM-105 has an intermediate particle size of 47 μm. Development of the reaction in HMX type C could also be seen in clusters (**Figure 4.26** in Chapter 4); which could be because the heat from the burning surface transfers more readily between smaller particles, as smaller particles have a lower heat capacity and therefore heat faster. They also have smaller interspatial voids to cross, therefore the hot-spots do not have to be as hot (compared to larger particles) to transfer the reaction, and as such they are not as bright. Additionally, the burning surface is visibly smaller in smaller particles; therefore to the naked eye it is more difficult to identify discrete points.

The dim cluster effect seen in the hot-spots of smaller particles could indicate that the mechanism for the reaction might be created by different pathways, depending on particle size. For example larger particles could be more susceptible to hot-spots by adiabatic compression of gases within voids or defects, which are fewer in number but brighter. Smaller particles in turn may respond to friction or shearing mechanisms, due to a lower probability of a crystal containing a defect leading to adiabatic compression and ignition of hot-spots as a result. These different mechanisms could affect the light output of the hot-spots, with larger and brighter hot-spots being generated in the adiabatic compression mechanism. These theories are based on limited evidence as friction and shear effects have not been analysed here, but it could provide a reasonable explanation to the observations. More evidence could be obtained using friction test apparatus to investigate and compare the effect on the brightness of the hot-spots generated in large and small particle sizes, but this is beyond the current scope of work.

The length of the reaction in LLM-105 is longer than that observed for HMX and is comparable to the length of reaction for PETN. The time to reaction from impact is comparable across all of the explosives, with only PETN varying due to its possible melting stage prior to initiation.

HMX type C has shown occasional evidence of a melt (see the transparent region of **Figure 5.7**) which does not occur in the HMX type A. This observation implies that the reaction in HMX type C gets hotter than HMX type A in a localised region; however the melting point of HMX is around 280 ºC, which is around double that of PETN, and would require significant heating of a large area of the sample. It seems unlikely that melting would occur under the current experimental conditions due to the rise in temperature required. The melt in HMX type C, if it is a real effect, could be attributed to the difference in particle size and the transfer of heat, as previously noted. Alternatively the transparent region may be caused by the sudden release of a build-up of trapped reaction gas that is pushing unreacted material aside.

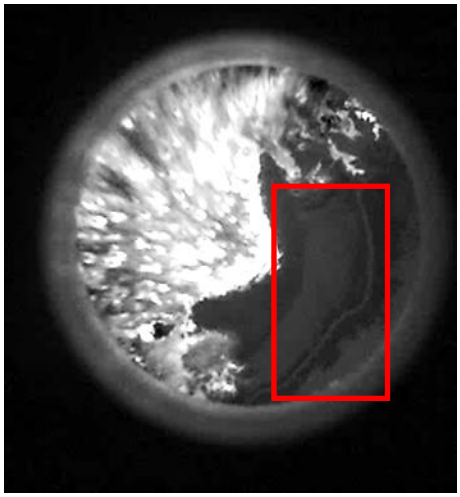

Figure 5.7: Frame taken from the sequence of HMX type C reacting in the drop-weight, showing a transparent region in the bottom-right section of the sample (highlighted by the red box), possibly indicating melting behaviour similar to PETN. Melting seems unlikely due to the high melting point of HMX. This occurrence is by exception for the HMX, but is reproducible for PETN. LLM-105 does not demonstrate this behaviour

There was no evidence of a melt stage present prior to, or during, the reaction in LLM-105. What is unique to LLM-105 is the visible occurrence of a gas burst which displaces unreacted powder (**Figure 5.2**) prior to the development of visible hot-spots. This feature is reproducible in the LLM-105 experiments and is therefore likely to be reaction gases, as all samples were dried prior to impact testing, eliminating the likelihood of the presence of any residual water or process solvent in the material.

An estimation of the area of the sample producing light in the growing reaction in all of the materials can be manually measured from the film frames to plot the development of the burn diameter (**Figure 5.8**). This method differs from the reading given by the photodiode (**Figure 5.3**) as it relates directly to the spread of reaction area rather than the brightness or intensity of the light produced. The burn area and photodiode data combined give an indication of the heat of the reaction.

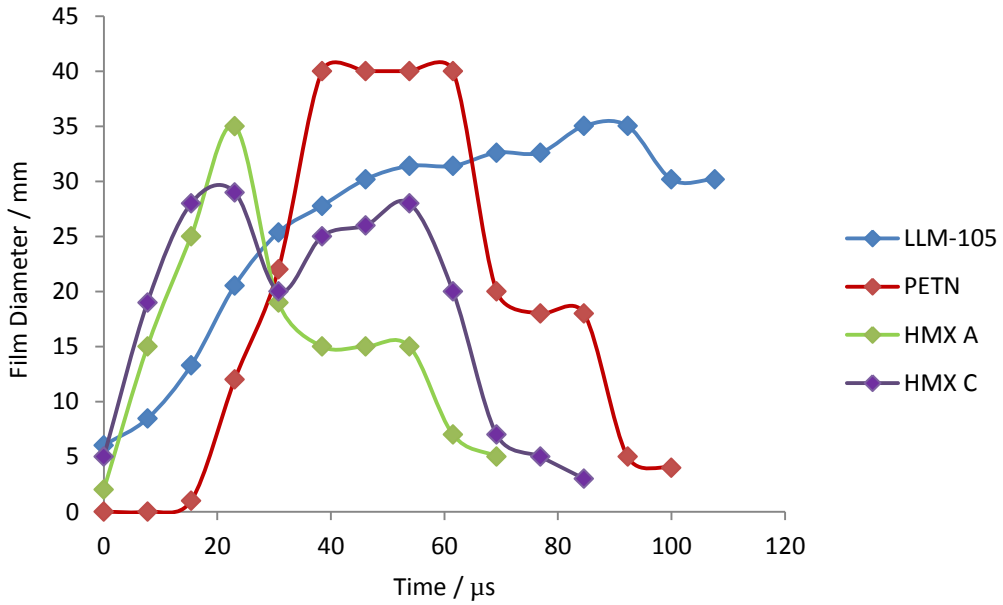

Figure 5.8: Diameter of burning reactions measured on the film frames allowing an estimate of the growth of reaction. The experiments chosen to represent the data points on the graph are typical of each of the materials characterised, with the exclusion of any anomalies. The graphs indicate the area covered by the reacting material, where the photodiode measures the intensity of the light. The traces start point is determined by high speed video, where light can first be observed in the reacting sample. For PETN, the start of reaction is the melt stage and therefore appears delayed compared to the HMX and LLM-105

The initial speed of the burn (diameter of reaction area varying over time) is comparable between HMX and PETN; time zero is given by the first sign of reaction. The start of the traces was aligned to the start of reaction as identified by high speed video; in the case of HMX and LLM-105, this was the first frame containing light produced by the sample. For PETN the start point occurs at the melting stage. LLM-105 starts slower, gains

in pace and then plateaus. As noted, the delay in the start of the PETN reaction is owed to its melting stage, however once hot-spots have developed the speed of the burn is very similar to HMX. All of the explosives tested show more than one peak, which demonstrates a shrinkage in the initial burn before the reaction gains enough energy to grow again. This implies that the hot-spots cool, but not enough to die out, then continue expanding or join together with other smaller regions of light.

The range of results from the photodiode output are presented in **Figure 5.3** and shown in **Table 5A**. The average photodiode peak output can be divided by the maximum burning area to ascertain an intensity per unit area. The larger particles of HMX (type A) give out a less intense light signal than the smaller HMX particles (type C). The burn from the HMX type C is also brighter than the PETN, which given that the growth of reaction is comparable, implies that the HMX type C burns hotter than PETN. The light output from LLM-105 is two orders of magnitude smaller than the PETN and HMX type C from the photodiode data, though it takes longer for the reaction light to dim. As noted in Chapter 4, the error on the photodiode is expected to be 0.02 %.

Explosive Material	PETN	HMX A	HMX C	LLM-105
Photodiode Peak Voltage / V	1.04 - 1.11	0.44 - 0.45	1.87 - 1.98	0.017-0.02
Voltage per unit Area / V/mm^2	0.00085	0.00046	0.00291	0.00002

Table 5A: Range of results from photodiode readings during the reaction of explosives on the drop-weight. Due to small quantities of material available, 5-10 drops were carried out per material, and the range of data presented here is representative of the readings obtained for the "Go" reactions

As discussed earlier, the microphone has difficulty picking up "Go" results from LLM-105 (**Figure 5.4** and **Figure 5.5**) when the other diagnostics can distinguish the reaction. Of the seven "Go" reactions in LLM-105, only two were recognised by the microphone using the threshold as calibrated in Chapter 4, which highlights an issue with this diagnostic as it is the least reliable for this material when compared with the other methods.

Without the other diagnostics to compliment it, use of the microphone alone could lead to false "No go" results being interpreted. Where recalibration of the microphone baseline may be appropriate to account for the LLM-105 results, the "Go" for LLM-105 also overlaps with the "No Go" readings, which in turn overlap with the trace produced by

vibrations in the equipment, making it virtually impossible to baseline a "No Go" for LLM-105 using the current experimental arrangement. Other drop-weight users could experience similar issues with their equipment and microphone diagnostic if a new material undergoing evaluation is not carefully monitored using other means of evaluation. The microphone does not appear useful as a tool for impact assessment of explosives.

The ratio of decomposition gasses (NO : CO_2) produced during reaction in LLM-105 is similar to HMX, though both LLM-105 and HMX produce a significantly lower proportion of CO_2 than PETN. The results from the drop-weight reactions were compared to the output of the Cheetah thermochemical code, however they did not align well for comparison. This mismatch could be due to the code being designed for detonation of explosives, and the reaction from impacted explosives is a deflagration or burning reaction. Additionally, there are points that gas could escape prior to sampling from the mass spectrometer; from o-rings between the equipment and joins in the sampling pipe.

The reduced quantity of CO_2 could be because when comparing the chemical formulae and molecular structure of the explosives (**Figure 5.9**), PETN has a higher carbon and oxygen content. The Kistiakowsky-Wilson rules for the decomposition of an explosive state the initial product formed on reaction is carbon monoxide, followed by water, then carbon dioxide if any oxygen remains, and finally dinitrogen. PETN is the most likely molecule to have remaining oxygen, which can then react with the carbon monoxide, and therefore the expected behaviour is consistent with the higher CO_2 ratio values obtained during experiments.

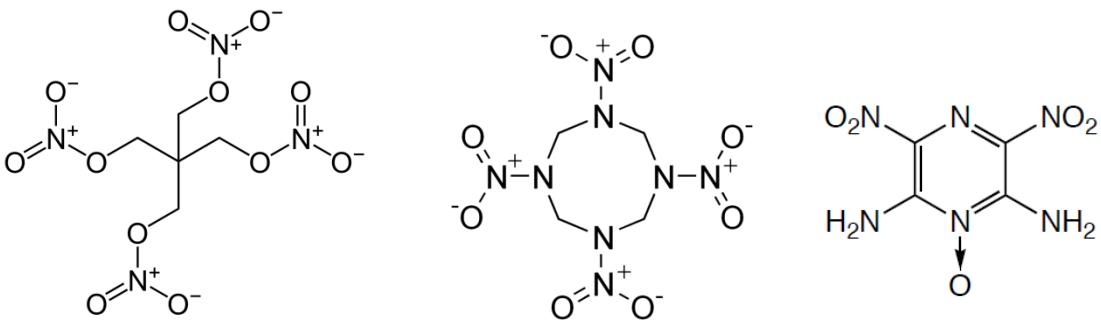

$C_5H_8N_4O_{12}$ $C_4H_8N_8O_8$ $C_4H_4N_6O_5$

Figure 5.9: The molecular structures and chemical formulae of (left to right) PETN, HMX and LLM-105. PETN has a higher carbon and oxygen content, which will contribute to the higher ratio of CO_2 identified in decomposition

The final observation from the LLM-105 responses in the drop-weight comes from residues after the reaction. LLM-105 is the only material studied that has undergone a colour change. HMX type C left a white residue of unreacted or melted material on occasion, but LLM-105 consistently produced an orange residue, darker than the original yellow material following a reaction (**Figure 5.10**). This discolouration is indicative of a probable decomposition reaction, and possibly a partially reacted state. It was not possible to recover a sample of the orange residue owing to its small quantity, but further analysis using DSC or NMR could potentially identify the products and allude to a decomposition pathway.

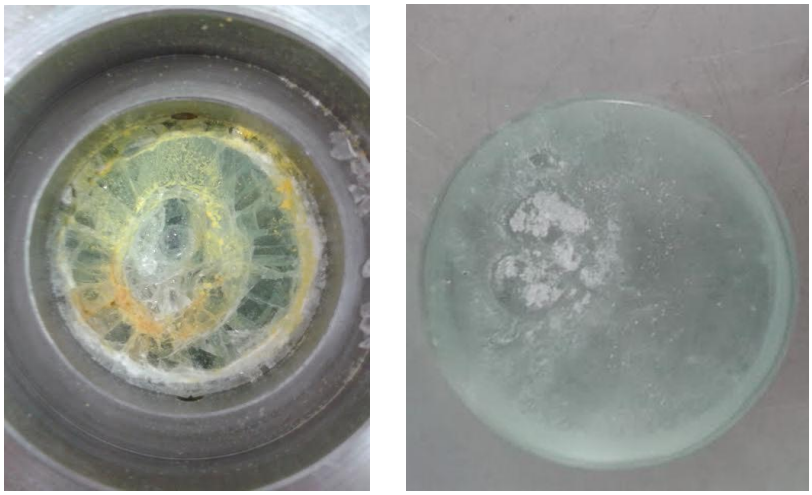

Figure 5.10: Unmodified LLM-105 discolouration (left) compared to HMX C residue (right) after reaction. In this case the gas from the LLM-105 reaction has resulted in the glass anvil breaking

LLM-105 behaved differently to the HMX, PETN and TATB. While the HMX and PETN produce definite “Go” reactions, and the TATB yields a consistent “No go”; LLM-105 sits on a borderline, where it generates a reaction approximately half of the time. The characteristics of a “Go” are also different to the standard CHEs tested, which proves the beneficial use of all of the diagnostics together, increasing the quantity of data obtained and removing the potential for biased judgement on behalf of the operator.

5.2 Milled LLM-105

The ball milled LLM-105 was characterised using the same experimental technique as the pristine LLM-105. Due to small quantities of material available, between five and ten drops were carried out on both this and the rest of the explosives discussed in this chapter. Though a limited number of drops reduces the statistical accuracy of reaction probability, it allows for enough data to be acquired to assess whether the features distinguished during a "Go" are representative traits. Similarly the Langlie method for the Rotter Impact Test only uses ten drops and is still valid in appropriate situations, though it is known to be less accurate than the fifty drop Bruceton method.

The milled LLM-105 had an 80 % probability of producing a "Go" in the drop-weight, as determined by the high speed video and mass spectrometer (being the most accurate techniques). Analysis of the high speed camera footage shows a reduced number of dim hot-spots compared to the pristine LLM-105, where the hot-spots have the tendency to form in small, dim clusters (**Figure 5.11**). The length of the reaction for which the milled LLM-105 produces light is also shorter than for the pristine LLM-105. The time to reaction from the impact and gas production phase lasts for approximately the same length of time in both materials.

The photodiode captured readings between 0.0096 V and 0.0098 V (± 0.02 %), around half the value of the pristine LLM-105. The microphone values obtained during testing sit between 0.23 V and 0.36 V, meaning that the microphone failed to identify any of the "Go" reactions in the milled LLM-105, as the readings all sit below the 0.4 V threshold. These observations; a lower intensity of light and sound output; do not correlate with the increased likelihood of obtaining a "Go" for milled LLM-105 i.e. the sensitiveness is higher, but the explosiveness is less than the pristine LLM-105.

As before, the mass spectrometer consistently identifies "Go" reactions; in one case where the camera, photodiode and microphone all failed to interpret a reaction. In this instance, a gas burst was not visible on the camera, nor were hot-spots, but the mass spectrometer recognised decomposition products, and upon inspection after the experiment, the sample showed evidence of decomposition through colour change. The majority of the sample was compacted, but an area of dark orange marbled through the material highlighting where there had been a reaction. This was seen for all of the milled LLM-105 samples that produced a "Go". The quantity of CO_2 for the ratio of NO : CO_2 was slightly higher for the milled LLM-105 compared to the pristine LLM-105, which

possibly indicates a lower chance of the molecule breaking up, or a smaller quantity of the sample doing so in the milled material (i.e. a lesser extent of reaction).

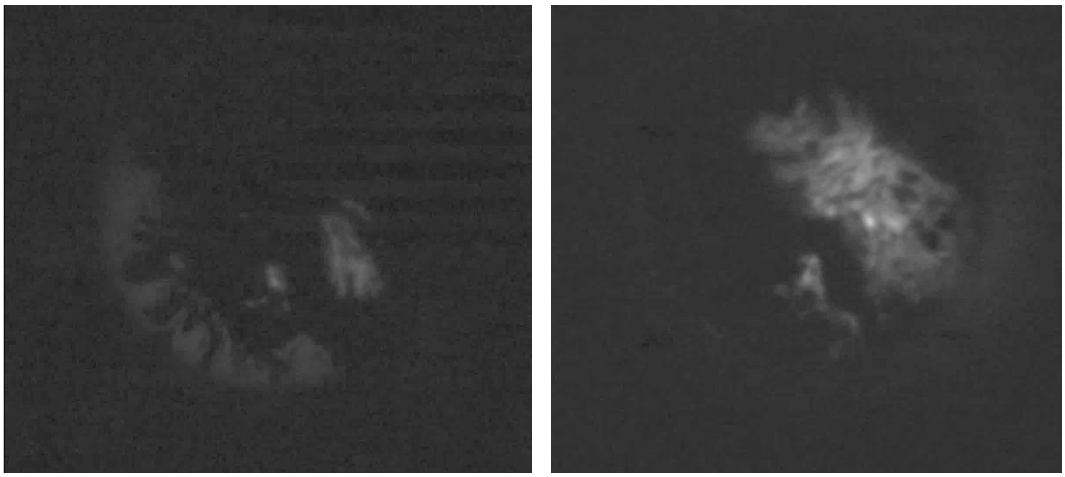

Figure 5.11: Frames from a typical high speed photography sequence of milled LLM-105. The frame on the left shows the initial cluster of hot-spots formed on impact, and the frame on the right shows the reaction at its brightest. These reactions are considerably dimmer than the pristine LLM-105 and this observation is reflected in the values obtained using the photodiode (note the images have been artificially brightened to allow the reader to observe the reaction)

5.3 Formulated LLM-105

The pristine LLM-105 was formulated with a Viton binder in a filler : binder ratio of 95 : 5, using a solvent paste mixing process. The purpose of formulating an explosive with an inert binder is to improve both the mechanical and safety properties of the neat material. Viton is a fluoropolymer, and is typical of the kind of rubbery elastomer used to binderise explosives. It is expected that the formulated LLM-105 would have lower impact sensitiveness compared to the neat LLM-105.

The formulated LLM-105 was subjected to the same experimental regime as the pristine and milled LLM-105. When characterised in the drop-weight, the formulated material produced an undisputable "Go" each time, with evidence from the high speed camera footage and mass spectrometer. The sequence obtained from an example of the high speed footage is presented in **Figure 5.12**. These samples tended to produce more than one region of hot-spot activity, which may be the reason a higher reading from the

photodiode was also observed. The light output recorded by the photodiode showed values between 0.050 V and 0.051 V; twice as bright as the pristine LLM-105. The raw data from the photodiode comparison is shown in **Figure 5.13**. There was also evidence in the video footage of a characteristic LLM-105 gas burst occurring after hot-spot ignition stage, which was usually seen only before ignition in the pristine and milled LLM-105.

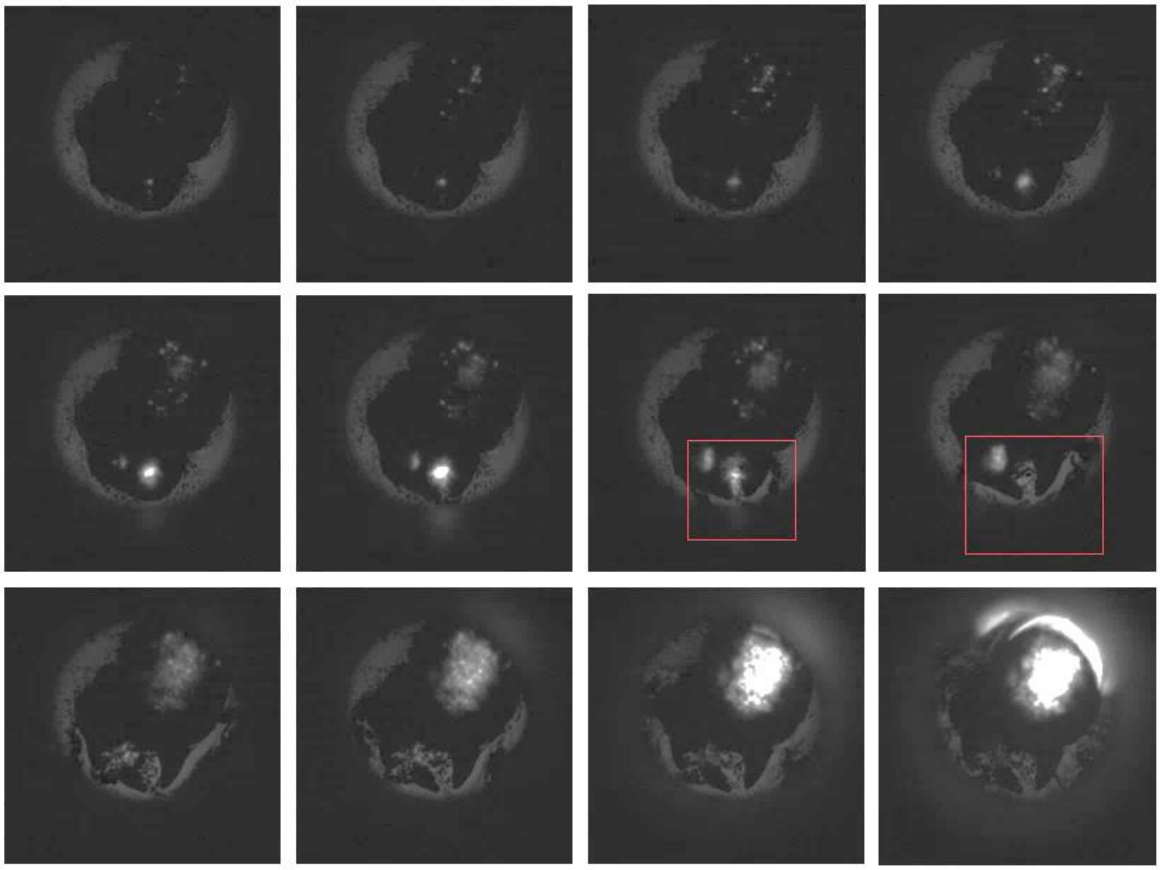

Figure 5.12: The initiation and growth of a typical reaction in formulated LLM-105 on the drop-weight as recorded using high speed video (sequence runs left to right, frames are 7.69 µs apart). The reaction is brighter than the pristine LLM-105 and there is evidence of a gas burst after the hot-spot ignition; highlighted in frames seven and eight. The reaction was violent enough to cause the glass anvils to break after the final frame shown in this figure. Note that the images have been artificially brightened for clarity

The microphone data for this material again sat below the threshold of 0.4 V, with values between 0.22 V and 0.38 V, failing to correctly identify the "Go" reaction. The NO : CO_2 ratio provided by the mass spectrometer data varied widely between the experiments; which is likely to be caused by the additional presence of the binder, in

comparison to other experiments which contain a single component of sample. The binder decomposition during reaction will lead to different reaction products, which will alter the overall ratio measured. A large quantity of unreacted material remained after each of the drops on formulated LLM-105, with the characteristic orange marking reaction in small areas of the sample.

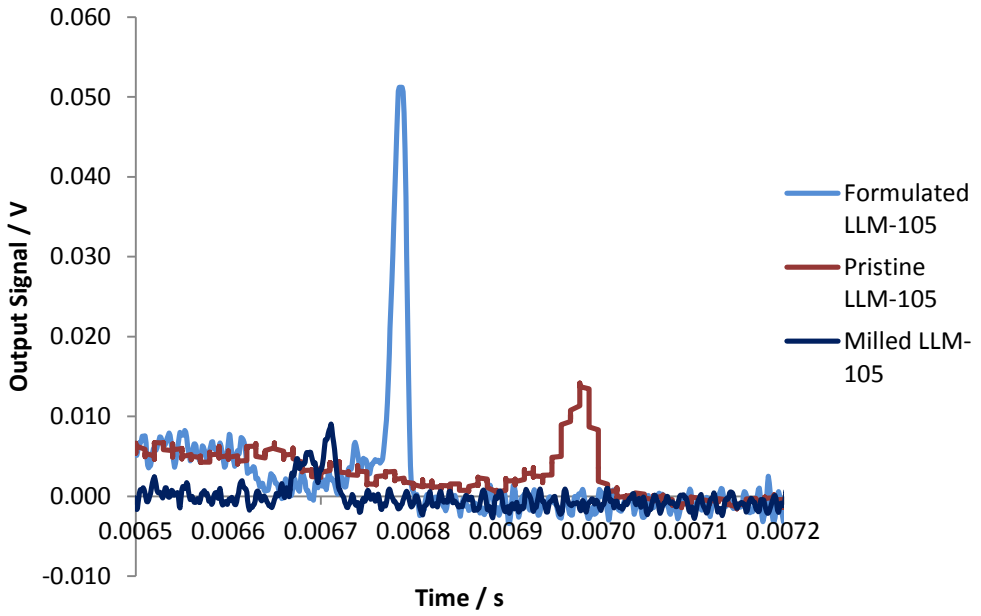

Figure 5.13: Raw data from the photodiode output; the reaction of the formulated LLM-105 is twice as bright as the pristine LLM-105, and both are significantly brighter than the milled LLM-105

It is unusual for the addition of binder to increase impact sensitiveness of an explosive, and in this case it has made the results less consistent. Adding Viton to RDX, for example, was shown to improve its impact sensitiveness [143], and increasing the percentage of binder desensitised it further. When considering the structure of the formulated material, there are binder-coated particles of LLM-105 which form agglomerates held together by the binderised areas. It is feasible that there may be pores (or pockets of air) trapped between the particle surface and the binder, or in any binder-rich regions, such that an ideal area for the ignition of a hot-spot by adiabatic compression of gas is created. Any variation of roughness in the surface of the crystal will exacerbate this effect. However, the rubbery binder usually has a damping effect on the energy imparted by the shock of impact. The unusual gas burst in LLM-105 has been seen after

hot-spot ignition in the formulated material. This is different to the results from other LLM-105 samples and it may be that the binder coating actually traps these reaction gases, causing further adiabatic compression, until the gases are hot enough to melt or decompose the polymer, leading to a localised build-up of heat and pressure. This is a probable cause of the unexpected increase in sensitiveness, compared with other explosives that don't have an observable gas burst.

The melting point of Viton is over 200 °C, and the decomposition temperature of LLM-105 as determined by DSC is over 300 °C. It is possible that the gas burst observed in LLM-105 would be hot enough to melt or soften the polymer and cause it to flow in such a way that contributed to the reaction. The intensity of the light is brighter than for the pristine LLM-105, implying the Viton does contribute in some way, either chemically or by confining the reaction gases.

5.4 Different Particle Sizes

In Chapter 3, different particle sizes and morphologies of LLM-105 were produced to undertake a comparative study on impact sensitiveness of the material, aiming to characterise any differences between size and shape. The features of the different particle sizes and morphologies are summarised in **Table 5B**. Of relevance to this section are the pristine material (which was presented in Section 5.1) and the milled material (Section 5.2). In the same category for particle size assessment is LLM-105 batch 105G. These three batches are all block morphology of varying size. Similarly, batches 105F and 105D are both needle shaped, but different size, so will be compared here. Experiments on the drop-weight were carried out in the same manner as for the pristine and milled LLM-105.

Morphology Type	Particle Size / μm	Sample
Block	47	Pristine LLM-105
	8	Milled LLM-105
	1	105G
Needle	20 (length)	105F
	4 (length)	105D
Block/Needle	2	105E
Twinned Crystal	38	105C

Table 5B: The different particle sizes and morphologies of LLM-105 available for comparison (as produced in Chapter 3)

The research batch 105G has a particle size of 1 μm, considerably smaller than both the pristine and milled LLM-105, which are 47 μm and 8 μm respectively. In the drop-weight the 105G produced a "Go" in 20 % of the experiments, during which only the high speed camera and mass spectrometer identified the reaction (**Figure 5.14**). The hot-spots were dim, and unlike other LLM-105 batches, it was not possible to see the burst of gas prior to the generation of light.

The photodiode did not produce a reading for the dim reaction, and the microphone readings again sat below the threshold, between 0.26 V and 0.37 V. None of these LLM-105 batches of varying particle size registered an audible "Go" using the threshold identified by earlier calibration of the microphone using the HMX and PETN.

The mass spectrometer remained reliable during this experiment, identifying the reaction and giving standard NO and CO_2 peaks for the gas products. There was also indication of reaction by inspecting the sample after impact and finding small orange markings in the remains of the compacted LLM-105. However there was no obvious correlation between the reaction product ratio and the different particle sizes of LLM-105. It is still an extremely useful diagnostic to detect a "Go" reaction, but does not discern physical differences in the explosive in the same way as the time resolved photodiode appears to.

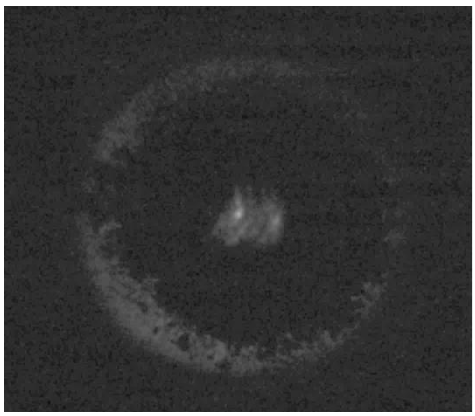

Figure 5.14: The peak of reaction recorded for the smallest block shaped particles; no gas burst was observed and the hot-spots were not bright enough to identify a peak for the photodiode. Note the image has been artificially brightened

Comparing the batch 105G with the pristine and milled LLM-105, the probability of a "Go" reaction followed a pattern of 50 %, 80 % and 20 % with decreasing particle size from 47 μm, 8 μm and 1 μm respectively. The photodiode showed that the hot-spots in the

8 μm material were dimmer than the 47 μm LLM-105 by a factor of two, and the hot-spots in the 1 μm LLM-105 were not bright enough to register a reading on the photodiode, but could be observed in high speed video.

The three LLM-105 materials discussed here all showed a tendency towards generating hot-spots in dim clusters, compared to the PETN and HMX which show individual visible points. The milled LLM-105 showed the opposite trend in reaction intensity to HMX; the milled HMX type C (approximately 1.9 V peak on the photodiode) was around four times as bright when reacting compared to the HMX type A, but the milled LLM-105 (0.01 V) was almost half as bright as the pristine LLM-105. The comparable particle sizes between the HMX type C and milled LLM-105 are 4 μm and 8 μm. The hot-spots in the 1 μm particle size LLM-105 were too dim to produce a reading on the photodiode in its current experimental arrangement (**Figure 5.14**).

There are two particle sizes of needle shaped LLM-105 to investigate in addition to the block morphology. Batch 105F is 20 μm in length and 105D is 4 μm; these were shown to have a 20 % and 60 % chance of reaction correspondingly. The reaction in 105F produced a photodiode value of around 0.014 V, and the hot-spots are visible in the high speed video, though the time to reaction from impact to the gas burst is longer than for many of the other LLM-105 batches. 105D with the smaller particle size has a lower light output; 0.006 V. This is fully summarised below in **Table 5C**.

Particle Size / μm	**Probability of Reaction ± 10%**	**Average Photodiode Output / V ± 0.02%**
47 - blocks	50 %	0.019
20 - needles	20 %	0.014
8 - blocks	80 %	0.010
4 - needles	60 %	0.006
1 - blocks	20 %	N/A

Table 5C: The correlation between particle size and achieving a "Go" reaction during impact in the drop-weight, and the intensity of light produced in that reaction. It can be seen that independent of morphology, the decreasing particle size consistently results in a dimmer reaction, however there does not appear to be a link with the chance of reaction occurring

A clear relationship exists between LLM-105 particle size and the light intensity of the reaction; a larger particle size produces a brighter reaction independent of its shape.

This is opposite to the trend observed between HMX type A and type C. There also does not appear to be a correlation between particle size and the likelihood of reaction occurring when impacted in the drop-weight; this assessment is not relevant to HMX which produces a consistent reaction every time for either the larger or smaller particle size. Morphology may have an effect and this will be discussed further in the next section.

The mass spectrometer data for both batches identified "Go" reactions correctly, but like the block morphology LLM-105, there was no apparent correlation of reaction products with particle size. What was unusual in both 105F and 105D was the intermittent identification of a "Go" using the microphone diagnostic. Although it was not reproducible for every experiment that produced a reaction, 105F passed the threshold with a "Go" value of 0.45 V, and similarly 105D measured up to 0.53 V. These readings are in the equivalent range of HMX type C (4 μm in size) as quantified using the microphone. As these results are not consistently reproducible it still casts doubt as to how effective the microphone is as a diagnostic, but it does separate the behaviour of the 105F and 105D from the LLM-105 examined thus far, and indicates a difference in reaction violence that cannot be captured optically.

5.5 Different Morphologies

LLM-105 has a preference to form block shaped and needle shaped crystals. Chapter 3 yielded different batches of both shapes to examine in the drop-weight, and additionally a mixed morphology batch. The twinned crystals will also be characterised in this section.

Continuing the discussion from the previous section, the probability of reaction in the LLM-105 needle-shaped batches (105F and 105D) with decreasing particle size demonstrates the same behaviour as the block shaped materials. The blocks increase in probability of a "Go" reaction when the particle size was reduced from 47 μm to 8 μm. The needles also increase in probability of reaction when reduced from 20 μm to 4 μm. However when the blocks were reduced to 1 μm in size, they demonstrated equivalent reactivity to the 4 μm needles and a decrease in probability overall compared to their own morphology.

Both needles and blocks appear to give less light output on the photodiode when particle size is reduced. The previous section established there was a relationship between particle size and the output of a reaction in terms of light intensity (**Table 5C**). The

relationship between particle shape and the reaction occurring is less obvious. The 8 μm blocks (milled LLM-105) and 4 μm needles (105D) have roughly similar probabilities of reaction (80 % and 60 %), however the 47 μm blocks (pristine LLM-105) have a 50 % chance of reacting under impact, and the 20 μm needles (105F) only react in 20 % of experiments. These trends may be related to the aspect ratio of the crystals; the ratio of the crystal length to its width.

The 20 μm needles (105F) have a higher aspect ratio i.e. it is a longer needle than the 4 μm needles (105D) in comparison its width, meaning they are likely to be more susceptible to fracture [144]. As such, it is plausible that such a crystal would require less energy to break under impact, reducing the possibility of generating hot-spots through compression of any defects. However, when the reaction does occur, it does produce an intensity of light that fits into the trend observed with the various particle sizes.

It is therefore possible that if the crystal breaks more readily, there is a different mechanism for the ignition of the hot-spots in the longer crystals, relating to the low probability of reaction observed. This kind of reaction could conceivably be related to friction between fracture edges of broken crystals, rather than adiabatic heating of gas. It is possible that the friction mechanism is a less dominant for hot-spot ignition in LLM-105, as the probability of reaction appears to be lower in this instance. Further evidence could be collected from friction testing the samples.

The gas product ratios identified by the mass spectrometer do not vary significantly between the needles and blocks. What was unusual about the needle batches were the values obtained from the microphone. In some cases these crossed the reaction threshold of 0.4 V to identify a “Go”; something that has not been seen in any of the other modified LLM-105 batches. Although it was by exception, and not entirely repeatable, it could be that there is something different happening in the reaction occurring for the 20 μm needles (105F) and 4 μm needles (105D), though the microphone has been shown to be unreliable to draw conclusions from. It was also noted through the high speed video that the 105F in particular took up to twice as long to produce the characteristic gas burst post-impact. The timescale of build-up and release of this gas burst may be related to the audible characteristics on LLM-105 reactions.

One of the experimental batches, 105E, was a mixture of blocks and needles, with an average particle size of 2 μm. The reaction probability was 60 % chance of “Go”;

comparable with the 4 µm needles; identified by high speed video, photodiode and the mass spectrometer.

However the intensity of the reaction as determined by photodiode had more variation than either the individual needle or block batches of similar particle size. Values ranged between 0.013 V and 0.020 V (**Figure 5.15**), which more closely resembles the intensity of the pristine LLM-105 or 20 µm needles. This variation suggests mixed shapes in a batch are able to both increase the likelihood and intensity of a reaction, compared to a single morphology. There was also one instance of a "Go" reaction identified by microphone, with a measurement of 0.61 V. The microphone "Go" characteristic seems to be more likely to occur in the presence of needle-shaped LLM-105.

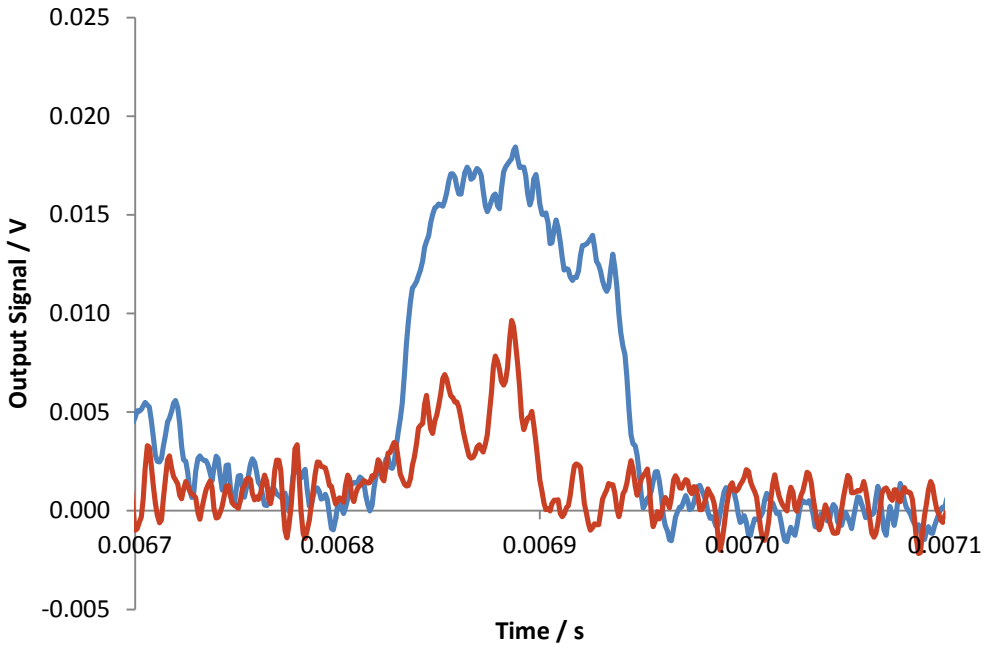

Figure 5.15: The variation seen in photodiode peaks for the mixed morphology LLM-105. The maximum peak values vary between experiments; the data has been intentionally overlaid

Finally, batch 105C, the twinned crystals with an average particle size of 38 µm was tested in the drop-weight. No positive results were obtained for any experiment, with every diagnostic repeatedly establishing a "No go" outcome. The sample was compacted during each test, with no discolouration that may indicate a reaction observed afterwards. A lack of reaction would be unexpected for twinned crystals, as by definition they contain more defects and therefore more credible points of ignition for hot-spots. Friction along

fracture edges would be expected, similar to the process occurring when the needle morphology batches are tested.

Examining the SEM images in Chapter 3 (in particular **Figure 3.11**), the individual components of the twinned crystals are more block-like, than needle-like. It may be that the structures are fragile enough to readily break apart, and the resulting block-like components are less susceptible to friction than a needle crystal of LLM-15 would be. These particles would be useful to develop for further use owing to their low sensitiveness, but the compositions they would produce would generate poor density products owing to low packing efficiency from the irregular shape; this in turn would have a detrimental effect.

5.6 Overall Comparison of Results

An overall summary of all of the experimental data for the glass anvil drop-weight investigation is presented in **Table 5D**. The table compares all of the LLM-105 materials with the HMX and PETN characterised before it in Chapter 4. All factors are considered in this matrix, including outputs from each calibrated diagnostic, the particle size and shape of the material tested, the average sample size and powder density of each batch, and any additional features which are typical of a particular reaction. This table can be used to read across commonalities and differences between the explosives' behaviour under impact.

First, to address the similarities; all of the explosives that were tested and are presented in **Table 5D** produced visible hot-spots of various size and intensity during reaction. Evidence of decomposition was also observable for each material during a reaction, through gaseous reaction products, which were consistently identified by the mass spectrometer. Beyond these aspects, there were different behaviours noted between each of the explosives tested.

Diagnostic		Material									
		PETN	**HMX type A**	**HMX type C**	**Pristine 105**	**Milled 105**	**105C**	**105D**	**105E**	**105F**	**105G**
Camera	Hot-spot number	3 - 6	5 - 10	Cluster	5 - 8	Cluster	N/A	Cluster	Cluster	Cluster	Cluster
	Type of Hot-spots	Bright	Bright	Bright	Dim	Dim	N/A	Dim	Dim	Dim	Dim
	Average Time to Reaction / µs (±8)	260	360	350	300	310	N/A	320	330	560	310
	Length of Reaction / µs (±8)	100 - 130	40 - 60	190 - 220	100 - 130	90 - 110	N/A	110 - 170	150 - 220	20 - 30	30 - 40
Microphone Voltage Peak / V (± 0.01 %)		0.78 - 0.96	0.41 - 0.60	0.45 - 0.56	0.12 - 0.67	0.23 - 0.36	N/A	0.26 - 0.53	0.23 - 0.61	0.29 - 0.45	0.26 - 0.37
Photodiode Voltage Peak / V (± 0.02 %)		1.04 - 1.11	0.44- 0.45	1.90 - 1.98	0.017 - 0.020	0.0096 - 0.0098	N/A	0.0063 - 0.0066	0.013 - 0.020	0.013 - 0.014	N/A
Mass Spec Avg NO:CO_2		1 : 5.7	1 : 2.3	1 : 2.6	1 : 3.4	1 : 3.9	N/A	1 : 3.3	1 : 3.4	1 : 3.0	1 : 3.9
Additional Comments		Melts for 40 - 80 µs. Sample Consum-ed	Some white residue	More residue left than type A. Melting seen once	Gas burst. Yellow/ orange residue	Gas burst. Sample contains orange residue	Sample compact-ed, no orange residue	Gas burst. Yellow/ orange residue. Sample left	Gas burst. Sample contains orange residue	Time delay to gas. Sample contains orange residue	No gas burst. Sample contains orange residue
Probability of Reaction		100 %	100 %	100 %	50 %	80 %	0 %	60 %	60 %	20 %	20 %
Particle Size / µm		N/A	405	4	47	8	38	4	2	20	1
Particle Shape		N/A	Block	Block	Block	Block	Twin	Needle	Block/ needle	Needle	Block
Average Mass of Sample / mg (±0.01)		25.2	26.0	26.2	25.3	24.8	22.1	22.3	26.1	24.7	23.2
Sample Density / g/cm^3		0.63	0.65	0.66	0.63	0.62	0.55	0.56	0.65	0.62	0.58

Table 5D: Summary of data obtained from the drop-weight experiments on all materials tested

The number and type of hot-spots observed in the impact reaction varied between the explosive molecules (i.e. a chemical influence), and the particle size also affected the hot-spot behaviour. HMX type A and the pristine LLM-105 produced a comparable number of initial hot-spots, and the PETN appeared to yield fewer. It is also notable that when the particle size of any material is 20 μm or less (i.e. HMX type C or LLM-105 other than the pristine batch), individual hot-spots cannot be discerned in the high speed camera footage, and instead a "cluster" effect is seen instead of discrete points. In the case of the HMX type C (4 μm) the intensity of light as interpreted by the photodiode is bright, however for the LLM-105 batches (20 μm or less) the light in these clusters was very dim, and was initially difficult to detect. It is likely that the smaller particle sizes have smaller interspatial and internal voids, making the hot-spots smaller too.

There is a correlation between particle size of the LLM-105 and the light intensity measured by the photodiode; the smaller particle sizes burned dimmer (refer back to **Table 5C**). The opposite effect was observed between the HMX batches analysed, implying the smaller particle size HMX burns hotter than its larger class, but the finer LLM-105 burning reaction gets cooler as particle size decreases. There is a difference of approximately 70 °C in decomposition temperature of HMX and LLM-105; LLM-105 decomposes at approximately 350-360 °C and HMX is around 280 °C; therefore the LLM-105 requires more energy than HMX to propagate reaction. In the smaller particle sizes of LLM-105, it is also likely that there would be fewer and smaller defects and voids as noted above. The fewer sites for potential hot-spot initiation, coupled with a higher decomposition temperature than HMX, and its general lower sensitiveness compared to HMX (not a 100 % probability of a "Go") are likely all contributing factors to the contradictory behaviours observed.

There was no obvious relationship between any of the explosives and the length of time from impact to the material reacting, or the overall length of light-emitting reaction. This in part relates to some of the behaviours observed prior to hot-spot ignition. For PETN, a possible melt stage is apparent and in LLM-105 a gas burst can be depicted prior to any light. These unique mannerisms are a feature of the chemical characteristic of each material; all of the LLM-105 batches showed the gas burst, independent of particle size or shape, with the exception of the smallest particle size batch, 105G. It is possible that the particles for this batch were so fine that when a reaction did happen, it was not violent enough to produce anything that could be observed to move particles by the high speed

camera. It was also the only reaction that the photodiode could not obtain any measurement for.

The microphone was able to consistently identify a “Go” reaction above the 0.4 V threshold for both PETN and HMX. However it was very unreliable when used with any of the LLM-105 materials. A reaction correctly interpreted by the microphone was generally by exception, and only occurred in the pristine LLM-105 and batches containing needle morphology. It may be that the characteristic LLM-105 gas burst somehow disperses the audible output of the reaction. It also suggests the behaviour of the reaction in needle-morphology is different to that occurring in the block shaped particles. It could be that a different mechanism for hot-spot ignition dominates in each case, possibly friction in the instance of the needles fracturing and shearing against broken surfaces. More testing under a friction regime would clarify this; however the microphone has not shown to be a reliable diagnostic in this study.

The mass spectrometer is always reliable as an indicator of a reaction. The ratios of NO : CO_2 do not appear to differentiate between physical properties of a particular explosive as the LLM-105 batch ratios are all comparable within error. There is a noticeable difference between the ratios obtained for PETN, both HMX batches and all of the LLM-105 batches as a group. The varying ratio values in this case indicate that the mass spectrometer is able to differentiate between chemical aspects of the explosive, which if applied to a broader range of materials may prove useful as a means of identifying small quantities of an unknown explosive based on its decomposition properties.

For the block morphology LLM-105, the likelihood of reaction occurring increases in the milled material (8 μm), but decreases for the smaller recrystallized particle sizes. However the output of the reaction (light intensity) decreases in the milled LLM-105, and continues to decrease as particle size is reduced. This suggests that the initiation and propagation of reaction is related to the particle size, but the probability of reaction is more related to the number of defects and hence the ignition mechanism.

It is expected that there would be more defects present in milled material compared to recrystallized powder due to the mechanical insult of the milling process. The number of defects is likely to be the reason that it reacts more readily. The literature review captured in Chapter 2 indicates that if there is enough energy to cause ignition of reaction, then the growth of reaction will be greater for smaller particle sizes – under a shock regime. The drop-weight experiment is considered relatively slow speed in terms of impact velocity;

therefore it is not unreasonable that LLM-105 behaves a different way. However these results show that the HMX reaction increases in intensity when the particle size is reduced, which does denote a difference in the properties of LLM-105 and HMX of comparable morphology.

According to the literature, the sensitiveness of explosives to impact (as discussed in Chapter 4, Section 4.1) increases with larger, more angular particles and a higher number of defects present in the material. It is likely from the LLM-105 results that the number of defects present has the highest influence on the materials sensitiveness properties. The pristine LLM-105 typically also contains a very small percentage of impurity from the synthetic route (less than 4 %), which will be removed during both milling and recrystallization; however removal of this impurity is expected to have the same effect chemically on both milled and recrystallized LLM-105.

For the needle shaped LLM-105, the probability of reaction increased as the particle size was reduced; the opposite to the effect seen in the block morphology. However when the actual particle sizes of the batches are compared, the smallest 4 μm needles (105D) with the 8 μm blocks (milled LLM-105), the probability of reaction is comparable, as is the 2 μm block/needle mixture. The intensity of reaction light produced also reduced for the smaller needle particle size, relating to the average powder density of the samples. The weight of each powder sample was taken before impact testing and an average for the batch of material was determined.

The evidence suggests that particle size has a greater effect on the ignition of hotspots than particle shape, but the shape very much alters the packing density (as it may be expected) leading to a greater influence on the growth of reaction. There is generally better packing between crystals if the aspect ratio is closer to 1 i.e. round or block-shaped. Two different particle sizes also increase packing efficiency, which would increase reactivity; this explains why the block/needle mixture that is 2 μm (105E) has a higher density and a higher photodiode measurement, comparable with the 20 μm needles (105F). It could also explain why no reaction was observed in the twinned crystals, which exhibit the lowest density of all of the materials studied.

It was not anticipated that density would have such an influential effect on the burning reactions initiated by drop-weight impact; the literature reviewed in this thesis does however identify that density is important when evaluating shock sensitivity of an explosive, and that both the size and distribution of voids have an effect. It can be

interpreted from these results that a higher density powder (more efficient packing) leads to a smaller void space to heat by adiabatic compression, making it easier for hot-spots to reach a critical temperature and propagate more readily.

In conclusion, the particle size has a greater influence on ignition of hot-spots than particle shape, but the particle shape (which in turn alters the packing efficiency and density) has more of an effect on the propagation of the reaction. Both of these effects are secondary to the influence that defects have on reactivity of explosive powder; where a greater number of defects in the crystal or on the crystal surface will overshadow both particle size and shape effects.

5.7 Summary

This Chapter has presented the application of the experimental techniques developed in Chapter 4 to research materials in order to investigate the behaviour of explosives whilst subjected to impact. In particular, LLM-105 has been studied as a material of interest, and the results from the pristine explosive have been compared with LLM-105 batches that have modified physical characteristics (developed and characterised in Chapter 3).

When compared with conventional explosives such as HMX and PETN, the LLM-105 was less likely to react in the drop-weight with the same experimental configuration, demonstrating an overall lower sensitiveness to impact and as such agreeing with the literature. The output of the LLM-105 reaction was also reduced; the hot-spots yielded during a "Go" were both dimmer and smaller than the other explosives studied, and the photodiode reading produced a lower peak intensity. The mass spectrometer again confirmed the presence of gaseous degradation products; however the unusual feature of a visible gas burst was also captured by the high speed video for LLM-105. The microphone failed to correctly distinguish some of the "Go" reactions in LLM-105, making it the least useful diagnostic technique in this study.

The milled and recrystallized LLM-105 products were examined and it was found that although the particle size does influence the response of an explosive when impacted, the presence of defects (i.e. caused by milling) had a greater effect on ignition sensitiveness. Also, the reaction growth is more strongly linked to the particle shape and overall bulk density of the material; this is due to the packing efficiency of low aspect ratio particles.

The diagnostics and overall drop-weight system that was developed in Chapter 4 were fundamental to the interpretation of the reactions present, and it has allowed for a comparison of particle size and shape effects on an explosive under impact. The microphone performed poorly as an analytical technique; this could inform future decisions for experimental development in explosives characterisation.

Chapter 6: Particle Size Effects on the Shock Sensitivity of LLM-105

The sensitivity and growth of reaction in an explosive is important to understand for both safety and performance reasons. In particular, it allows for more effective design of an initiation train during new material development. In Chapter 1 an overview of detonation theory was given to provide the reader with an introduction; the relevant experimental technique will be discussed in greater detail here. This informs the investigation undertaken to understand the behaviour of formulated LLM-105 under shock loading.

Chapter 2 had previously described the methods used to measure shock sensitivity of an explosive; the data in this Chapter was acquired using a high fidelity technique able to monitor reaction growth – a particle velocity gauge embedded within a sample whilst it is subjected to a shock designed to detonate the material. The embedded particle velocity gauge technique was chosen as the primary diagnostic as it is able to identify run to detonation behaviour in explosives. The data gathered provides in-situ measurements of the reaction growth, and the method is used to compare particle size effects between two LLM-105 formulations.

6.1 Background

The theory of the detonation of an explosive was presented in Chapter 1, to provide context for the body of this thesis. To briefly summarise, a shockwave is a disturbance that moves through a medium faster than the materials sound speed, typically generated by a high velocity impact. As previously mentioned, the Hugoniot allows for a materials shock parameters to be determined, assuming the material behaves hydrodynamically. Most materials under the experimental conditions described in this Chapter will behave approximately hydrodynamically as the pressure from the shock significantly exceeds the material strength.

When a shock is applied to a material as an initial pulse, deformation can occur elastically (reversibly), or plastically (irreversibly) once the elastic limit of the material has been exceeded. The propagation of the input shockwave described in this Chapter will be

treated as plastic in nature, transitioning instantaneously between initial and reactive states, allowing the Rankine-Hugoniot conservation equations (described in Chapter 1 and re-iterated below) to be applied;

$$\rho_0 U = \rho_1 (U - u_p),$$

$$P_1 - P_0 = \rho_0 U u_p ,$$

$$E_1 - E_0 = \frac{1}{2} u_1^2 \left(\frac{P_1 + P_0}{P_1 - P_0}\right)$$

For the shockwave to be considered a detonation there has to be an irreversible exothermic chemical reaction occurring within the material, releasing energy and reaction products. As noted in Chapter 1, this energy is released over a very short timescale, with the reaction zone occurring just behind the shock front. The difference between a shockwave and a detonation wave is this chemical energy; however as detonation is a shockwave, the Rankine-Hugoniot relationships apply. As internal chemical energy is released, it adds to the strength of the wave, inducing a self-sustaining shock front. Steady state detonation is achieved when the energy lost to heat and expanding gas is in equilibrium with the energy generated at the shock front, and the wave is stable and self-sustaining.

Chapter 1 also described the use of a flyer to input a one dimensional shock into a material to experimentally characterise its shock response (or achieve detonation). Here in Chapter 6, the flyer used to shock load the explosive is driven by a gas gun in what is known as a plate impact experiment. High pressure gas from a compressed tank is used to drive the flyer which is mounted on a sabot down a smooth bore barrel and into the explosive target.

To conduct a plate impact experiment using a gas gun, the target is mounted onto an extension of the barrel so that it can be aligned with its surface parallel to the flyer to ensure a one dimensional shock input. The entire target assembly is contained in a vacuum chamber, preventing damage to the equipment from pressure generated during a reaction from the impacted material. A basic schematic of a gas gun is shown in **Figure 6.1**.

When the target is impacted by the flyer, there is a shock that travels into the target from the point of impact, and there is a reflected shock transmitted back through the flyer. When the opposing shock reaches the back of the flyer the pressure is partly released and a

rarefaction wave is reflected, travelling back through the flyer towards the target. The rarefaction will then propagate into the target, attenuating the shock, potentially disrupting the shock to detonation process. The timescale of this effect is such that the diagnostics employed to characterise shock response will already have taken the required measurements. As such, rarefactions are not an issue in this study, as the experiments have been carefully designed to avoid release waves reaching the experiment prior to completion of the data acquisition phase.

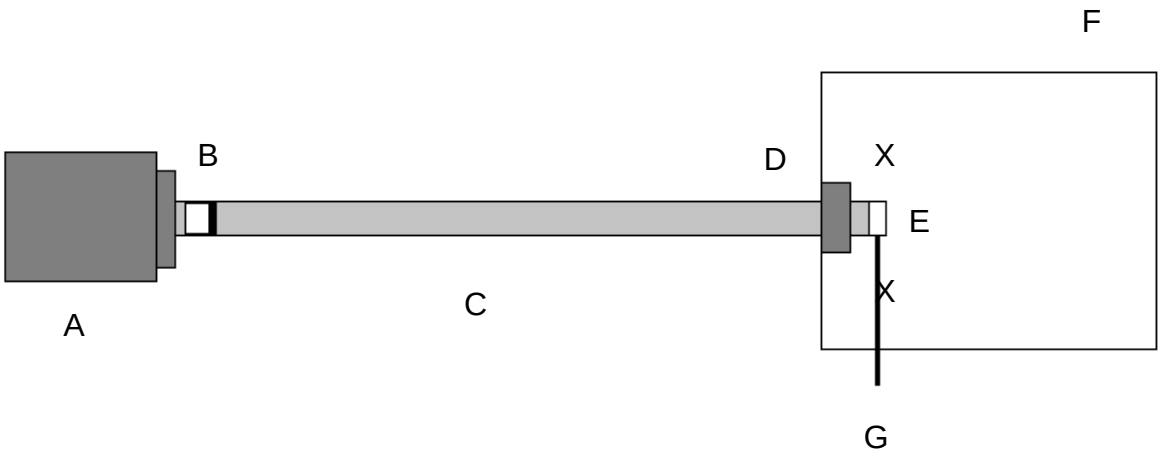

Figure 6.1: Diagram of a gas gun set up to run a plate impact experiment (not to scale). A flyer mounted on a sabot (B) is driven by high pressure gas pumped into the breech (A), which is released via a bursting disc mechanism before traveling down the barrel (C – not representative scale) to impact the target (E) mounted such that a one dimensional shock is put into the sample. The velocity of the flyer is determined (D) and the diagnostics cabling (G) for the target gauge is fed through the target chamber (F). Magnets for use with the gauge diagnostic, to be discussed later, are positioned at the two X points

In Chapter 1, the initiation of an explosive with respect to hot-spot theory was discussed. The adiabatic compression of trapped gases within voids of the material leads to an accelerating and self-sustaining reaction culminating in detonation. The distance over which this acceleration takes place is referred to as the "run to detonation" in an explosive. An explosives sensitivity to shock usually correlates with its density (and hence porosity) owing to this hot-spot mechanism.

The run to detonation in a particular explosive will become shorter with increasing shock input pressure, as well as increasing density. The relationship between the run

distance and shock pressure is linear when plotted on logarithmic axes, and is this graphical representation is known as a Pop plot as noted in Chapter 2.

The gas gun in **Figure 6.1** is known as a single stage gas gun, which is typically able to propel a flyer up to approximately 1 km/s depending on the gas used [145]. Reducing the bore size of the barrel in stages (i.e. using a multiple stage gas gun) can produce higher velocities; the two stage gas gun at LANL in the US can accelerate a projectile up to 3 km/s [146]. The advantage of a higher velocity capability is the ability to initiate materials which are not highly sensitive to shock, for example TATB-containing explosives.

6.2 Gauge Diagnostic

A method to assess changes in the target material as it is subjected to shock is required. The most useful diagnostic to track the shock moving through the explosive target is an embedded particle velocity (PV) gauge. The embedded PV gauge moves as the material is shocked and the technique allows an internal view of the reaction as it happens, and provides data on the run to detonation. There are a number of examples in the literature where this method has been shown to provide quantifiable data in the reaction build-up to detonation [146][147][148][149].

The gauge is comprised of a number of metallic elements which move as the shock passes through; when this occurs in an applied magnetic field, a voltage signal is generated as per Faraday's law of induction;

$$V = l\,u\,B$$

Where l is the gauge length, u is the velocity and B is the strength of magnetic field. As the active part of the gauge element moves and crosses magnetic field lines, a voltage is generated (**Figure 6.2**).

The generated voltage can be measured and is proportional to velocity, allowing the particle velocity within the material to be determined at a number of points. It is assumed that the gauge elements move at the same velocity as the material around it. The values of l and B are characterised beforehand. The experiment is typically set up so that the gauge lies in the one dimensional zone of the target; i.e. in the region of the target not affected by release waves post-impact until the relevant measurements have been made.

The release waves move inwards from the edges and back of the target, back towards the impact surface.

The gauge itself is mounted at an angle, embedded within the material. The angled position means that gauge elements are at different depths to the impact face, and also that each element is not shadowed by another, affecting the one dimensional flow of the shock. A thin glue layer sandwiches the gauge in between two target pieces. A typical gauge package material may be aluminium or copper, encased in an insulating material such as Teflon; the insulating material increases the durability of the gauge.

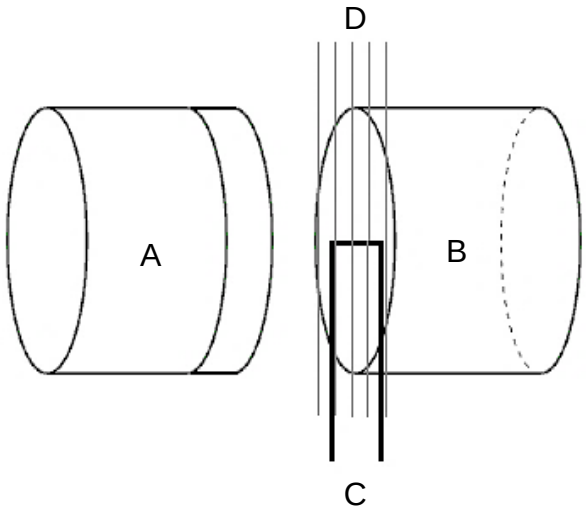

Figure 6.2: The flyer mounted on a sabot (A) impacts the target (B) containing a conductive PV gauge (C), moving horizontally from left to right. The gauge moves in the same horizontal direction, crossing the perpendicular magnetic field (D) and inducing a voltage

An example PV gauge is shown in **Figure 6.3**. The gauge has an array of elements so that multiple voltage readings (analogous to particle velocity) are made in one experiment. The wave-like elements are known as shock trackers, which provide data on the shock arrival for a large number of points within the material. There are three shock trackers on the gauge in **Figure 6.3**.

When the gauge is mounted in the angled position in a reacting target, the shock passes through the material and compresses it, simultaneously accelerating the successive elements of the shock tracker. As the gauges cross the magnetic field, current is induced in each moving element, and (as they are connected) the current is cancelled when pairs of gauges are moving together. This has the effect of producing an oscillating voltage output.

Also, the shock tracker is effectively lengthened the deeper into the sample it is positioned, due to its connected wave-like shape. As the voltage output varies with the gauge length ($V = l\ u\ B$), the readings taken from the shock tracker positioned deeper in the target are higher than the voltage measurements closer to the point of impact.

The voltage recorded by the shock tracker varies with time. The peak voltage points read across to the gauge positions in the target, which can be marked on a distance-time plot to calculate the velocity of the shock in the target material. The shock velocity is determined by the gradient of the line plotted. A change in gradient shows the shock velocity transitioning to detonation velocity within the target material.

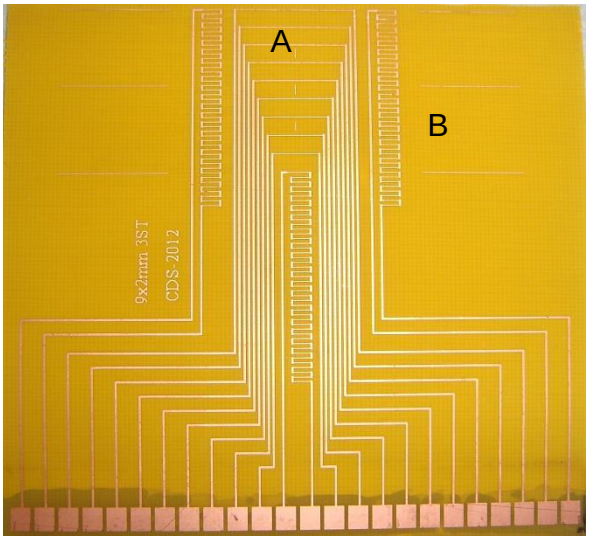

Figure 6.3: A PV gauge used to track particle velocity within a shocked material. Each gauge element (9 in this case - A) produces a voltage signal in the magnetic filed, giving multiple readings for one shock experiment. The wave-like elements (3 on this gauge - B) are shock trackers, which allow the shock velocity and detonation velocity to be determined. There are three shock trackers on this gauge package. The square pads along the bottom of the gauge connect to cabling

The errors in using the gauge technique are generally caused by the assembly of the target material with the gauge, and its mounting position in the experimental equipment. The resulting error creates an inaccuracy in the particle velocity interpreted. The positional error on the 30 degree plane of the material is approximately 0.25 mm, which is doubled to 0.5 mm to account for the error when mounted into the system on the target ring. Additionally, the voltage resolution on the oscilloscope used to interpret the particle

velocity data will introduce an error of ± 8 mV. The overall error on the measurements is estimated to be approximately ± 2 %.

6.3 Formulating and Preparing LLM-105 for Assessment

A formulation comprised of 95 wt. % LLM-105 and 5 wt. % Viton A fluoropolymer was produced, known as Sample A. 500 g of Sample A moulding powder was manufactured using an IKA HKV1 planetary mixer installed at Cranfield University (Shrivenham Campus) using a solvent paste coating method. The binder lacquer was pre-prepared (25g of Viton in 100 ml MEK) and added to 475 g of dry LLM-105 and a further 200 ml of MEK.

The mix was carried out with various stages of inspection during solvent removal, without the addition of water, yielding a damp yellow powder. The powder was spread into trays and dried under vacuum at 60 ˚C overnight. Once dry, a portion of Sample A was removed for hazard testing and the results are shown in **Table 6A**; indicating the formulation is suitably low sensitiveness for pressing into target pieces.

This process was repeated for two more LLM-105 formulations; referred to as Sample B and Sample C. Both are formulated with 5 wt. % Fluorel as the binder, which is chemically equivalent to Viton A, but requires fewer pre-processing steps for the formulator and is hence preferable. Sample A was made to be used as a trial LLM-105 target, as it was uncertain that the gas gun capability available would be able to initiate a LLM-105 formulation to detonation. Sample B uses the same grade of LLM-105 as Sample A (47 µm, as characterised in Chapter 3), and Sample C contains the fine particle size LLM-105 (8 µm). All formulations contain 5 wt. % fluoropolymer binder, which is common to all the samples.

Test	**Result**
Rotter Impact	FoI 59
Spark Sensitiveness	no ignitions at 4.5 J
Mallet Friction	0 % all surfaces
Temperature of Ignition	325 ˚C
Ease of ignition	no ignitions
Train	ignites and supports train steadily
Vacuum Stability	0.3 ml - satisfactory

Table 6A: Hazard data for Sample A indicating suitably low enough sensitiveness for pressing

In order to generate samples for the plate impact studies, new tooling had to be designed and manufactured. There are currently no available facilities for isostatic pressing small enough quantities of research material. To remove the requirement for subsequent machining into wedges (and wasting further material) it was decided that the tooling could be designed to press two different wedges using shaped inserts, and these would fit together with a 30º angle for the gauge to sit in.

New tooling allowed for the samples to be manufactured in a uniaxial press, which is suitable for small quantities of material and produces reproducible samples with respect to density, once the loading conditions have been experimentally determined. The samples were designed to be 50 mm diameter by 25 mm high, aligning with experimental techniques used at LANL in the US, and therefore potentially allowing comparison of data.

The press tool (**Figure 6.4**) was fitted with a shim to enable double end pressing and no tamping of the powder was required. The tool was placed in a heater jacket at 90 ˚C and pressed using a conventional uniaxial press under a loading of fifty tons. The temperature was increased during pressing to aid the flow of the binder and allow it to distribute evenly around the compact. The temperature was reduced to 25 ˚C to eject the pellet once pressed; there was no evidence of any pitting or staining on any of the samples.

Non cylindrical explosive components are unsafe to produce in a uniaxial die tool as the press tool could pinch material in regions of sharp metal-to-metal contact introducing a hazard to the process; therefore an additional lip was pressed onto the top target piece (**Figure 6.5**), which could later be removed via skimming after the gauge was glued in place.

The wedges were characterised for density using an Archimedes immersion method. The bottom wedge was also characterised using a drop height gauge and placed into a target assembly jig. The angled surface of the wedge had a uniform layer of Baycol adhesive applied (chosen for its compatibility with other explosive compositions), and the gauge pack was positioned using alignment lines provided on the gauge. Realignment of the gauge pack was necessary if any slippage on the wedge face occurred. The jig was mounted in a clamp stand with a weight to ensure intimate contact between the gauge pack and the explosive, and left to cure for twenty four hours. The top wedge was glued onto the other side of the gauge using the same method, resulting in the component shown in **Figure 6.6**.

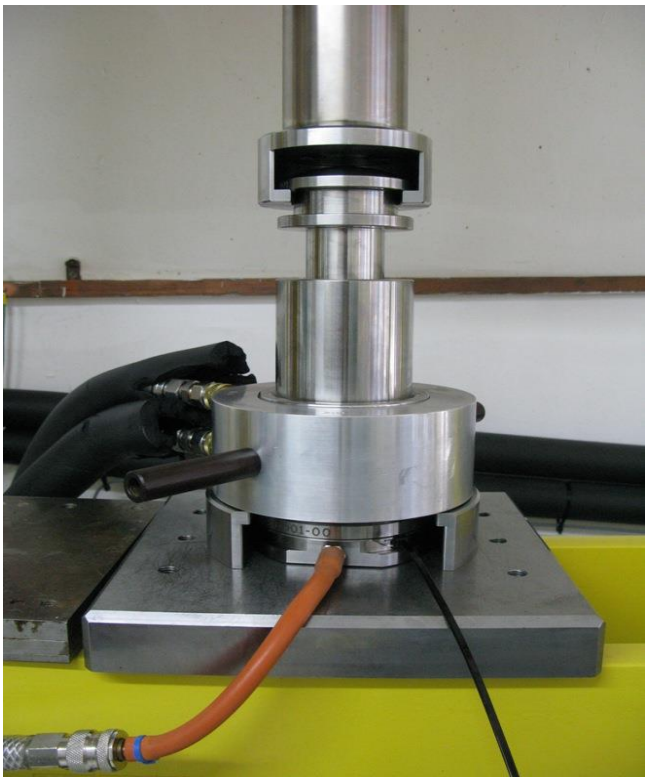

Figure 6.4: The wedge pellet press tool mounted in a uniaxial press. The tool requires a heating jacket and is evacuated in situ with the pressing process

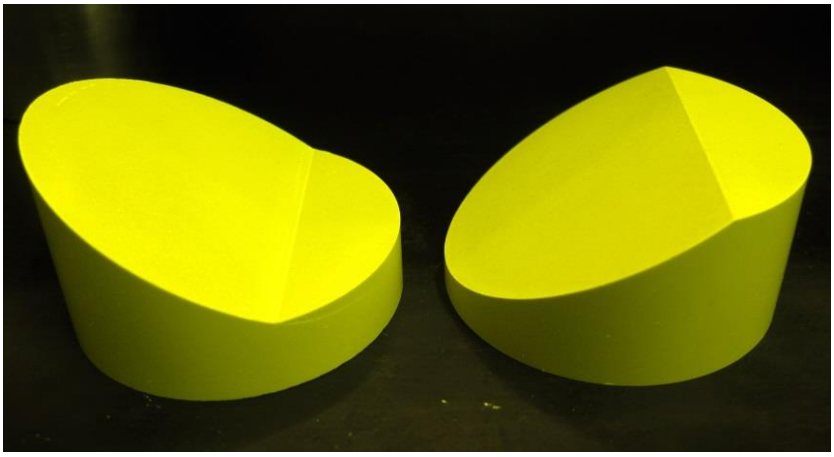

Figure 6.5: Explosive wedge pellets pressed to form the top (left) and bottom (right) of a target assembly. The gauge pack is glued in between the two on the angled plane and the top ledge of the left pellet is skimmed flat later

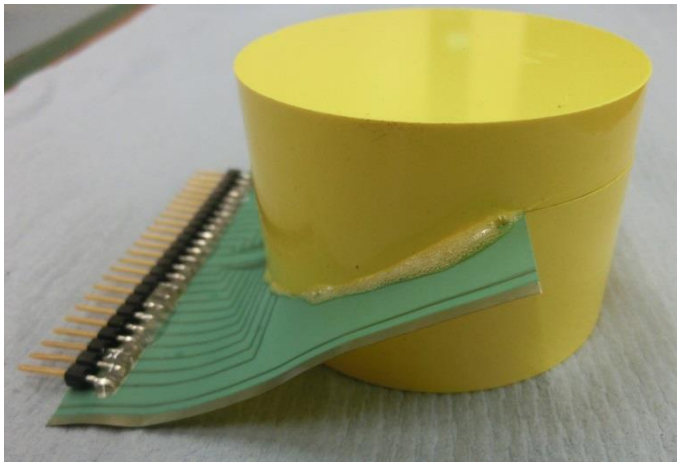

Figure 6.6: The gauge pack glued into the LLM-105 target wedges. Note excess adhesive has been extruded out of the side of the explosive by the weight and vice used in the assembly procedure. This ensures a smooth interface between the explosive and the gauge array. A top ledge on the right side of the target assembly is present as part of a production aid for the explosive samples

As can be seen in **Figure 6.6**, a large ledge sits over the starting edge of the gauge pack. The ledge has to be present for the production of the wedges, but has to be removed prior to any gas gun experiments. The target was skimmed using a remotely controlled fly cutter, leaving a flat surface (characterised by drop height gauge again) which lay around 0.2 mm below the original bottom wedge surface, exposing the edge of the gauge package (see **Figure 6.7**).

The final stage of target assembly involved gluing the explosive to an aluminium target ring. The target ring is later fixed to a barrel extension in the gas gun and ensures that the explosive and gauge are correctly placed for the experiment.

Two target assemblies of Sample B were produced in order to assess the reproducibility of the experimental parameters, and baseline the unmodified LLM-105. A summary of the target assemblies manufactured for firing are summarised in **Table 6B**.

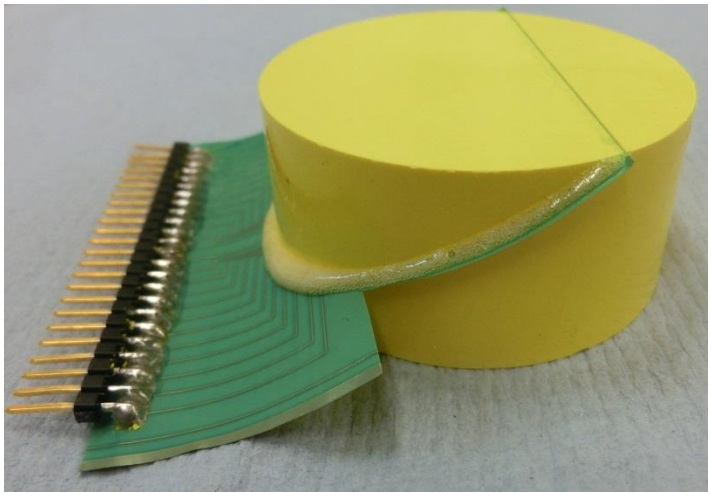

Figure 6.7: Skimmed LLM-105 target with a trimmed gauge pack ready for gluing into a target ring. As in Figure 6.6, excess adhesive has been extruded out of the side of the explosive by the weight and vice used in the assembly procedure

Sample	Density / g/cm^3	Density / % of theoretical maximum	Binder	LLM-105 Particle Size / μm	LLM-105: Binder Ratio
A	1.800	94.3	Viton	47	95:5
B1	1.811	94.8	Fluorel	47	95:5
B2	1.815	95.0	Fluorel	47	95:5
C	1.806	94.6	Fluorel	8	95:5

Table 6B: Summary of LLM-105 target assemblies produced for assessment

6.4 Experimental Configuration

The aim of the experiments is to be able to directly compare the run to detonation behaviour in different particle sizes of LLM-105. The Cranfield University 50 mm bore single stage "Blue Gun" was used as the gas gun for these experiments, as the target chamber is designed to accommodate the pressure increase from the explosive sample detonation. It uses a mixture of helium and air to drive the sabot, and a bursting disk mechanism so that at a pressure of 300 bar, a projectile approximately 300 g in mass will be accelerated up to 1 km/s. The whole gun system is evacuated to a pressure of 12 mbar prior to firing, and the explosive limit (to prevent damage from the release of the

expanding gaseous detonation products) is 160 g. The targets used for this work were made from 90 g of explosive.

The bursting disk assembly works with three gas reservoirs, separated by two perforated aluminium discs, which are designed to give at a certain pressure. The breech of the gun is filled with air/helium to a desired pressure (350 bar in this case), and the middle gas reservoir is filled to approximately half this value (175 bar). The middle reservoir is then rapidly evacuated resulting in over pressurisation and subsequent failure of the disks very quickly in succession. The gas is released at high pressure to the gun barrel, to drive the sabot towards the target at speed.

The sabot was made from Acetal, and a 10 mm thick Sintox FA Ballistic aluminium oxide ceramic flyer was mounted on the face using epoxy. Sintox was chosen as it is a high impedance material, and a metallic flyer would not be suitable as it would interfere with the magnetic field. The PV gauges used were provided by Cranfield University (Shrivenham), originally purchased from Quickcircuits; and are pictured in **Figure 6.3**; and are made from 35 μm copper and a 25 μm polyimide insulating layer, with a 5 μm top layer. There are nine gauge elements monitoring particle velocity, and three shock trackers. The overall thickness of the gauge and glue layer is estimated to be approximately 90 μm. Each gauge was checked for continuity with a voltmeter prior to target assembly.

To connect the gauge elements to the diagnostics system, PCB connectors were used and cables were soldered in place on the gauge pack. The cabling was connected to an oscilloscope (Agilent Acqiris DC270) in order to record the voltages induced in the gauge elements via motion through the magnetic field. The resistance of the cables and scope were captured so that a correction could be made to adjust the measured voltage of the gauge, accounting for resistance in the diagnostic circuit.

Another oscilloscope (Tektronics TDS 5104) was used to measure the velocity of the projectile using the infra-red light gate system fitted to the gun. The field strength and homogeneity of the magnetic field in the target chamber was measured prior to insertion of the target assembly, and was found to be 193 mT. Finally, aluminium rods were used to hold the target assembly onto the barrel extension in a backmount system, see **Figure 6.8**.

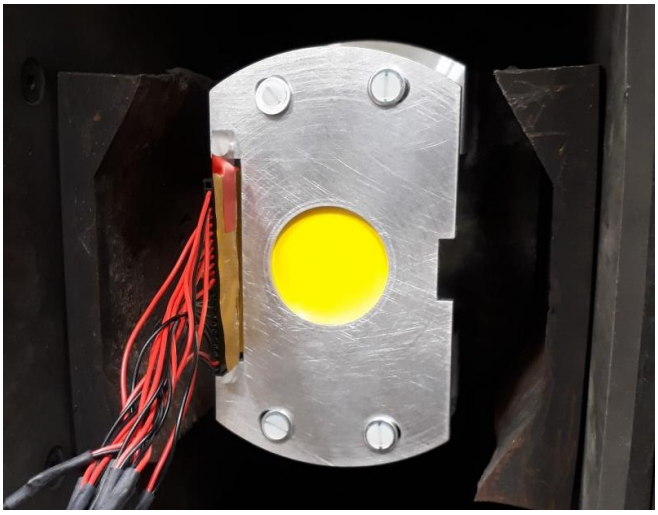

Figure 6.8: The full target assembly mounted in the gas gun. The explosive is glued onto an aluminium target ring which is held onto the gun barrel extension with aluminium rods. The gauge pack can be seen to the left of the target ring, attached to cables leading to an oscilloscope

6.5 Results from Firing

The raw data generated form the firing is in the form of time resolved voltages, giving the profile of the particle velocity through the target as it reacts to shock. Using the measured magnetic field and the lengths of the gauge element, it is possible to determine the velocity of the gauge (as per Faraday's Law), and hence the local particle velocity of the material around it. For the shock trackers, the time between the voltage peaks in the data can be plotted against the position of the tracker in the material to determine both the shock and ensuing detonation velocities.

6.5.1 Preliminary Firing

Sample A, with a density of 1.800 g/cm^3, was fired as a preliminary experiment to determine if the configuration (a 10 mm Sintox flyer at approximately 1 km/s) was appropriate to initiate a detonation in an LLM-105 formulation. The final flyer velocity was 880 m/s and an input pressure of 5.52 GPa was achieved. The entirety of the particle velocity data for all of the gauges are shown in **Figure 6.9**. The shock trackers are the oscillating lines, the gradients of which can be seen to change between gauge 5 and gauge 6 in the pack, at approximately 1.2 μs and 1.4 μs respectively. The change in gradient indicates an increase in velocity around this point, which infers the transition to detonation

in the explosive. The time intervals between each of the nine gauges decrease simultaneously as the gradient of the shock trackers change, correlating with the increase in velocity.

To derive the input shock velocity and detonation velocity of Sample A, the time interval of the shock tracker peaks (shown in full in **Figure 6.10**) can be plotted against the gauge distance embedded in the target as per **Figure 6.11**. The intercept gives the point of detonation, and hence the run distance to detonation in the material. For Sample A the detonation velocity was calculated to be 7.12 ± 0.14 mm/μs and the run distance was 5.90 ± 0.12 mm, which are reasonable values compared to a formulated explosive such as HMX [150]. Inspection of the target chamber post firing confirmed that the target had been consumed and detonation had been successful.

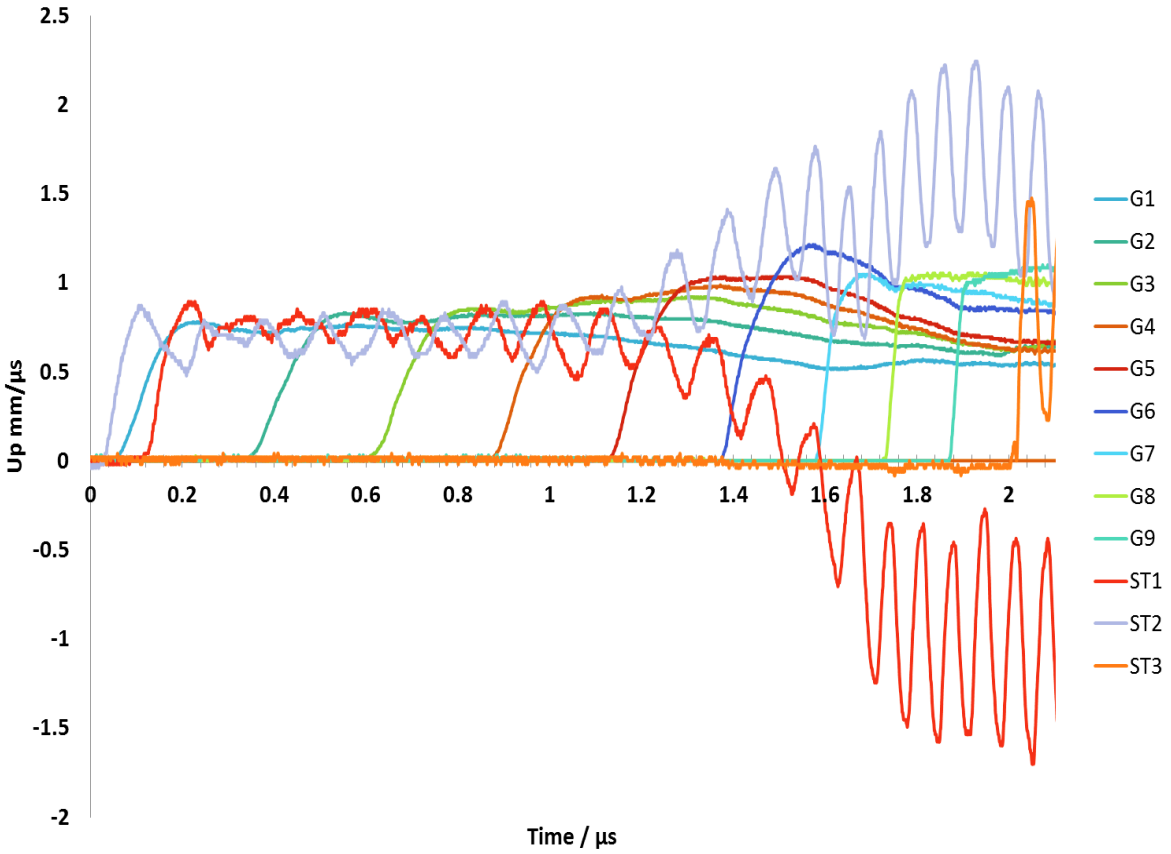

Figure 6.9: Experimental results from firing Sample A with an embedded PV gauge pack. The oscillating lines are the shock trackers, indicating a change in velocity between gauge 5 and gauge 6 in the pack at approximately 1.2 μs and 1.4 μs respectively. The particle velocity increases towards detonation in all of the gauges, simultaneously as the time interval between each gauge element decreases

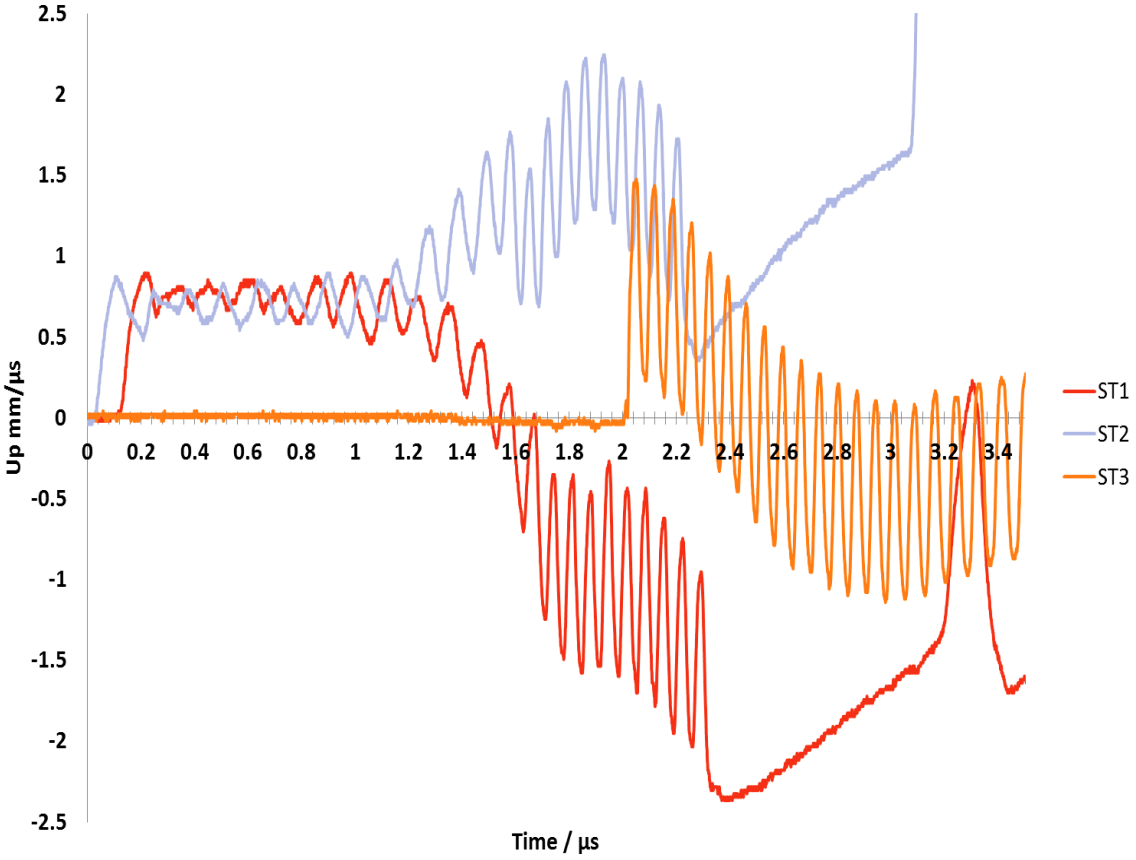

Figure 6.10: The raw data generated by the shock trackers in Sample A. The time interval of the shock tracker peaks can be plotted against the gauge distance embedded in the target to derive the input shock velocity and detonation velocity

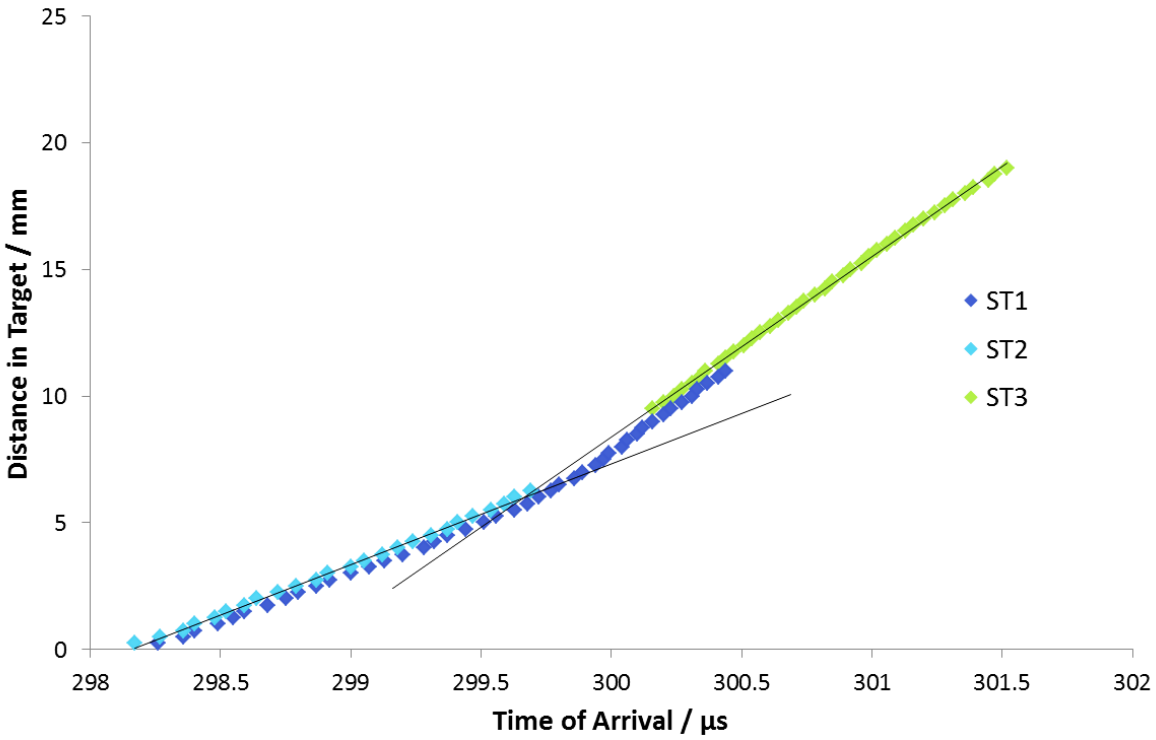

Figure 6.11: A plot of each element of the shock trackers' time against their position in the target. The gradients of the lines give the input shock velocity and then the detonation velocity. The intercept of the two lines give the detonation point, and hence the run to detonation distance of the material. The detonation velocity was calculated to be 7.12 mm/µs and the run distance was 5.90 mm

A run distance of 5.90 mm confirms that the turnover to detonation occurred just before gauge 6. A detailed examination of the gauge traces can be made using **Figure 6.12** which represents each of the nine gauge elements. It can be seen that the time intervals between the gauges become shorter indicating acceleration of the velocity consistent with a reaction build up to detonation. As the wave passes through the formulation, hot-spot sites such as voids or defects are initiated as discussed in Chapter 1, leading to the occurrence of a chemical reaction in the explosive. This reaction contributes to the increase in particle and shock velocity until detonation is achieved. The time intervals between gauge activation are at their narrowest after gauge 6, past the turnover to detonation.

The evidence of reactive growth is furthered by the increasing particle velocity as the shock passes through the target. The peak reaches a maximum at gauge 6, where

detonation has been achieved. What is unusual about the trace is that the particle velocity then decreases, where it would be expected to remain constant or increase owing to the material response to detonation. It is hypothesized that the gauge material was a poor impedance match for the detonated explosive, or delamination of the adhesive occurred post-detonation, skewing the measurements taken. Compared with results of a similar experiment using a HMX PBX, the peaks of the particle velocity traces are more rounded, and shorter [147], the effect of which could also be as a result of a non-ideal gauge pack material.

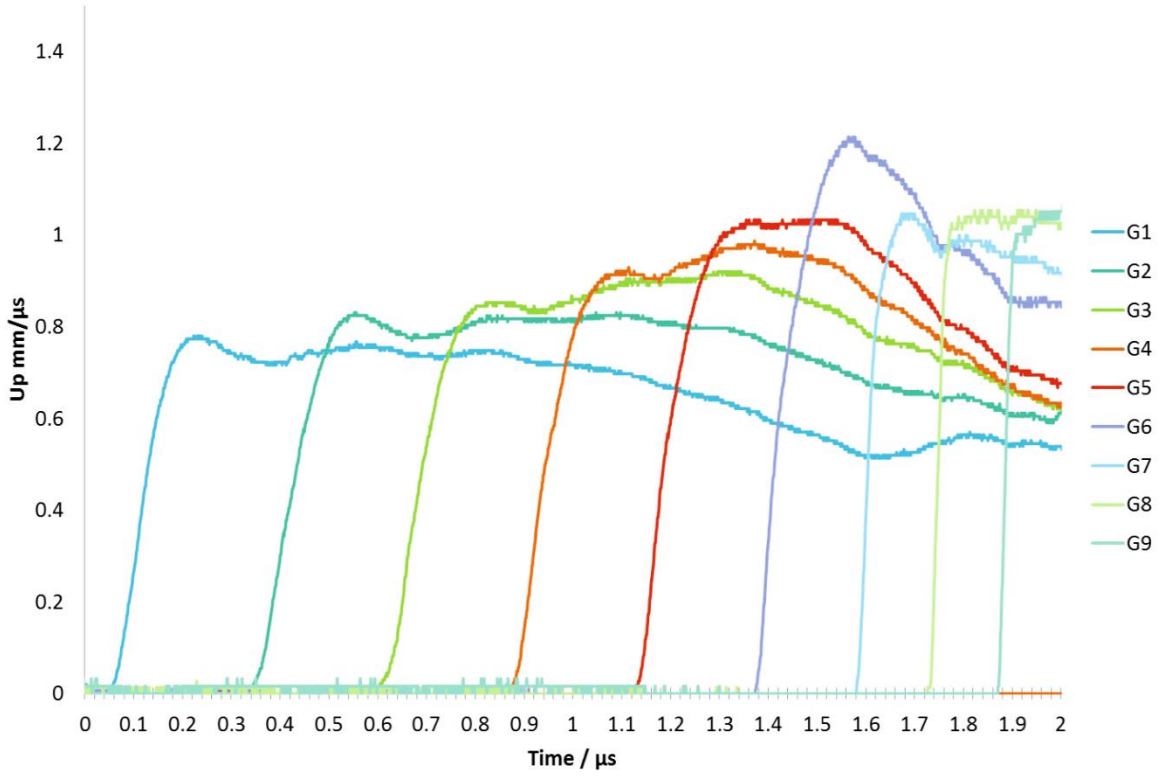

Figure 6.12: The particle velocity trace for each of the nine gauges in the Sample A target. As reactive growth accelerates towards detonation, the time intervals between gauge activation shorten and the particle velocity increases. The rounded peaks and decrease in particle velocity are attributed to impedance from the gauge affecting the results

It is suggested that the gauge pack had an impedance effect on the shock; i.e. its position in the explosive disrupted the shock wave. Though the gauge packs are mounted at an angle to prevent the cumulative effect of multiple gauges perturbing the one

dimensional shock, the presence of it could still have an effect as a single gauge point. Higher accuracy of results is achieved by making the gauge pack and glue layers very thin, and choosing gauge pack materials that have a comparable acoustic impedance match with the target material. Aluminium/Teflon gauge packs have a better acoustic impedance match with explosive targets (owing to a better matched density) than the copper/polyimide gauge packs used for this experiment, however they were not available at the start of this work and are significantly higher cost per experiment.

Despite the limitations the gauge packs put on the results (accurate readings of particle velocity post-detonation), they are still suitable for these experiments. The activation time of the gauges and the acceleration of reaction growth are the key focus areas; and a detonation velocity and run distance can be successfully established using the shock trackers. These aspects allow for an effective comparison of different formulations pre-detonation behaviour under the same experimental configuration. Improvements to the gauge packs are beyond the current scope of the thesis and can form part of a future research investigation. As such, this method is appropriate for the assessment of the LLM-105 target assemblies.

6.5.2 LLM-105 Firings

As the method described in the previous section was proven to generate suitable data for Sample A, the experiment was repeated with Sample B1 (same particle size of LLM-105, 47 μm, with the Fluorel binder) at a density of 1.811 g/cm^3. The aim of this experiment is to generate a baseline to compare the fine particle size of LLM-105 with. The raw data from the shock trackers is shown in **Figure 6.13**, with the analysis presented in **Figure 6.14**.

The shock trackers showed that the detonation velocity and run distance in Sample B1 are 7.62 ± 0.15 mm/μs and 7.26 ± 0.15 ± 0.15 mm respectively. The nine PV gauge traces for Sample B1 are shown in **Figure 6.15**. The PV gauge traces (as shown in **Figure 6.15**) correlate with the run distance to detonation estimated by the shock trackers at 7.26 mm, as the highest peak is at gauge 8 (8 mm into the material).

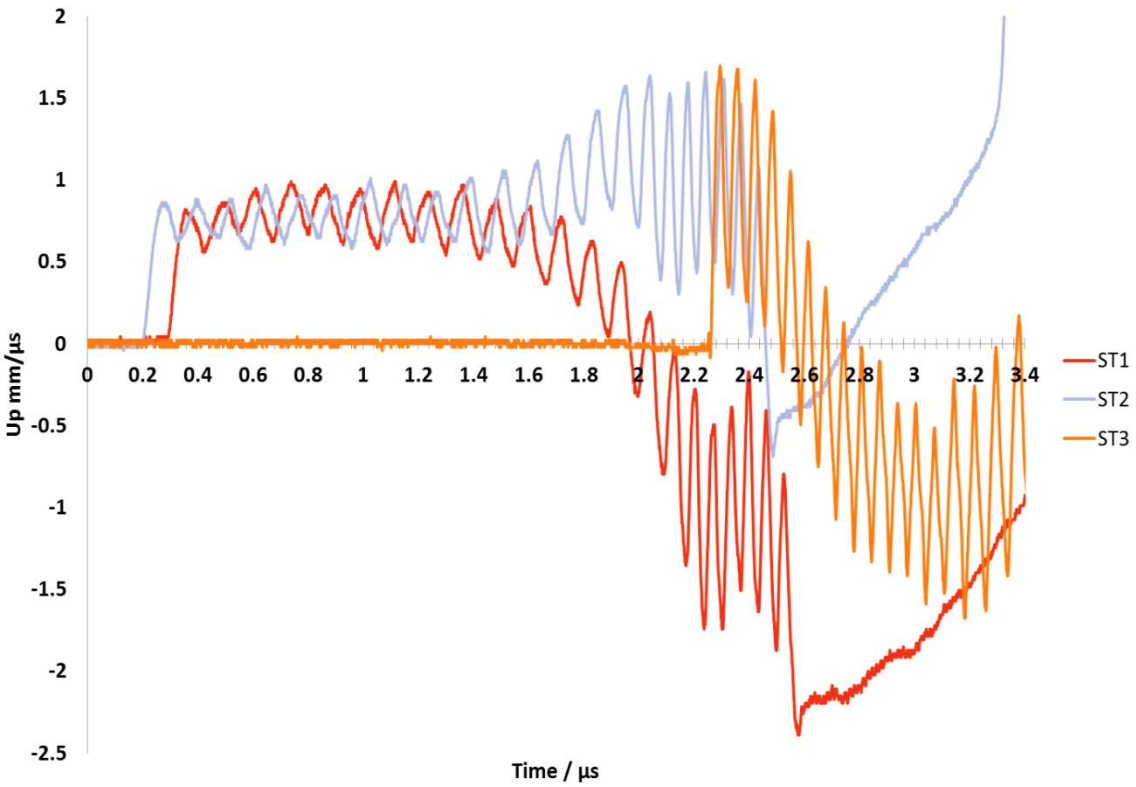

Figure 6.13: The raw data generated by the shock trackers in Sample B1

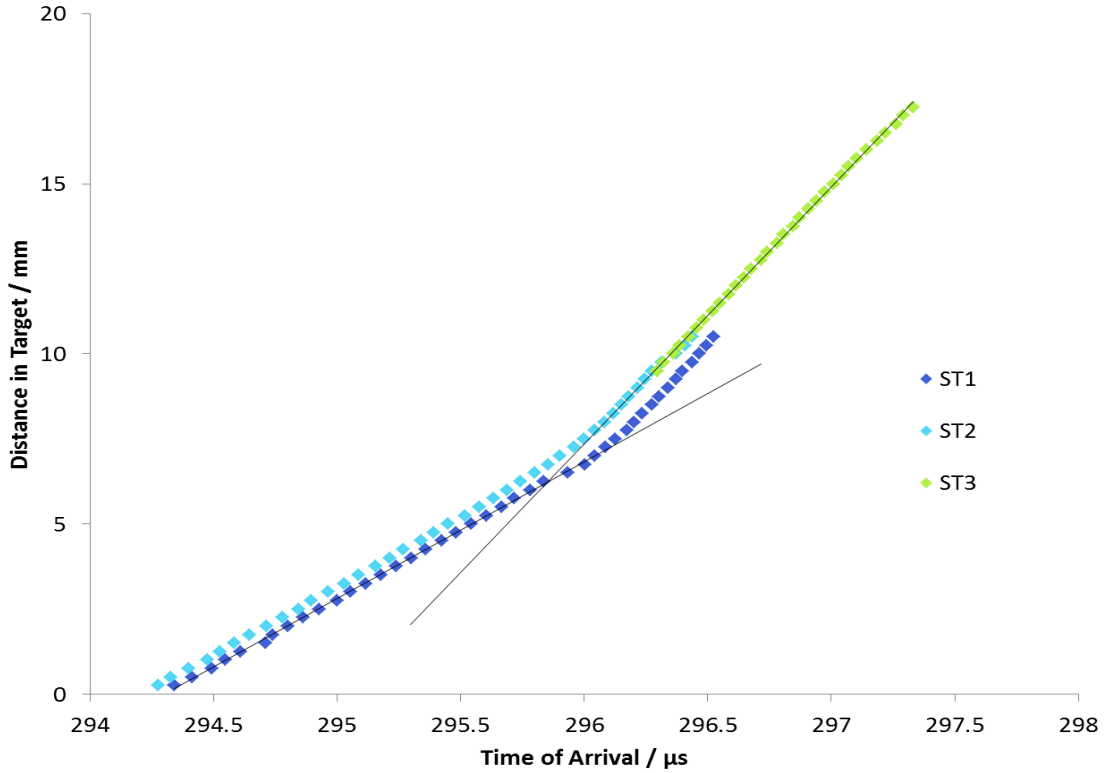

Figure 6.14: A plot of the shock trackers' time against their position in the Sample B1 target

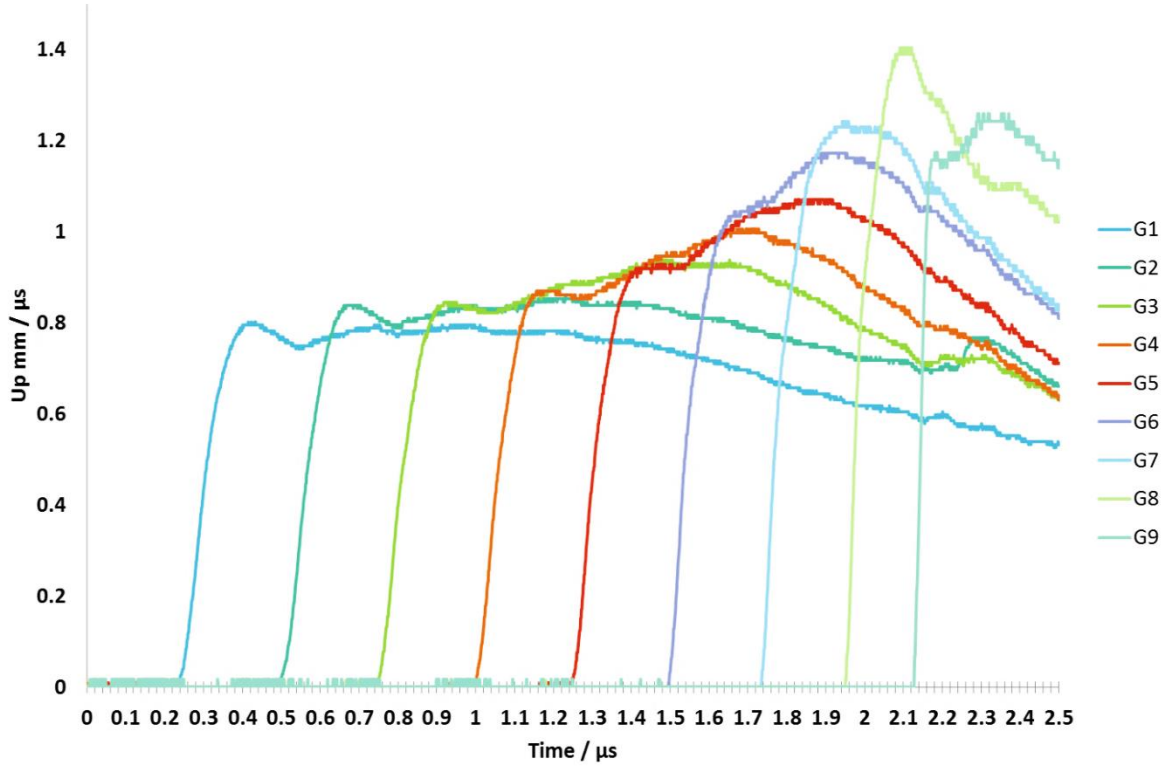

Figure 6.15: The particle velocity trace for the nine gauges within the Sample B1 target. The highest peak at gauge 8 corroborates the run distance estimate of 7.26 mm from the shock trackers. As previously noted in Sample A, the particle velocity values are low and the peaks have not fully resolved into spikes that would be expected to be seen for detonation, but the growth and acceleration of reaction can clearly be observed as time intervals narrow between gauges

The experiment with Sample B1 was repeated at a slightly higher flyer velocity for Sample B2 to investigate the effect of detonation behaviour from a higher input pressure; however the gauge yielded poor results (**Figure 6.16**). A detonation was achieved (noted via inspection of the chamber after firing), but it appears that the gauge failed, possibly due to delamination from the material after impact from the flyer. This experiment was conducted at a higher velocity, and it is suggested that this could be the cause; a higher input shock pressure caused sample and gauge separation. The readings taken from the gauge imply that the gauge was not fully in contact with the target material; gauge failure then occurred around 2.1 µs. There was no further material to repeat this experiment again.

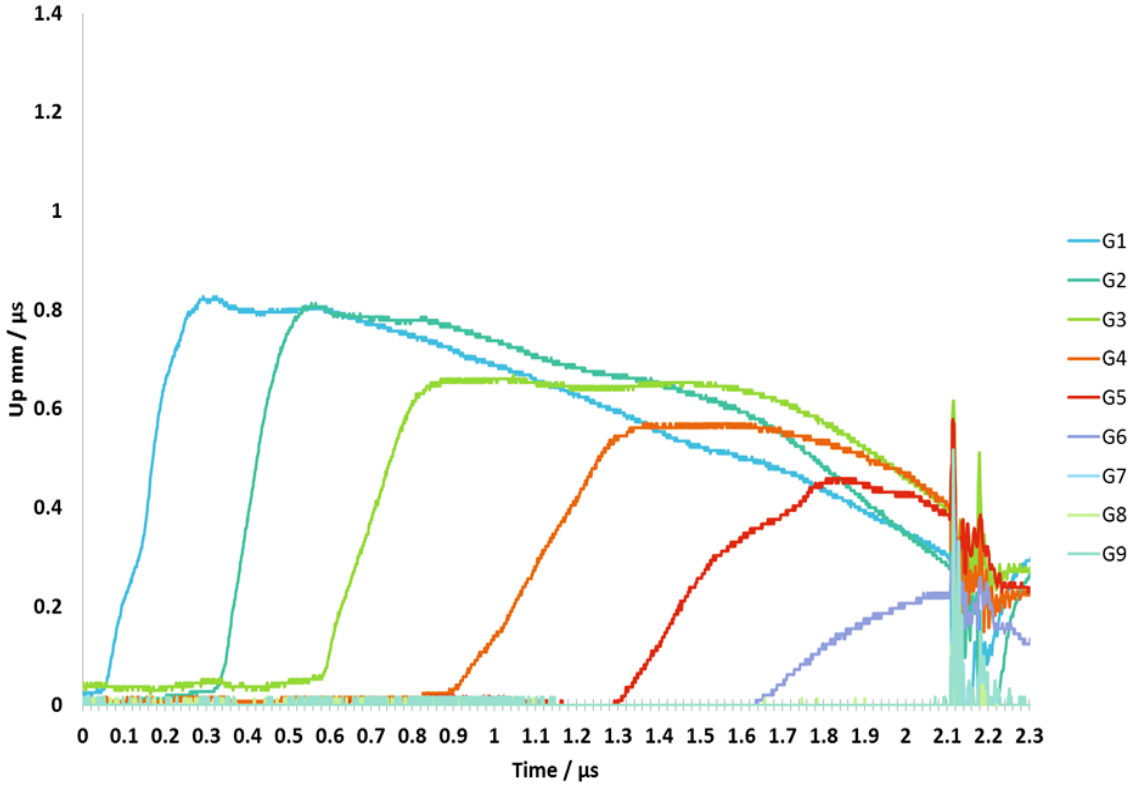

Figure 6.16: Repeat of Sample B1 firing at a higher flyer velocity for Sample B2. The gauge pack failed and no usable measurements were taken; these traces show no trend of reaction growth. The shock trackers could not be resolved

Sample C (containing a finer particle size of LLM-105) was fired last under the same conditions as Sample A and Sample B1, at a density of 1.806 g/cm^3. In this instance the second shock tracker on the gauge pack failed, but the first and third were still able to produce a detonation velocity and run distance (**Figure 6.17**), which were 7.62 ± 0.15 mm/µs and 3.51 ± 0.07 mm. The trace of the first shock tracker also shows an unusual step at the transition to detonation; which potentially results in early estimation of the run distance via the gradient intercept method.

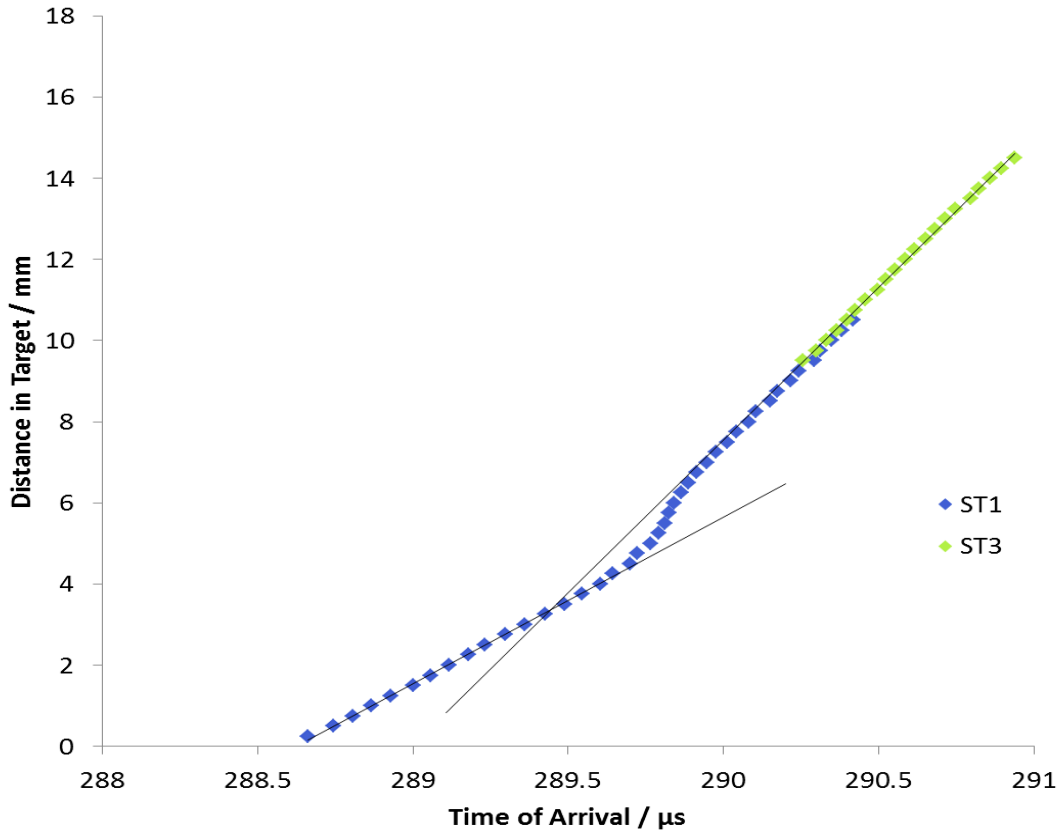

Figure 6.17: The shock tracker traces from Sample C; the second tracker gauge failed. There is an unusual step with two gradients in the first shock tracker at the detonation transition point. There appears to be an increase in shock velocity before settling into the final detonation velocity as matched by the third shock tracker

The nine gauge traces from Sample C can be seen in **Figure 6.18**. The turnover to detonation does occur between gauge 3 and 4, as denoted by the highest peak at gauge 4. This makes the run distance estimated by the shock trackers reasonable without the second shock tracker to confirm the placement. Gauges 6 through to 9 appear to contain a lot of noise and it is possibly because the gauges are not able to perform fast enough to resolve the detonation.

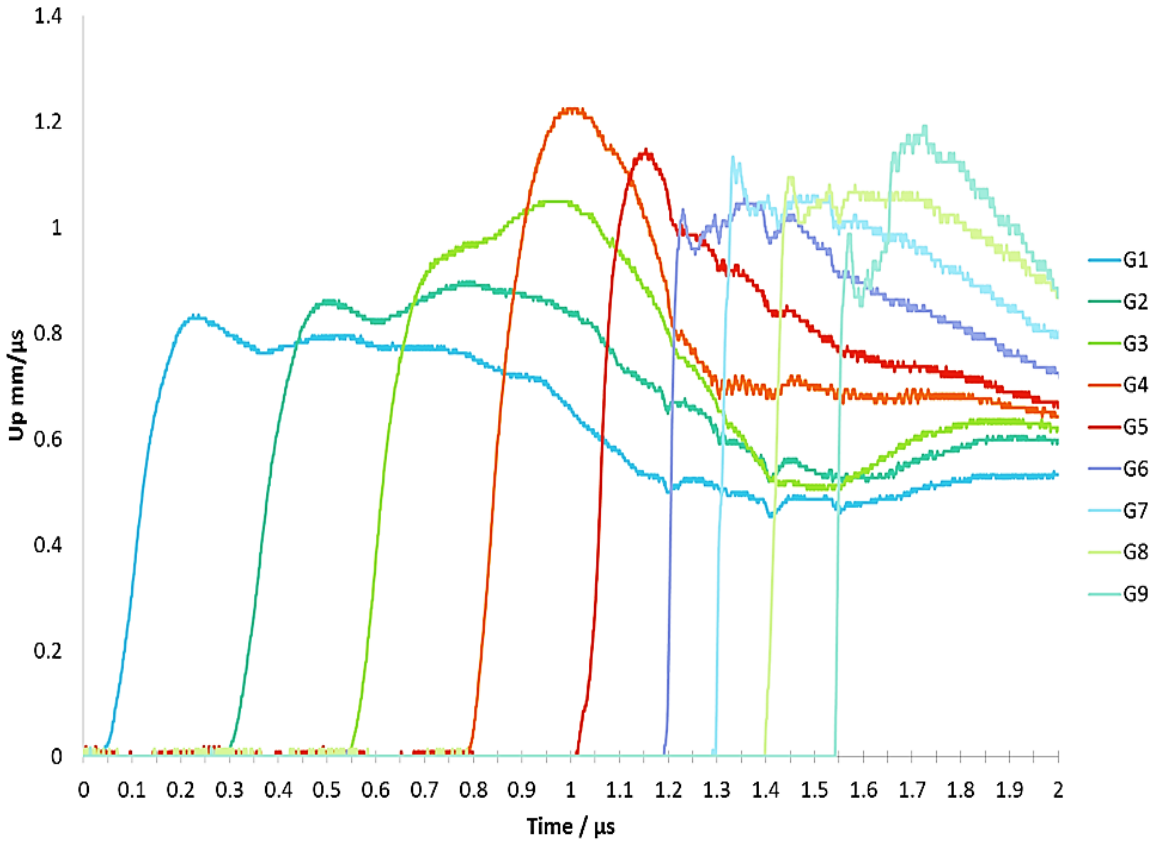

Figure 6.18: The nine gauge traces from CR/4. The transition to detonation occurs between gauge 3 and gauge 4, agreeing with the shock trackers. Past gauge 5, the signals are noisy and it is likely the detonation has disrupted the gauge pack so that the readings are not clearly resolved

6.6 Discussion

The shock trackers in Sample B1 allowed a detonation velocity and run distance to be measured within the material; 7.62 mm/µs and 7.26 mm respectively. These results show a slight improvement in detonation velocity over Sample A (7.12 mm/µs), but this could be attributed to the slightly higher density of Sample B1; detonation velocity is usually proportional to the density of an explosive.

It is interesting that the run distance in Sample B1 increased compared to Sample A (5.90 mm), suggesting a longer build up to reaction and thus a drop in sensitiveness. Both formulations contain a binder of comparable chemical nature and specific gravity, and the same proportion of unmodified LLM-105, so it is unlikely to be related directly to the ingredients. It is possibly because the higher density of the Sample B1 (0.5 % of the

theoretical maximum density higher) has left fewer voids or pores that lead to the hot spot sites. Sample A and Sample B1 would be expected to produce similar results.

The PV gauge traces for Sample B1 (as shown in **Figure 6.15**) correlate with the run distance to detonation estimated by the shock trackers at 7.26 mm, as the highest peak is at gauge 8 (8 mm into the material). The detonation spikes that would be expected to be seen on top of gauge 8 and gauge 9 are poorly resolved, as noted earlier for Sample A; again the poor resolution can be attributed to the gauge materials. However, the build-up of reaction and acceleration towards detonation can clearly be observed between the gauges as the time intervals decrease.

The run distance in Sample C is significantly shorter than for Sample B1 (with the same binder and quantity of LLM-105, but Sample C has a finer particle size), though the final detonation velocities are comparable. This result is to be expected as the detonation velocity is known to relate to density rather than physical nature of the explosive particles. The particle size does have a significant effect on the run to detonation, from 7.26 mm in Sample B1 (47 μm) to 3.51 mm in Sample C (8 μm). The peaks of the PV gauges for both samples have been plotted along the same time axis in **Figure 6.19** to visualise the difference in reaction growth up to the point of detonation.

Figure 6.19 shows how the PV gauge measurements vary between Sample B1 (coarser particle size LLM-105) and Sample C (finer particle size LLM-105) during the run to detonation. The gauge peaks are plotted against the same timescale from the point of the flyer impact in order to compare the reaction growth. The value of the peak particle velocity for both formulations is not being considered owing to the gauges issue with resolving this particular aspect, but it can be seen that the finer particle size encourages a much faster rate of reaction than the coarser LLM-105, accelerating and reaching detonation more quickly.

The published value of run to detonation for LLM-105 at 6.0 GPa is 4.6 mm, though the particle size distribution is not specified (density 1.79 g/cm^3) [151]. The run distance values from the Sample B1 and Sample C firings sit either side of the literature value. However, the observation that finer particles react more quickly is in agreement with the literature captured in Chapter 2 for other explosives such as RDX for comparison.

The results from firing all of the formulations are presented in **Table 6C**. As discussed earlier, the detonation velocities for Sample B1 and Sample C are comparable, but the run distance to detonation is significantly less in Sample C, which has a fine particle size. This is because there is likely to be a larger number of smaller hot-spot sites

for pressed compacts containing smaller particle sizes, which a high pressure shock readily activates. The larger particle size material will most likely contain fewer, larger voids between particles, which are also readily activated, but as they are fewer in number, lead to smaller reaction growth.

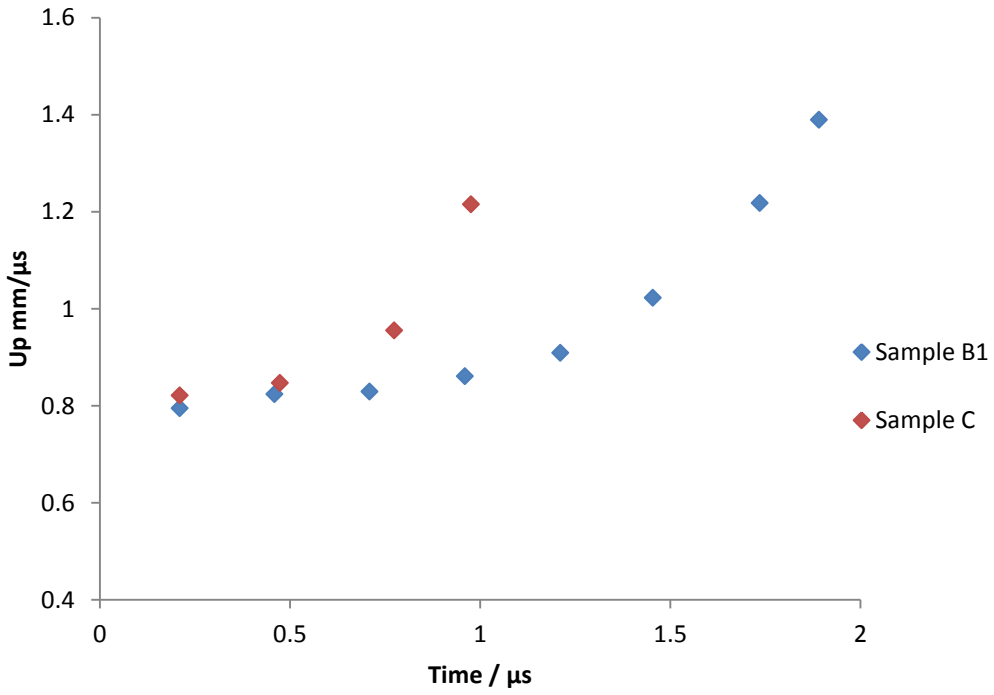

Figure 6.19: The acceleration of reaction in Sample B1 and Sample C as captured by the in-material PV gauges. Sample C contains finer particle size LLM-105 and the reaction growth is significantly faster, which is in agreement with other explosive formulations presented in literature

Sample	Density / g/cm^3	Density / % of theoretical maximum	Flyer Velocity / m/s	Input Pressure / GPa	Run Distance / mm	Velocity of Detonation / mm/µs
A	1.800	94.3	880	5.52	5.90	7.115
B1	1.811	94.8	920	5.95	7.26	7.616
B2	1.815	95.0	1040	6.16	N/A	N/A
C	1.806	94.6	930	6.17	3.51	7.625

Table 6C: The data obtained from the LLM-105 formulation firings. The Sample B2 shot was unsuccessful

6.7 Summary

This Chapter has produced data for two LLM-105 research formulations using a high fidelity characterisation technique to determine detonation velocity and growth of reaction within the explosive. While the resolution of the gauges was poor for determining particle velocity, they were able to demonstrate the acceleration of reaction and turnover to detonation, which was the aim of the research. Improvement to the gauges is recommended for any future work beyond the scope of this thesis.

The fine particle size LLM-105 showed a shorter run distance than the coarse particle size LLM-105, which is likely to be caused by the number of potential hot-spot sites available in voids within the pressed formulation. This increase in voids will lead to faster growth of reaction and a shorter run to the detonation turnover. These results are in keeping with the literature for other conventional explosives, demonstrating that LLM-105 behaves in the same way as RDX or HMX.

Further experiments of this design on LLM-105 formulations would allow a pop-plot to be derived, an example of which is shown below in **Figure 6.20** [152]. This could be considered for future work.

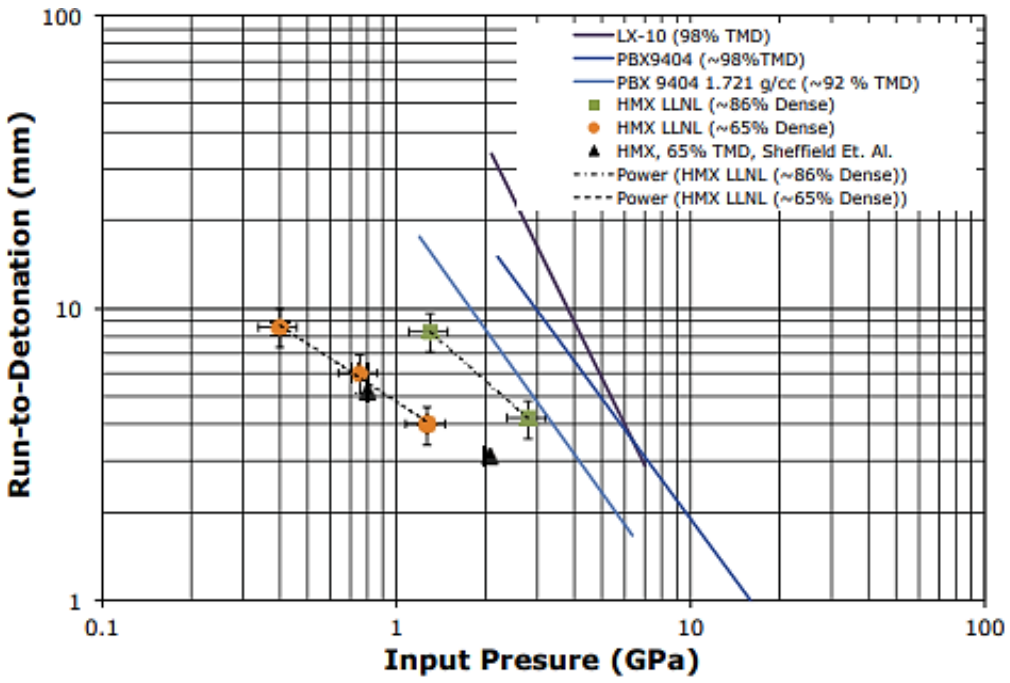

Figure 6.20: Pop-plot of HMX and its formulations at varying densities taken from Reference [152]. It shows the change in run distance to detonation behaviour with pressure

Chapter 7: Conclusions and Further Work

The aim of this thesis was to conduct research on LLM-105 as a new material of interest, for the purpose of developing an understanding of its impact sensitiveness and response under shock conditions. Its sensitiveness with respect to impact is of particular interest as there are numerous standard test methods available, which interpret results in a different way. LLM-105 was modified in its particle size and shape, and the new batches were fully characterised with respect to their physical and chemical nature. The LLM-105 was then investigated for impact sensitiveness using an improved experimental technique and compared with other conventional explosives.

The standard accredited methods available for characterising an explosive's impact sensitiveness were improved with additional and simultaneous diagnostics added to the glass anvil drop-weight. The new diagnostics included a high speed camera, a mass spectrometer, a photodiode and a microphone, where conventionally just a microphone or visual inspection post-impact would be made by the operator. The new equipment proved to be an ideal research tool for developing understanding of material behaviour, and highlighted the limitations of the current standard techniques; especially in relation to the microphone. The microphone proved to be a poor diagnostic for new materials, and this finding will be of great interest to the wider explosives safety community. Quantifiable data was obtained, showing that the techniques incorporated were sensitive enough to differentiate between physical variations in an explosive material, such as particle size and shape.

When compared with conventional explosives such as HMX and PETN, the LLM-105 was less likely to react in the drop-weight with the same experimental configuration, demonstrating an overall lower sensitiveness to impact and as such was consistent with the literature. The output of the LLM-105 reaction was also reduced; the hot-spots produced during a "Go" were both dimmer and smaller than the other explosives studied. The mass spectrometer diagnostic proved to be the most reliable analysis technique used, and the microphone was the least accurate. Again, this finding is valuable for scientists characterising explosive safety or developing assessment methods.

The modified LLM-105 produced in this work was examined and it was found that although the particle size does influence the response of an explosive when impacted, the presence of defects (i.e. caused by milling) had a greater effect overall on ignition sensitiveness. Also, the reaction growth was shown to be more strongly linked to the particle shape and packing density of the material; this is due to the packing efficiency of low aspect ratio particles. The diagnostics and overall drop-weight system that was developed in Chapter 4 were fundamental to the interpretation of the reactions present, and it has allowed for a comparison of particle size and shape effects on an explosive under impact.

It is also of note that LLM-105 is certainly more sensitive to impact than TATB, as shown by comparing the two materials in the glass anvil drop-weight. These direct observations could not have been made without the experimental set-up described in this work. The safety advantage of TATB does not mean that LLM-105 should be disregarded as a promising material for future formulations, but in a ranking, TATB has the lower sensitiveness. The result broadly complies with the literature that suggests LLM-105 "sits between" HMX and TATB in terms of its safety. It would be of interest to understand if the small scale sensitiveness behaviour of LLM-105 powder (i.e. the gas burst) is replicated on larger scales, and this could be the subject of a future investigation.

The final Chapter of this research concentrated on two different particle sizes of LLM-105 which were formulated and characterised using a high fidelity in-material gauge technique. The formulations were fired in the Cranfield University Blue Gas Gun, achieving successful detonation.

The results from the firings showed that the fine particle size LLM-105 has a shorter run distance to detonation than the coarse, which is likely to be caused by the number of potential hot-spot sites available in voids within the pressed formulation. These results agree with the literature prediction (Chapter 2) as a greater number of hot-spot sites will lead to faster growth of reaction and a shorter run to the detonation turnover.

While the resolution of the gauges used was poor for determining particle velocity, they were able to demonstrate the acceleration of reaction and turnover to detonation, which was the aim of the study. Improvement to the gauges is recommended for any future work, prior to any repetition or parameter alteration of the experiments, to obtain the highest quality data.

There are a number of areas from the drop-weight investigation that would be suitable for further research. One aspect would be to further investigate the gas burst effect

as noted above, and assess if it is a hazard when larger samples are used; this could be for both bulk powder and formulated pressed charges. A suitable test might be a small scale spigot [153] or plate and window arrangement at various impact velocities. Measurements such as the thermal conductivity of LLM-105 and its formulation would be useful for interpreting data in trials such as these.

There was also discussion in this thesis regarding potentially different ignition mechanisms for the hot-spots in LLM-105 dependant on the particle shape. It was noted that brittle or long aspect ratio crystals may be more susceptible to ignition by friction in fracture edges. It would therefore be of interest to carry out an investigation on the effect of friction on different particle shapes to provide evidence towards substantiating this theory.

Finally, in some of the drop-weight trials where LLM-105 reacted, an orange discoloured residue was left behind in small quantities. Using the small (around 25 mg quantity) samples on the glass anvil drop-weight did not allow for enough sample to be recovered such that chemical analysis could be conducted. If larger scale trials were to take place, it is likely that more discoloured material would be produced, and enough could potentially be collected to allow for analytical techniques such as NMR to be carried out. This would mean that the molecular structure of the reaction products could be identified, which would then provide insight into the decomposition mechanism of LLM-105.

Appendix A: Particle Size Distribution Curves for Melamine (In µm)

Pristine Melamine

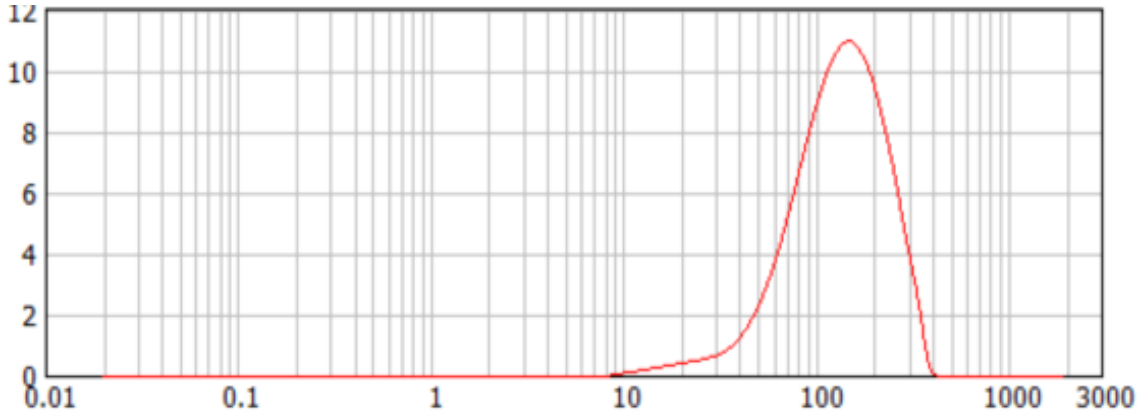

1melA

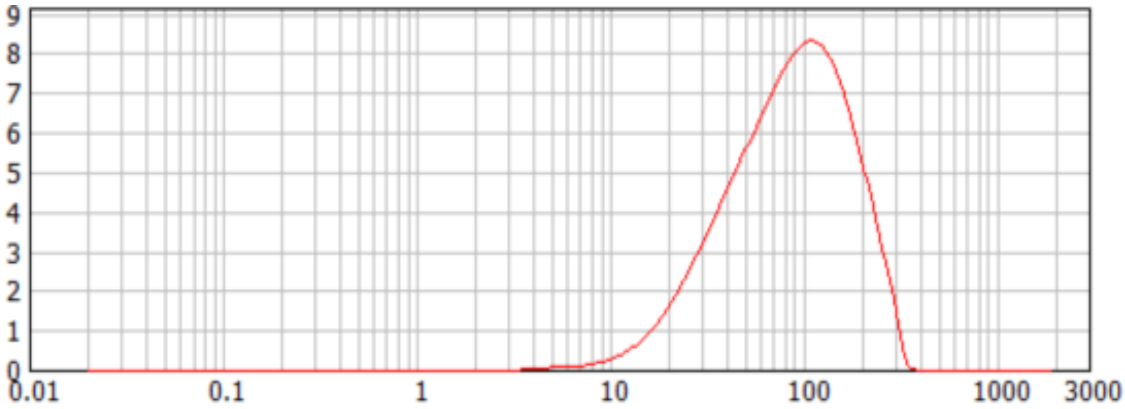

1melB

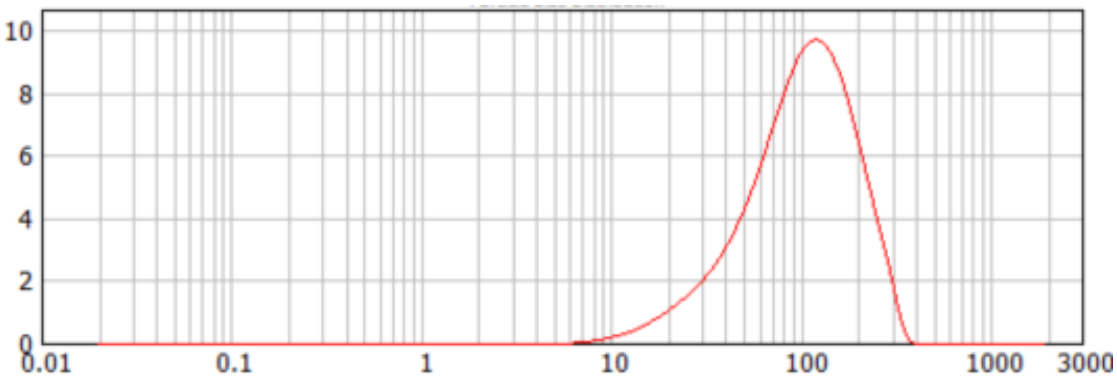

1melC

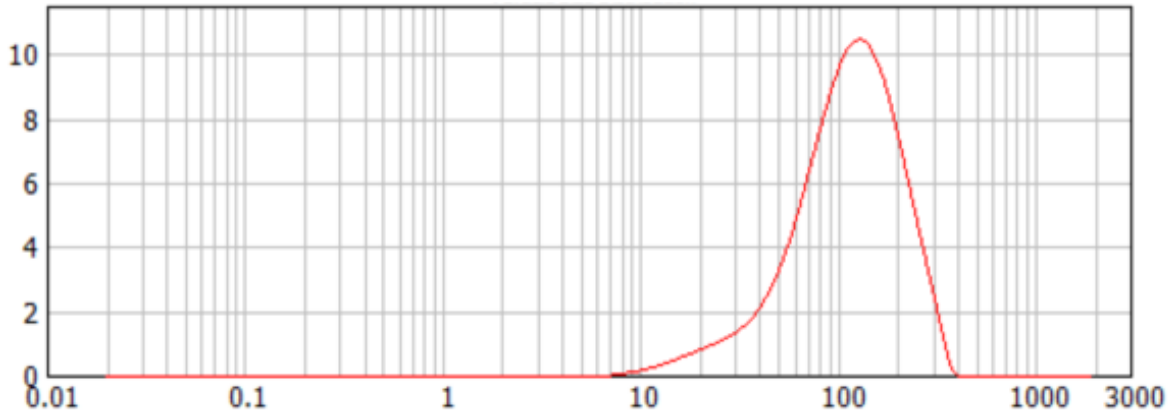

2melD

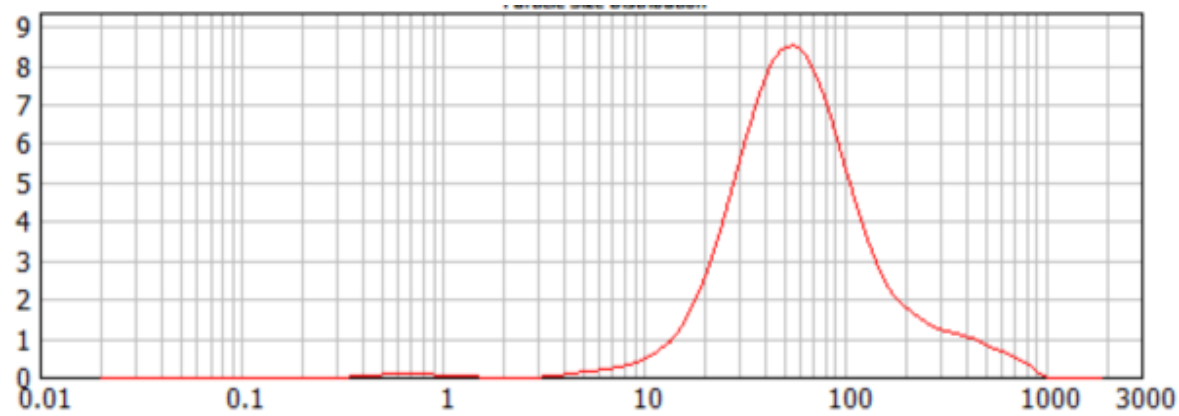

2melE

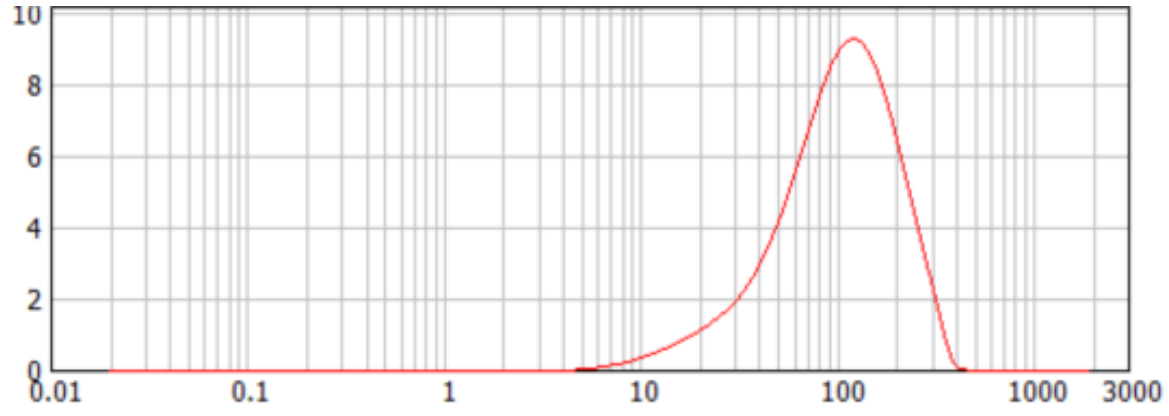

2melF

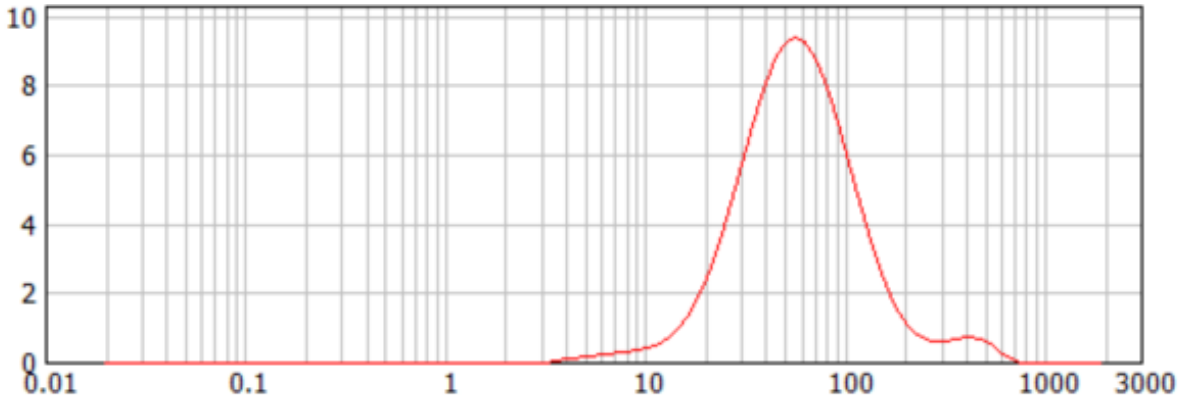

3melG

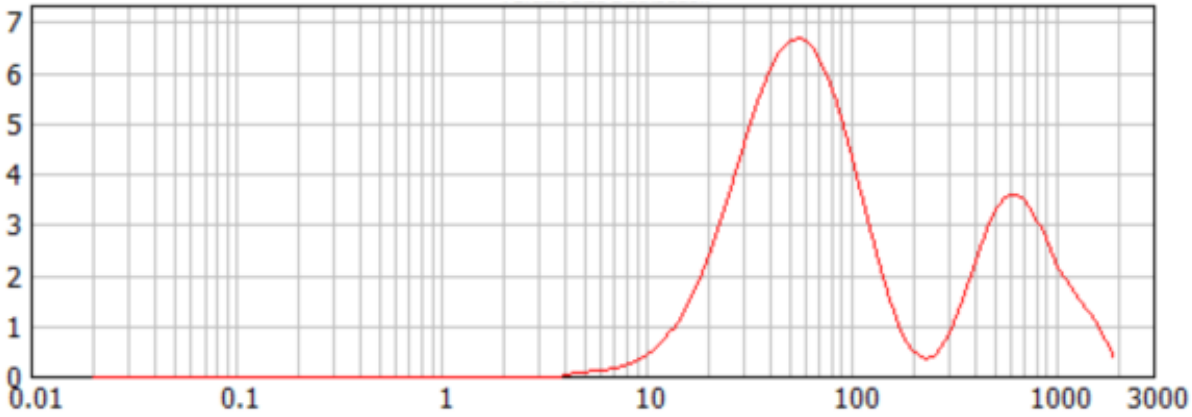

3melH

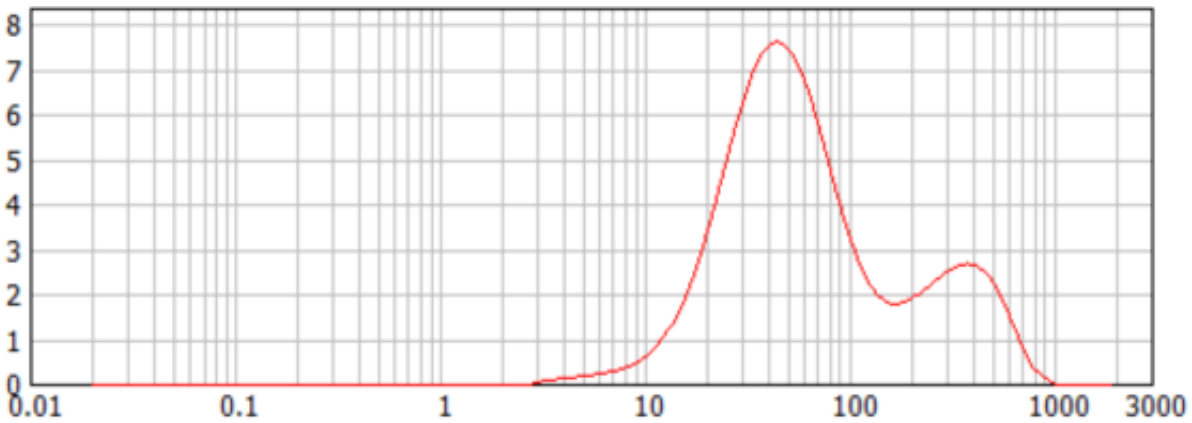

3melI

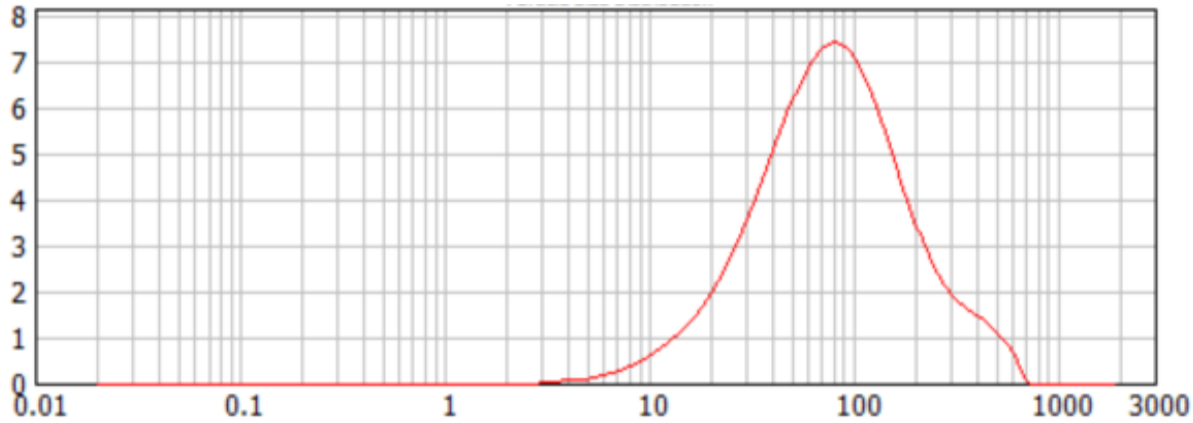
8
7
6
5
4
3
2
1
0
0.01
0.1
1
10
100
1000
3000

4melJ

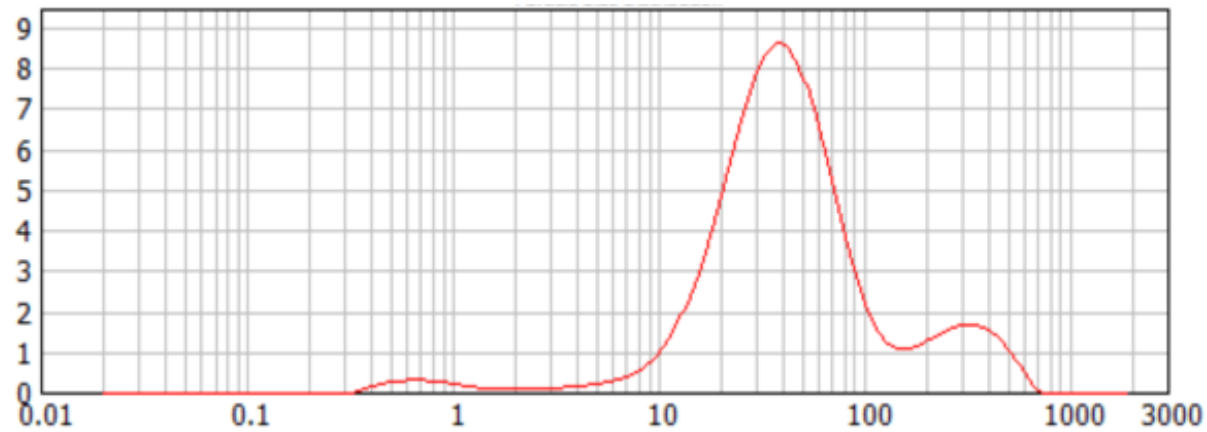
9
8
7
6
5
4
3
2
1
0
0.01
0.1
1
10
100
1000
3000

Bibliography

[1] P.W. Cooper, S.R. Kurowski, Introduction to the Technology of Explosives, *VCH Publishers Inc*, **1996**

[2] J.A. Zukas, W.P. Walters, Explosives Development and Fundamentals of Explosive Technology, *Springer*, **1998**

[3] C. Souers, P. Vitello, S. Esen, J. Kruttschnitt, H.A. Bilgin, *Propellants, Explosives, Pyrotechnics*, **2004**, 29, 19-26

[4] F.P. Bowden, A.D. Yoffe, Initiation and Growth of Explosion in Liquids and Solids, *Cambridge University Press*, **1952**

[5] J.E. Field, *Accounts of Chemical Research*, **1992,** 25, 489-496

[6] A.N. Dremin, Toward Detonation Theory, *Springer*, **1999**

[7] S.S. Rybanin, Y.M. Mikhailov, *Doklady Physical Chemistry*, **2006**, 409, 214-217

[8] R.E. Winter, J.E. Field, *Proceedings of the Royal Society of London A*, **1975**, 343, 399-413

[9] J.H.S. Lee, The Detonation Phenomenon, *Cambridge University Press*, **2008**

[10] J.W. Forbes, Shockwave Compression of Condensed Matter, *Springer*, **2012**

[11] A.N. Dremin, *Combustion, Explosion and Shock Waves*, **2000**, 36, 704-715

[12] E.N Aleksandrov, V.A. Veretennikov, A.N Dremin, K.K Shvedov, *Combustion, Explosion and Shock Waves*, **1967**, 3, 285-293

[13] C. Zhang, X. Wang, H. Huang, *Journal of the American Chemical Society*, **2008**, 130, 8359-8365

[14] R.D. Gilardi, R.J. Butcher, *Acta Crystallographica Section E- Structure Reports Online*, **2001**, 57, 657-658

[15] K.D.M. Harris, M. Tremayne, P. Lightfoot, P.G. Bruce, *Journal of the American Chemical Society*, **1994**, 116, 3543-3547

[16] C. Tarver. P. Urtiew, T. Tran, *Journal of Energetic Materials*, **2005**, 23, 183-203

[17] T. Tran, P. Pagoria, D. Hoffman, B. Cunningham, R. Simpson, R. Lee, L. Cutting, *Proceedings of the Twelfth International Detonation Symposium*, **2002**, 440-450

[18] J.L. Cutting, H.H Chau, R.L. Hodgin, D.M. Hoffman, F. Garcia, R.S. Lee, E. McGuire, A.R. Mitchell, P.F. Pagoria, R.D. Schmidt, R.L. Simpson, P.C. Souers, R.W. Swansiger, *Proceedings of the Eleventh International Detonation Symposium*, **1998**, 828-835

[19] A.W. Campbell, W.C. Davis, J.B. Ramsay and J.R. Travis, *Physics of Fluids*, **1961**, 4, 511-521

[20] R.H. Dinegar, R.H. Rochester, M.S. Millican, *Los Alamos National Laboratory Report LADC-5715*, **1962**

[21] C.L. Scott, *Proceedings of the Fifth International Detonation Symposium*, **1970**, 259-266

[22] J. Roth, *Proceedings of the Fifth International Detonation Symposium*, **1970**, 219-230

[23] D. Price, *Journal of Energetic Materials*, **1988**, 6, 283-317

[24] M.C. Chick, *Proceedings of the Fourth International Detonation Symposium*, **1965**, 349-358

[25] C.A. Honodel, J.R. Humphrey, R.C. Weingart, R.S. Lee, P. Kramer, *Proceedings of the Seventh International Detonation Symposium*, **1981**, 425-435

[26] Y. de Longueville, C. Fauquignon, H. Moulard, *Proceedings of the Sixth International Detonation Symposium*, **1976**, 105-114

[27] H. Moulard, J.W. Kury, A. Delclos, *Proceedings of the Eighth International Detonation Symposium*, **1985**, 902-913

[28] A.C. Schwarz, *Proceedings of the Seventh International Detonation Symposium*, **1981**, 1024-1028

[29] R.E. Setchell, *Combustion and Flame*, **1984**, 56, 343-345

[30] F. Schledbauer, A. Kretschmer, *Proceedings of the Tenth International Detonation Symposium*, **1993**, 876-880

[31] H. Moulard, *Proceedings of the Ninth International Detonation Symposium*, **1989**, 18-24

[32] C.M. Tarver, J.O. Hallquist, L.M. Erickson, *Proceedings of the Eighth International Detonation Symposium*, **1985**, 951-961

[33] Z. Wang, Y. Liu, J. Zhang, *Proceedings of the Fifth International Symposium on Test and Measurement*, **2003**, 849-852

[34] R.L. Simpson, F.H. Helm, P.C. Crawford, J.W. Kury, *Proceedings of the Ninth International Detonation Symposium*, **1989**, 25-38

[35] M.F. Gogulya, M.A. Brazhnikov, *Russian Journal of Physical Chemistry B*, **2010**, 4, 286-303

[36] G. Yang, F. Nie, H. Huang, L. Zhao, W. Pang, *Propellants, Explosives, Pyrotechnics*, **2006**, 31, 390-394

[37] K.Y. Lee, D.S. Moore, B.W. Asay, A. Llobet, *Journal of Energetic Materials*, **2007**, 25, 161-171

[38] Z. Yongxu, L. Daebin, L. Chunxu, *Propellants Explosives, Pyrotechnics*, **2005**, 30, 438-441

[39] H. Qiu, V. Stepanov, T. Chou, A. Surapaneni, A.R. Di Stasio, W.Y. Lee, *Powder Technology*, **2012**, 226, 235-238

[40] R.B. Patel, V. Stepanov, S. Swaszek, A. Surapaneni, H. Qiu, *Propellants, Explosives, Pyrotechnics*, **2015**, 40, 210-214

[41] V. Stepanov, T. M. Willey, J. Illavsky, J. Gelb, H. Qui, *Propellants, Explosives, Pyrotechnics*, **2013**, 38, 386-393

[42] V. Stepanov, V. Anglade, W.A.B. Hummers, A.V. Bezmelnitsyn, L.N. Krasnoperov, *Propellants, Explosives, Pyrotechnics*, **2011**, 36, 240–246.

[43] H. Qiu, V. Stepanov, A.R. Di Stasio, T. Chou, W.Y. Lee, *Journal of Hazardous Materials*, **2011**, 185, 489-493

[44] R.L. Simpson, P.A. Urtiew, D.L. Ornellas, G.L. Moody, K.J. Scribner, D.M. Hoffman, *Propellants, Explosives, Pyrotechnics*, **1997**, 22, 249-255

[45] D. Wang, B. Gao, G. Yang, F. Nie, H. Huang, *Journal of Nanomaterials*, **2016**, Article Number 5462097

[46] R.B. Patel, V. Stepanov, S. Swaszek, A. Surapaneni, H. Qiu, *Propellants, Explosives, Pyrotechnics*, **2016**, 41, 114-119

[47] Y. Bayat, R. Soleyman, M. Zarandi, *Journal of Molecular Liquids*, **2015**, 206, 190-194

[48] X. Guo, G. Ouyang, J. Liu, Q. Li, L. Wang, Z. Gu, F. Li, *Journal of Energetic Materials*, **2015**, 33, 24-33

[49] T. Hussain, Y. Liu, F. Huang, Z. Duan, *Journal of Energetic Materials*, **2016**, 34, 38-48

[50] H. Eyring, R.E. Powell, G.H. Duffrey, R.B. Darlin, *Chemical Reviews*, **1949**, 45, 69-181

[51] B.A. Khasainov, B.S. Ermolaev, H-N. Presles, P. Vidal, *Shock Waves*, **1997**, 7, 89-105

[52] B.C. Taylor, L.W. Ervin, *Proceedings of the Sixth International Detonation Symposium*, **1976**, 3-10

[53] P. Howe, R. Frey, B. Taylor, V. Boyle, *Proceedings of the Sixth International Detonation Symposium*, **1976**, 11-19

[54] J. Waschl, D. Richardson, *Journal of Energetic Materials*, **1991**, 9, 269-282

[55] H. Czerski, W.G. Proud, *Journal of Applied Physics*, **2007**, 102, 113515

[56] J.W. Addiss, W.G. Proud, *New Trends in Research of Energetic Materials*, **2008**, 40-51

[57] N.M. McGregor, A.J. Lindfors, *Proceedings of the American Physical Society Topical Group on Shock Compression of Condensed Matter*, **2007**, 955, 841-844

[58] M.L. Buses, S.M. Caulder, *Applied Magnetic Resonance*, **2004**, 25, 383-393

[59] S.M. Caulder, P.J. Miller, K.D. Gibson, J.M. Kelley, *Proceedings of the Thirteenth International Detonation Symposium*, **2006**, 656-661

[60] L. Borne, C. Patedoye, C. Spyckerelle, *Propellants, Explosives, Pyrotechnics*, **1999**, 24, 255-259

[61] L. Borne, *Proceedings of the Eleventh International Detonation Symposium*, **1998**, 657-663

[62] L. Borne, A. Beaucamp, *Proceedings of the Twelfth International Detonation Symposium*, **2002**, 35-43

[63] L. Borne, *Proceedings of the Tenth International Detonation Symposium*, **1993**, 286-293

[64] V. J. Bellitto, M.I. Melnik, *Applied Surface Science*, **2010**, 256, 3478-3481

[65] C.A. Stoltz, B.P. Mason, J. Hooper, *Journal of Applied Physics*, **2010**, 103527

[66] X. Song, Y. Wang, C. An, X Guo, F. Li, *Journal of Hazardous Materials*, **2008**, 159, 222-229

[67] Y.H. Kim, K. Lee, K.K. Koo, Y.G. Shul, S. Haam, *Crystal Research and Technology*, **2002**, 37, 928-944

[68] A.C. van der Steen, E. Skjold, *Joint Government/Industry Symposium on Insensitive Munitions Technology*, **1990**, 235

[69] H. Li, R. Xu, B. Kang, J. Li, X. Zhou, C. Zhang, F. Nie, *Journal of Applied Physics*, **2013**, 113, 203519

[70] N. Liu, Y. Li, S. Zeman, Y. Shu, B. Wang, Y. Zhou, Q. Zhaoc, W. Wang, *CrystEngComm*, **2016**, 18, 2843-2851

[71] R.M. Doherty, D.S. Watt, *Propellants, Explosives, Pyrotechnics*, **2008**, 33, 4-13

[72] M. Rhodes, Introduction to Particle Technology, *John Wiley and Sons Ltd*, **2008**

[73] N. Straessler, M. Mileham, M. Kramer, *Insensitive Munitions and Energetic Materials Technology Symposium*, **2012**, 13899

[74] A. Parker, R.P. Claridge, J. Hamid, W.G. Proud, *Propellants, Explosives, Pyrotechnics*, **2008**, 33, 55-59

[75] U. Teipel, *Propellants, Explosives, Pyrotechnics*, **1999**, 24, 134-139

[76] U Teipel, I. Mikonsaari, *Propellants, Explosives, Pyrotechnics*, **2002**, 27, 168-174

[77] N. Zhang, J. Xiong, E. Ding, *Journal of Inorganic Materials*, **2012**, 27, 855-859

[78] F.S.Romanski, E. Jayjock, F.J. Muzzio, M.S. Tomassone *Journal of Pharmaceutical Innovation*, **2011**, 6, 97-106

[79] G. Guiquan, G. Weiping, L. Jian, *Rare Metal Materials and Engineering*, **2011**, 40, 1827-1831

[80] C. Schilde, C. Mages-Sauter, A. Kwade, H.P. Schuchmann, *Powder Technology*, **2011**, 207, 353-361

[81] M.B. Talawar, A.P. Agarwal, M. Anniyappan, G.M. Gore, S.N. Asthana, S. Venugopalan, *Journal of Hazardous Materials*, **2006**, 137, 1848-1852

[82] M.N. Patil, G.M. Gore, A.B. Pandit, *Ultrasonics Sonochemistry*, **2008**, 15, 177-187

[83] Z. Yongxu, L. Dabin, L. Chunxu, *Propellants, Explosives, Pyrotechnics*, **2005**, 30, 438-441

[84] V. Stepanov, L.N. Krasnoperov, I.B. Elkina, X. Zhang, *Propellants, Explosives, Pyrotechnics*, **2005**, 30, 178-183

[85] O.A. Nafday, R. Pitchimani, B.L. Weeks, *Propellants, Explosives, Pyrotechnics*, **2006**, 31, 376-381

[86] Y. Bayat, V. Zeynali, *Journal of Energetic Materials*, **2011**, 29, 281-291

[87] M.W. Park, S.D. Yeo, *Chemical Engineering Research and Design*, **2012**, 90, 2202-2208

[88] A.F.M. Barton, *Chemical Reviews*, **1975**, 75, 731-753

[89] J. Chen, L.L. Wang, G.C. Yang, *Advanced Materials Research*, **2011**, 242, 2942-2945

[90] P.F. Pagoria, A.R. Mitchell, R.D. Schmidt, R.L. Simpson, F. Garcia, J.W. Forbes, R.W. Swansiger, D.M. Hoffman, *Lawrence Livermore National Laboratory Report UCRL-JC- 130518*, **1998**

[91] R. Weese, A. Burnham, H Turner, T. Tran, *Journal of Thermal Analysis and Calorimetry*, **2007**, 89, 465-473

[92] A.K. Sikder, G. Maddala, J.P. Agrawal, H. Singh, *Journal of Hazardous Materials*, **2001**, 84, 1-26

[93] S. Zeman, *Journal of Hazardous Materials*, **2006**, 132, 155-164

[94] J.L. Maienschein, *Journal of Physics: Conference Series 500*, **2014**, 052027

[95] R.W. Armstrong, C.S. Coffey, V.F. DeVost, W.L. Elban, *Journal of Applied Physics*, **1990**, 68, 979-984

[96] C.S. Coffey, J. Sharma, *Physical Review B*, **1999**, 60, 9365-9371

[97] C.L. Lu, J.L. Zhang, *Theory and Practice of Energetic Materials*, **2003**, 5, 677-680

[98] Y. Li, X. Zheng, *Science and Technology of Energetic Materials*, **2016**, 77, 34-39

[99] Q. Zhang, S. Hu, H. Liang, *Defence Science Journal*, **2013**, 63, 108-113

[100] R.H.B. Bouma, A.G. Boluijt, H.J. Verbeek, A.E.D.M. van der Heijden, *Journal of Applied Physics*, **2008**, 103, 093517

[101] R. Sivabalan, G.M. Gore, U R. Nair, A. Saika, S. Venugopalan, B.R. Gandhe, *Journal of Hazardous Materials*, **2007**, 139, 199-203

[102] H. Chen, L. Li, S. Jin, S. Chen, Q. Jiao, *Propellants, Explosives, Pyrotechnics*, **2012**, 37, 77-82

[103] H. Huang, J. Wang, W. Xu, R. Xie, *Propellants, Explosives, Pyrotechnics*, **2009**, 34, 78-83

[104] Recommendations on the Transport of Dangerous Goods: Manual of Tests and Criteria, Fifth Edition, *United Nations, New York*, **2009**

[105] Energetic Materials Testing and Assessment Policy Committee (EMTAP) Manual of Tests, *Defence Ordnance Safety Group*, **2016**

[106] R. Robertson, *Journal of the Chemical Society*, **1921**, 119, 1–29

[107] R. Robertson, *Nature*, **1921**, 107, 524-527

[108] H.N. Mortlock, J. Wilby, *Explosivstoffe*, **1966**, 14, 49-55

[109] H. Koenen, K.H. Ide, K.H. Swart, *Explosivstoffe*, **1961**, 9, 30-42

[110] F. Trimborn, *Explosivstoffe*, **1970**, 18, 49-56

[111] W.J. Dixon, A.M. Mood, *Journal of the American Statistical Association*, **1948**, 43, 109-126

[112] L.R. Simpson, M.F. Foltz, *Los Alamos National Laboratory Report UCRL-ID-119665*, **1995**

[113] L. Avrami, M.S. Kirshenbaum, *Dover Large Caliber Weapon Systems Laboratory Report no. ARLCDTR-81010*, **1981**

[114] D.C. Mullenger, *14th International Pyrotechnics Seminar*, **1989**, 293-313

[115] R. Bowes, *Second International Symposium on Fireworks*, **1994**, 19-31

[116] K.R. Becker, R.W. Watson, *Conference Proceedings of The Standardization of Safety and Performance Tests for Energetic Materials*, **1977**, 1, 415-430

[117] L.C. Smith, *Conference Proceedings of The Standardization of Safety and Performance Tests for Energetic Materials*, **1977**, 1, 397-414

[118] M. Alouaamari, M.H. Lefebvre, C. Perneel, M. Herrmann, *Propellants, Explosives, Pyrotechnics*, **2008**, 33, 60-65

[119] G.W. Brown, M.M. Sandstrom, D.N. Preston, C.J. Pollard, K.F. Warner, D.N. Sorensen, D.L. Remmers, J.J. Phillips, T.J. Shelley, J.A. Reyes, P.C. Hsu, J.G. Reynolds, *Propellants, Explosives, Pyrotechnics*, **2015**, 40, 221-232

[120] N. Radacsi, R.H.B. Bouma, E.L.M. Krabbendam-la Haye, J.H. ter Horst, A.I. Stankiewicz, A.E.D.M. van der Heijden, *Propellants, Explosives, Pyrotechnics*, **2013**, 38, 761-769

[121] M. Berthelot, Explosives and Their Power, *J. Murray*, **1892**

[122] W. Taylor, A. Weale, *Proceedings of the Royal Society of London A*, **1932**, 138, 92-116

[123] W. Taylor, A. Weale, *Transactions of the Faraday Society*, **1938**, 34, 995-1003

[124] K.K. Andreev, J.B. Chariton, *Transactions of the Faraday Society*, **1935**, 31, 797-804

[125] F.P. Bowden, M.F.R. Mulcahy, R.G. Vines, A. Yoffe, *Proceedings of the Royal Society of London A*, **1947**, 188, 291-311

[126] F.P. Bowden, O.A. Gurton, *Proceedings of the Royal Society of London A*, **1949**, 198, 337-349

[127] E.K. Rideal, A.J.B. Robertson, *Proceedings of the Royal Society of London A*, **1948**, 195, 135-150

[128] J.E. Balzer, J.E. Field, M.J. Gifford, W.G. Proud, S.M. Walley, *Combustion and Flame*, **2002**, 130, 298-306

[129] J.D. Blackwood, F.P. Bowden, *Proceedings of the Royal Society of London A*, **1952**, 213, 285-306

[130] S.N. Heavens, J.E. Field, *Proceedings of the Royal Society of London A*, **1974**, 338, 77-93

[131] S.N. Heavens, J.E. Field, *Combustion and Flame*, **1972**, 18, 473-476

[132] S.M. Walley, J.E. Field, R.A. Biers, W.G. Proud, D.M. Williamson, A.P. Jardine, *Propellants, Explosives, Pyrotechnics*, **2015**, 40, 351-365

[133] J.E. Field, G.M. Swallowe, S.N. Heavens, *Proceedings of the Royal Society of London A*, **1982**, 382, 231-244

[134] G.M. Swallowe, J.E. Field, *Proceedings of the Royal Society of London A*, **1982**, 379, 389-408

[135] J.E. Field, N.K. Bourne, S.J.P. Palmer, S.M. Walley, *Philosophical Transactions of the Royal Society of London A*, **1992**, 339, 269-283

[136] S. M. Walley, J. E. Field, S. J. P. Palmer, *Proceedings of the Royal Society of London A*, **1992**, 438, 571-583

[137] S.M. Walley, J.E. Balzer, W.G. Proud, J.E. Field, *Proceedings of the Royal Society of London A*, **2000**, 456, 1483-1503

[138] J.E. Balzer, C.R. Siviour, S.M. Walley, W.G. Proud, J.E. Field, *Proceedings of the Royal Society of London A*, **2004**, 460, 781-806

[139] Y.Q. Wu, F.L. Huang, Z.Y. Zhang, *RSC Advances*, **2012**, 2, 4152-4163

[140] Y.Q. Wu, F.L. Huang, *Combustion Science and Technology*, **2013**, 185, 269-292

[141] Y. Wen, X. Long, Y. Xiang, S. Yu, X. Dai, M. Li, *Propellants, Explosives, Pyrotechnics*, **2015**, 40, 433-438

[142] D.N. Preston, G.W. Brown, B.C. Tappan, D.M. Oshwald, J.R. Koby, M.L. Schoonover, *Journal of Physics: Conference Series*, **2014**, 500, 182033

[143] P.B. Wagh, S.V. Ingale, R. Kumar, R.H. Naina, T.C. Kaushik, S.C. Gupta, *Defence Science Journal*, **2015**, 65, 4, 287-291

[144] A. Norazirah, S.H.S. Fuad, M.H.M. Hazizan, *Procedia Chemistry*, **2016**, 19, 702-708

[145] N.K. Bourne, *Measurement Science and Technology*, **2003**, 14, 273-278

[146] S.A. Sheffield, R.L. Gustavsen, A.R. Martinez, R.R. Alcon, *Los Alamos National Laboratory Report LA-UR-96-3875*, **1996**

[147] R.E. Winter, S.S. Sorber, D.A. Salisbury, P. Taylor, R. Gustavsen, S. Sheffield, R. Alcon, *Shock Waves*, **2006**, 15, 89-101

[148] R.R Alcon, R.N. Mulford, *AIP Conference Proceedings*, **1996**, 370, 1057-1060

[149] R.L. Gustavsen, R.R. Alcon, L.L. Davis, S.A. Sheffield, *Los Alamos National Laboratory Report LA-UR-01-5016*, **2001**

[150] K.S. Vandersall, M.R. DeHaven, S.L. Strickland, C.M. Tarver, H.K. Springer, M.R. Cowan, *AIP Conference Proceedings*, **1979**, 100045

[151] F. Garcia, K.S. Vandersall, C.M. Tarver, P.A. Urtiew, *Proceedings of the American Physical Society Topical Group on Shock Compression of Condensed Matter*, **2007**, 955, 907-910

[152] F. Garcia, K.S. Vandersall, C.M. Tarver, *Journal of Physics: Conference Series 500*, **2014**, 052048

[153] D. Ma, P. Chen, Q. Zhou, *Journal of Applied Physics*, **2013**, 114, 113505